UNIVERSITY OF SOUTHAMPTON

FACULTY OF NATURAL AND ENVIRONMENTAL SCIENCES

Chemistry

Development of X-Ray Absorption Fine Structure Techniques for the Study of Reactions of Heavy Metal Complexes in Solution

by

Richard Alexander Ilsley

Thesis for the degree of Doctor of Philosophy

January_2015

UNIVERSITY OF SOUTHAMPTON

ABSTRACT

FACULTY OF NATURAL AND ENVIRONMENTAL SCIENCES

Chemistry

Thesis for the degree of Doctor of Philosophy

DEVELOPMENT OF X-RAY ABSORPTION FINE STRUCTURE TECHNIQUES FOR THE STUDY OF REACTIONS OF HEAVY METAL COMPLEXES IN SOLUTION

Richard Alexander Ilsley

Extended X-ray absorption fine structure spectroscopy (EXAFS) has been used to characterise polyoxometalate (POM) species and study their reactions on the minute time-scale. Lindqvist-type tungstates have been characterised using quick extended X-ray absorption fine structure spectroscopy (QEXAFS). Differentiation between $[LMW_5O_{18}]^{3-}$ species with different heterometals has been demonstrated. The formation of $[W_6O_{19}]^{2-}$ and $[(Ph_2PO_2)(ZrW_5O_{18})_2]^{6-}$ have been studied. Intermediates in the formation reaction for $[W_6O_{19}]^{2-}$ may include a cluster with 3 tungsten atoms and a cluster with 5 tungsten atoms.

Keggin-type molybdates have also been characterised using QEXAFS. EXAFS data has been collected up to 20.7 $Å^{-1}$ and distances of 6.2 Å have been resolved. Differentiation between different capped $[PMo_{12}O_{40}(MX)_2]^{n-}$ species, where the capping species is bound to the core $[PMo_{12}O_{40}]^{3-}$ by 4 bridging oxygen atoms, and reduced $[PMo_{12}O_{40}]^{n-}$ species has been demonstrated. The Mo···Mo distances in reduced POMs are longer than in unreduced POMs. Addition of metal ions to electron-rich Keggin-type POMs by reductive aggregation has been studied and shifting peaks in Fourier transform spectra show the formation of clusters around the metal ions.

$[Cu(dmp)_2][PF_6]$ was studied using X-ray absorption near edge spectroscopy (XANES), X-ray absorption fine structure spectroscopy (XAFS), resonant inelastic X-ray spectroscopy (RIXS) and X-ray emission spectroscopy (XES). Distances of 4.4 Å have been resolved using XAFS spectroscopy. RIXS has been used to demonstrate the 4 eV difference between the K_α peaks for Cu^{I} and Cu^{II}. The Cu^{II} state was generated electrochemically and differentiation between Cu^{I} and Cu^{II} has been possible using K_α XES.

Contents

List of tables

List of figures

DECLARATION OF AUTHORSHIP

I, Richard Alexander Ilsley

declare that the thesis entitled

Development of X-Ray Absorption Fine Structure Techniques for the Study of Heavy Metal Complexes in Solution

and the work presented in the thesis are both my own, and have been generated by me as the result of my own original research. I confirm that:

- this work was done wholly or mainly while in candidature for a research degree at this University;
- where any part of this thesis has previously been submitted for a degree or any other qualification at this University or any other institution, this has been clearly stated;
- where I have consulted the published work of others, this is always clearly attributed;
- where I have quoted from the work of others, the source is always given. With the exception of such quotations, this thesis is entirely my own work;
- I have acknowledged all main sources of help;
- where the thesis is based on work done by myself jointly with others, I have made clear exactly what was done by others and what I have contributed myself;
- none of this work has been published before submission.

Signed: ……..

Date:……

Acknowledgements

I would like to express my gratitude to my supervisors, Professor John Evans, Professor Moniek Tromp and Professor Andy Dent, and to my advisor, Professor W. Levason, for their guidance, help and support, for their insights and the contributions they have made throughout the project.

I would also like express my gratitude to Doctor R. J. Errington and his research group at Newcastle University, Professor Andrea Russell, Doctor Stephen Price and Doctor Michelle Hamilton for their help and contributions to the project. I would like to thank Alan Glass and the team in the mechanical workshop for their efforts in fabricating the XAS solution cell and to my research group for their help and advice during the project.

I would like to thank Diamond Light Source, the University of Southampton and the Research Complex at Harwell for funding the project and for the use of facilities.

I would also like to thank my parents and family for their support throughout the duration of the project and, in particular, during the time I have spent writing this thesis.

I would like to dedicate this thesis to my wife, Ceren, who has been an invaluable source of support and encouragement to me throughout the project. I hope that this research will make a positive contribution to her future.

Definitions and Abbreviations

Bcp – 2,9-dimethyl-4,7-diphenyl-1,10-phenanthroline

Dbp – 2,9-dibutyl-1,10-phenanthroline

Dmp – 2,9-dimethyl-1,10-phenanthroline

Dpp – 2,9-diphenyl-1,10-phenanthroline

EDE – Energy dispersive extended X-ray absorption fine structure

EXAFS – Extended X-ray absorption fine structure

F-C – Franck Condon

FT-IR – Fourier transform infrared

HERFD – High energy resolution fluorescence detection

ISC – Intersystem crossing

LCF – Linear combination fit

MLCT – Metal to ligand charge transfer

NMR – Nuclear magnetic resonance spectroscopy

POM – Polyoxometalate

QEXAFS – Quick extended X-ray absorption fine structure

TA – Transient Absorption

T-D DFT – Time-dependent density functional theory

UV / Vis – Ultraviolet / Visible spectroscopy

XAFS – X-ray absorption fine structure

XANES – X-ray absorption near edge spectroscopy

XAS – X-ray absorption spectroscopy

XES – X-Ray emission spectroscopy

1. Introduction

1.1 Introduction

1.1.1 Project Aims

Different chemical reactions occur at different rates ranging from nanoseconds to hours. Two examples are: the formation reaction of polyoxometalate (POM) species which can take minutes to hours to reach completion and the photo-excitation of copper(I) diimine complexes which occurs on a nanosecond time-scale. As there is such a diversity of the time-scales on which reactions occur, different time-resolved methods are necessary to study the nature of the reactions.

The focus of this project is the development of time-resolved X-ray absorption fine structure (XAFS) techniques. The formation of Lindqvist-type POM species will be studied and the intermediates in the formation reaction will be identified using XAFS spectroscopy for the first time. These POM species will be characterised in solution using XAFS for the first time and intermediates species in the formation reaction will be observed. A method for characterising the reaction intermediates will be developed.

Studies of the photo-excitation of these complexes give information about the nature of the electron transfer process which takes place on a nanosecond time scale. X-ray absorption spectroscopy (XAS) and X-ray emission spectroscopy (XES) studies have been carried out on the ground and electrochemically excited states of copper diimine complexes the techniques used can be applied to photo-excitation experiments.

1.2 Polyoxometalates

1.2.1 Introduction

POMs are soluble molecular metal oxide species which are analogous to extended solid oxide materials. They can be used as catalysts or catalyst supports and are useful in the synthesis of functional materials, such as catalysts and in nanoscale devices. POMs have good potential as active catalysts, catalyst precursors, supports for immobilised homogeneous catalysts or as molecular models for heterogeneous metal oxide catalysts and can be used as Brønsted acids or oxidation catalysts. Heterometallic POMs are potential models for heterogeneous catalysts in which an active metal site is supported on or within another metal oxide matrix. Using POMs as model heterogeneous catalysts allows the study of the reactivity of isolated heterometal sites giving an understanding of the activity of mixed oxide catalysts. Tungsten oxide supported on titanium or zirconium oxide is strongly acidic. Studies suggest that Brønsted acid activity is associated with the formation of polynuclearoxo-tungsten aggregates.[1] X-ray crystallography has been used to provide crystallographic structures for POMs in the solid state and structural information about POM structures in solution has been provided by multinuclear NMR spectroscopies,[2] electrochemical analyses[3] and Raman spectroscopy.[4] Extended X-ray absorption fine structure (EXAFS) spectroscopy can be used to provide a structural characterisation of POM structures[5,6] and provide an indication of the disorder in the interatomic distances.

1.2.2 Structure and Synthesis of Polyoxometalates

A general formula for POM structures can be given as $M_mO_y^{n-}$ (isopolyanions) and when the POM contains a heteroatom the formula $X_xM_mO_y^{n-}$ (heteropolyanions) can be used. The heteroatom in a heteropolyanion is not limited to metal species; over 70 elements exist in heteropolyanionic species.

POMs exist in many forms (for example, hexametalates and decametalates) and there are many types, for example, Lindqvist, Keggin[7] and Dawson.[8] The hexametalate structure (figure 1.1) was discovered by Lindqvist[9] and $[W_6O_{19}]^{2-}$ is an example of this structure. The tungsten atoms are arranged in an octahedron around the interstitial oxygen atom. $[W_6O_{19}]^{2-}$ can be synthesised by the hydrolytic aggregation of $[WO_4]^{2-}$ and $WO(OR)_4$ (equation 1.1). $WO(CH_3O)_4$ exists as a dimeric species, $[\{WO(CH_3O)_4\}_2]$, which exhibits dynamic solution behaviour involving initial cleavage of one of the bridging methoxide groups.[10] POMs with heteroatoms can also be synthesised in a similar fashion, for example the heterometallicalkoxide species $[(RO)MW_5O_{18}]^{3-}$ (M = Ti, Zr, Sn, equation 1.2) and $[(RO)NbW_5O_{18}]^{2-}$ (equation 1.3).

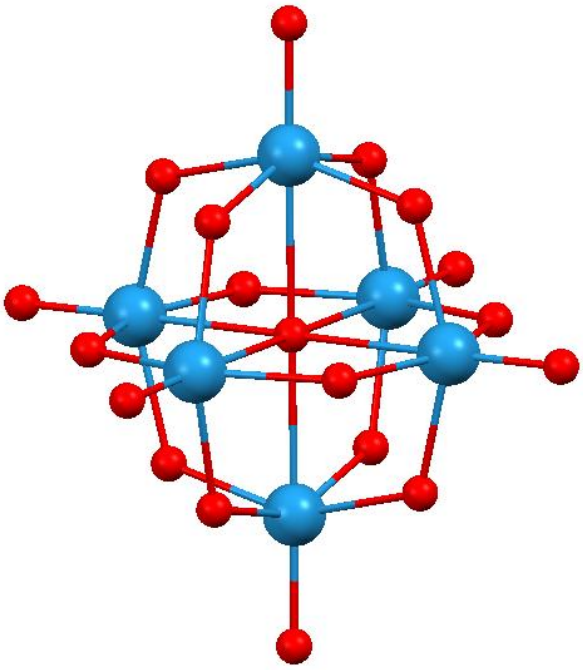

Figure 1.1: Lindqvist-type polyoxometalate. Blue spheres are metal atoms, red spheres are oxygen atoms.

$$[WO_4]^{2-} + 5\ WO(OR)_4 + 10\ H_2O \rightarrow [W_6O_{19}]^{2-} + 20\ ROH \qquad \text{(Equation1.1)}$$

$$3\ [WO_4]^{2-} + 7\ WO(OR)_4 + 2\ M(OR)_4 + 17\ H_2O \rightarrow 2\ [(RO)MW_5O_{18}]^{3-} + 34\ ROH \qquad \text{(Equation 1.2)}$$

$[WO_4]^{2-} + 4\ WO(OR)_4 + Nb(OR)_5 + 10\ H_2O \rightarrow [(RO)NbW_5O_{18}]^{2-} + 20\ ROH$

(Equation1.3)

$[W_5O_{18}]^{6-}$ is a virtual species, for which some spectroscopic evidence has been reported.[11–13] The synthesis of this species is given in equation 1.4. This virtual precursor can be used in the synthesis of $[ClTiW_5O_{18}]^{3-}$ (equation 1.5), $[(L)CoW_5O_{18}]^{4-}$ (equation 1.6) and $[(L)FeW_5O_{18}]^{4-}$.[11] The kinetic stability of $[W_5O_{18}]^{6-}$ in aqueous reaction involving the dissociation of $[Ce(W_5O_{18})_2]^{8-}$ has been demonstrated.[13] $[W_6O_{19}]^{2-}$ has O_h symmetry and replacing one of the tungsten atoms with a heterometal results in lowering of this symmetry. The higher charge of the heteropolyanion causes a bathochromic shift in the W-O vibrations. Synthesis of POMs can be carried out in non-aqueous conditions, but syntheses are most commonly carried out in aqueous solution.

$3\ [WO_4]^{2-} + 2\ WO(OR)_4 + 4\ H_2O \rightarrow [W_5O_{18}]^{6-} + 8\ ROH$ (Equation1.4)

$[W_5O_{18}]^{6-} + TiCl_4 \rightarrow [ClTiW_5O_{18}]^{3-} + 3\ Cl^-$ (Equation1.5)

$[W_5O_{18}]^{6-} + CoCl_2 \rightarrow [(L)CoW_5O_{18}]^{4-} + 2\ Cl^-$ (Equation1.6)

There are many approaches to the synthesis of heteropolyanionic POMs: incorporating the heterometal into pre-formed structures - usually Keggin[7] or Dawson-type;[8,14] the formation of pentagonal M_5 structures in acidified aqueous solution;[15,16] alkaline hydrolysis of metal oxides;[17] and hydrolytic aggregation.[18] An alkoxido group can be substituted with protic reagents[12,19] and this chemistry makes it possible to bind the hexametalate to a surface.[20] The ability of POM monomers to dimerise is determined by steric demands and the incorporation of aryloxide groups allows large structures incorporating many POM units to be synthesised with defined geometry.

Heteropolyanion structures, $[VW_5O_{19}]^{3-}$ and $[V_2W_4O_{19}]^{4-}$, have been studied and the results revealed that the hexametalate structures are distorted from the octahedral $[M_6O_{19}]^{n-}$ and in structures with 2 heteroatoms only the cis isomer was present.[2] A W···W distance of 3.27 Å was observed and a V···W distance of 3.197 Å in $[VW_5O_{19}]^{3-}$ and 3.20 Å in $[V_2W_4O_{19}]^{4-}$ was observed. M-O-W bridging

oxygen sites are the most basic sites in a heteropolyanion.[21,22] The CoW_5 Lindqvist-type anion exists as a dimer – $[\{CoW_5O_{18}H\}_2]^{6-}$ (figure 1.2) and the cobalt is present as Co^{II}. Two protons are associated with Co-O-W bridging oxygen atoms, one of which is located in a hydrogen bond between the two $[CoW_5O_{18}]^{3-}$ units, whereas the other is disordered between an adjacent oxygen atom and its symmetry related site on the other $[CoW_5O_{18}]^{3-}$ unit. Treatment with pyridine cleaves this dimer to give $[(py)CoW_5O_{18}H]^{3-}$.

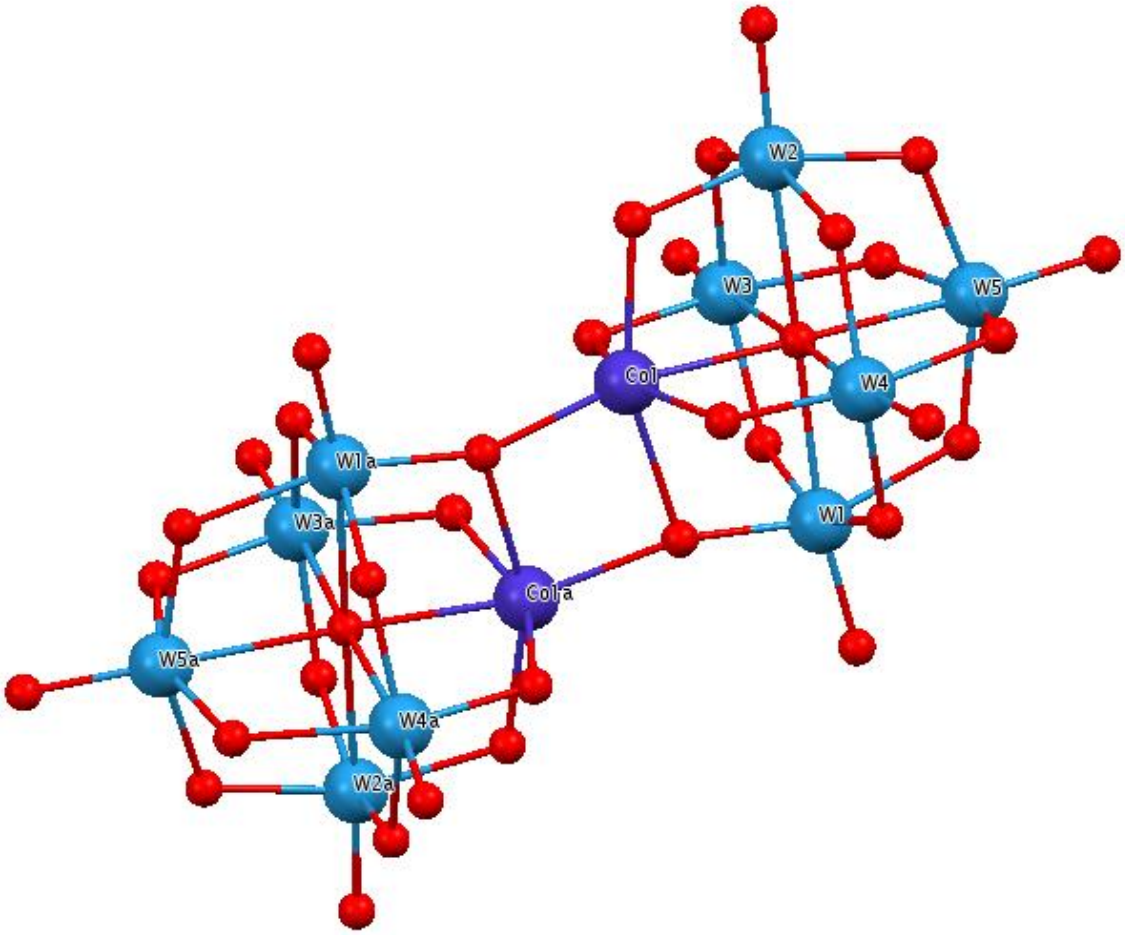

Figure 1.2: Structure of $[\{CoW_5O_{18}H\}_2]^{6-}$. Red spheres represent oxygen atoms, blue spheres represent metal atoms.

Metals from groups 8 - 11 have been incorporated into Keggin-type POMs and larger structures constructed from various fragments of Keggin units, but substitution into Lindqvist structures has been limited to the electrophilic metals from groups 4, 5, 6 and 14. $[X_2(M_5O_{18})]^{n-}$ POM derivatives have been reported in which Ag, Pt or lanthanide atoms have been bonded exo to the POM unit.[23–26] The synthesis of a Co substituted Lindqvist-type tungstate in acetonitrile is demonstrated in equations 1.7 – 1.9:[11]

$$3\ WO_4^{2-} + 2\ WO(CH_3O)_4 + 4\ H_2O \rightarrow W_5O_{18}^{6-} + 8\ CH_3OH \qquad \text{(Equation 1.7)}$$

$$[W_5O_{18}]^{6-} + Co^{2+} \rightarrow ½\ [\{CoW_5O_{18}H\}_2]^{6-} \qquad \text{(Equation 1.8)}$$

$$[\{CoW_5O_{18}H\}_2]^{6-} + 2\ C_5H_5N \rightarrow 2\ [(C_5H_5N)CoW_5O_{18}H]^{3-} \qquad \text{(Equation 1.9)}$$

1.2.2.1 Titanium in Heteropolytungstates

Tungsten oxide supported on titania is a promising solid acid catalyst with redox and photo-catalytic activity. Its uses include selective reduction of NO_x in exhaust gases and alkene conversions.[19] The reactivity of the titanium in the POM cage has been studied[19] and it has been proposed that metal alkoxide species are intermediates in the activation of hydrocarbons on solid heteropolyacids. Activation barriers are lower and chemisorption energies are more exothermic for the formation of alkoxide groups than for analogous reactions on zeolites.[27]

A non-aqueous hydrolytic synthesis of $[TBA]_6[(CH_3O)TiW_5O_{18}]$ in acetonitrile has been reported (equation 1.10).[18] The OR group can be substituted by reacting the $[(CH_3O)TiW_5O_{18}]^{3-}$ anion with ROH at 90 – 100 ˚C for several days (equation 1.11). In $[XTiW_5O_{18}]^{2-}$ salts, the titanium is always 6-coordinate.

$$3\ WO_4^{2-} + 7\ WO(CH_3O)_4 + 2\ Ti(CH_3O)_4 + 17\ H_2O \rightarrow 2\ [(CH_3O)TiW_5O_{18}]^{3-} + 34\ CH_3OH \qquad \text{(Equation 1.10)}$$

$[(CH_3O)TiW_5O_{18}]^{3-} + ROH \leftrightarrow [(RO)TiW_5O_{18}]^{3-} + CH_3OH$ (Equation 1.11)

Hydrolysis of $[(CH_3O)TiW_5O_{18}]^{3-}$ has resulted in the production of a dimeric species, $[(\mu\text{-}O)(TiW_5O_{18})_2]^{6-}$, which is a reversible reaction.[19] Aryloxide derivatives can be synthesised by reacting $[(CH_3O)TiW_5O_{18}]^{3-}$ with a phenol. NMR studies have indicated that there may be an intermediate in the reaction between $[(CH_3O)TiW_5O_{18}]^{3-}$ and 4-MeC_6H_4OH which may be formed by a stepwise proton transfer process.[19]

The W-O bond in Ti-O-W is shorter than the W-O bond in W-O-W. The shorter Ti-OC bonds and larger Ti-O-C angles for alkyloxide derivatives suggest that a greater degree of O to Ti π donation is present than in the aryloxide derivatives. In these aryloxide derivatives there can be different degrees of O to M π bonding depending on the orientation of the aryloxide group. There is evidence that the alkoxide ligand is a non-innocent[28] ligand and it has been shown that γ-H abstraction can take place in the vapour phase decomposition of group 4 metal alkoxides at temperatures exceeding 300 °C.[29–31] In the reaction between $[(CH_3O)TiW_5O_{18}]^{3-}$ and HX it is unlikely that a seven-coordinate intermediate is formed with X coordinated to Ti due to the size of the titanium atom. There are peaks in NMR spectra[19] that may be due to intermediates in a step-wise reaction. It is possible that the oxygen in the $[CH_3O]^-$ or Ti-O-W are protonated in a first step of this reaction.[32] Where $[CH_3O]^-$ is protonated CH_3OH will be lost and the X^- can then coordinate to the titanium atom. Where Ti-O is protonated, the proton migrates to the alkoxide and CH_3OH is lost. Protonation at Ti=O and Ti-O-W are both exothermic.

1.2.2.2 Zirconium in Heteropolytungstates

Zirconia-supported oxides are promising catalysts for isomerisation of light alkanes to high octane gasoline. $[NBu^n_4]_6[\{(\mu\text{-}CH_3O)ZrW_5O_{18}\}_2]$ is a Zr^{IV}-substituted Lindqvist-type POM that is bridged by a methoxo group and can be synthesised as reported previously.[12] H^1 NMR studies show no evidence of the dissociation of $[NBu^n_4]_6[\{(\mu\text{-}CH_3O)ZrW_5O_{18}\}_2]$ in solution and further NMR studies have

revealed that an intermediate, $[(\mu\text{-}CH_3O)(\mu\text{-}HO)(ZrW_5O_{18})_2]^{6-}$, is formed during the hydrolysis of $[NBu^n_4]_6[\{(\mu\text{-}CH_3O)ZrW_5O_{18}\}_2]$. In $[\{XZrW_5O_{18}\}_n]^{3-}$, the steric interactions between X and $[ZrW_5O_{18}]^{3-}$ are important. The coordination number of the zirconium is restricted to 6 for aryloxide ligands, but if chelating ligands are present a coordination number of 7 is possible. Upon recrystallisation of $[(Ph_2PO_2)ZrW_5O_{18}]^{3-}$, $[\{(\mu_3\text{-}OH)_2(ZrW_5O_{18})_3H]$ was formed. The protonated sites are the oxygen atoms in the Zr-O-Zr and Zr-O-W sites. Studies have shown that activation barriers for the formation of surface alkoxides in this system are lower than those for similar reactions on zeolites.[27] Zr/W POMs could allow the development of an understanding of molecular level reactions which occur on zirconia-supported tungsten oxide catalysts. By using a non-aqueous route for the synthesis of $[(RO)MW_5O_{18}]$, where M is a group 4 or 5 transition metal, the extent of hydrolysis can be controlled and alkoxide groups at the heterometal sites can be retained.[12] This can allow studies of the reactivity of the species and ^{183}W and ^{17}O NMR experiments have been carried out with the products of this reaction.[12] Crystallographic characterisation has revealed that $[(CH_3O)ZrW_5O_{18}]^{3-}$ exists as a dimer with bridging hydroxide groups. A variable-temperature ^1H NMR study has revealed that dissociation into monomeric units between ambient temperature and 75 °C is slow.[12] Hydrolysis of this product results in a hydroxide bridged dimer via an intermediate, $[(\mu\text{-}OH)(\mu\text{-}CH_3O)ZrW_5O_{18}]^{6-}$.

In $[\{(\mu\text{-}OH)ZrW_5O_{18}\}_2]^{6-}$ there are hydrogen bonds between the H of the OH group and an oxygen from each $[ZrW_5O_{18}]^{3-}$ unit. It has been proposed that it is possible that these hydrogen bonds are also present in $[\{(\mu\text{-}CH_3O)ZrW_5O_{18}\}_2]^{6-}$.[12] Aryloxide derivatives such as $[(C_6H_6O)ZrW_5O_{18}]^{3-}$ are monomeric. The high charge of the ZrW_5 unit and the basicity of the Zr-O-W oxygen sites[21] means that during a reaction with HX, it is possible that the Zr-O-W oxygens are protonated and the proton migrates to the methoxide and results in cleavage of the bridge. X^- can then coordinate to the Zr and MeOH is lost. However, it is possible that the dimer dissociates into monomers first, promoted by donor solvents, allowing HX to coordinate to Zr followed by loss of MeOH.

Oxygen exchange occurs between water and the oxometalate cage.[12,33] ^{17}O NMR studies suggest that either cleavage of one or both of the Zr-(μ-OH) bonds in $[\{(\mu\text{-}OH)ZrW_5O_{18}\}_2]^{6-}$ gives asymmetric Zr_2W_{10} or ZrW_5 intermediates with bound water or formation of $[Zr_4(OH)_8(H_2O)_{16}]^{8+}$. $[CH_3O]^-$ exchange occurs slowly (0.03

s^{-1} at 75 °C) between M-CH_3O and CH_3OH. The reactivity of the $[CH_3O]^-$ group in $[TBA]_6[(CH_3O)ZrW_5O_{18}]$ allows it to be substituted for larger alkoxide groups in reactions where protic reagents are used (HOR). This kind of reaction has been carried out in equimolar amounts at a temperature of 80 °C for several hours.[12] During a crystal structure analysis of $[TBA]_6[(CH_3O)ZrW_5O_{18}]$, it was observed that the anion exists as a dimer with crystallographic inversion symmetry. The Zr atoms are 7-coordinate, which is made possible due to the size of the atom, and bonded symmetrically to 2 bridging methoxide groups. Another example of a 7 coordinated zirconium is $[\{2\text{-}(CHO)C_6H_4O\}ZrW_5O_{18}]^{3-}$. Zirconium exist as an 8 coordinate species in $[(\mu\text{-}OH)_2(ZrW_5O_{18})_3H]^{7-}$.

1.2.3 Keggin-Type Polyoxometalates

Capped Keggin-type POMs have received much interest and have applications such as building units[34,35] in metal-organic frameworks and spintronics.[36,37] $[PMo_{12}O_{40}(VO)_2]^{3-}$ is a capped Keggin-type POM containing 2 delocalised magnetic moments that are connected through a redox-active $[Mo_{12}O_{40}]^{3-}$ cluster. This POM may have applications as a spin qubit for molecular spintronics, for example in quantum computing. The $[Mo_{12}O_{40}]^{3-}$ cluster is mixed valence, containing both Mo^{IV} and Mo^{V} ions. There are problems with disorder when characterising these POMs using single-crystal X-ray diffraction and in solution magnetic species cannot be studies using NMR spectroscopy. Labile interactions cause problems in ESI mass spectrometry experiments.

Capped POMs can be synthesised under mild conditions by reductive aggregation. This involves the addition of electrons to a core POM structure which causes the surface basicity of the POM to increase and electrophilic capping groups can then bind to the surface of the POM.[38–41] Equation 1.12 gives a general synthetic route to capped Keggin POMs and equations 1.13 – 1.17 give some specific examples.

$[PMo_{12}O_{40}]^{3-} + x\ LMCl_n + nx\ e^- \rightarrow [PMo_{12}O_{40}(LM)_x]^{3-} + nx\ Cl^-$ (Equation 1.12)

$[PMo_{12}O_{40}]^{3-} + n\ Na/Hg \rightarrow [PMo_{12}O_{40}Na_n]^{(3+n)-}$ (Equation 1.13)

$[PMo_{12}O_{40}]^{3-} + n\ Zn/Hg \rightarrow [PMo_{12}O_{40}(LZn)_n]^{(3+2n)-}$ (Equation 1.14)

$[PMo_{12}O_{40}]^{3-} + CoCl_2 + 2\ e^- \rightarrow [PMo_{12}O_{40}\{Co(MeCN)_2\}]^{3-} + 2\ Cl^-$ (Equation 1.15)

$[PMo_{12}O_{40}]^{3-} + 2\ VOCl_3(DME) + 6\ e^- \rightarrow [PMo_{12}O_{40}(VO)_2]^{3-} + 6\ Cl^-$ (Equation 1.16)

$[PMo_{12}O_{40}]^{3-} + 2\ SbCl_3 + 6\ e^- \rightarrow [PMo_{12}O_{40}Sb_2]^{3-} + 6\ Cl^-$ (Equation 1.17)

Crystallographic data and spectroscopic experiments have provided much information about the structure of a number of Keggin-type POM species and the chemistry and reactivity of particular groups in the POM unit. However, little is known about the aggregation mechanism or intermediates that are formed during their synthesis. XAFS studies have been conducted on some POM species[5,6] and this has provided information about the fine structure of the species. It is possible that XAFS may be useful as a technique to elucidate the nature of the intermediates that are formed during the synthesis of POM species and the mechanism by which aggregation of the metal atoms occurs.

1.3 Copper(I) Diimine Complexes

Photo-excited states of molecules are useful in applications such as the generation of solar energy, photosensitization and photocatalysis. For this reason they are a subject of much interest. Until *ca.* 2003 it had not been possible to obtain structural information about molecules in their photoexcited state. Time resolved X-ray analysis now makes it possible to determine the structures of excited states of species and studies have been conducted on the photochemistry of $[Cu(dmp)_2]^+$ (dmp = 2,9-dimethyl-1,10-phenanthroline).[42] Equation 1.18 describes the process by which $[Cu(dmp)_2]^+$ undergoes photo-excitation and figure 1.3 shows the photo-excitation and relaxation mechanisms of copper bis-phenanthroline complexes. It has also been suggested that the "exciplex" is converted to an excited Cu^I state before decaying back to the ground state.[43]

$$[Cu^I(dmp)_2]^+ + h\upsilon \rightarrow [Cu^{II}(dmp^-)(dmp)]^+ \qquad \text{(Equation1.18)}$$

In the ground state Cu^I has a d^{10} electron configuration and has pseudo-tetrahedral geometry.[44-49] The absorption of a photon causes an electron from the metal to be promoted to a π* obital of one of the ligands - the generation of a Franck-Condon (F-C) state. This state remains in the same geometry as the ground state, but the copper centre is now in the 2+ oxidation state and has a d^9 configuration.[42,50] One of the dmp ligands has been reduced and this causes a structural reorganisation. This excited state has a hole in the dσ* orbital.[50] A metal complex with a d^9 electron configuration is susceptible to Jahn-Teller distortion and the result of this distortion is to flatten the geometry of the complex and reduce the angle between the ligands giving the flattened metal to ligand charge transfer (MLCT) state.[42,50]

Time-dependent density functional theory (T-D DFT) calculations have suggested that the flattened geometry weakens the spin-orbit coupling. This was attributed to a slow intersystem crossing (ISC) process.[43,51] In strong Lewis basic solvents, the complex in the flattened MLCT state can coordinate another

ligand by inner sphere reorganisation and become 5 coordinate to form an exciplex.[42] Evidence for this has also been provided by time-resolved X-ray absorption spectroscopy.[42] The bond formed between the copper centre and the solvent ligand uses an electron from the z* orbital of one of the phenanthroline ligands. Therefore, there is no change in the oxidation state of the copper centre when a fifth ligand is coordinated.[50]

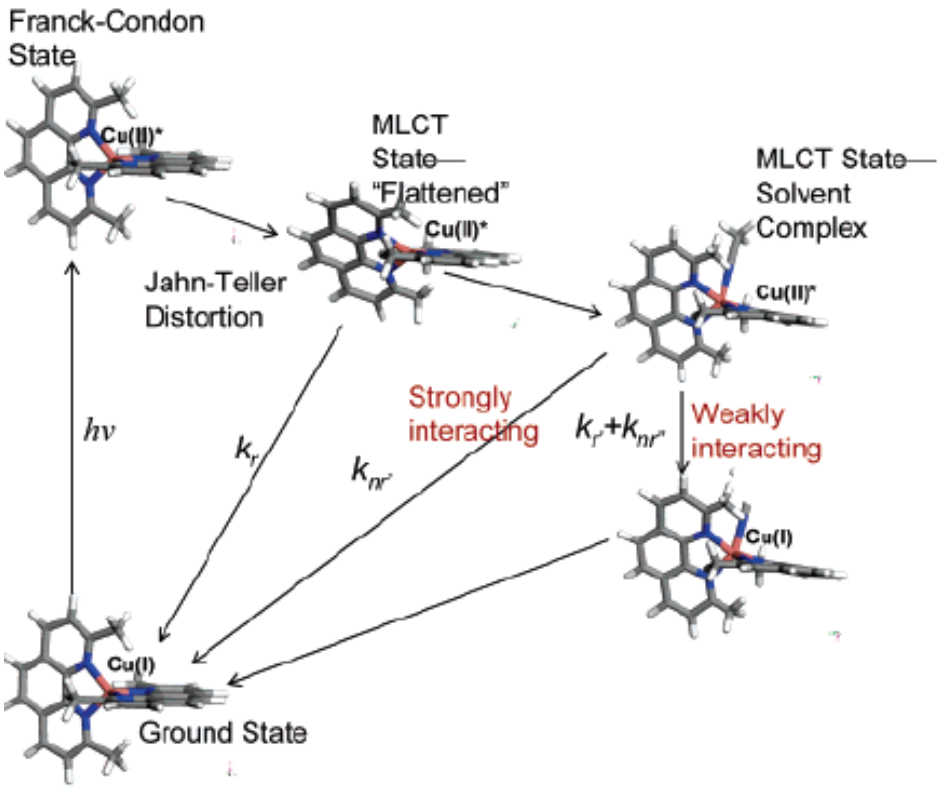

Figure 1.3: $[Cu(dmp)_2]^+$ excitation and MLCT state decay in acetonitrile.[43]

When the copper diimine complex is in the flattened MLCT state, the orbital that was the HOMO in the ground state and the orbitals at energy levels just below acquire ligand π-character and the contribution from the metal orbitals diminishes.[42] X-ray absorption near edge spectroscopy (XANES) experiments suggest that a $1s \rightarrow 4p_z$ transition is occurring in the excited state species and that this reflects a higher coordination number in the excited state. The copper $4p_z$ orbital is empty and delocalised when the metal centre is tetra-coordinated, but localised over the ligands when it is penta-coordinated or hexa-coordinated

and this allows the 1s → $4p_z$ transition. XAFS spectra also suggest an increased coordination number and shorter Cu-N bond distance in the excited state.[42]

As the angle between the ligand planes is not 90˚, but somewhere between 80˚ and 90˚, the symmetry of the complex is D_2 rather than the D_{2d}. Upon excitation, the angle between the ligand planes is lowered to 58.5˚, one of the ligands is observed to rock slightly and the Cu-N bond distance is observed to shorten by 0.04 Å.[42] It appears that when the complex becomes penta-coordinated, steric hinderance prevents the new ligand from approaching close to the metal centre. $[Cu^{I}(dmp)_2]^+$and $[Cu^{I}(dpp)_2]^+$ (dpp = 2,9-diphenyl-1,10-phenanthroline) both acquire flattened ligand geometry in the MLCT states. π-conjugation of the phenyl groups in $[Cu^{I}(dpp)_2]^+$ stabilises the photoexcited electron in the MLCT excited state, whereas methyl groups are electron donating and as a result the $[Cu^{I}(dmp)_2]^+$ is destabilised. A bulky group such as a tertiary butyl group would reduce the distortion of the complex on excitation and prevent a solvent molecule coordinating to the copper centre.

In the XANES spectrum of the ground state of $[Cu^{I}(dmp)_2]^+$, there is a shoulder feature which does not appear in the spectrum for $[Cu^{II}(dmp)_2]^{2+}$. This is due to the effect the different coordination environment has on the $4p_z$ orbital. When the complex is in a tetrahedral geometry the $4p_z$ orbital is localised, allowing a 1s-$4p_z$ transition which is responsible for the shoulder feature. When the copper atom is penta-coordinated the $4p_z$ orbital is delocalised over the ligand and the 1s to $4p_z$ transition peak becomes broad and cannot be seen in the spectrum. The Cu-N peak in the Fourier transformed XAFS spectrum for the excited state $[Cu^{I}(dmp)_2]^+$ is higher and shifted to a shorter distance in comparison to the ground state $[Cu^{I}(dmp)_2]^+$ Fourier transform spectrum suggesting an increase in coordination number.[42]

In the structural studies of the MLCT state of $[Cu^{I}(dmp)_2]^+$ dissolved in acetonitrile using pump-probe XAFS spectroscopy,[42] the experiments were conducted with a time resolution of 100 ps. The MLCT state was found to be penta-coordinated and this exciplex structure was confirmed in Lewis basic solvents. The room temperature lifetime of the MLCT excited state of $[Cu^{I}(dmp)_2]^+$ in acetonitrile is 2.0 ± 0.3 ns[52] and the X-ray pulse of 100 ps, which occurred less than 200 ps after the laser pulse, was short enough to probe the structure of the flattened MLCT state which lived for 2 ns, but it was too long

for following the atomic evolution from the F-C MLCT state to the longer lived MLCT state. The $[Cu^{I}(dmp)_2]^+$ MLCT state decays in 1.6 ns in acetonitrile at room temperature.[42] The fluorescence lifetime of the ^{1}MLCT state is 13 – 16 ps at room temperature.[51]

Tetrakis(acetonitrile)copper(I) hexafluorophosphate has been reported as a precursor for the synthesis of copper phenanthroline complexes.[53] Equation 1.19 shows the synthesis of tetrakis(acetonitrile)copper(I) hexafluorophosphate.

$$Cu_2O + 2\,HPF_6 \xrightarrow{CH_3CN} 2\,[Cu(CH_3CN)_4][PF_6] + H_2O \qquad \text{(Equation 1.19)}$$

Tetrakis(acetonitrile)copper(I) hexafluorophosphate can then be used in a reaction with 2,9-dimethyl-1,10-phenanthroline to produce $[Cu(dmp)_2][PF_6]$. A chemical equation for this reaction is given in equation 1.20.[54]

$$[Cu(CH_3CN)_4][PF_6] + 2\,dmp \rightarrow [Cu(dmp)_2][PF_6] \qquad \text{(Equation 1.20)}$$

2,9-dimethyl-1,10-phenanthroline can be synthesised by reacting 1,10-phenanthroline with methylithium. Different phenanthroline derivatives can be synthesised using different organo-lithium reagents. An example of this is shown in figure 1.4, in which an alkyllithium is used as the reagent to convert 1,10-phenanthroline to 2,9-dialkyl-1,10-phenanthroline.[55]

Details about the structure and behaviour of the excited states of $[Cu(dmp)_2]^+$ and $[Cu(dpp)_2]^+$ have been reported and the two complexes have been found to show similar characteristics, although it has been reported that the bulkier the 2 and 9 substituents are on phenanthroline derivative, the more the copper centre is protected from coordination of a solvent ligand. There have been many XAS investigations into the photo-excited state of copper diimine complexes and a time resolution of 100 ps has been achieved.

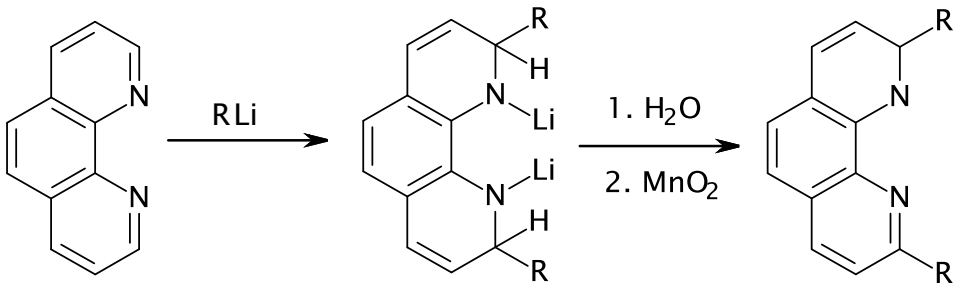

Figure 1.4: Synthesis of 2,9-dialkyl-1,10-phenanthroline.

2. Experimental Methods

2.1 Introduction

There are many spectroscopic techniques that can be used to characterise molecules, but most have limitations. For example, NMR spectroscopy is limited by the magnetism of the molecule. UV / Vis spectroscopy is limited by the absorption range of the molecule – if the molecule does not absorb electromagnetic radiation at frequencies in the ultra violet or visible regions of the electromagnetic spectrum the technique will not be informative. X-ray absorption spectroscopy is not restricted by these limitations, can give information about the local structure around a specific atomic species in any phase and can be tuned to give information regarding almost any atomic species. XAFS is a powerful spectroscopic technique and has been used to characterise species and monitor reactions.

The specificity of XAFS arises from the differing energies of the core orbitals of different elements. Core-valence transitions provide information about the coordination geometry of the element and core-continuum transitions generate photoelectrons that are scattered by neighbouring atoms back to the absorbing atom. This back-scattering results in modulations in the intensity of the X-ray absorption. The periodicity of this modulation provides information about the interatomic distances between the absorbing atom and the neighbouring atoms and the intensity indicates the number of back-scattering atoms that are present. The electronic transitions are much faster than molecular vibrations so the interatomic distance that is observed for a particular pair of atoms is an average of the variations in the equilibrium bond length (static Debye-Waller factor) and the variations due to vibrations within the molecule (Dynamic Debye-Waller factor). Where more than one chemical species is present, the observed structural information will be an average of the local chemical environments in all the species containing the absorbing element and experiments have been carried out in which reactions have been followed.[56]

XAS can be coupled with other spectroscopic techniques. For example, cyclic voltammetry and XAS have been applied together in studies of oxidation and reduction reactions.[57-61] Mass spectrometry has been coupled with XAS spectroscopy in studies of gas-solid systems[62-66] and solid and powder systems have been studied using a combination of X-ray diffraction and XAFS spectroscopy.[67,68] The latter combination of spectroscopic techniques has been used in structural studies of heterogeneous catalysts.[69,70]

2.2 X-ray Absorption Spectroscopy

2.2.1 Introduction

An EXAFS spectrum of the W L_{III} edge of $[NBu^n_4]_2[W_6O_{19}]$ is shown in figure 2.1. The XANES part of the spectrum falls typically within 30 eV of the absorption edge and gives information about the electronic properties, geometry and oxidation state of the absorbing atom. The XAFS part of the spectrum gives information about the number and type of atomic species that are coordinated to the absorbing atom, the distance between the absorbing atom and the neighbouring atoms and the disorder in the interatomic distance. In an XAFS spectrum the probability of absorption is plotted as a function of energy in eV. The sharp rise in $\chi\mu(E)$ is the absorption edge – when the energy of the X-rays is equal to the binding energy of the core electrons – and the part of the spectrum around this white line is the XANES region. The region of the spectrum following this is the XAFS – where information from backscattering photoelectrons is found.

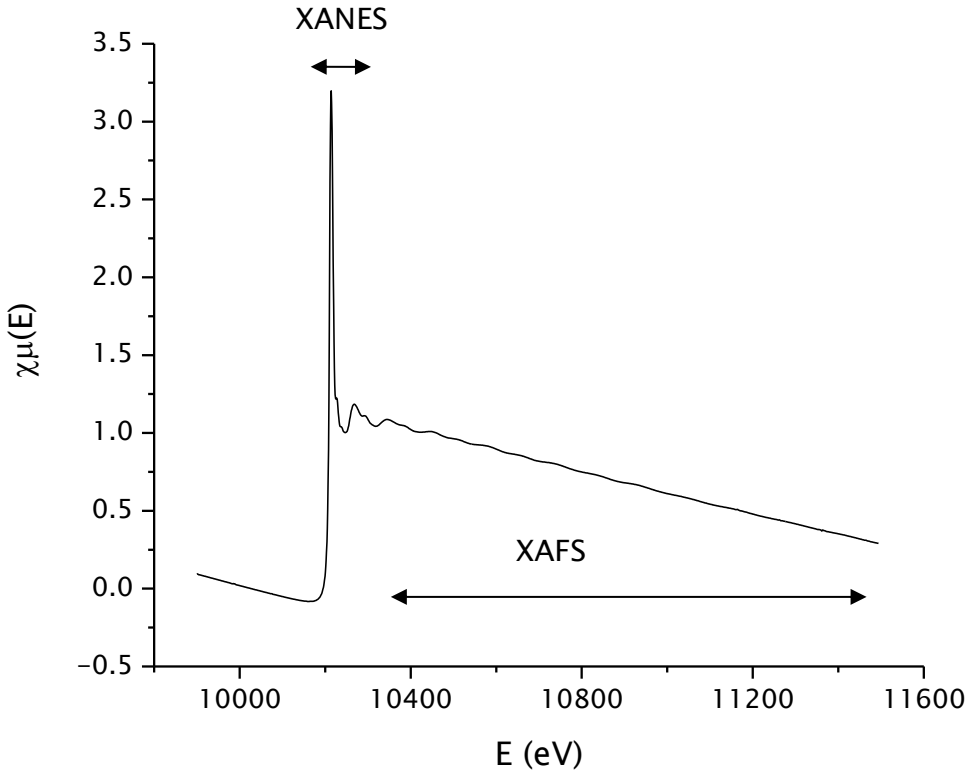

Figure 2.1: XAFS spectrum of the W L_{III} edge of $[NBu^n_4]_2[W_6O_{19}]$ in the solid state.

2.2.2 XAFS Theory

XAFS is a measurement of the energy dependence of the absorption coefficient, μ, at and above the energy level of the core electrons of a known atomic species. μ varies with energy and is dependent on the sample density, the atomic number, the atomic mass and the energy of the incident X-rays according to equation 2.1:

$$\mu \approx \frac{\rho Z^4}{AE^3}$$

(Equation 2.1)

where μ is the absorption coefficient, ρ is the sample density, Z is the atomic number, A is the atomic mass and E is the X-ray energy. Equation 2.1, however, does not treat electrons as though they are in orbitals and so the rises in absorption due to electronic transitions shown in figure 2.2 are not accounted for by this equation. As such, XAFS is heavily dependent on the atomic species and this is demonstrated in figure 2.2, which shows how the core electron binding energies of Pb, Cd, Fe and O are different from each other.

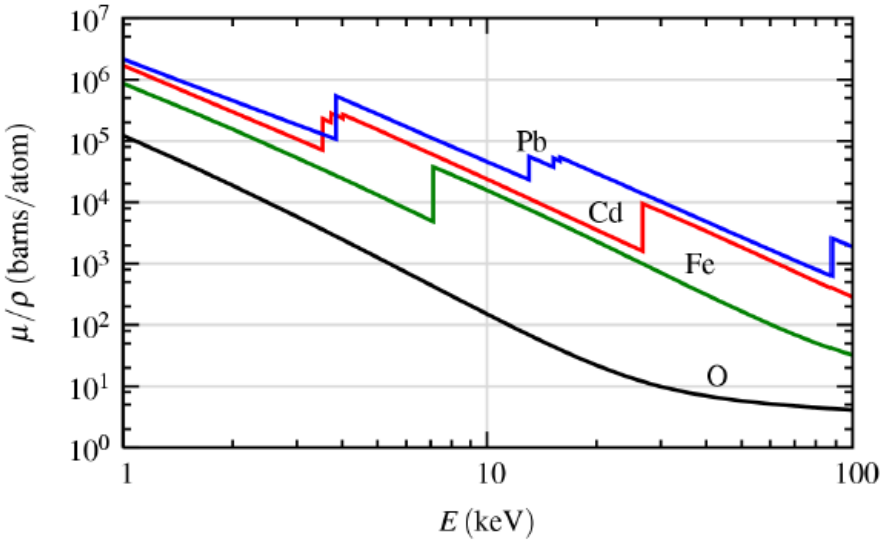

Figure 2.2: Absorption cross-section, μ/ρ, for Pb, Cd, Fe and O.[71]

X-rays are absorbed by atoms via a process called the photoelectric effect (figure 2.3), in which the X-rays are absorbed by core electrons. The incident X-rays must be of equal or higher energy than the binding energy of the electron that is taking part in the process, otherwise the electron will not be excited from its quantum state. During the absorption process the energy from the X-rays allow the electrons to overcome their binding energy and the energy that is in excess of the binding energy is transferred to a photo-electron which is ejected from the atom with wave number, k.

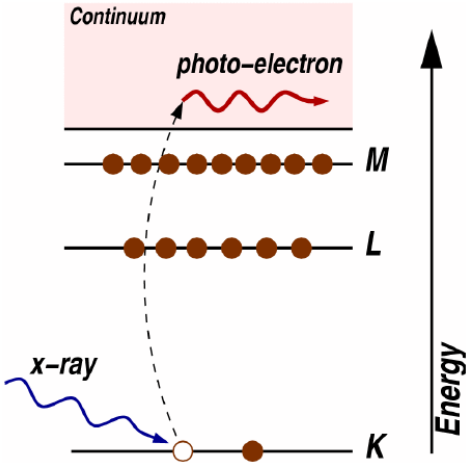

Figure 2.3: The photoelectric effect.[71]

The absorption edge, when the incident X-rays are of equal energy to the binding energy of the core electron, corresponds to the excitation of the electron to the valence orbital and gives rise to the XANES. When a core-continuum transition occurs, a photoelectron is generated that can be scattered by a neighbouring atom. This alters the absorption coefficient and gives rise to the XAFS.

There are two mechanisms by which relaxation of the excited state occurs – fluorescence and the Auger effect (figure 2.4). In the fluorescence mechanism an electron from a higher energy level drops into the core-hole that is left when the core electron is excited by the X-ray absorption event. When the electrons drop into the core-hole a photon is emitted from the atom. In the Auger effect an electron drops into the core-hole and another is excited into the continuum. The different binding energies characteristic of the core atoms in different elements means that XAFS is element specific so the energy required to excite the core electrons is different in every atomic species. Therefore different absorption edges will be more informative for different elements. Due to the lower energy of the core orbitals in lighter elements, the K edge is accessible, but for heavier elements the L_{III} edge is more informative because the photon energy would need to be very high to probe the K edge (figure 2.5), the core hole lifetime decreases and the Heisenberg uncertainty broadening increases. The transitions must obey the dipole selection rule, $\Delta l = \pm 1$. The K edge

represents absorptions for s→p transitions and the L_{III} edge represents absorptions for p→d transitions.

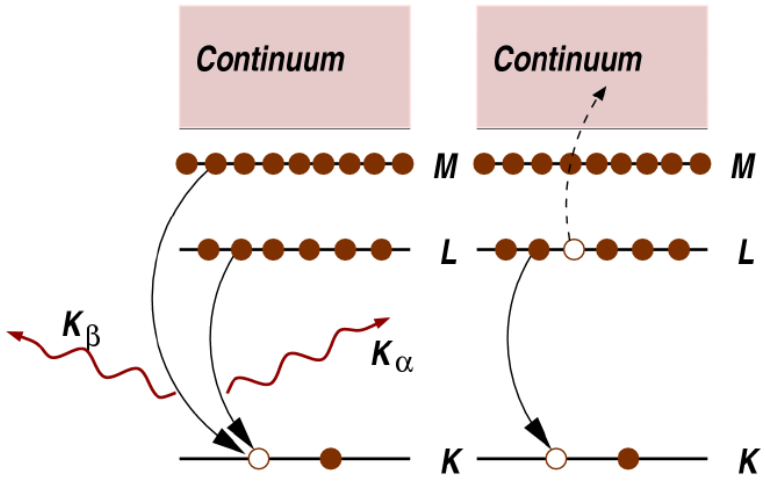

Figure 2.4: Excited state decay by X-ray fluorescence (left) and the Auger effect (right).[71]

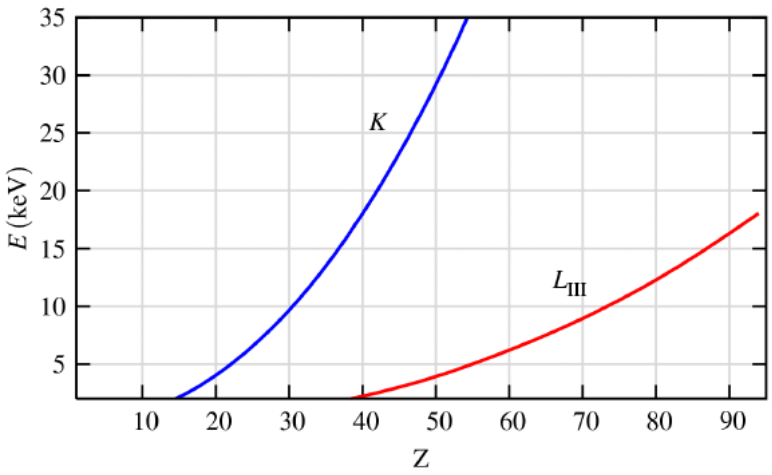

Figure 2.5: The energy of the X-ray K and L_{III} absorption edges as a function of atomic number.[71]

The photo-electrons that are generated when the absorbing atom absorbs X-rays can be thought of as a spherical wave which can be scattered back to the absorbing atoms by neighbouring atoms. This gives an interference pattern

and the observed XAFS is the combination of the interference patterns produced by many scattered photo-electrons. The observed XAFS is therefore determined by the type and the position of the neighbouring atoms. The XAFS is proportional to the amplitude of the scattered photo-electron at the absorbing atom and the XAFS fine structure, χ(E), can be defined by equation 2.2:

$$\chi(E) = \frac{\mu(E) - \mu_0(E)}{\Delta\mu_0(E)}$$

(Equation 2.2)

Where μ(E) is the measured absorption coefficient, μ_0(E) is a smooth background function representing the absorption of an isolated atom and $\Delta\mu_0$ is the measured jump in the absorption at the threshold energy. XAFS is described in terms of the wave behaviour of the photo-electron that is created in the absorption process. Therefore, the X-ray energy is converted to k, the wavenumber of the photo-electron, with dimensions 1/distance and is defined by equation 2.3:

$$k = \sqrt{\frac{2m(E - E_0)}{\hbar^2}}$$

(Equation 2.3)

Where E_0 is the absorption edge energy and m is the electron mass. XAFS is measured as χ(k) – oscillations as a function of photo-electron wave number. Different frequencies in the XAFS oscillations correspond to the different coordination shells (different elements at different distances from the absorbing atom) and using Fourier transforms in XAFS analysis is therefore beneficial. Oscillations decay quickly in an XAFS spectrum, so to emphasise the oscillations at higher wave numbers, χ(k) can be multiplied by a power of k (eg.

K^2 or k^3). The EXAFS equation (equation 2.4) describes different near-neighbour coordination shells and can be used to model this and determine the number of neighbouring atoms, the distance to the neighbouring atom and the disorder in this distance.

$$\chi(k) = \sum_{j=1}^{Shells} S_0 e^{-2R_j/\lambda} \frac{N_j F_j(k) e^{-2\sigma^2_j k^2}}{kR_j^2} \sin(2kR_j + \varphi_j(k))$$

(Equation 2.4)

k Photoelectron wave number

j jth coordination shell

R_j Distance of the absorbed atom to this coordination shell

$\Phi_j(k)$ Phase shift experienced by photoelectron

N_j Coordination number

$F_j(k)$ Magnitude of backscattering amplitude (element specific)

S_0^2 Amplitude reduction factor (loss in intensity to many body effects)

λ Mean free path of photoelectron

$e^{-2Rj/\lambda}$ Accounts for finite lifetime of photoelectron

σ^2 Debye-Waller factor: Thermal motion and structural disorder

Approximations must be made: the potential energy of the photoelectron propagating through the solid is approximated as that of spherically symmetric atoms with a flat region between them; only a single electron is directly excited, which interacts with the electron gas in the material, giving rise to a mean free path (how far the photoelectron can travel before it is scattered inelastically and the core-hole is filled); only backscattering from each neighbouring atom is included, i.e. multiple scattering is neglected; and in the

scattering process the photoelectron is approximated as a plane wave. The behaviour of the photoelectron is modified as it interacts dynamically with the gas of other electrons in the material and due to these many body effects, the photoelectron does not behave as a free photoelectron.

Due to the electronic transition being faster than the vibrational movement of the molecule the observed XAFS obtained from an experiment will contain summations of the interatomic distances between pairs of atoms at different time intervals during the vibration. If more than one species containing the absorbing element is present then the observed XAFS will be a summation of the species that are present in the mixture. Identification of species containing the absorbing element which have the same neighbouring atoms has, in the past, been difficult.[72]

2.2.3 XAFS Spectroscopy

XAFS is a technique that can be used to analyse samples in any phase – solid, liquid or gas – provided enough time is allowed for individual scans. Small variations in the absorption coefficient, μ(E), are the feature of interest in XAFS experiments and these can be measured in transmission experiments. In a transmission experiment (figure 2.6) an incident X-ray beam passes through an ionisation chamber to detect the intensity (I_0) of the X-ray beam before it passes through the sample of length t, and then passes through a second ionisation chamber which detects the intensity (I) of the X-ray beam after it has passed through the sample. The energy dependence of the absorption coefficient μ(E) can then be measured by equation 2.5. XAFS experiments are carried out in transmission mode when the samples are concentrated – samples in which the absorbing element is the major component.

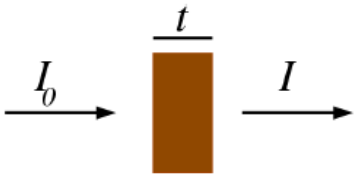

Figure 2.6: Transmission mode XAFS experiment.[71]

$$\mu(E) = \log (I_0 / I) \qquad \text{(Equation 2.5)}$$

For experiments in which the sample is of lower concentration a fluorescence mode experiment is used. This type of experiment is illustrated in figure 2.7, [71] where θ is the incident angle and ϕ is the exit angle. The X-rays emitted include the fluorescence of the absorbing element, the fluorescence of other elements in the sample and elastically and inelastically scattered X-rays. Since the X-rays from a synchrotron are polarized in the plane of the synchrotron, elastically and inelastically scattered X-rays are not emitted isotropically from the sample. The polarization suppresses the elastic scatter at 90 ° to the incident beam, in the horizontal plane. For this reason the fluorescence detector is placed at 90 ° to the incident beam.

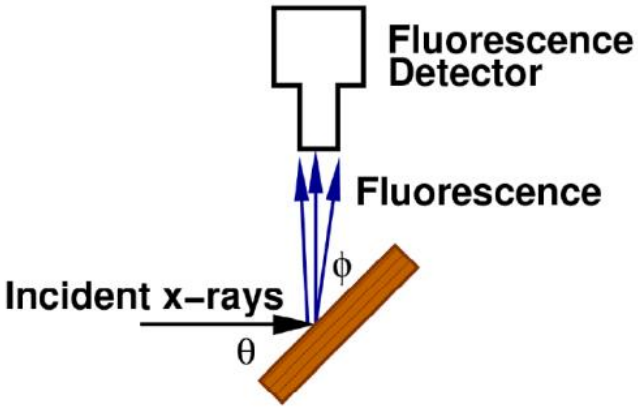

Figure 2.7: Fluorescence mode XAFS experiment. [71]

The fluorescence intensity and therefore the XAFS oscillations measured in a fluorescence experiment are damped due to self-absorption. This occurs when there is high interaction between the X-rays and the absorbing element within the distance the X-rays penetrate into the sample. In a particularly thick or concentrated sample all the x-rays are absorbed by the element of interest and this can be avoided by changing the penetration depth into the sample. The energy dependence of the absorption coefficient in a fluorescence experiment can be measured by equation 2.6.

$$\mu(E) \propto I_f / I_0 \qquad \text{(Equation 2.6)}$$

As the X-rays have to travel into and back out of the sample, the measured fluorescence intensity is better described by equation 2.7. This accounts for the attenuation of X-rays by matter in the sample, the distance the X-rays penetrate into the sample, the angle of incidence and the exit angle of the X-rays.

$$I_f = I_0 \frac{\epsilon \Delta\Omega}{4\pi} \frac{\mu_\chi(E)\{1 - e^{-\left[\frac{\mu_{tot}(E)}{sin\theta} + \frac{\mu_{tot}(E_f)}{sin\phi}\right]t}\}}{\mu_{tot}(E) sin\theta + \frac{\mu_{tot}(E_f)}{sin\phi}}$$

(Equation 2.7)

where ϵ is the fluorescence efficiency, $\Delta\Omega$ is the solid angle of the detector, $\mu_\chi(E)$ is the absorption from the element of interest, θ is the incident angle, ϕ is the exit angle, E_f is the energy of the fluorescent x-ray and $\mu_{tot}(E)$ is the total absorption in the sample.

If XAFS experiments can be carried out on a fast enough time scale then intermediate species formed during a reaction can be detected and monitored. The structure of these intermediates can therefore be determined.[56] Quick EXAFS (QEXAFS)[73-75] and energy dispersive EXAFS (EDE)[76] are 2 developments of

EXAFS that allow fast data acquisition. QEXAFS uses the standard EXAFS experiment, but the monochromator is moved rapidly during the experiment so that a range of X-ray energies can be used. The technique is limited by the speed at which the monochromator can be moved and the time required to collect data of suitable quality by means of a point-by-point data collection mode. EDE allows the sample to be illuminated by X-rays of a range of energies at the same time. This is achieved by the use of a bent monochromator to focus the polychromatic X-ray beam on the sample and although the background scan cannot be acquired simultaneously to the experimental scan, there is no need for monochromator movement and so EDE is not limited by the speed at which the monochromator can be moved. As scans are conducted at all X-ray energies simultaneously, there is no need for point-by-point data acquisition and so the scan time for a spectrum is significantly faster, and can give faster time resolution. However, the data will contain higher levels of noise and these spectra will therefore provide less information.

2.3 X-ray Emission Spectroscopy

Other types of experiments are made possible by the X-ray absorption process. One example is XES which also provides information about the local structure around the absorbing atom. In the X-ray absorption process, the incident X-rays excite core electrons into an empty electronic state. The photoelectrons generated by this process are detected in XAS. An X-ray absorption spectrum is related to the density of unoccupied states. After the core electron has been excited, the electron hole is filled by an electron from a higher orbital. In XES the fluorescence photons emitted in the relaxation process are measured. The fluorescence resulting from removal of electrons from the K shell (1s orbital) is referred to as K fluorescence and fluorescence resulting from removal of electrons from the L shell (2s or 2p orbital) is referred to as L fluorescence, etc. The emission lines are called α, β, γ, etc. according to their intensity where α is the most intense. An X-ray emission spectrum is related to the density of occupied states. An energy diagram for the absorption and emission of a photon is presented in figure 2.8. This shows the X-ray absorption and

electronic excitation analysed in XAS experiments and the radiative decay process analysed in XES experiments. The energy transfer is the difference between the energies of the incident and emitted photons. An electronic state that arises from the interaction of the core hole with the valence electrons is represented by the dashed line in the final sate.[77]

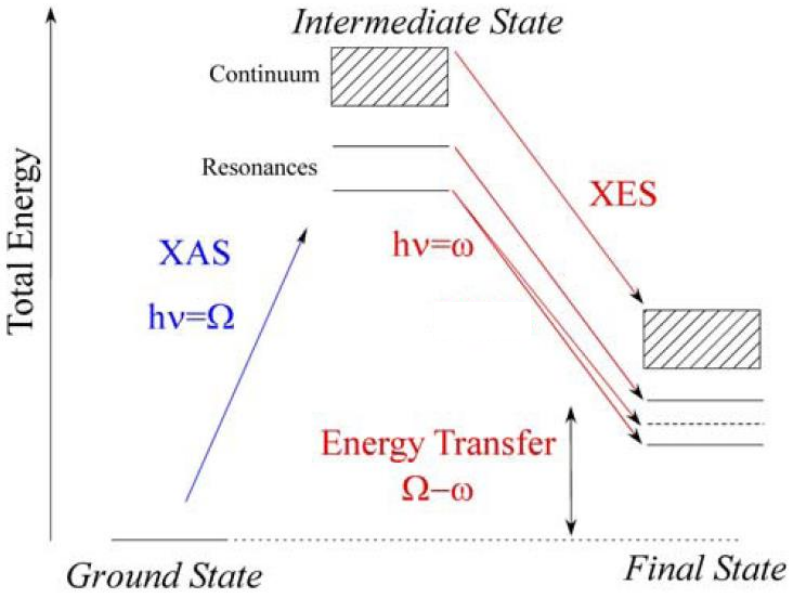

Figure 2.8: Energy diagram for the absorption of a photon with energy Ω and emission of a photon with energy ω in a X-ray absorption experiment.[77]

2.4 Resonant Inelastic X-ray Scattering

XAS and XES can be combined in a resonant inelastic X-ray scattering (RIXS) experiment in which the fluorescence X-rays emitted in the decay process, which are dependent on the incident energy, are studied. The X-ray photons that scatter inelastically off of matter are measured. The energy, momentum, and polarization of the photon are transferred to the electronic excitations within a sample. The changes in energy, momentum, and polarization of the scattered photons can be measured to provide information about the excitations. In a RIXS experiment the incident energy and analyser energy are

scanned and this makes it possible to plot a 2-dimensional map of energy levels. The energies of the incident photons used in experiments must be selected so that they resonate with the transitions within the system and this enhances the inelastic scattering cross section making it possible to probe the charge, magnetic, and orbital degrees of freedom of specific atoms in a sample.[78]

2.5 Data Acquisition

2.5.1 Synchrotron Light Sources

Synchrotron light sources are required to obtain the finely tuned X-rays which are required for XAFS experiments. The characteristics of the electromagnetic radiation produced by a synchrotron are: high flux (total number of photons per second in a beam); high brilliance (highly collimated photon beam generated by a small divergence and small source); high stability; polarisation (the X-ray polarisation of bending magnet radiation is entirely horizontally polarised in the orbital plane). Away from the orbital plane the X-ray beam acquires some degree of circular polarisation. A diagrammatical representation of a synchrotron is shown is figure 2.9.

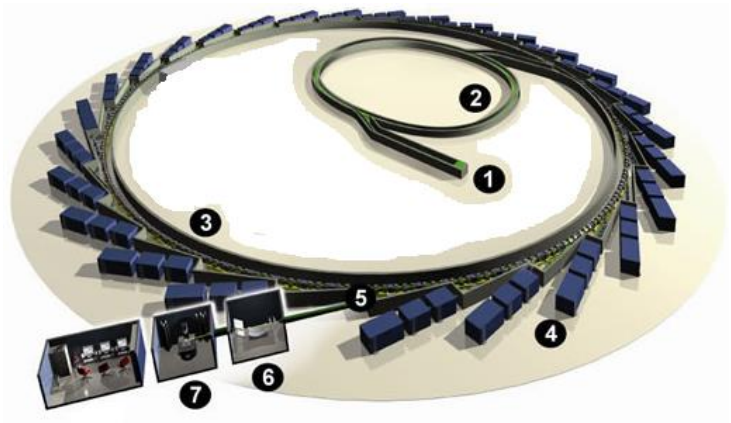

Figure 2.9: Synchrotron schematic.[79]

Electrons are generated and emitted from the electron gun (1) and accelerated using a linear accelerator to relativistic energy. They are accelerated to a speed near the speed of light in the booster synchrotron (2) and then moved to the storage ring (3) which contains insertion devices – undulators and wigglers – where the trajectory of the electron bunches are changed and this causes X-rays to be generated. The X-rays are channelled into the beamlines (4 and 5) at certain points on the storage ring. The X-rays are focused in the optics hutch (6) for use in the experimental hutch (7) where specific experimental equipment is set up for data collection. The direction the electrons travel in can be controlled using bending magnets which cause X-rays to be generated. Due to having many source points, insertion devices produce beams which have high brilliance. As the electrons pass through these devices they are made to change direction and so they accelerate and emit X-rays (conservation of momentum). The X-rays travel down the beamlines to experimental hutches where they can be used in a variety of different experiments.

2.5.2 Data Collection

Solid samples are placed in a hole in the centre of an aluminium sample holder (figure 2.10). Samples must be homogeneous, and to achieve this in the solid phase, sample pellets are made. The pellets are attached to the sample holder using Kapton tape. The sample holder is placed on a moveable stage which can be moved by motors so that the beam passed through the sample.

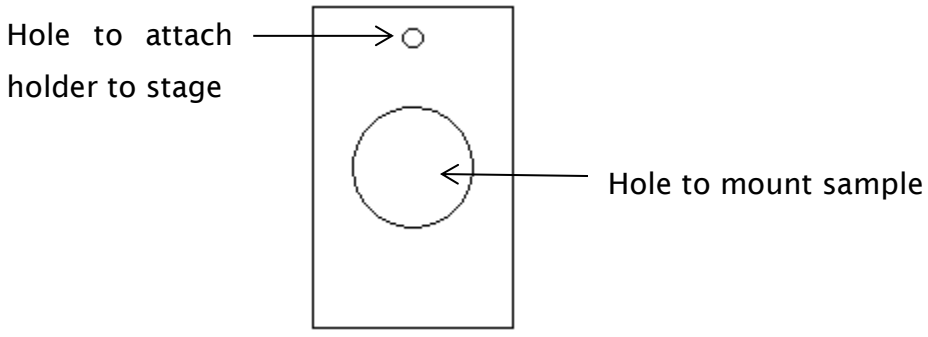

Figure 2.10: Cross section of XAS cell for solid samples.

A XAS solution cell made up of 3 plates (figures 2.11 and 2.12) was designed to provide a sample thickness of 3 mm. The cell was also designed to accommodate cartridge heaters so that the sample could be heated. Solution samples are injected into the cell through the inlet holes. Once the solution is in the cell, stoppers are placed on the inlet holes and the cell is then be placed in the path of the beam so that the beam passes through the sample in the solution chamber. Figure 2.13 shows how the solution cell is constructed and figure 2.14 show a cross section through the cell.

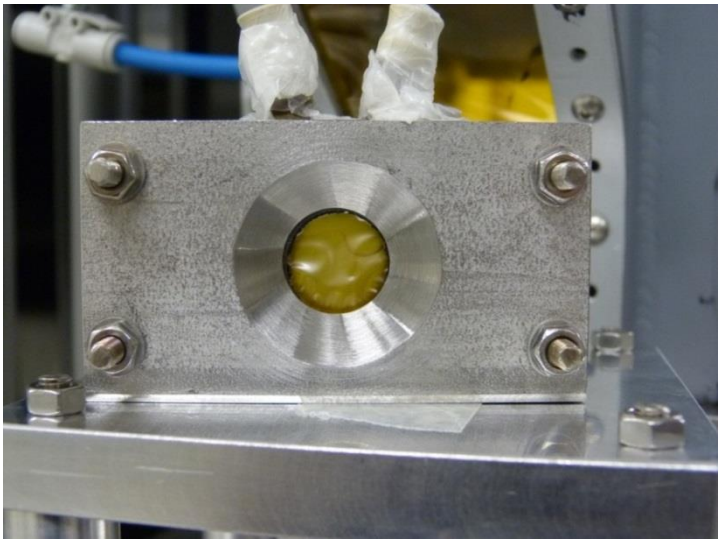

Figure 2.11: XAS solution cell.

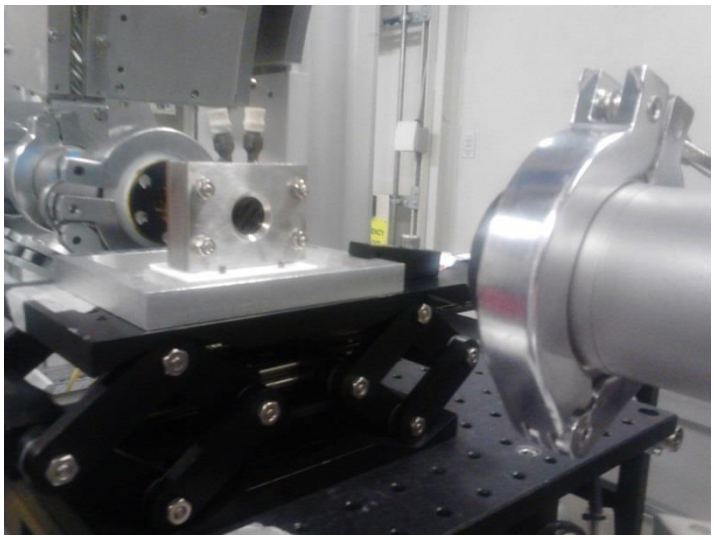

Figure 2.12: XAS solution cell mounted on a beamline sample stage.

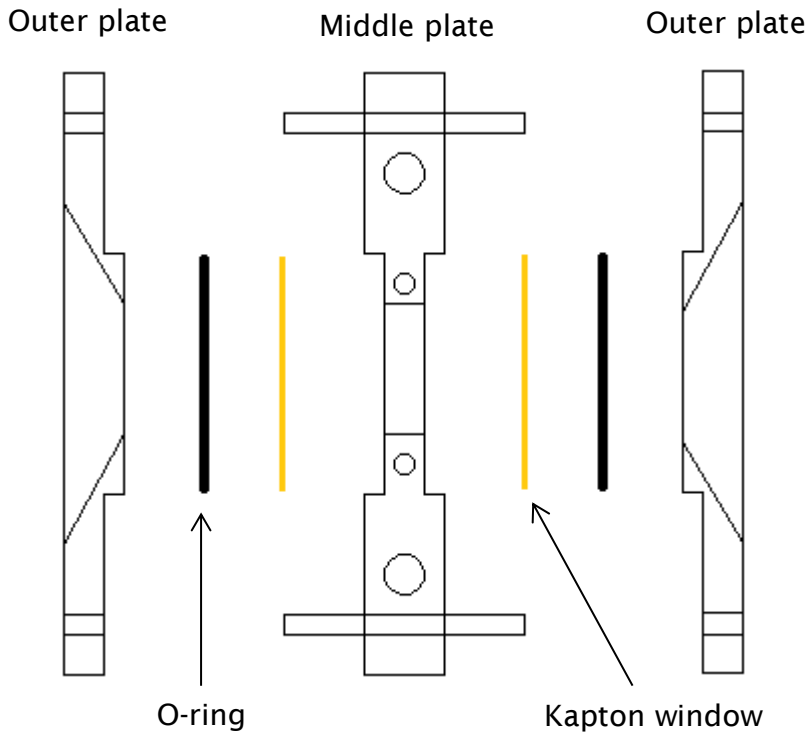

Figure 2.13: Construction of XAS solution cell.

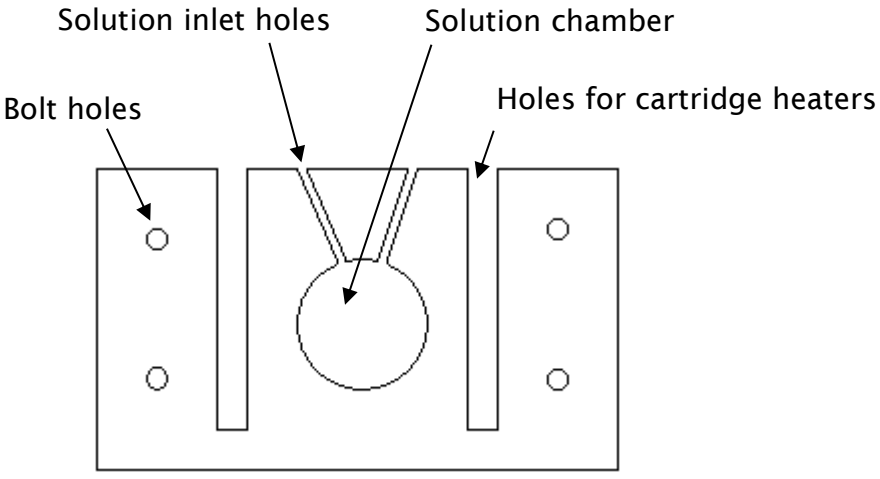

Figure 2.14: Cross-section through middle plate of XAS solution cell.

2.6 Data Analysis

2.6.1 IFEFFIT

There are a number of programs available for the analysis of EXAFS - EXCURVE, GNXAS and FEFFIT are 3 examples.[80,81] At present FEFFIT is the most commonly used. FEFFIT calculates EXAFS using four internal modules: POTPH, PATHS, GENFMT and FEFFIT. POTPH creates atomic potentials based on the geometrical distribution of atoms, overlaps their wave functions and calculates the scattering phase shifts based on their potentials. The Paths module identifies all single and multi-scattering paths for an arbitrary cluster of atoms. The GENFMT module uses the results of POTPH and PATHS to calculate the XAFS contribution from each path. The results are described by a simplified version of the EXAFS equation for each path, j (equation 2.8):

$$\chi_j(k) = \frac{N_j F_j(k) \exp[-2R_j/\lambda(k)]}{kR_j^2} \exp[i2kR_j + i\delta_j(k)] \qquad \text{(Equation 2.8)}$$

where N_j is the number of equivalent paths, $F_j(k)$ is the effective scattering amplitude, $\delta_j(k)$ is the effective total phase shift (including contributions from the central atom and all scattering atoms), and R_j is half the total length of the scattering path. k is the wavenumber and λ(k) is the mean free path of the photoelectron. FF2CHI performs the sum over paths j to generate the complex χ(k) using equation 2.9:

$$\chi(k) = \Sigma \chi_j(k) \exp(-2k^2\sigma_j^2) \qquad \text{(Equation 2.9)}$$

Because the estimate of the uncertainty of the data is not always reliable, the uncertainties estimated this way are rescaled by $\chi^2/ v^{1/2}$ where $v = N_{info} - P$. Both

χ^2 and χ^2/v are reported, as is an EXAFS R factor that gives the misfit relative to data size. IFEFFIT is an interactive version of FEFFIT and this shall be used in these studies. The Athena program is used for data background removal and the Artemis program is used for the curve-fitting analysis. Crystallographic data can be fitted to data by importing the data into the Atoms program. A FEFF calculation can then be run using the Atoms data.

Models for spectra obtained for solid POM samples were constructed by running a FEFF calculation with crystallographic data that had been imported into an atoms page. Models for spectra obtained for solution phase POM samples were constructed by writing a FEFF input file. Atomic coordinates for the FEFF input files were used based on an average of interatomic distances in the crystallographic structures. The R-factors and Chi-square values give an indication of how well a model fits the data. The lower these values are, the better the fit represents the data. The spectra can be weighted so that different parts of the spectrum can be emphasised. The models will fit the spectra differently with different weighting so a R-factor is reported for each weighting (k=1,2 and 3). In a good fit the R-factor and Chi-square values will be below 10 %.

It is important that the R-factor is low with every k weighting because it means that the model fits the experimental data in all parts of the spectrum. The Debye-Waller factors should be low because there cannot be much disorder in a tightly bonded cluster and they must be positive because there cannot be an absence of disorder in the molecule. The paths obtained from the models were added one at a time, fitting the model against the experimental data each time a path was added. The fits that gave the best sets of refined parameters are reported and the optimised path distances and Debye-Waller factors are presented.

2.6.2 The Nyquist Formula

New Δr and σ^2 parameters must be added for each shell that is added to a fit. The amplitude and E_0 value must also be included in the list of parameters and

if contributions from different sites must be included in the fit then parameters must be included to account for this. The maximum number of independent parameters that can be used in IFEFFIT can be determined using the Nyquist formula (equation 2.10):

$$N_{idp} = \frac{2.\,del(k).\,del(R)}{\pi}$$

(Equation 2.10)

3. Formation of Lindqvist-Type Polyoxometalates in Solution

3.1 Introduction

Lindqvist-type POM species have been studied by XAFS in the solid and in solution. In previous studies, data has been collected up to k = 18 $Å^{-1}$ and co-ordination numbers have been set at those that have been predicted from structural information.[5] Shells have been added starting with the closest shell to the absorbing atom and adding shells one at a time as they get more distant from the absorbing atom.[5] $[W_6O_{19}]^{2-}$ (figure 3.1) and some heteropolyanion tungstate species have been studied. The most significant peaks in the Fourier transform spectra for the W L_{III} edge of $[W_6O_{19}]^{2-}$ are due to the first shells of oxygen atoms and tungsten atoms. The peaks for the different oxygen and tungsten sites are highlighted in figure 3.2. Previously, W···W distances of 3.281-3.296 Å have been reported[82] for $[W_6O_{19}]^{2-}$ and the results reported in this chapter are in agreement with this.

In this investigation, 20 QEXAFS scans were recorded for each sample and these were merged (with the exception of poor spectra) to produce a single spectrum representing an average of all the individual spectra. This resulted in a spectrum with a higher signal to noise ratio and a higher wave vector could then be used in the analysis of the data. R-factors are below 10% for every k-weighting and most of the Debye-Waller factors for single scattering paths for the atoms bound to the absorbing atom are low and positive. Negative Debye-Waller factors that are reported can be explained by difficulties in modelling the static and vibrational disorder across pathways involving non-bonded atoms. The EXAFS spectra and the Fourier transforms show that the models have been fitted well to the experimental data and show that the peaks in the spectra are real. The spectra are not phase corrected. When no error margins are given in the tables, this indicates that the parameter was set to the given value.

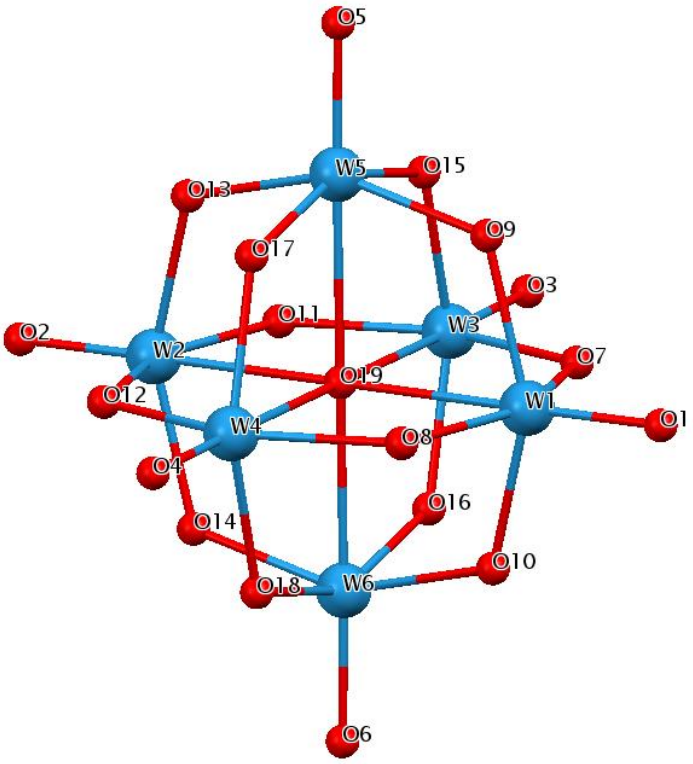

Figure 3.1: Structure of $[W_6O_{19}]^{2-}$.

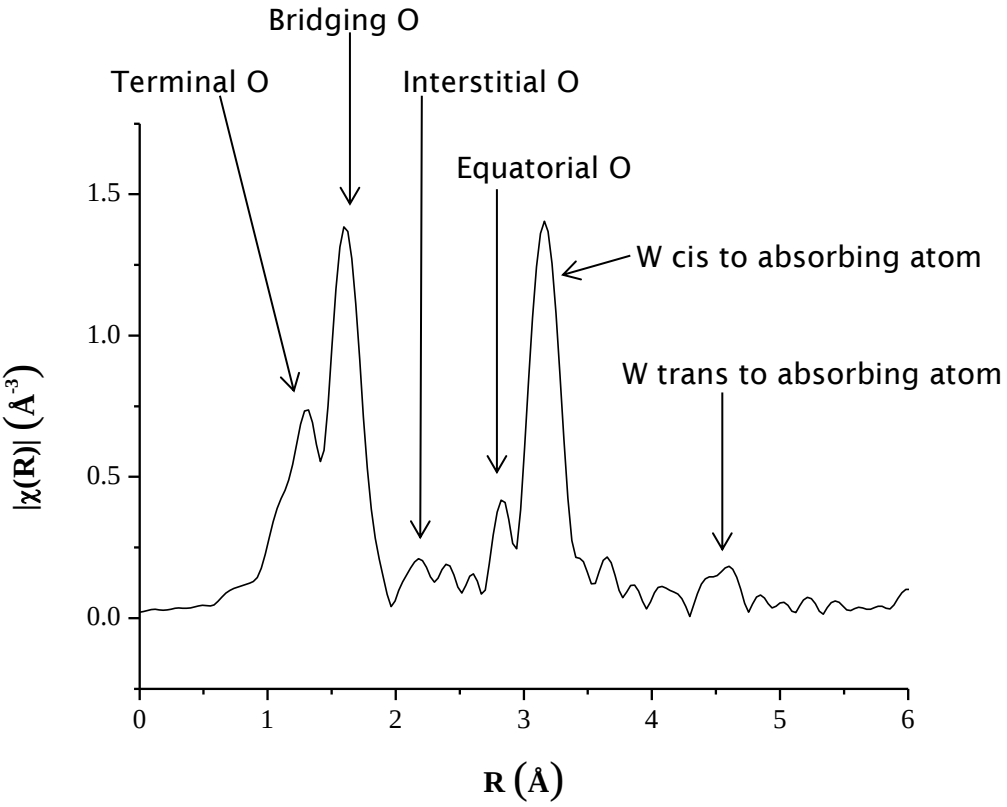

Figure 3.2: k^2-weighted Fourier transform for W L_{III} edge EXAFS of $[W_6O_{19}]^{2-}$.

3.2 Results and Discussion

EXAFS spectroscopy has been used to provide characterisations of $[W_6O_{19}]^{2-}$ and $[LMW_5O_{18}]^{n-}$ heteropolyanions (where M is a metal and L is a ligand) and the formation of some of these POMs have been followed. The starting materials used in the formation reaction for $[NBu^n_4]_2[W_6O_{19}]$ consist of 1 or 2 tungsten atoms. The intermediate species formed during the reaction have never been identified, but it has been postulated that a "virtual" precursor, $[W_5O_{18}]^{6-}$, is formed in Lindqvist-type POM syntheses.[11] A metal ion can react with this precursor without the presence of water to produce a $[MW_5O_{18}L]^{n-}$ heteropolyanion. This investigation develops a technique for investigating the nature of these intermediates and provides some insight into how the POM cluster grows to a structure consisting of 6 metal atoms.

As the reactions were slow, EXAFS spectra were recorded in situ on the beamline. To investigate the nature of the intermediates formed during the formation of $[NBu^n_4]_2[W_6O_{19}]$ a linear combination fit was run and a difference spectrum was created with contributions from the starting reagents and side products of the reaction removed from the EXAFS. $[WO_4]^{2-}$and $WO(OCH_3)_4$ are the precursors required in the synthesis of Lindqvist-type tungstates. The contributions from these reactants and other side-products of the reactions needed to be understood in order to carry out an analysis of the reaction mixture for the synthesis of $[NBu^n_4]_2[W_6O_{19}]$. $[NBu^n_4]_2[WO_4]$ and $WO(OCH_3)_4$ have therefore been studied using EXAFS to provide an understanding of the initial state of the reaction mixture.

In solution, $[LMW_5O_{18}]^{n-}$ has higher symmetry than in the solid state so the four tungsten sites cis to the heterometal atom can be accounted for in the same FEFF calculation. The amplitude reduction factor for the tungsten site trans to the heterometal atom accounts for 20% of the total amplitude reduction factor and the tungsten sites cis to the titanium atom account for 80% of the total amplitude reduction factor. All paths in the same shell (for example, W5→O9, W5→O13, W5→O15 and W5→O17 in figure 3.1) were included in the fit by fitting one path with a coordination number equal to the number of paths that would be used if each path were fitted with a coordination number of 1. There

are 2 different tungsten sites in $[LMW_5O_{18}]^{3-}$; 4 tungsten sites cis to the heterometal atom (W1, W2, W3 and W4 in figure 3.3) and 1 tungsten site trans to the titanium atom (W5 in the diagrams of the POMs).This was accounted for in curve fitting analyses for the heteropolyanions by using 2 FEFF calculations- one for the tungsten site trans to the heterometal and one for the tungsten sites cis to the heterometal. In fits for the heteropolyanions, the amplitude reduction factor was divided up into contributions from each tungsten site.

Including multiple-scattering paths in the fits helped to refine the EXAFS-derived structural parameters, but only the shells of single scattering paths below 4 Å have been included in the tables. Analyses of all the complexes in solution were carried out in acetonitrile and all the complexes were prepared by R. J. Errington et. al.[11,12]

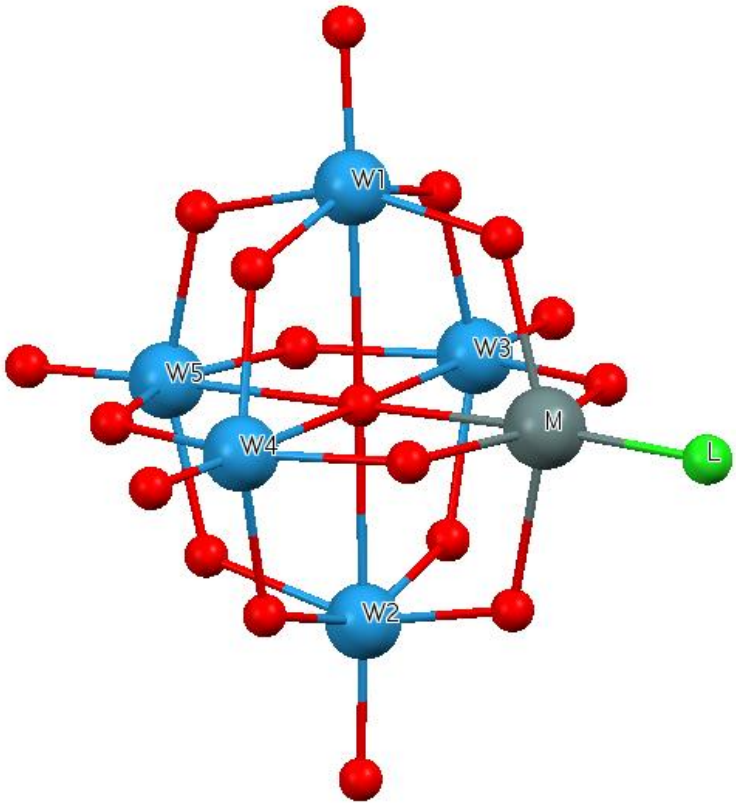

Figure 3.3: Structure of $[LMW_5O_{18}]^{n-}$. W is tungsten, M is a metal, L is a ligand and red spheres are oxygen atoms.

3.2.1 QEXAFS Study of $[NBu^n_4]_2[W_6O_{19}]$

The EXAFS-derived structural parameters for $[NBu^n_4]_3[W_6O_{19}]$ and all reaction precursors for the formation of this POM are presented in table 3.1 and the data regarding the quality of the fits for the anions are presented in table 3.2 (where O_t is the terminal oxygen, O_b is the bridging oxygen and O_i is the interstitial oxygen). The EXAFS spectrum and the Fourier transform for the W L_{III} edge of $[WO_4]^{2-}$ are presented in figure 3.4. The $[WO_4]^{2-}$ model used in the curve-fitting analysis was constructed using first shell theory and the W-O bond lengths refined in this fit are 1.79 Å and are consistent with previously reported bonds in $[WO_4]^{2-}$.[83] The amplitude reduction factor refined in this fit is 0.88, and to determine whether this was reliable, a range of values for the amplitude reduction factor were set for the same fit. The R-factors given by these fits have been plotted against the amplitude reduction factor used in the fit (figure 3.5) to determine whether the amplitude reduction factor that gives the lowest R-factor is the same as the refined amplitude reduction factor given when the amplitude is not set and this analysis give a minimum R-factor when the amplitude reduction factor is set to a value between 0.80 and 0.90.

The W L_{III} edge EXAFS spectrum and Fourier transform for the W L_{III} edge of $WO(OCH_3)_4$ (figure 3.6) is only of sufficient quality to fit 2 shells. 6 oxygen atoms in the first shell and 4 carbon atoms in the second shell have been included in the fit for this spectrum. This provides evidence that $WO(OCH_3)_4$ exists as a dimer in solution as oxygen atoms must be being shared by tungsten atoms.

Crystallographic data was imported into Artemis to provide a model for the curve-fitting analysis for the W L_{III} edge of $[NBu^n_4]_2[W_6O_{19}]$ in the solid state. The W L_{III} edge EXAFS spectrum and Fourier transform of $[NBu^n_4]_2[W_6O_{19}]$ in the solid state are presented in figure 3.7. The average bond length for the W-O_b bond (where O_b is a bridging oxygen) measured by EXAFS is 1.913 Å. The tungsten atom trans to the absorbing tungsten atom has been included in the fit and its distance from the absorbing tungsten is 4.545 Å. There are also forward scattering paths that are scattered by the interstitial oxygen atom as well as the tungsten atom trans to the absorbing tungsten atom. These multiple scattering paths contribute significantly to the EXAFS and collectively

contribute to the peak with an amplitude of 0.2 at about 4.5 Å in the Fourier transform.

In solution the $[W_6O_{19}]^{2-}$ anion has higher symmetry so a FEFF template was written using averages of the bond lengths in the crystallographic data to provide a model with higher symmetry. This FEFF template was used in the curve-fitting analysis for the W L_{III} edge of $[NBu^n_4]_2[W_6O_{19}]$ in acetonitrile. The W L_{III} edge EXAFS spectrum and Fourier transform of $[W_6O_{19}]^{2-}$ in the acetonitrile are presented in figure 3.8. The average bond length for the bridging oxygen in the crystal structure is 1.913 Å. This is 0.005 Å longer than the EXAFS derived distance in acetonitrile, but the error in a XAFS experiment is 0.02 Å, so this bond length should be regarded as equal in acetonitrile and in the solid state. The bond to the interstitial oxygen in the crystal structure is 0.035 Å longer than it is in acetonitrile. The W5···W6 distance (figure 3.1) is 4.527 Å and 4.764 Å when the complex is in the solid state and in acetonitrile, respectively. In the crystallographic data the average distance for this path is 4.651 Å.

The same analysis of the effect of the amplitude reduction on the R-factor that was conducted for $[WO_4]^{2-}$ in acetonitrile was also carried out for $[W_6O_{19}]^{2-}$ in the solid state. The results of this study are presented in figure 3.9. Again, the set amplitude reduction factor that resulted in the lowest R-factor was in agreement with the amplitude reduction factor that was refined by the curve fitting analysis reported.

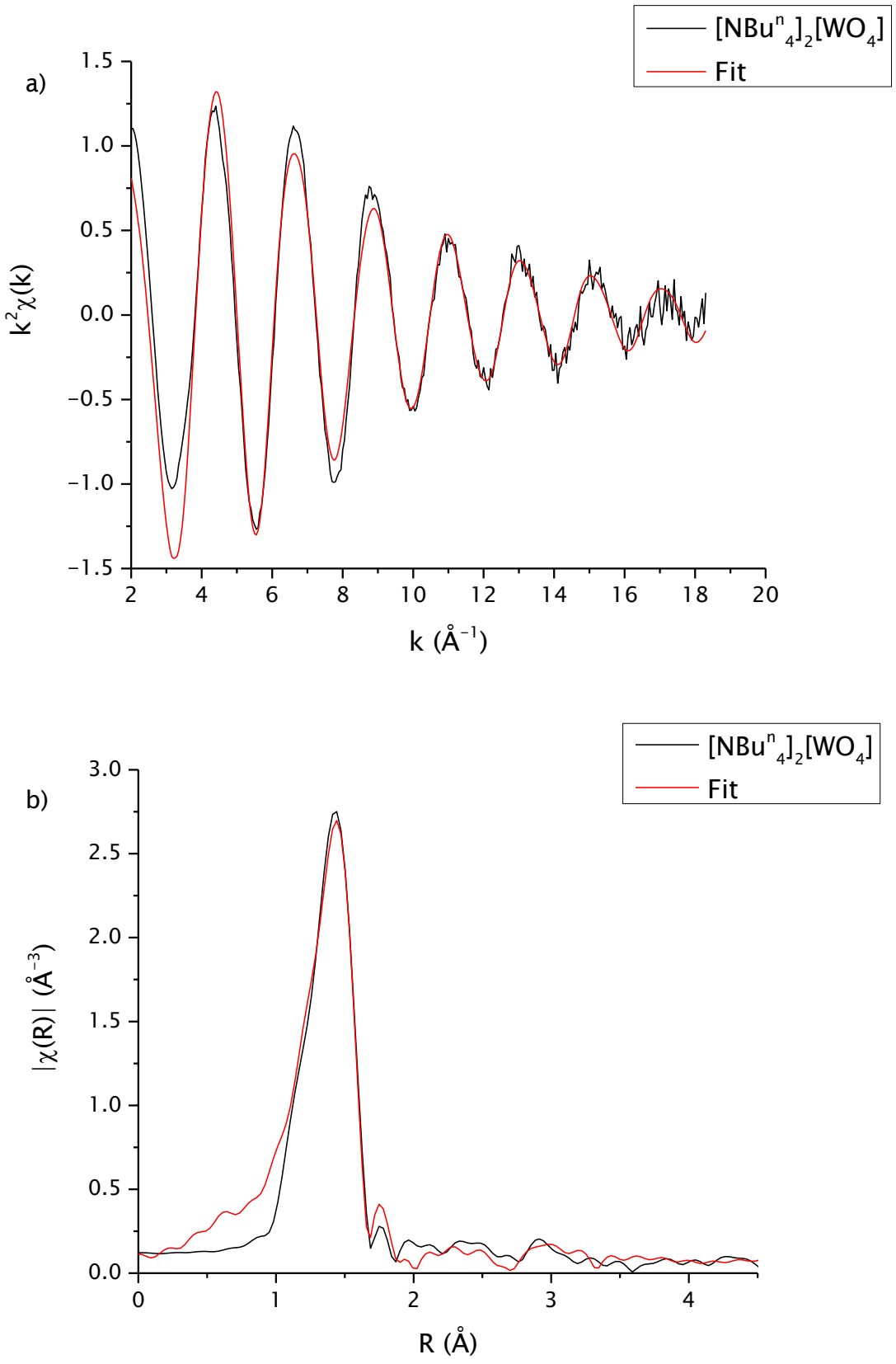

Figure 3.4: W L_{III} edge k^2-weighted a) EXAFS spectrum and b) Fourier transform of [NBu$^n_4$]$_2$[WO$_4$] in acetonitrile.

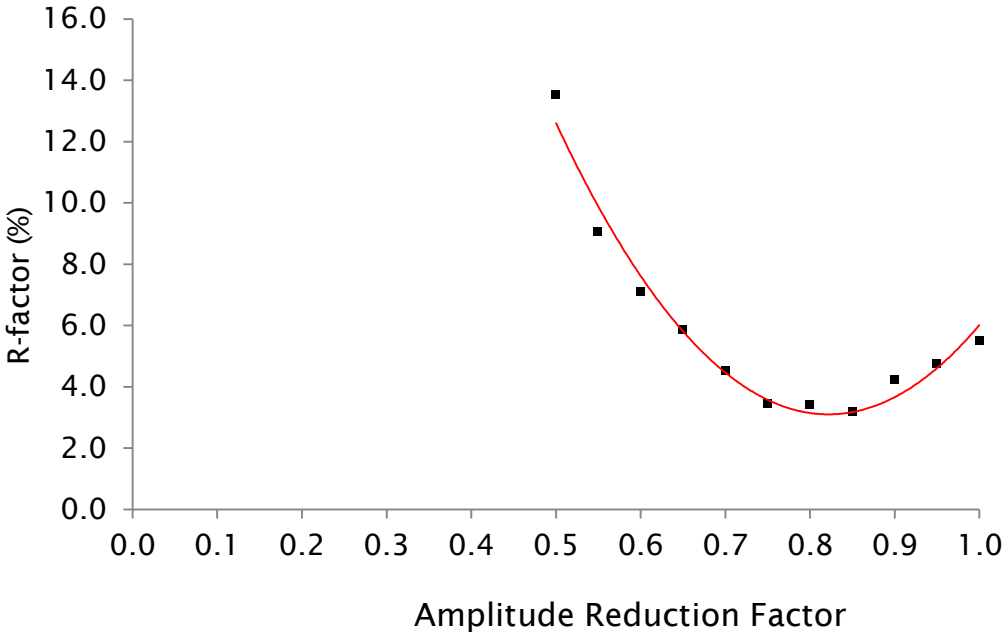

Figure 3.5: Effect of amplitude reduction factor on the R-factor for $[NBu^{n}_{4}]_{2}[WO_{4}]$.

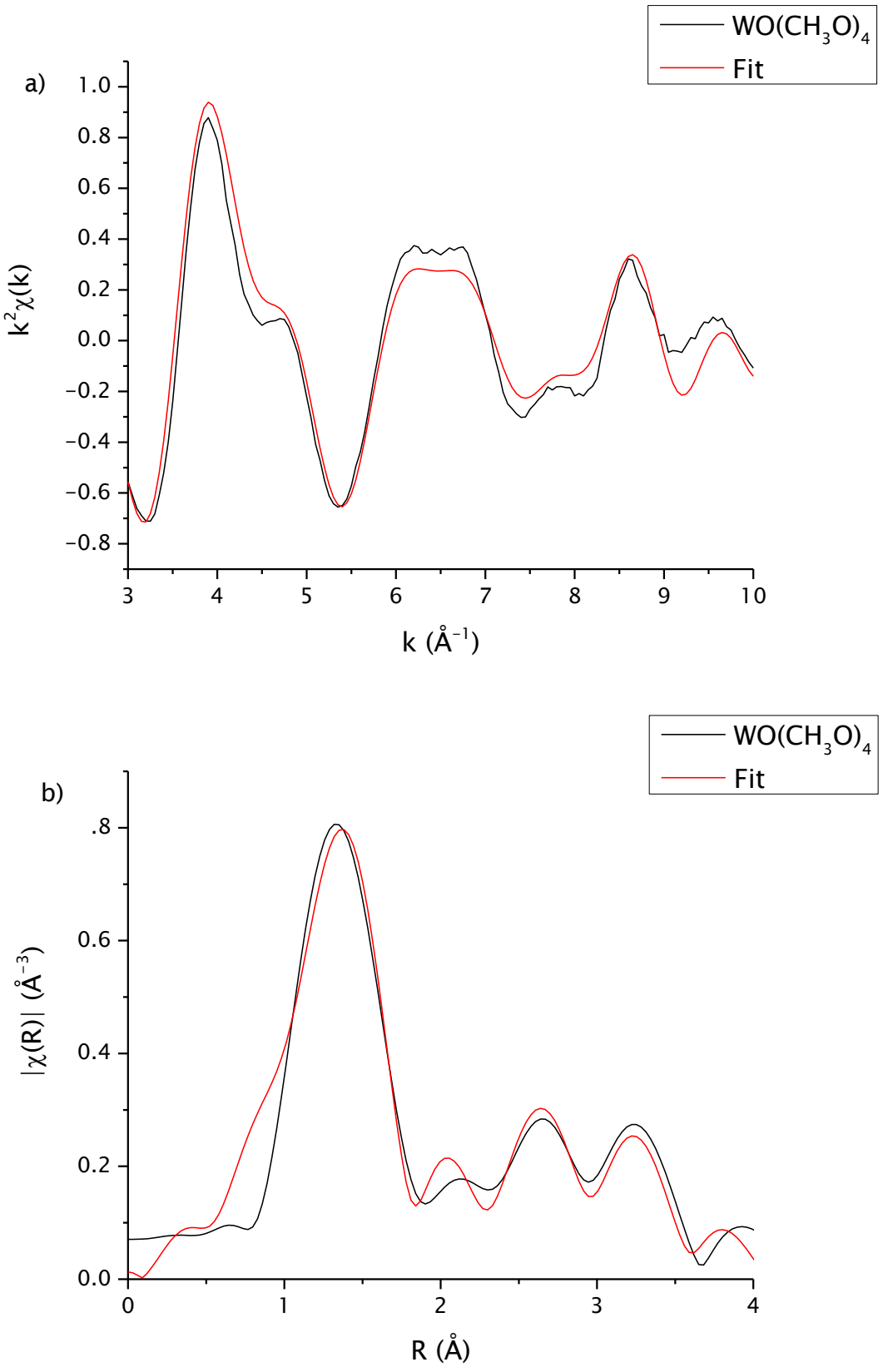

Figure 3.6: W L_{III} edge k^2-weighted a) EXAFS spectrum and b) Fourier transform of $WO(CH_3O)_4$ in acetonitrile.

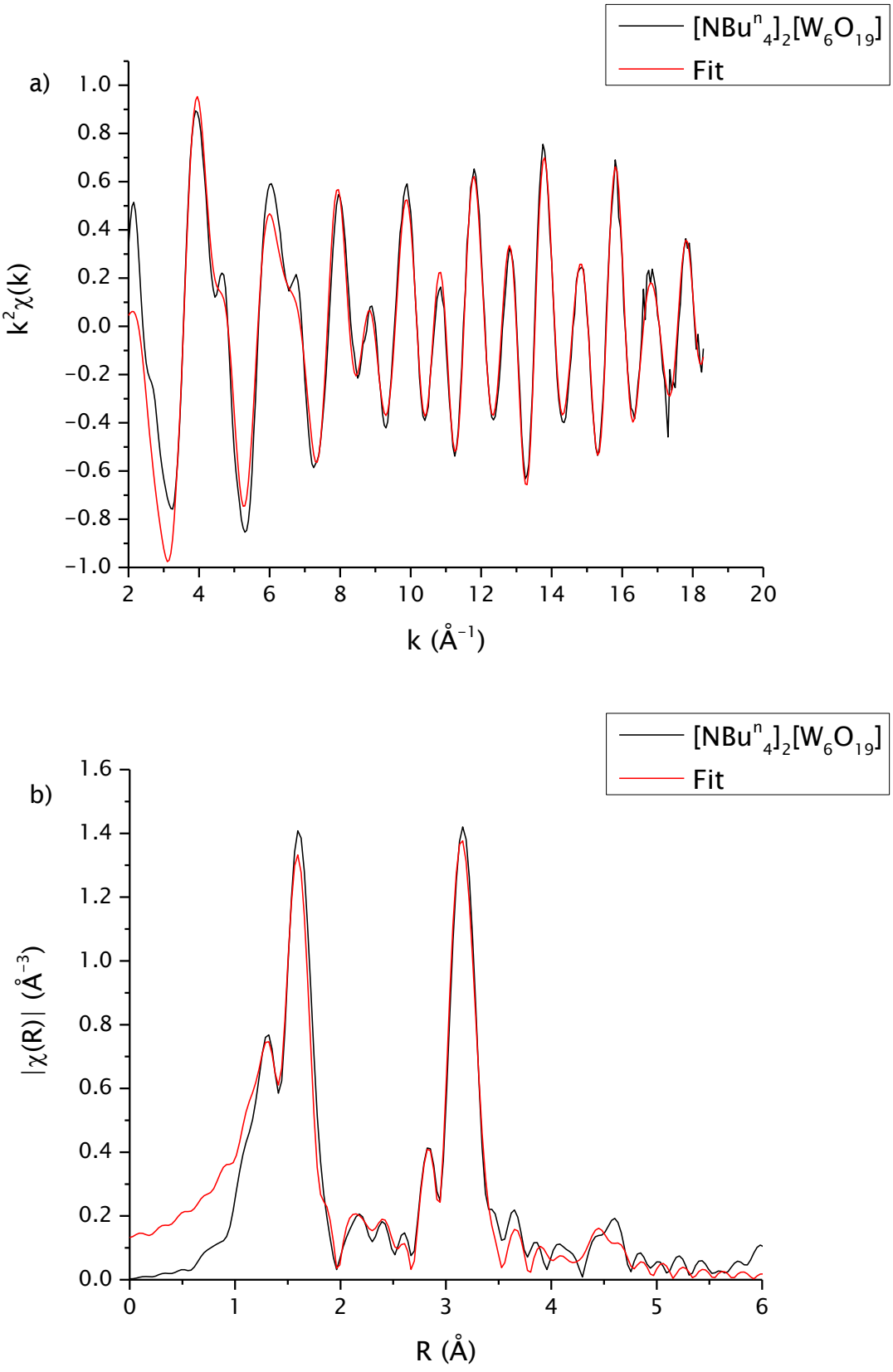

Figure 3.7: W L_{III} edge k^2-weighted a) EXAFS spectrum and b) Fourier transform of [NBu$^n_4$]$_2$[W$_6$O$_{19}$] in the solid state.

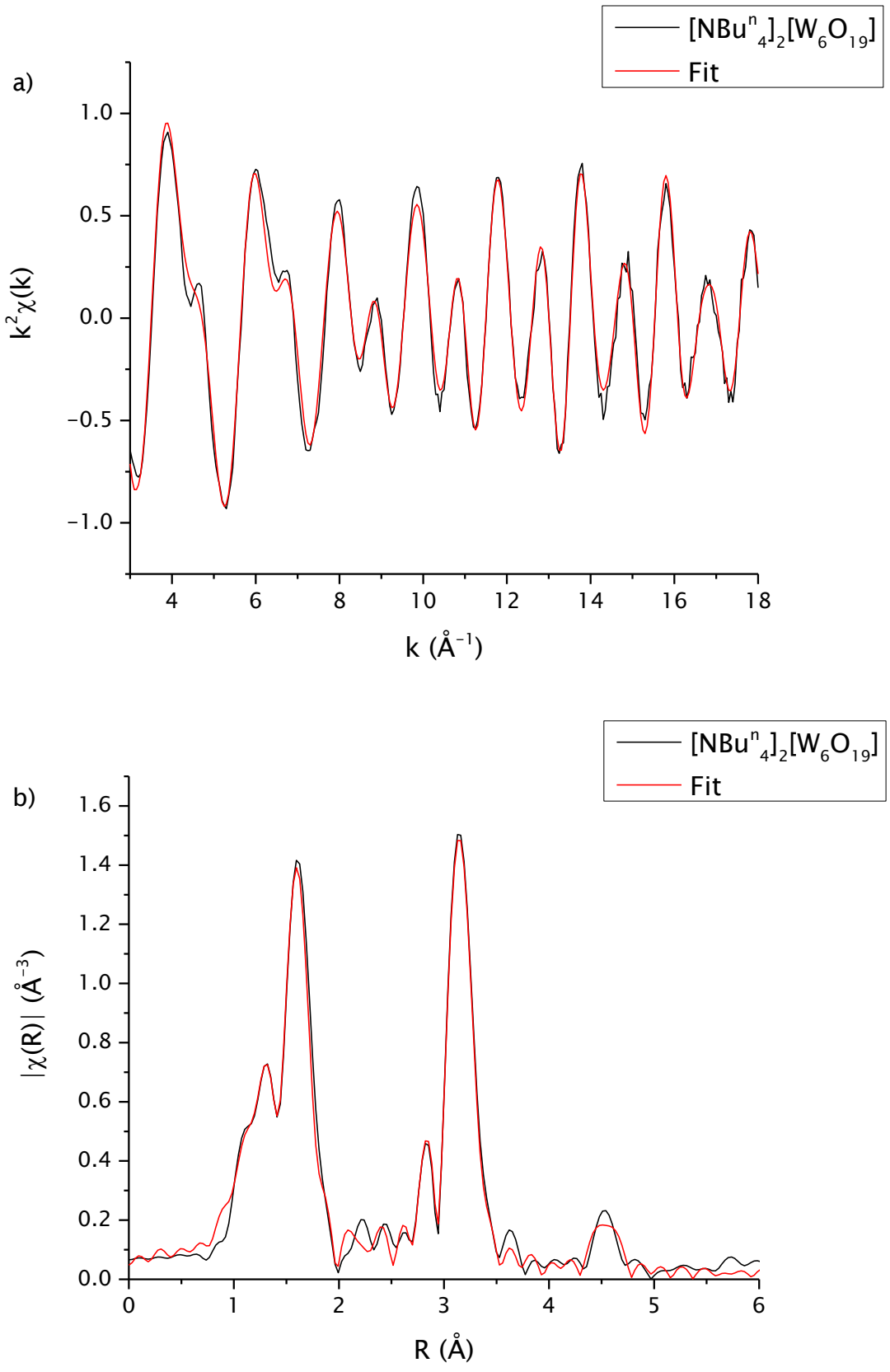

Figure 3.8: W L_{III} edge k^2-weighted a) EXAFS spectrum and b) Fourier transform of [NBu$^n_4$]$_2$[W$_6$O$_{19}$] in acetonitrile.

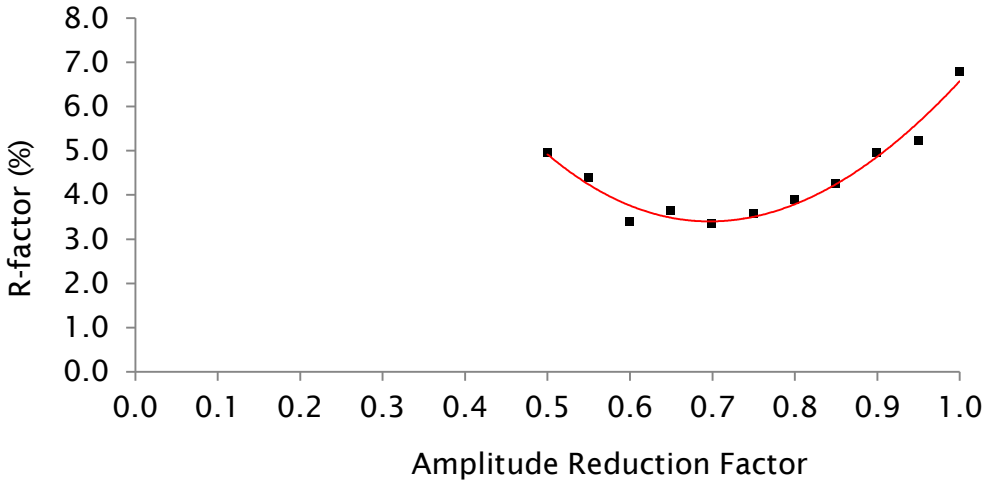

Figure 3.9: Effect of amplitude reduction factor on R for $[NBu^n_4]_2[W_6O_{19}]$.

Anion	Edge	Path	Degeneracy	σ^2 / Å^2	r / Å	r / Å (XRD)
$[WO_4]^{2-}$	W L_{III}	W↔O	4	0.00159 ± 0.00041	1.787 ± 0.003	-
Solution		W→O→O→W	12	0.00108 ± 0.01516	3.277 ± 0.084	-
		W→O→W→O→W	4	-0.00404 ± 0.00494	3.652 ± 0.064	-
		W→O→W→O→W	12	-0.00231 ± 0.02323	4.678 ± 0.117	-
$WO(OMe)_4$	W L_{III}	W↔O	1	0.00580 ± 0.00603	1.591 ± 0.033	-
Solution		W↔O	1	0.00580 ± 0.00603	1.771 ± 0.033	-
		W↔O	1	0.00580 ± 0.00603	1.774 ± 0.033	-
		W↔O	1	0.00580 ± 0.00603	1.781 ± 0.033	-
		W↔O	1	0.00580 ± 0.00603	1.917 ± 0.033	-
		W↔O	1	0.00580 ± 0.00603	2.143 ± 0.033	-
		W↔C	1	0.01841 ± 0.02696	2.916 ± 0.142	-
		W↔C	1	0.01841 ± 0.02696	2.941 ± 0.142	-
		W↔C	1	0.01841 ± 0.02696	2.944 ± 0.142	-
		W↔C	1	0.01841 ± 0.02696	2.978 ± 0.142	-
$[W_6O_{19}]^{2-}$	W L_{III}	W↔O_t	1	0.00057 ± 0.00076	1.702 ± 0.012	1.696
Solid		W↔O_b	1	0.00309 ± 0.00090	1.902 ± 0.006	1.908
		W↔O_b	1	0.00309 ± 0.00090	1.911 ± 0.006	1.918
		W↔O_b	1	0.00309 ± 0.00090	1.916 ± 0.006	1.923
		W↔O_b	1	0.00309 ± 0.00090	1.922 ± 0.006	1.929
		W↔O_i	1	0.00167 ± 0.00230	2.321 ± 0.024	2.321
		W↔W	1	0.00252 ± 0.00047	3.286 ± 0.007	3.281
		W↔W	1	0.00252 ± 0.00047	3.291 ± 0.007	3.286
		W↔W	1	0.00252 ± 0.00047	3.292 ± 0.007	3.287
		W↔W	1	0.00252 ± 0.00047	3.301 ± 0.007	3.296
Solution	W L_{III}	W↔O_t	1	0.00061 ± 0.00083	1.704 ± 0.010	1.683
		W↔O_b	4	0.00344 ± 0.00092	1.908 ± 0.006	1.941
		W↔O_i	1	0.00200 ± 0.00214	2.286 ± 0.022	2.325
		W↔W	4	0.00301 ± 0.00073	3.281 ± 0.007	3.288

Table 3.1: The EXAFS-derived structural parameters for anions involved in the synthesis of $[W_6O_{19}]^{2-}$. Solution samples are in acetonitrile.

Anion	Edge	Parameter	Value
$[WO_4]^{2-}$	W L_{III}	R (%)	1.36
Solution		R, k = 1 (%)	4.50
		R, k = 2 (%)	2.42
		R, k = 3 (%)	2.91
		Chi-square	4090
		Reduced chi-square	158
		Amplitude reduction factor	0.88 ± 0.05
		k range ($Å^{-1}$)	2.0 - 18.3
		R range (Å)	1.0 - 4.5
		No. of independent parameters	52
		No. of variables	8
$WO(OMe)_4$	W L_{III}	R (%)	0.76
Solution		R, k = 1 (%)	0.75
		R, k = 2 (%)	1.75
		R, k = 3 (%)	4.57
		Chi-square	5844
		Reduced chi-square	5008
		Amplitude reduction factor	1.07 ± 0.55
		k range ($Å^{-1}$)	3.0 - 10.0
		R range (Å)	1.0 - 4.0
		No. of independent parameters	13
		No. of variables	12
$[W_6O_{19}]^{2-}$	W L_{III}	R (%)	3.37
Solid		R, k = 1 (%)	9.17
		R, k = 2 (%)	2.90
		R, k = 3 (%)	1.44
		Chi-square	4565
		Reduced chi-square	195
		Amplitude reduction factor	0.68 ± 0.07
		k range ($Å^{-1}$)	2.0 - 18.3
		R range (Å)	1.0 - 6.0
		No. of independent parameters	28
		No. of variables	51
Solution	W L_{III}	R (%)	0.72
		R, k = 1 (%)	1.84
		R, k = 2 (%)	1.46
		R, k = 3 (%)	1.39
		Chi-square	3774
		Reduced Chi-square	284
		Amplitude reduction factor	0.84 ± 0.09
		k range ($Å^{-1}$)	3.0 - 18.0
		R range (Å)	1.0 - 6.0
		No. of independent parameters	47
		No. of variables	34

Table 3.2: Refined parameters for fits to anions involved in the synthesis of $[W_6O_{19}]^{2-}$. Solution samples are in acetonitrile.

A 1:1 mixture of $[NBu^n_4]_2[WO_4]$ and $WO(OCH_3)_4$ reacts in acetonitrile at room temperature to produce $W_2O_5(OCH_3)_4$ (figure 3.10). This has been demonstrated using EXAFS spectroscopy by recording spectra of a reaction solution containing a 1:1 mixture of $[NBu^n_4]_2[WO_4]$ and $WO(OCH_3)_4$ and conducting a curve fitting analysis using crystallographic data for $W_2O_5(OCH_3)_4$ as a model. This model fit the data. The EXAFS spectrum and the Fourier transform for the W L_{III} edge of $[W_2O_5(OCH_3)_4]^{2-}$ are presented in figure 3.11. The EXAFS-derived structural parameters for $[W_2O_5(OCH_3)_4]^{2-}$ are presented in table 3.3 and the data regarding the quality of the fits are presented in table 3.4.

The reaction between $WO(OMe)_4$ and $[NBu^n_4]_2[WO_4]$ in the presence of water (equation 3.1) has been monitored by EXAFS spectroscopy. A linear combination fit (LCF) was run for the averaged spectrum for the reaction solution. The weightings of contributions from 3 standards – $WO(OMe)_4$, $[NBu^n_4]_2[WO_4]$ and $[W_2O_5(OCH_3)_4]^{2-}$ were calculated in the fit, with the sum of the weightings of each component being equal to one. However, all the weighting of the fit was attributed to contributions from $[W_2O_5(OCH_3)_4]^{2-}$.

$$[WO_4]^{2-} + 5\ WO(OR)_4 + 10\ H_2O \rightarrow [W_6O_{19}]^{2-} + 20\ ROH \qquad \text{(Equation 3.1)}$$

A difference spectrum between the data and the LCF was created for the merged spectrum, leaving a spectrum that contained no contribution from $[NBu^n_4]_2[WO_4]$, $WO(OMe)_4$ or $[NBu^n_4]_2[W_2O_5(OCH_3)_4]$. Attempting to create a difference spectrum in norm(E) resulted in the loss of the absorption edge in the difference spectrum, so the procedure was carried out using $\chi(k)$ as the fitting space and a difference spectrum was created in $\chi(k)$. From this spectrum it is clear that there are other species present in the reaction solution apart from $[NBu^n_4]_2[WO_4]$, $WO(OCH_3)_4$ and $[NBu^n_4]_2[W_2O_5(OCH_3)_4]$.

To elucidate the nature of the intermediates formed during the synthesis of $[W_6O_{19}]^{2-}$ various structures were fitted to the difference spectrum. 3 structures are reported which have been fit to the difference spectrum and have well refined structural parameters from curve fitting analyses: $[W_3O_{10}]^{n-}$, $[W_5O_{16}]^{n-}$ and $[W_5O_{14}N_4]^{n-}$ (figures 3.12, 3.13 and 3.14 respectively).

$[W_3O_{10}]^{n-}$ is made up of 3 5-coordinate tungsten atoms. Each tungsten atom is coordinated by 2 terminal oxygen atoms and 1 oxygen atom that bridges each pair of tungsten atoms. The trinuclear complex is capped by an oxygen atom (O19 in figure 3.12). Although it does not seem intuitive that the tungsten atoms should remain 5-coordinate when there is a wealth of potential coordinating solvent, this 5-coordinate arrangement means that there are only 2 terminal oxygen atoms on each tungsten atom. It has been observed that MO_6 octahedral unit never have more than two terminal oxygen atoms.[84] The terminal oxygen atoms are bound to the tungsten atoms by π-bonding more than 2 π-bonded terminal oxygen atoms would cause the bonds to the bridging oxygen atoms to break.[84] A trinuclear complex, $[Mo_3O_4(H_2O)_9]^{4+}$, has been reported previously[85], and the $[W_3O_{10}]^{n-}$ structure that has been refined in this EXAFS analysis does bear some resemblance to this molybdenum cluster. If acetonitrile does coordinate to the tungsten atoms after the $[W_3O_{10}]^{n-}$ has been formed then the complex may decompose and would not be observed. This may also offer some insight as to why the formation of $[W_6O_{19}]^{2-}$occurs on such a long timescale.

$[W_5O_{16}]^{n-}$ consists of 2 5-coordinate tungsten atoms (W3 and W4 in figure 3.13) and 3 6-coordinate tungsten atoms. The 6-coordinate tungsten atoms in this structure only have 1 terminal oxygen atom and the reason for there being no coordinated solvent on the 5-coordinate tungsten atoms is more unclear, as the coordinated solvent would not cause the complex to dissociate. However, a model with coordinated acetonitrile on W3 and W4 does not fit the difference spectrum.

$[W_5O_{14}N_4]^{n-}$ also fitted well with the difference spectrum. All the tungsten atoms in this structure are 6-coordinate. Heteropolyanions are formed by reacting a metal ion, for example Co^{2+}, with a pentanuclear precursor.[11] This can be achieved without the addition of water to the reaction solution, so it stands to reason that $[W_5O_{18}]^{6-}$ must be formed by the reaction under investigation. However, this structure has not been successfully fitted to the data. It is possible that the structures reported do not represent the real structures that are present in the reaction solution, as the observed EXAFS are an average of all the species present in the solution. If more than one structure is present then the only way to fit an accurate model to the experimental data is to simultaneously fit each structure.

Fits of $[W_3O_{10}]^{n-}$, $[W_5O_{16}]^{n-}$ and $[W_5O_{14}N_4]^{n-}$ to the difference spectrum created by removing contributions from $[NBu^n_4]_2[WO_4]$, $WO(OCH_3)_4$ and $[NBu^n_4]_2[W_2O_5(OCH_3)_4]$ from the W L_{III} edge spectrum for the reaction solution are presented in figure 3.15 – 3.17 respectively. The EXAFS-derived structural parameters for $[W_3O_{10}]^{n-}$, $[W_5O_{16}]^{n-}$ and $[W_5O_{14}N_4]^{n-}$ are presented in table 3.3 and the data regarding the quality of the fits are presented in table 3.4.

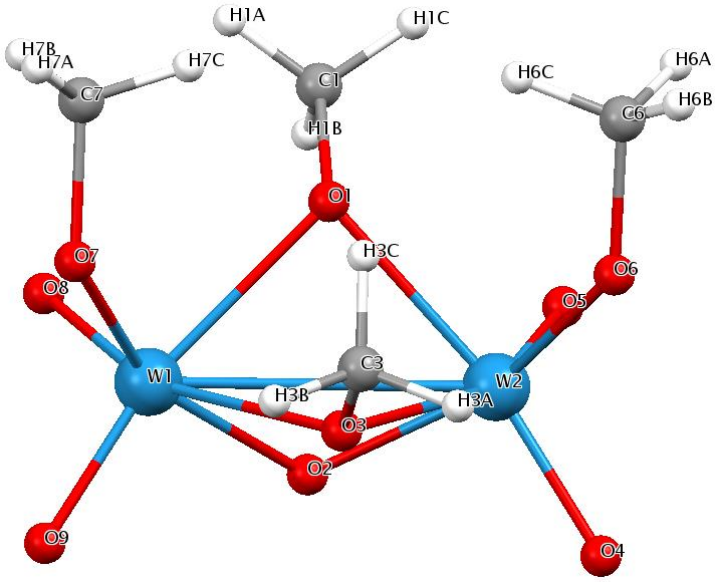

Figure 3.10: Structure of $[W_2O_5(CH_3O)_4]^{2-}$.

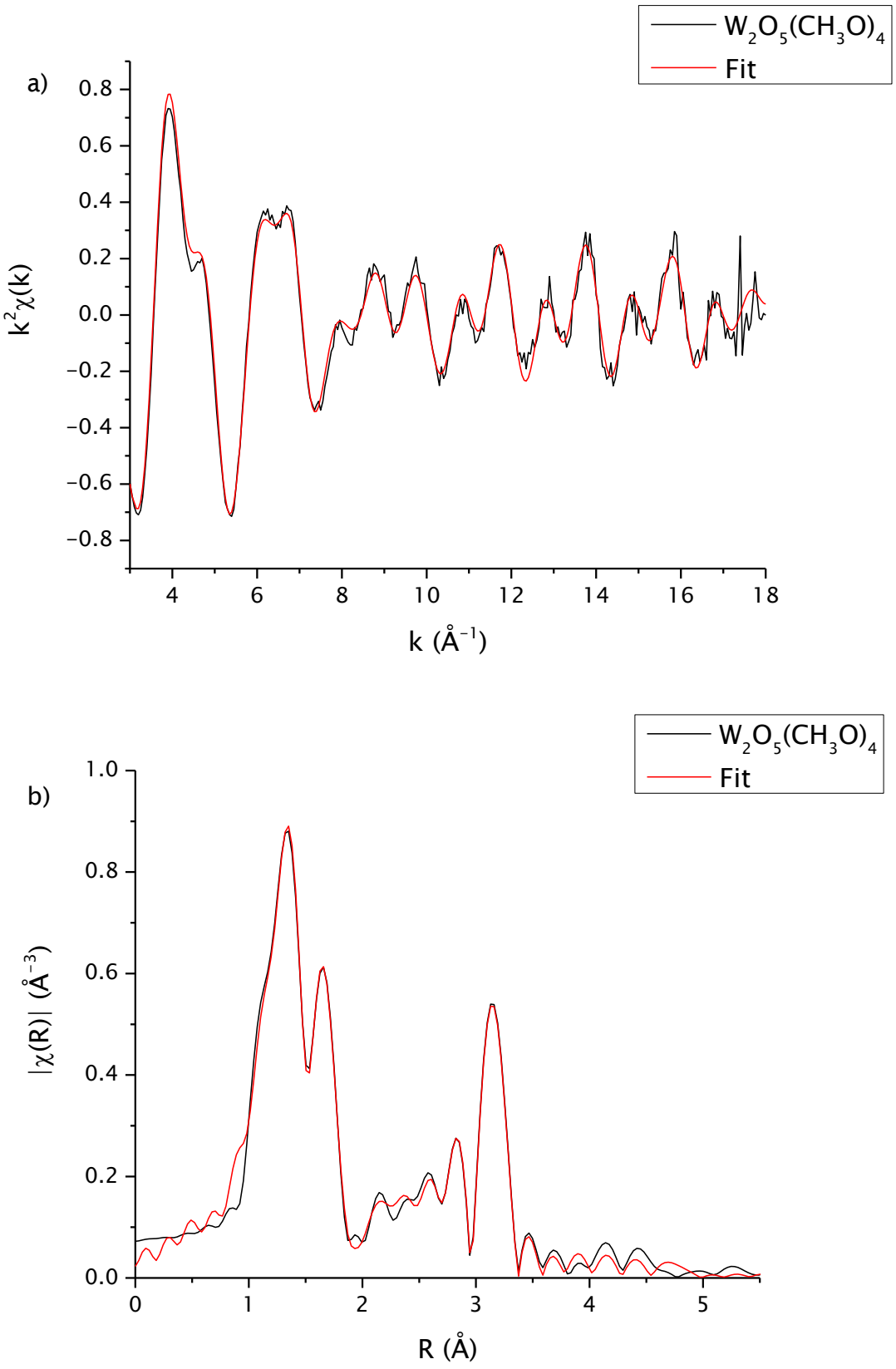

Figure 3.11: W L_{III} edge k^2-weighted a) EXAFS spectrum and b) Fourier transform of $[W_2O_5(OCH_3)_4]^{2-}$ in acetonitrile.

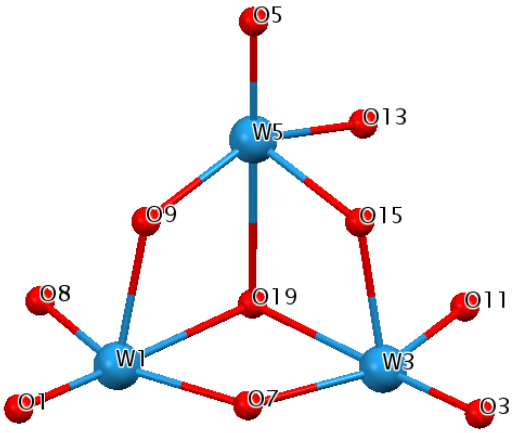

Figure 3.12: Structure of $[W_3O_{10}]^{n-}$.

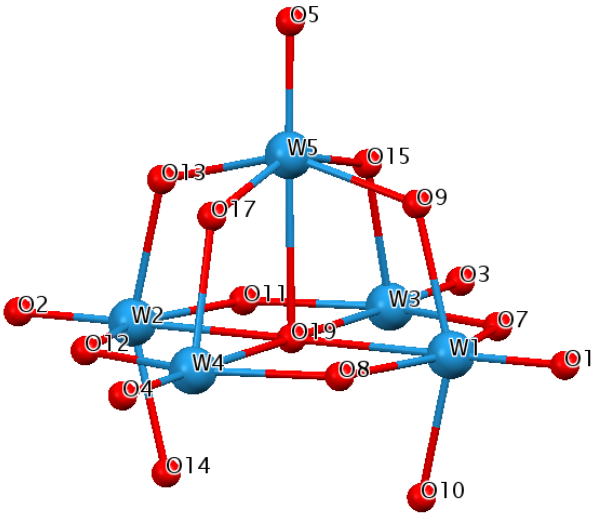

Figure 3.13: Structure of $[W_5O_{16}]^{n-}$.

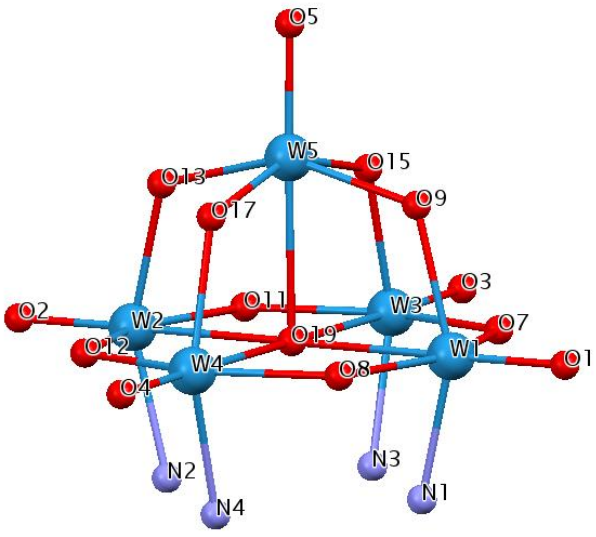

Figure 3.14: Structure of $[W_5O_{14}N_4]^{n-}$.

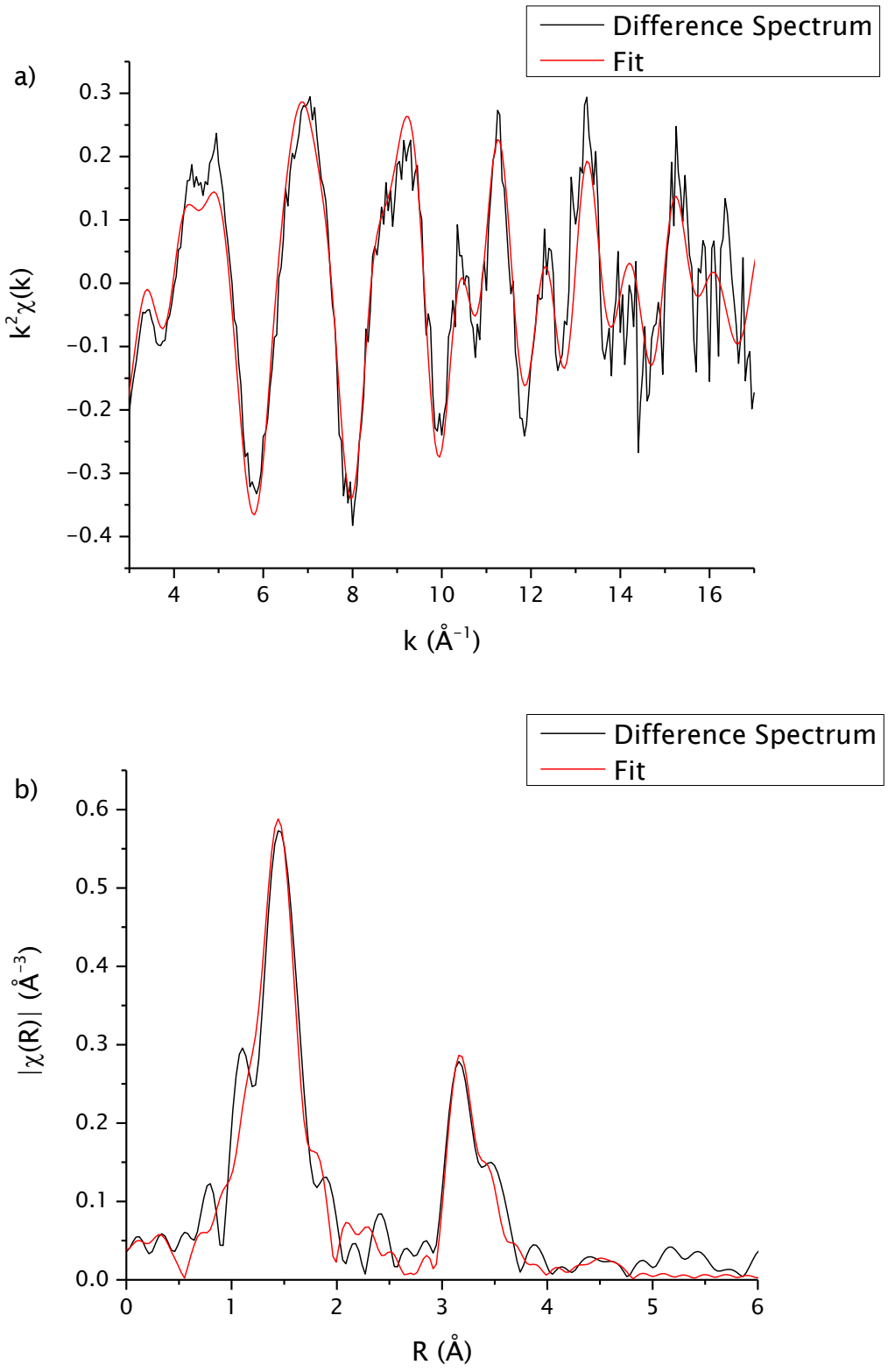

Figure 3.15: $[W_3O_{10}]^{n-}$ fit to W L_{III} edge k^2-weighted a) EXAFS spectrum and b) Fourier transform of the difference spectrum (with contributions from the starting materials and side products removed from the EXAFS for equation 3.1) in acetonitrile.

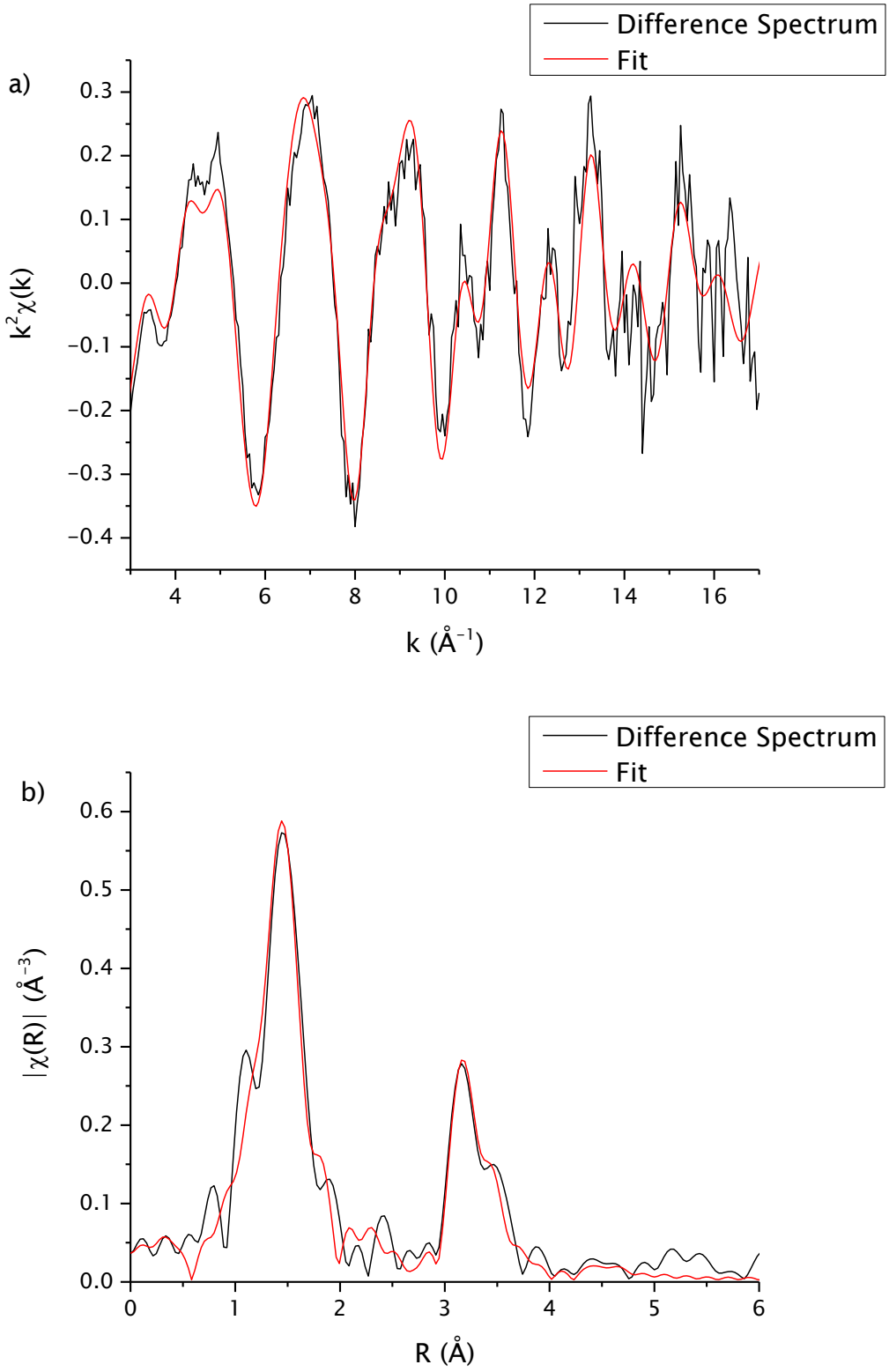

Figure 3.16: $[W_5O_{16}]^{n-}$ fit to W L_{III} edge k^2-weighted a) EXAFS spectrum and b) Fourier transform of the difference spectrum (with contributions from the starting materials and side products removed from the EXAFS for equation 3.1) in acetonitrile.

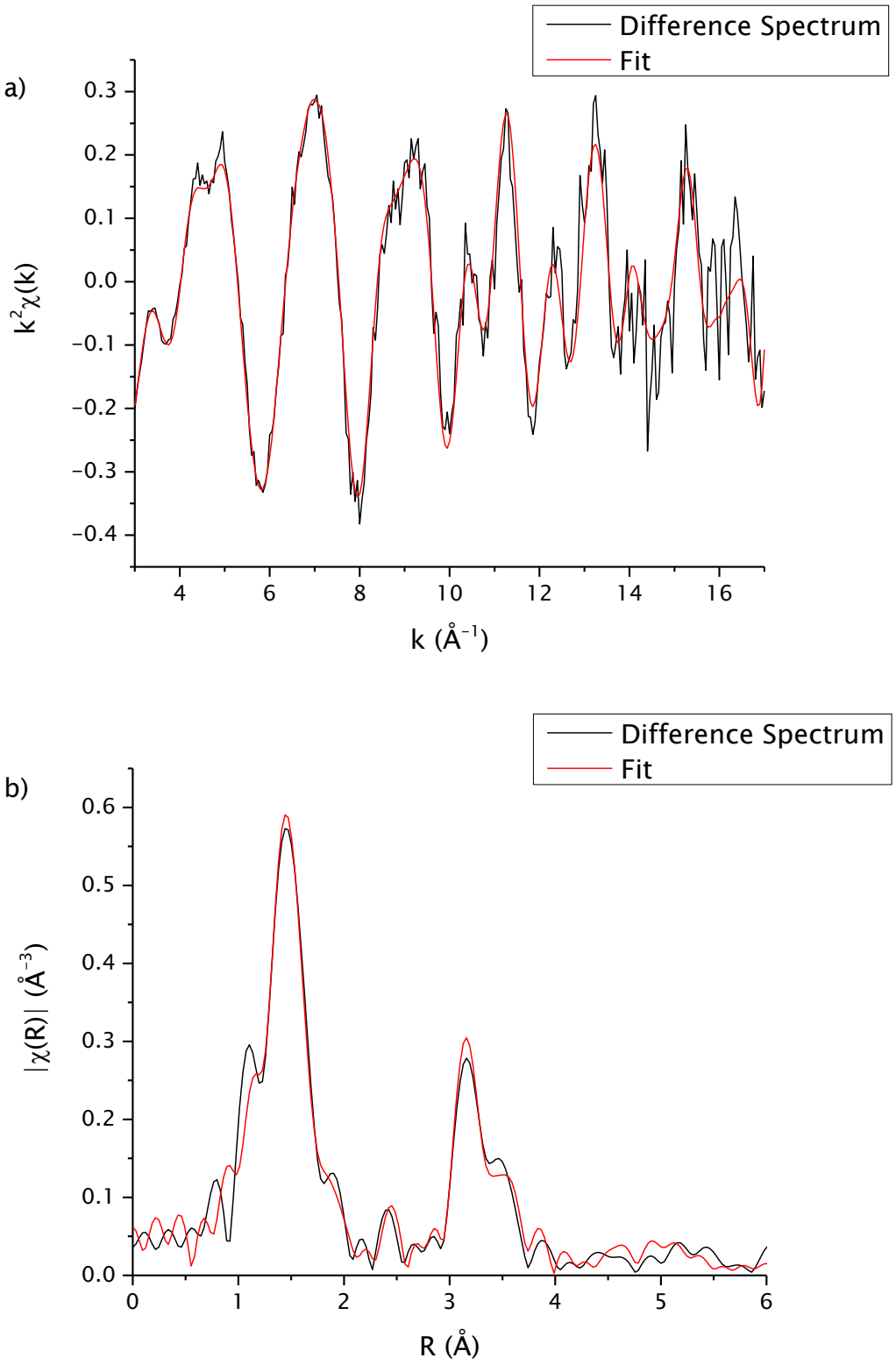

Figure 3.17: $[W_5O_{14}N_4]^{2-}$ fit to W L_{III} edge k^2-weighted a) EXAFS spectrum and b) Fourier transform of the difference spectrum (with contributions from the starting materials and side products removed from the EXAFS for equation 3.1) in acetonitrile.

Anion	Edge	W site	Path	Degeneracy	σ^2 / Å^2	r / Å	r / Å (XRD)
$W_2O_5(OCH_3)_4$	W L_{III}		W↔O	1	0.00233 ± 0.00035	1.733 ± 0.003	1.730
Solution			W↔O	1	0.00233 ± 0.00035	1.742 ± 0.003	1.739
			W↔O	1	0.00325 ± 0.00045	1.910 ± 0.004	1.931
			W↔O	1	0.00325 ± 0.00045	1.911 ± 0.004	1.932
			W↔O	1	0.00838 ± 0.00103	2.226 ± 0.007	2.178
			W↔O	1	0.00838 ± 0.00103	2.295 ± 0.007	2.247
			W↔W	1	0.00323 ± 0.00148	3.254 ± 0.020	3.075
			W↔O	1	0.00864 ± 0.00534	4.228 ± 0.033	4.135
			W↔O	1	0.00864 ± 0.00534	4.352 ± 0.033	4.259
			W↔O	1	0.00864 ± 0.00534	4.381 ± 0.033	4.288
			W↔C	1	0.01195 ± 0.00993	3.109 ± 0.057	2.992
			W↔C	1	0.00059 ± 0.00289	3.340 ± 0.026	3.206
			W↔C	1	0.00059 ± 0.00289	3.359 ± 0.026	3.226
$[W_3O_{10}]^{n-}$			W↔O	1	0.00139 ± 0.00289	1.752 ± 0.007	-
Solution			W↔O	3	0.03915 ± 0.00289	2.330 ± 0.007	-
			W↔O	1	0.00501 ± 0.00289	2.110 ± 0.007	-
			W↔W	2	0.00592 ± 0.00289	3.411 ± 0.007	-
$[W_5O_{16}]^{n-}$		W1	W↔O_t	1	0.00143 ± 0.00066	1.753 ± 0.007	-
Solution			W↔O_b	4	0.04217 ± 0.00547	2.330 ± 0.021	-
			W↔O_i	1	0.00517 ± 0.00160	2.109 ± 0.013	-
			W↔W	4	0.00694 ± 0.00070	3.409 ± 0.010	-
		W3	W↔O_t	1	0.00143 ± 0.00066	1.753 ± 0.007	-
			W↔O_b	3	0.04217 ± 0.00547	2.330 ± 0.021	-
			W↔O_i	1	0.00517 ± 0.00160	2.109 ± 0.013	-
			W↔W	3	0.00694 ± 0.00070	3.409 ± 0.010	-
		W5	W↔O_t	1	0.00143 ± 0.00066	1.753 ± 0.007	-
			W↔O_b	4	0.04217 ± 0.00547	2.330 ± 0.021	-
			W↔O_i	1	0.00517 ± 0.00160	2.109 ± 0.013	-
			W↔W	3	0.00694 ± 0.00070	3.409 ± 0.010	-
$[W_5O_{14}N_4]^{n-}$	W L_{III}	W5	W↔O_t	1	0.00105 ± 0.00159	1.758 ± 0.023	-
Solution			W↔O_b	4	0.01639 ± 0.00589	2.110 ± 0.054	-
			W↔O_i	1	0.01202 ± 0.04592	2.468 ± 0.076	-
			W↔W	4	0.00370 ± 0.05232	3.432 ± 0.363	-
		W1	W↔O_t	1	0.00105 ± 0.00159	1.758 ± 0.023	-
			W↔O_b	3	0.01639 ± 0.00589	2.110 ± 0.054	-
			W↔N	1	0.00967 ± 0.01906	1.684 ± 0.142	-
			W↔O_i	1	0.01202 ± 0.04592	2.468 ± 0.076	-
			W↔W	3	0.00370 ± 0.05232	3.432 ± 0.363	-

Table 3.3: The EXAFS-derived structural parameters for anions that fit the the reaction solutions. W sites match atom labels in figures 12, 13 and 14. Solution samples are in acetonitrile.

Anion	Edge	Parameter	Value
$W_2O_5(OCH_3)_4$ solution	W L_{III}	R (%)	0.79
		R, k = 1 (%)	0.15
		R, k = 2 (%)	0.52
		R, k = 3 (%)	1.61
		Chi-square	281
		Reduced chi-square	17
		Amplitude reduction factor	0.80 ± 0.04
		k range ($Å^{-1}$)	3.0 - 18.0
		R range (Å)	1.0 - 5.5
		No. of independent parameters	42
		No. of variables	26
$[W_3O_{10}]^{n-}$	W L_{III}	R (%)	6.41
		R, k = 1 (%)	2.47
		R, k = 2 (%)	5.25
		R, k = 3 (%)	11.10
		Chi-square	377
		Reduced chi-square	14
		Amplitude reduction factor	0.97 ± 0.11
		k range ($Å^{-1}$)	3.0 - 18.0
		R range (Å)	1.3 - 6.0
		No. of independent parameters	44
		No. of variables	18
$[W_5O_{16}]^{n-}$	W L_{III}	R (%)	6.21
		R, k = 1 (%)	2.31
		R, k = 2 (%)	5.04
		R, k = 3 (%)	10.94
		Chi-square	360
		Reduced chi-square	15
		Amplitude reduction factor	0.98 ± 0.12
		k range ($Å^{-1}$)	3.0 - 18.0
		R range (Å)	1.3 - 6.0
		No. of independent parameters	44
		No. of variables	20
$[W_5O_{14}N_4]^{2-}$ solution	W L_{III}	R (%)	0.23
		R, k = 1 (%)	0.17
		R, k = 2 (%)	0.19
		R, k = 3 (%)	0.34
		Chi-square	19
		Reduced chi-square	46
		Amplitude reduction factor	1.00
		k range ($Å^{-1}$)	3.0 - 17.0
		R range (Å)	1.3 - 6.0
		No. of independent parameters	41
		No. of variables	41

Table 3.4: Refined parameters for fits to anions that fit the the reaction solutions. Solution samples are in acetonitrile.

3.2.2 QEXAFS Study of $[NBu_4]_3[LTiW_5O_{18}]$

EXAFS spectroscopy has been used to characterise $[NBu^n_4]_3[(CH_3O)TiW_5O_{18}]$ in the solid state and $[NBu^n_4]_3[ClTiW_5O_{18}]$ in acetonitrile. The EXAFS-derived structural parameters for $[NBu^n_4]_3[(CH_3O)TiW_5O_{18}]$ in the solid state are presented in table 3.5. The EXAFS-derived structural parameters for $[NBu^n_4]_3[ClTiW_5O_{18}]$ in acetonitrile are presented in table 3.6. The data regarding the quality of both of these fits are presented in table 3.7.

Crystallographic data was imported as a model for $[NBu^n_4]_3[(CH_3O)TiW_5O_{18}]$ (figure 3.18). Since the POM unit is not exactly symmetrical all the tungsten sites have been incorporated in the fit separately. This was achieved by running FEFF calculations for each tungsten site and dividing the amplitude reduction factor by 5 for each path that was included in the fit. The interatomic distances refined in the fit are in agreement with crystallographic data from literature.[18] The average W-O_t, W-O_bW, W-O_bTi and W-O_i bond lengths are 1.701 Å, 1.899 Å, 1.887 Å and 2.327 Å respectively. This W-O_bW bond length is 0.014 Å shorter than it is in $[W_6O_{19}]^{2-}$, however the W-O_t and W-O_i bond lengths are more or less the same in both complexes. The Ti···W5 distance is 4.729 Å. The refined amplitude reduction factor is similar to the amplitude reduction factor obtained from the solid $[NBu^n_4]_2[W_6O_{19}]$ fit. The W L_{III} edge EXAFS spectrum and the Fourier transform for $[NBu^n_4]_3[(CH_3O)TiW_5O_{18}]$ in the solid state are presented in figure 3.19.

The model for the curve fitting analysis for $[ClTiW_5O_{18}]^{3-}$ in acetonitrile was constructed by writing a FEFF template, taking an average of the bond lengths in the crystallographic data and replacing the CH_3O group with a chlorine atom. The average W-O_bW bond in $[ClTiW_5O_{18}]^{3-}$ is 0.023 Å shorter than the W-O_b bonds in $[W_6O_{19}]^{2-}$. The W-O_t bond is 0.019 Å shorter and the W-O_l bond is 0.042 Å longer in $[ClTiW_5O_{18}]^{3-}$. The W L_{III} edge EXAFS spectrum and the Fourier transform for $[ClTiW_5O_{18}]^{3-}$ in acetonitrile are presented in figure 3.20.

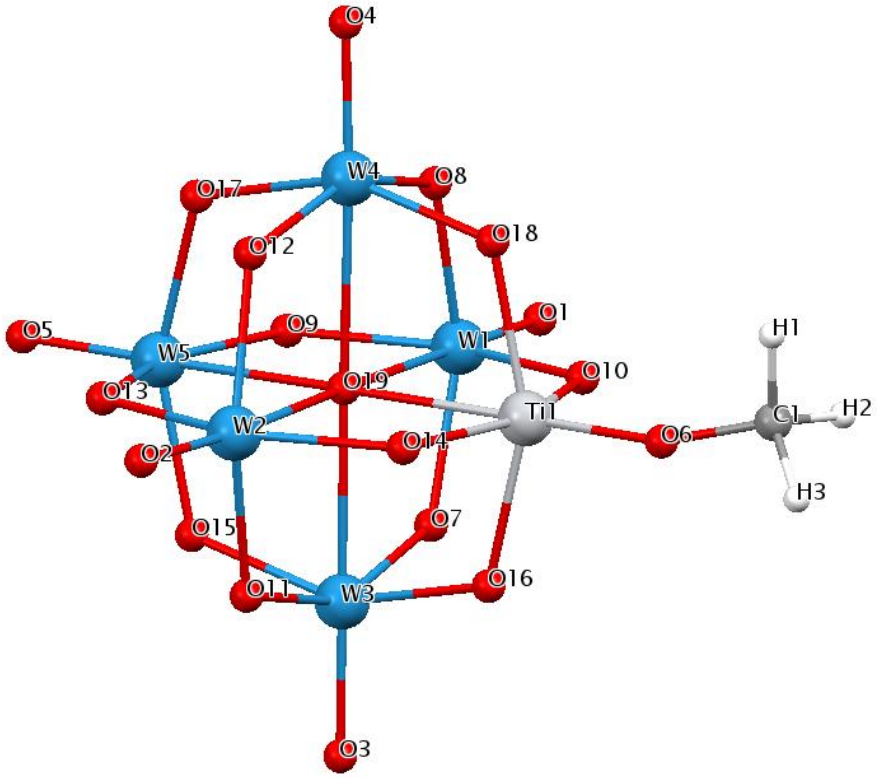

Figure 3.18: Structure of $[(CH_3O)TiW_5O_{18}]^{3-}$.

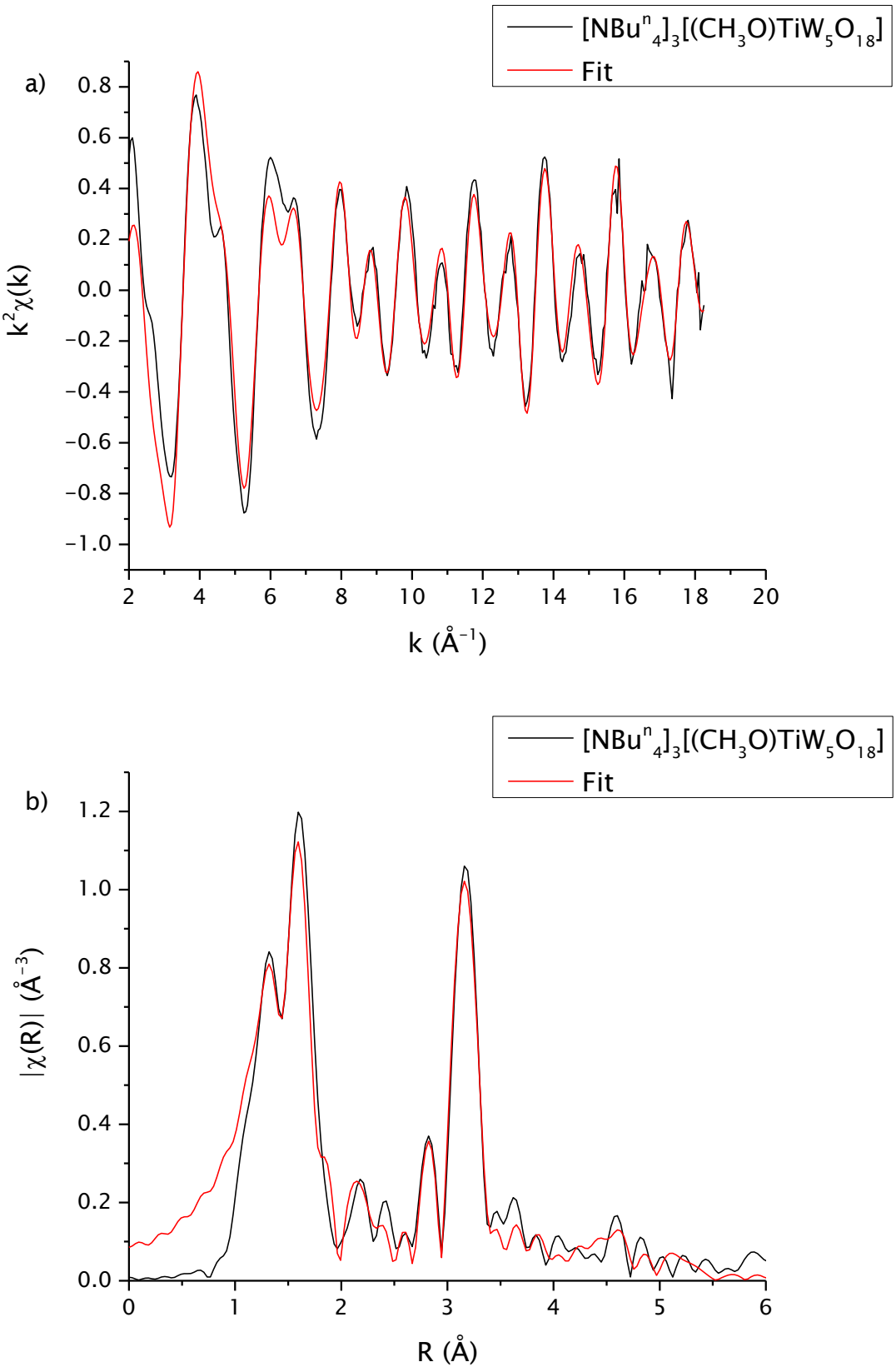

Figure 3.19: W L_{III} edge k^2-weighted a) EXAFS spectrum and b) Fourier transform of [NBu$^n_4$]$_3$[(CH$_3$O)TiW$_5$O$_{18}$] in the solid state.

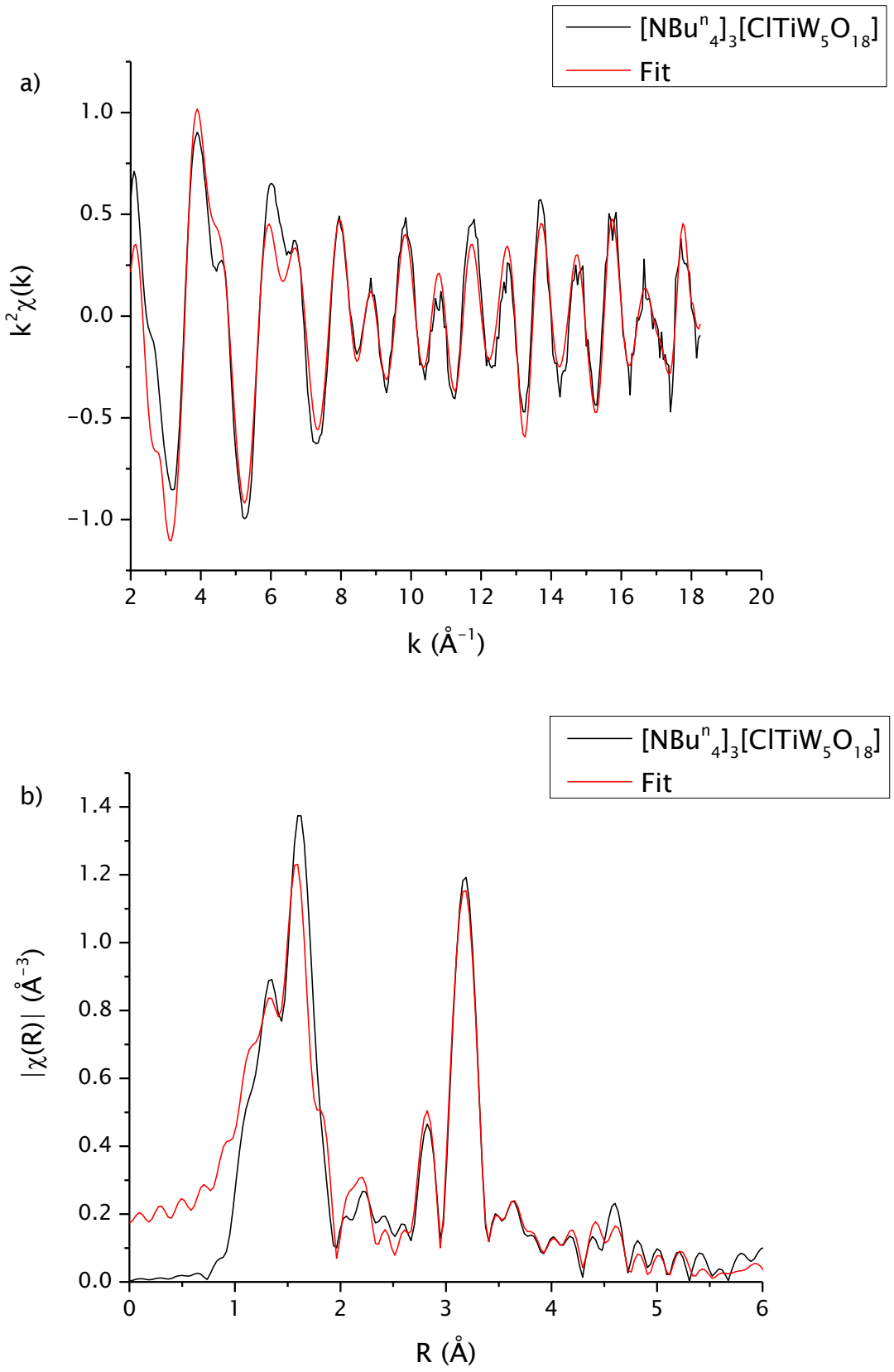

Figure 3.20: W L_{III} edge k^2-weighted a) EXAFS spectrum and b) Fourier transform of [NBu$^n_4$]$_3$[ClTiW$_5$O$_{18}$] in acetonitrile.

W site	Path	Degeneracy	σ^2 / Å^2	r / Å	r / Å (XRD)
W1	W↔O_t	1	0.00034 ± 0.00160	1.713 ± 0.019	1.721
	W↔O_bTi	1	0.00340 ± 0.00193	1.840 ± 0.014	1.874
	W↔O_bW	2	0.00340 ± 0.00193	1.906 ± 0.014	1.939
	W↔O_bW	1	0.00340 ± 0.00193	1.931 ± 0.014	1.964
	W↔O_i	1	0.00086 ± 0.00400	2.320 ± 0.042	2.323
	W↔W	1	0.00194 ± 0.00341	3.296 ± 0.095	3.288
	W↔W	1	0.00194 ± 0.00341	3.306 ± 0.095	3.297
	W↔W	1	0.00194 ± 0.00341	3.330 ± 0.095	3.321
	W↔Ti	1	0.00210 ± 0.02260	3.030 ± 0.118	3.233
W2	W↔O_t	1	0.00034 ± 0.00160	1.713 ± 0.019	1.722
	W↔O_bTi	1	0.00340 ± 0.00193	1.863 ± 0.014	1.897
	W↔O_bW	1	0.00340 ± 0.00193	1.900 ± 0.014	1.933
	W↔O_bW	1	0.00340 ± 0.00193	1.915 ± 0.014	1.949
	W↔O_bW	1	0.00340 ± 0.00193	1.961 ± 0.014	1.994
	W↔O_i	1	0.00086 ± 0.00400	2.300 ± 0.042	2.302
	W↔W	1	0.00194 ± 0.00341	3.296 ± 0.095	3.288
	W↔W	1	0.00194 ± 0.00341	3.301 ± 0.095	3.293
	W↔W	1	0.00194 ± 0.00341	3.314 ± 0.095	3.306
	W↔Ti	1	0.00210 ± 0.02260	3.048 ± 0.118	3.252
W3	W↔O_t	1	0.00034 ± 0.00160	1.708 ± 0.019	1.716
	W↔O_bTi	1	0.00340 ± 0.00193	1.848 ± 0.014	1.881
	W↔O_bW	1	0.00340 ± 0.00193	1.896 ± 0.014	1.930
	W↔O_bW	1	0.00340 ± 0.00193	1.900 ± 0.014	1.934
	W↔O_bW	1	0.00340 ± 0.00193	1.928 ± 0.014	1.961
	W↔O_i	1	0.00086 ± 0.00400	2.354 ± 0.042	2.356
	W↔W	2	0.00194 ± 0.00341	3.301 ± 0.095	3.293
	W↔W	1	0.00194 ± 0.00341	3.320 ± 0.095	3.311
	W↔Ti	1	0.00210 ± 0.02260	3.018 ± 0.118	3.221
W4	W↔O_t	1	0.00034 ± 0.00160	1.701 ± 0.019	1.710
	W↔O_bTi	1	0.00340 ± 0.00193	1.860 ± 0.014	1.893
	W↔O_bW	1	0.00340 ± 0.00193	1.906 ± 0.014	1.939
	W↔O_bW	1	0.00340 ± 0.00193	1.907 ± 0.014	1.940
	W↔O_bW	1	0.00340 ± 0.00193	1.909 ± 0.014	1.942
	W↔O_i	1	0.00086 ± 0.00400	2.329 ± 0.042	2.331
	W↔W	1	0.00194 ± 0.00341	3.300 ± 0.095	3.292
	W↔W	1	0.00194 ± 0.00341	3.306 ± 0.095	3.297
	W↔W	1	0.00194 ± 0.00341	3.318 ± 0.095	3.310
	W↔Ti	1	0.00210 ± 0.02260	2.951 ± 0.118	3.154
W5	W↔O_t	1	0.00034 ± 0.00160	1.693 ± 0.019	1.702
	W↔O_bW	1	0.00340 ± 0.00193	1.860 ± 0.014	1.893
	W↔O_bW	1	0.00340 ± 0.00193	1.890 ± 0.014	1.924
	W↔O_bW	1	0.00340 ± 0.00193	1.895 ± 0.014	1.928
	W↔O_bW	1	0.00340 ± 0.00193	1.902 ± 0.014	1.935
	W↔O_i	1	0.00086 ± 0.00400	2.332 ± 0.042	2.335
	W↔W	1	0.00194 ± 0.00341	3.314 ± 0.095	3.306
	W↔W	1	0.00194 ± 0.00341	3.318 ± 0.095	3.310
	W↔W	1	0.00194 ± 0.00341	3.320 ± 0.095	3.311
	W↔W	1	0.00194 ± 0.00341	3.330 ± 0.118	3.321

Table 3.5: The EXAFS-derived structural parameters for $[NBu^n_4]_3[(CH_3O)TiW_5O_{18}]$ in the solid state.

W site	Path	Degeneracy	σ^2 / Å^2	r / Å	r / Å (XRD)
Trans to Ti	W↔O_t	1	0.00194 ± 0.00234	1.685 ± 0.020	1.683
	W↔O_bW	4	0.00571 ± 0.00201	1.885 ± 0.012	1.941
	W↔O_i	1	0.00109 ± 0.00367	2.328 ± 0.036	2.325
	W↔W	4	-0.00032 ± 0.00472	3.354 ± 0.035	3.288
Cis to Ti	W↔O_t	1	0.00194 ± 0.00234	1.685 ± 0.020	1.683
	W↔O_bW	3	0.00571 ± 0.00201	1.885 ± 0.012	1.941
	W↔O_bTi	1	0.00571 ± 0.00201	1.901 ± 0.012	1.956
	W↔O_i	1	0.00109 ± 0.00367	2.328 ± 0.036	2.325
	W↔Ti	1	-0.00399 ± 0.00467	3.415 ± 0.068	3.286
	W↔W	3	-0.00032 ± 0.00472	3.354 ± 0.035	3.288

Table 3.6: The EXAFS-derived structural parameters for $[NBu^n_4]_3[ClTiW_5O_{18}]$ in acetonitrile.

Anion	Edge	Parameter	Value
$[(CH_3O)TiW_5O_{18}]^{3-}$ Solid	W L_{III}	R (%)	5.40
		R, k = 1 (%)	8.10
		R, k = 2 (%)	4.30
		R, k = 3 (%)	3.90
		Chi-square	14830
		Reduced chi-square	1093
		Amplitude reduction factor	0.67 ± 0.13
		k range (Å^{-1})	2.0 - 18.27
		R range (Å)	1.0 - 6.0
		No. of independent parameters	51
		No. of variables	38
$[ClTiW_5O_{18}]^{3-}$ Solution	W L_{III}	R (%)	5.20
		R, k = 1 (%)	5.00
		R, k = 2 (%)	4.80
		R, k = 3 (%)	5.90
		Chi-square	5491
		Reduced chi-square	474
		Amplitude reduction factor	0.81 ± 0.13
		k range (Å^{-1})	2.0 - 18.25
		R range (Å)	1.0 - 6.0
		No. of independent parameters	52
		No. of variables	42

Table 3.7: Refined parameters for fits to $[NBu^n_4]_3[(OCH_3)TiW_5O_{18}]$ in the solid state and $[NBu^n_4]_3[ClTiW_5O_{18}]$ in acetonitrile.

3.2.3 QEXAFS Study of $[NBu_4]_3[pyCoW_5O_{18}]$

Fitting the W L_{III} edge EXAFS of $[NBu^n_4]_3[pyCoW_5O_{18}]$ (figure 3.21), where py is a pyridyl group, in the solid state highlights the importance of including the multiple scattering paths in the fit. During the process of adding paths to the fits, the amplitude reduction factor often refined to a value greater than 1.00. When only the single scattering paths were included in the fit the amplitude reduction factor was refined to 0.54 which is too low. The amplitude reduction factor was therefore set to 0.68, as the curve fitting analysis of $[NBu^n_4]_2[W_6O_{19}]$ in the solid state refined the amplitude reduction factor to this value. The EXAFS spectrum and Fourier transform are presented in figure 3.22. In the EXAFS spectrum there are peaks at 4.5 $Å^{-1}$ and at 4 $Å^{-1}$. When only the single-scattering paths are included in the fit there is poor splitting between these peaks and there is also no splitting between the terminal and bridging oxygen atoms in the Fourier transform. Including multiple scattering paths in the fit resulted in better peak splitting for these peaks. Multiple scattering paths were therefore required to achieve a good fit for this data.

The EXAFS-derived structural parameters for $[NBu^n_4]_3[(py)CoW_5O_{18}]$ in the solid state and in acetonitrile are presented in table 3.8 and 3.9 respectively and the data regarding the quality of both of these fits are presented in table 3.10. Each tungsten site was included separately in the fit using the same methodology as was employed for $[NBu^n_4][(CH_3O)TiW_5O_{18}]$ in the solid state. The average W-O_t, W-O_bW, W-O_bCo and W-O_i bond lengths are 1.971 Å, 1.816 Å, 1.801Å and 2.302 Å respectively. The W-O_t distance in the crystallographic data is 1.709 Å. In the solid state, W-O bonds are shorter in W-O-Co than in W-O-W by 0.015 Å. In $[NBu^n_4]_3[pyCoW_5O_{18}]$, the W-$O_b$W andW-$O_i$ bonds are shorter than in $[NBu^n_4]_2[W_6O_{19}]$ by 0.019 Å and 0.097 Å respectively and the W-O_t bonds are 0.269 Å longer. The Co···W5 distance is 4.120 Å, 0.465 Å shorter than is previously reported in crystallographic data.[11]

In acetonitrile, the cobalt K edge EXAFS of $[NBu^n_4]_3[pyCoW_5O_{18}]$ was recorded. The cobalt K edge EXAFS and the Fourier transform are presented in figure 3.23.The data has a low amplitude, making it difficult to fit paths that are longer than 3.6 Å without the amplitude of the paths being magnified by forward scattering. Including multiple scattering paths in the fit helped to

refine the single scattering path distances and they fit the peaks at higher distance in the Fourier transform. In the Co K edge EXAFS-derived structural parameters, the Co-N bond is 0.037 Å shorter and the average Co-O bond distance is 0.030 Å longer than in the previously reported crystal structure for $[NBu^n_4]_3[pyCoW_5O_{18}]$. In the solid state the average Co···W distance is 0.211 Å longer in the crystallographic data than the distance reported in the EXAFS-derived structural parameters for the W L_{III} edge of $[NBu^n_4]_3[pyCoW_5O_{18}]$. The average Co···W distance reported in the EXAFS-derived structural parameters at the Co K edge is 0.070 Å shorter than in the crystallographic data.

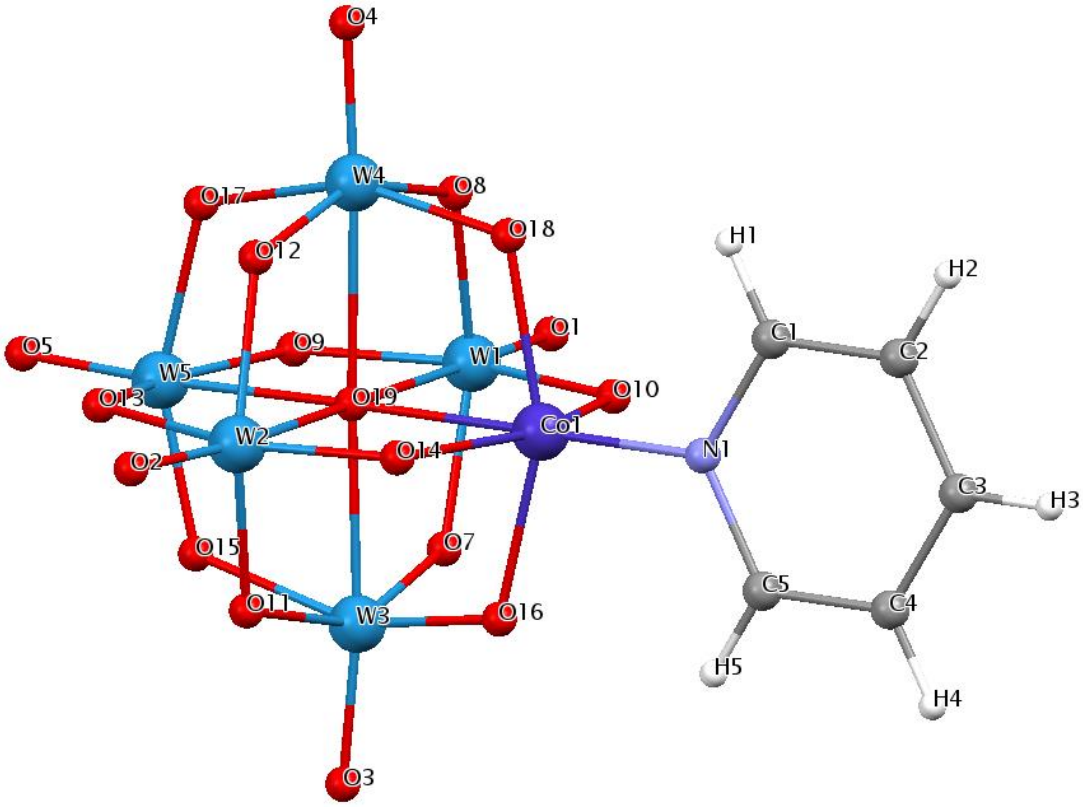

Figure 3.21: Structure of $[(py)CoW_5O_{18}]^{3-}$.

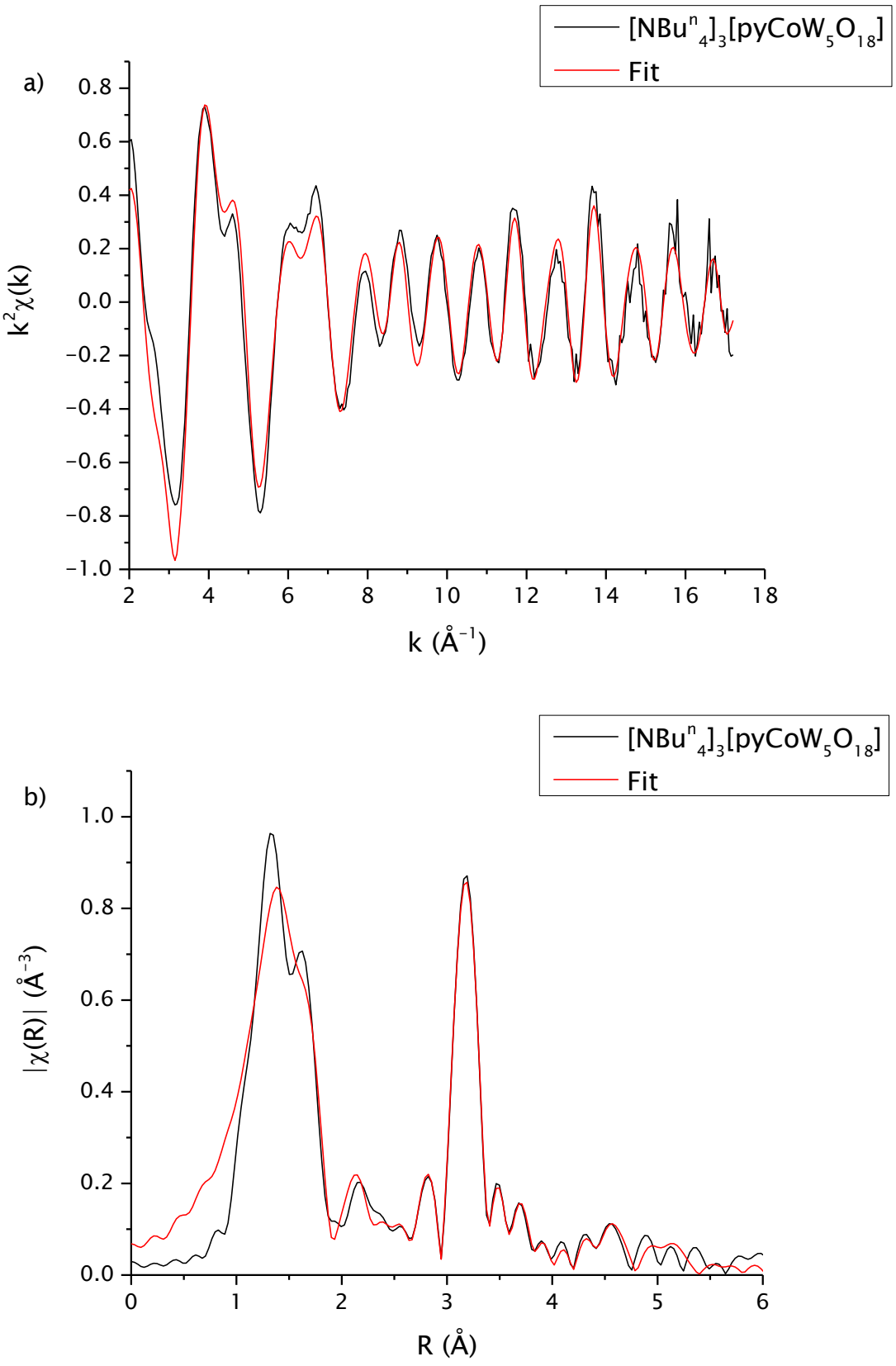

Figure 3.22: W L_{III} edge k^2-weighted a) EXAFS spectrum and b) Fourier transform of [NBu$^n_4$]$_3$[(py)CoW$_5$O$_{18}$] in the solid state.

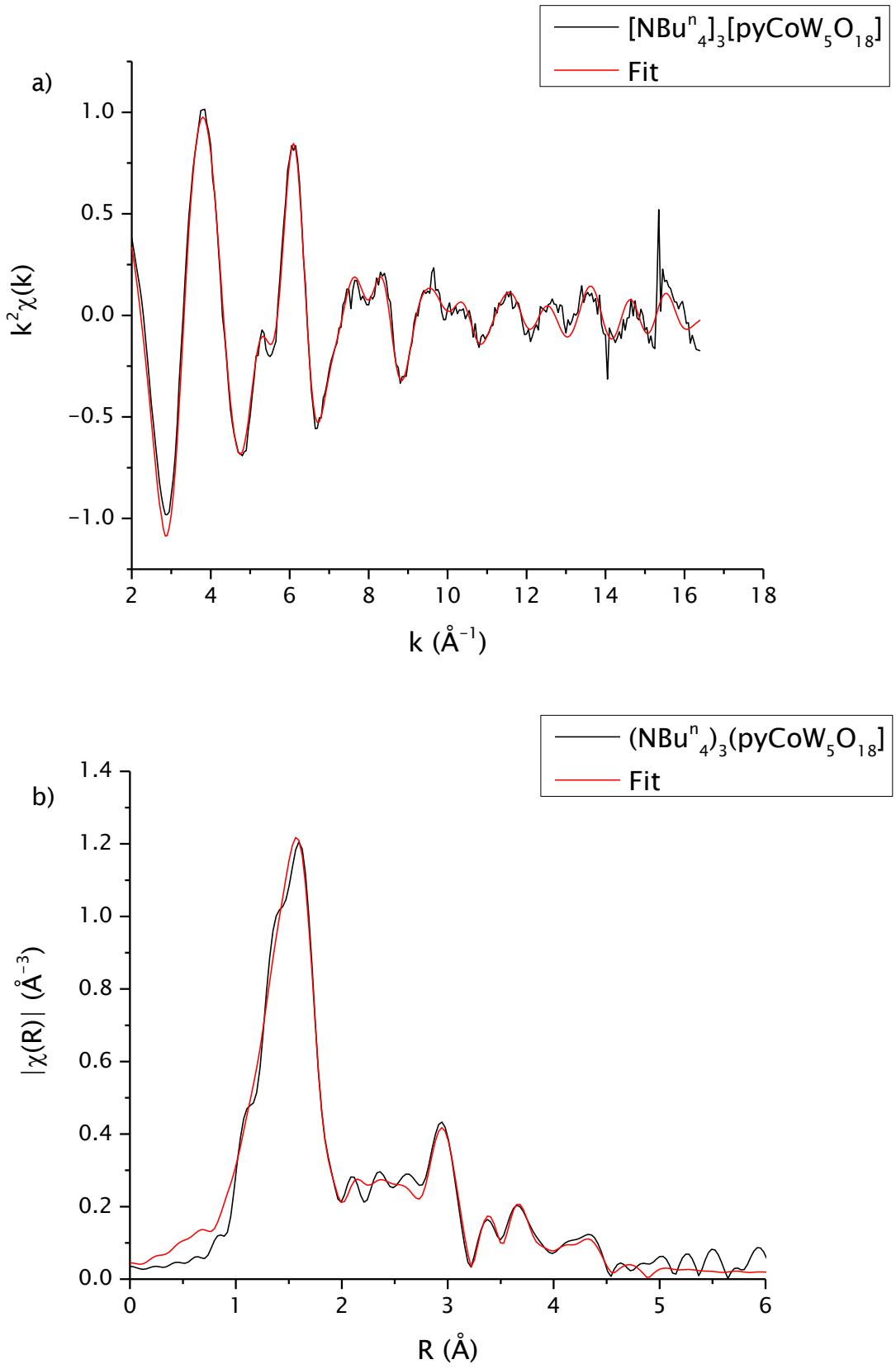

Figure 3.23: Co K edge k²-weighted a) EXAFS spectrum and b) Fourier transform of [NBu$^n_4$]$_3$[(py)CoW$_5$O$_{18}$] in acetonitrile.

W site	Path	Degeneracy	σ^2 / Å^2	r / Å	r / Å (XRD)
W1	W↔O_t	1	0.00112 ± 0.00464	1.973 ± 0.042	1.711
	W↔O_bCo	1	0.00585 ± 0.00297	1.809 ± 0.023	1.920
	W↔O_bW	1	0.00585 ± 0.00297	1.822 ± 0.023	1.934
	W↔O_bW	2	0.00585 ± 0.00297	1.830 ± 0.023	1.941
	W↔O_i	1	0.00324 ± 0.00799	2.323 ± 0.055	2.352
	W↔W	1	0.00153 ± 0.02325	3.145 ± 0.241	3.298
	W↔W	1	0.00153 ± 0.02325	3.152 ± 0.241	3.305
	W↔W	1	0.00153 ± 0.02325	3.164 ± 0.241	3.317
	W↔Co	1	-0.00144 ± 0.01645	2.967 ± 0.228	3.228
W2	W↔O_t	1	0.00112 ± 0.00464	1.983 ± 0.042	1.721
	W↔O_bCo	1	0.00593 ± 0.00297	1.652 ± 0.023	1.763
	W↔O_bW	1	0.00593 ± 0.00297	1.827 ± 0.023	1.938
	W↔O_bW	1	0.00593 ± 0.00297	1.828 ± 0.023	1.940
	W↔O_bW	1	0.00593 ± 0.00297	1.942 ± 0.023	2.053
	W↔O_i	1	0.00324 ± 0.00799	2.287 ± 0.055	2.317
	W↔W	1	0.00153 ± 0.02325	3.134 ± 0.241	3.287
	W↔W	1	0.00153 ± 0.02325	3.145 ± 0.241	3.298
	W↔W	1	0.00153 ± 0.02325	3.164 ± 0.241	3.317
	W↔Co	1	-0.00144 ± 0.01645	2.899 ± 0.228	3.159
W3	W↔O_t	1	0.00112 ± 0.00464	1.980 ± 0.042	1.718
	W↔O_bCo	1	0.00585 ± 0.00297	1.708 ± 0.023	1.820
	W↔O_bW	1	0.00585 ± 0.00297	1.811 ± 0.023	1.922
	W↔O_bW	1	0.00585 ± 0.00297	1.825 ± 0.023	1.937
	W↔O_bW	1	0.00585 ± 0.00297	1.919 ± 0.023	2.030
	W↔O_i	1	0.00324 ± 0.00799	2.293 ± 0.055	2.322
	W↔W	1	0.00153 ± 0.02325	3.134 ± 0.241	3.287
	W↔W	1	0.00153 ± 0.02325	3.138 ± 0.241	3.291
	W↔W	1	0.00153 ± 0.02325	3.163 ± 0.241	3.316
	W↔Co	1	-0.00144 ± 0.01645	2.988 ± 0.228	3.249
W4	W↔O_t	1	0.00112 ± 0.00464	1.945 ± 0.042	1.682
	W↔O_bCo	1	0.00585 ± 0.00297	1.802 ± 0.023	1.914
	W↔O_bW	1	0.00585 ± 0.00297	1.796 ± 0.023	1.908
	W↔O_bW	1	0.00585 ± 0.00297	1.823 ± 0.023	1.935
	W↔O_bW	1	0.00585 ± 0.00297	1.838 ± 0.023	1.949
	W↔O_i	1	0.00324 ± 0.00799	2.309 ± 0.055	2.339
	W↔W	1	0.00153 ± 0.02325	3.138 ± 0.241	3.291
	W↔W	1	0.00153 ± 0.02325	3.164 ± 0.241	3.317
	W↔W	1	0.00153 ± 0.02325	3.171 ± 0.241	3.324
	W↔Co	1	-0.00144 ± 0.01645	3.009 ± 0.228	3.270
W5	W↔O_t	1	0.00112 ± 0.00464	1.976 ± 0.042	1.714
	W↔O_bW	1	0.00593 ± 0.00297	1.732 ± 0.023	1.844
	W↔O_bW	1	0.00593 ± 0.00297	1.771 ± 0.023	1.882
	W↔O_bW	1	0.00593 ± 0.00297	1.842 ± 0.023	1.954
	W↔O_bW	1	0.00593 ± 0.00297	1.857 ± 0.023	1.969
	W↔O_i	1	0.00324 ± 0.00799	2.296 ± 0.055	2.325
	W↔W	1	0.00153 ± 0.02325	3.152 ± 0.241	3.305
	W↔W	1	0.00153 ± 0.02325	3.163 ± 0.241	3.316
	W↔W	1	0.00153 ± 0.02325	3.164 ± 0.241	3.317
	W↔W	1	0.00153 ± 0.02325	3.171 ± 0.241	3.324

Table 3.8: The EXAFS-derived structural parameters for the W L_{III} edge of $[NBu^n_4]_3[(py)CoW_5O_{18}]$ in the solid state.

Path	Degeneracy	σ^2 / Å^2	r / Å	r / Å (XRD)
Co↔N	1	0.00148 ± 0.00113	2.015 ± 0.018	2.052
Co↔O_b	4	0.00825 ± 0.00232	2.099 ± 0.017	2.069
Co↔O_i	1	0.02091 ± 0.01768	2.370 ± 0.124	2.261
Co↔W	4	0.00857 ± 0.00087	3.177 ± 0.012	3.247

Table 3.9: The EXAFS-derived structural parameters for $[NBu^n_4]_3[(py)CoW_5O_{18}]$ in acetonitrile.

Anion	Edge	Parameter	Value
$[pyCoW_5O_{18}]^{3-}$ Solid	W L_{III}	R (%)	3.50
		R, k = 1 (%)	1.70
		R, k = 2 (%)	3.10
		R, k = 3 (%)	5.70
		Chi-square	4737
		Reduced chi-square	930
		Amplitude reduction factor	0.68
		k range (Å^{-1})	2.0 - 17.21
		R range (Å)	1.0 - 6.0
		No. of independent parameters	48
		No. of variables	43
Solution	Co K	R (%)	2.50
		R, k = 1 (%)	2.60
		R, k = 2 (%)	1.00
		R, k = 3 (%)	6.20
		Chi-square	400
		Reduced chi-square	23
		Amplitude reduction factor	0.96 ± 0.14
		k range (Å^{-1})	2.0 - 16.4
		R range (Å)	1.0 - 6.0
		No. of independent parameters	45
		No. of variables	28

Table 3.10: Refined parameters for fits to $[NBu^n_4]_3[(py)CoW_5O_{18}]$ in the solid state and in acetonitrile.

3.2.4 QEXAFS Study of $[NBu_4]_3[ClSnW_5O_{18}]$

It is possible to look at the EXAFS of $[NBu^n_4]_3[ClSnW_5O_{18}]$ from 2 hard edges – the W L_{III} edge and the Sn K edge. The model for the curve fitting analysis of $[NBu^n_4]_3[ClSnW_5O_{18}]$ (figure 3.24) in the solid state was constructed by writing a FEFF template using the crystallographic data for $[NBu^n_4]_3[Bu^tOSnW_5O_{18}]$ and replacing the Bu^tO group with a chlorine atom. Curve fitting analyses were carried out using IFEFFIT Demeter version 0.9.18.2. Average distances for shells were used for each atom in the shell. The EXAFS-derived structural parameters for the W L_{III} and Sn K edges of $[NBu^n_4]_3[ClSnW_5O_{18}]$ in the solid state and in acetonitrile are presented in table 3.11 and the data regarding the quality of these fits are presented in table 3.12. The EXAFS spectra and Fourier transforms of the Sn K and W L_{III} edges of $[NBu^n_4]_3[ClSnW_5O_{18}]$ in the solid state and in acetonitrile are presented in figures 3.25 – 3.28.

The fit with no restrained or set parameters for the Sn K edge refined the Sn-O_i bond to 2.667 Å. This is 0.369 Å longer than the 2.271 Å given in the crystallographic data. The length of this bond may indicate that there is only a partial interaction between the tin and interstitial oxygen or possibly no interaction at all. A W5···Sn distance of 4.520 Å was refined in the curve fitting analysis; 0.112 Å shorter than the distance of 4.632 Å given in the crystallographic data. The refinement of the W L_{III} edge EXAFS gave a W-O_i bond of 2.326 Å and a W5···Sn distance of 4.904 Å. This refinement gives a Sn-O_i bond of ~ 2.6 Å. Within the error of the XAFS experiment, the interatomic distances reported in table 3.11 agree with the crystallographic data. In acetonitrile, the curve fitting analysis gave similar bond lengths to the refinement in the solid state supporting the EXAFS-derived structural parameters reported.

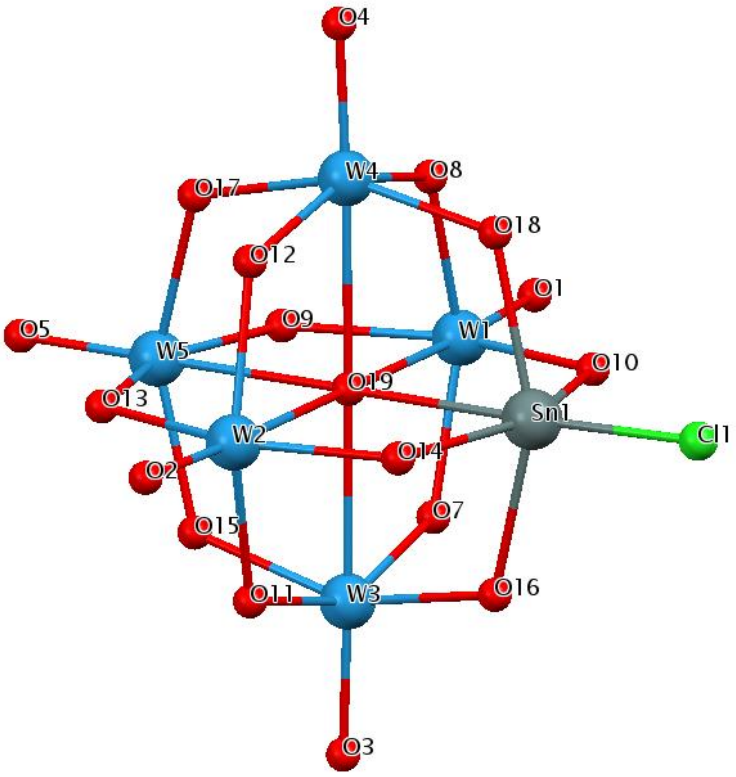

Figure: 3.24: Structure of $[ClSnW_5O_{18}]^{3-}$.

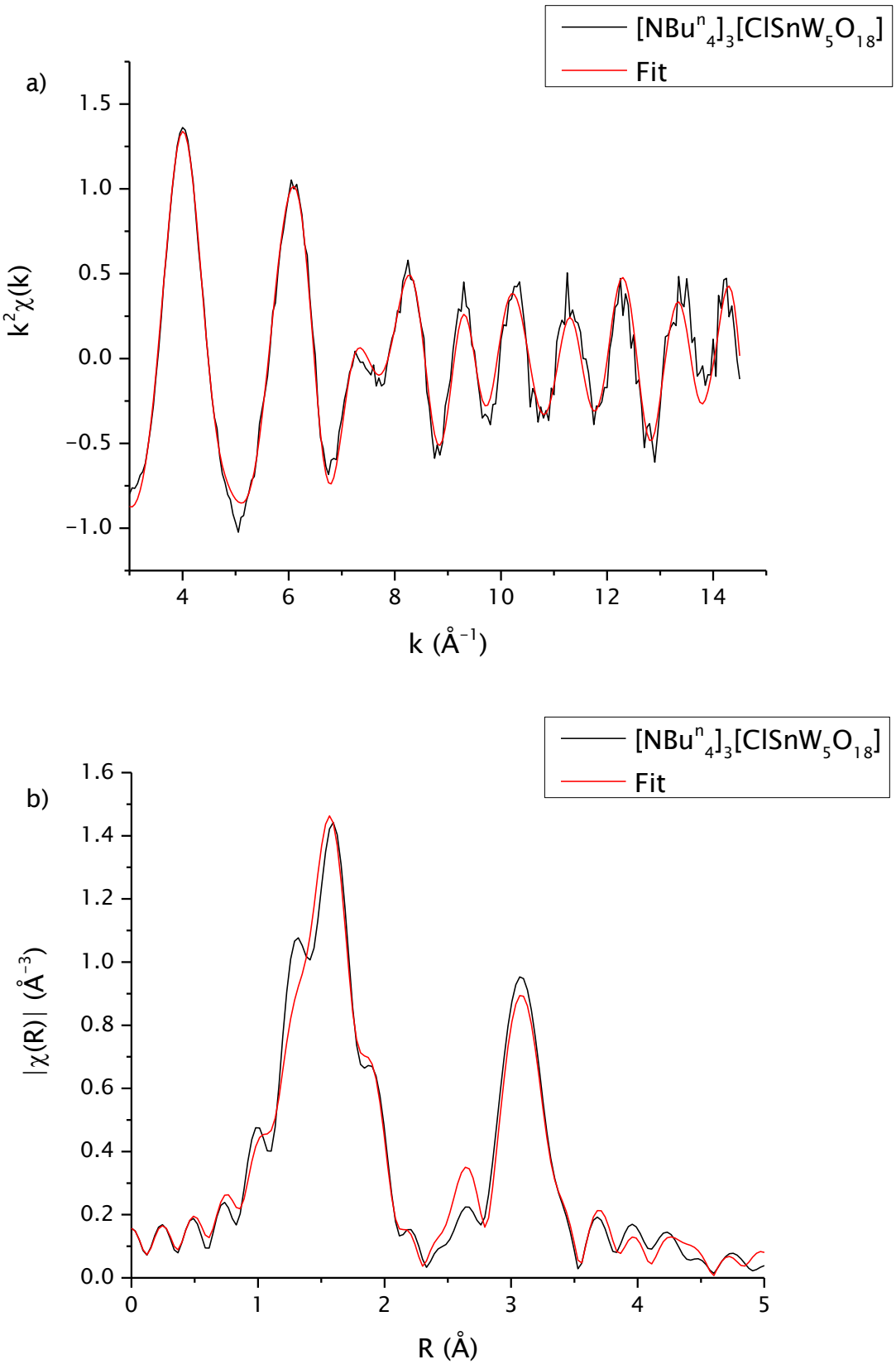

Figure 3.25: Sn K edge k^2-weighted a) EXAFS spectrum and b) Fourier transform of [NBu$^n_4$]$_3$[ClSnW$_5$O$_{18}$] in the solid state.

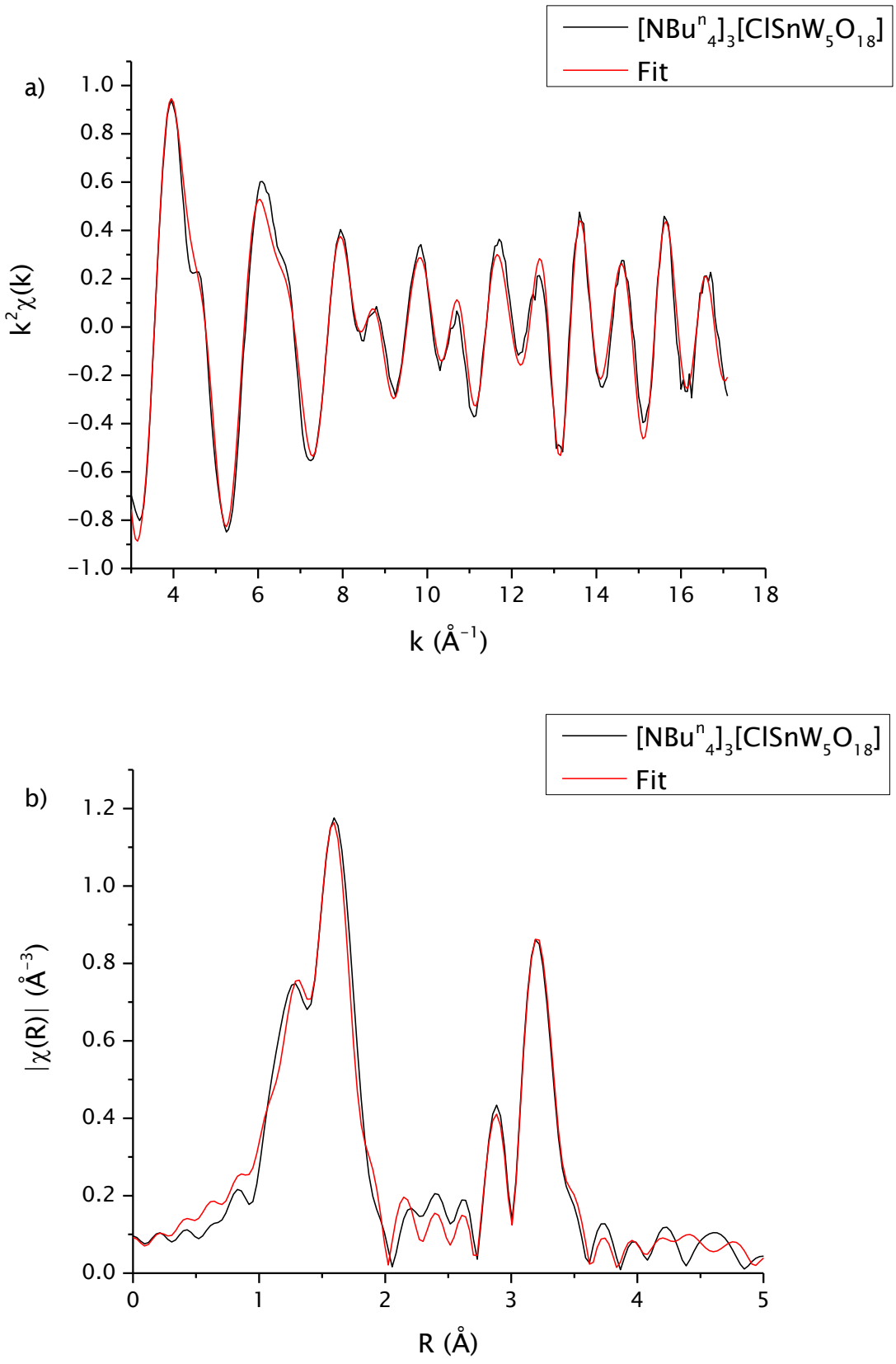

Figure 3.26: W L_{III} edge k^2-weighted a) EXAFS spectrum and b) Fourier transform of [NBu$^n_4$]$_3$[ClSnW$_5$O$_{18}$] in the solid state.

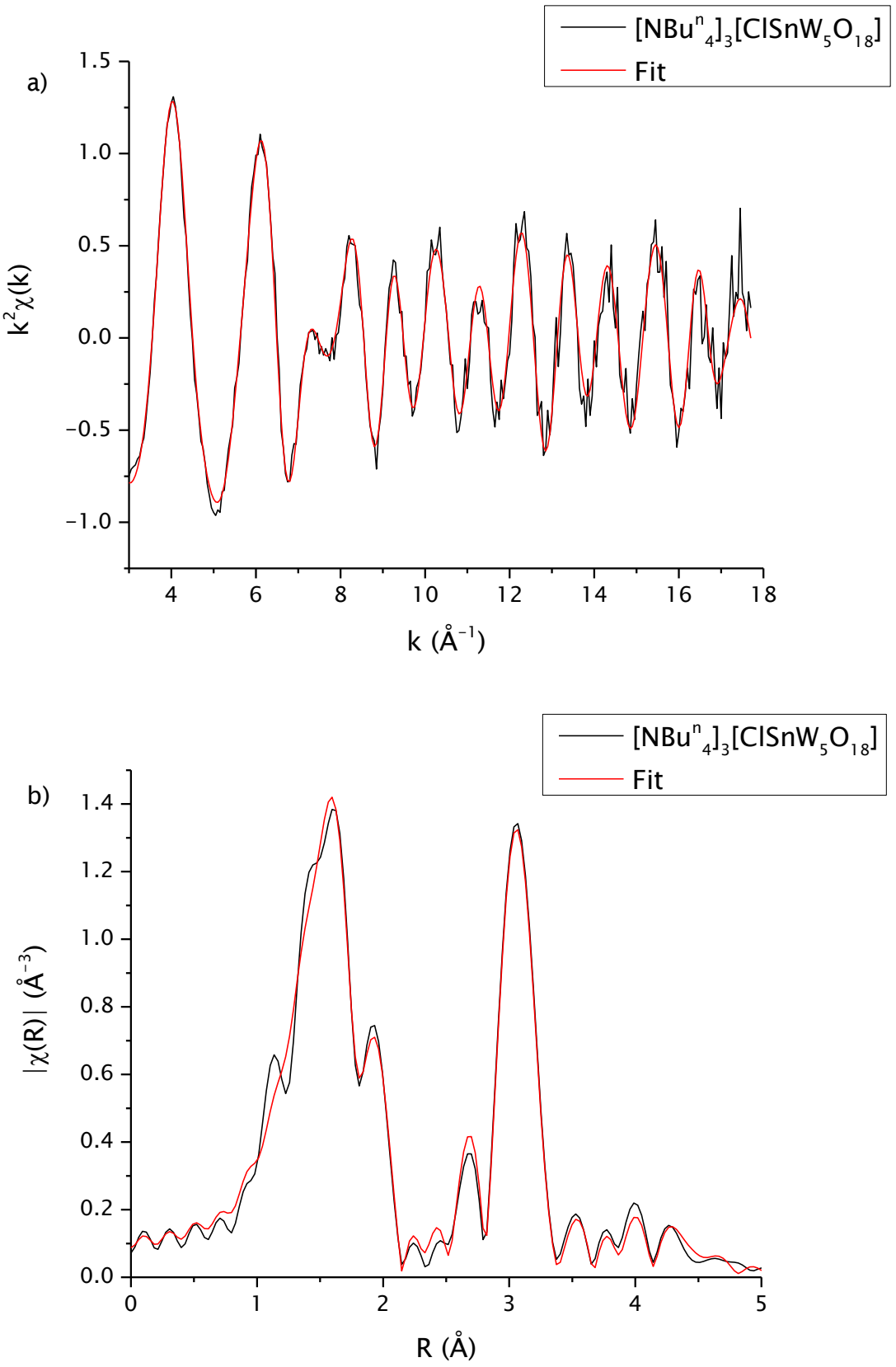

Figure 3.27: Sn K edge k²-weighted a) EXAFS spectrum and b) Fourier transform of [NBu$^n_4$]$_3$[ClSnW$_5$O$_{18}$] in acetonitrile.

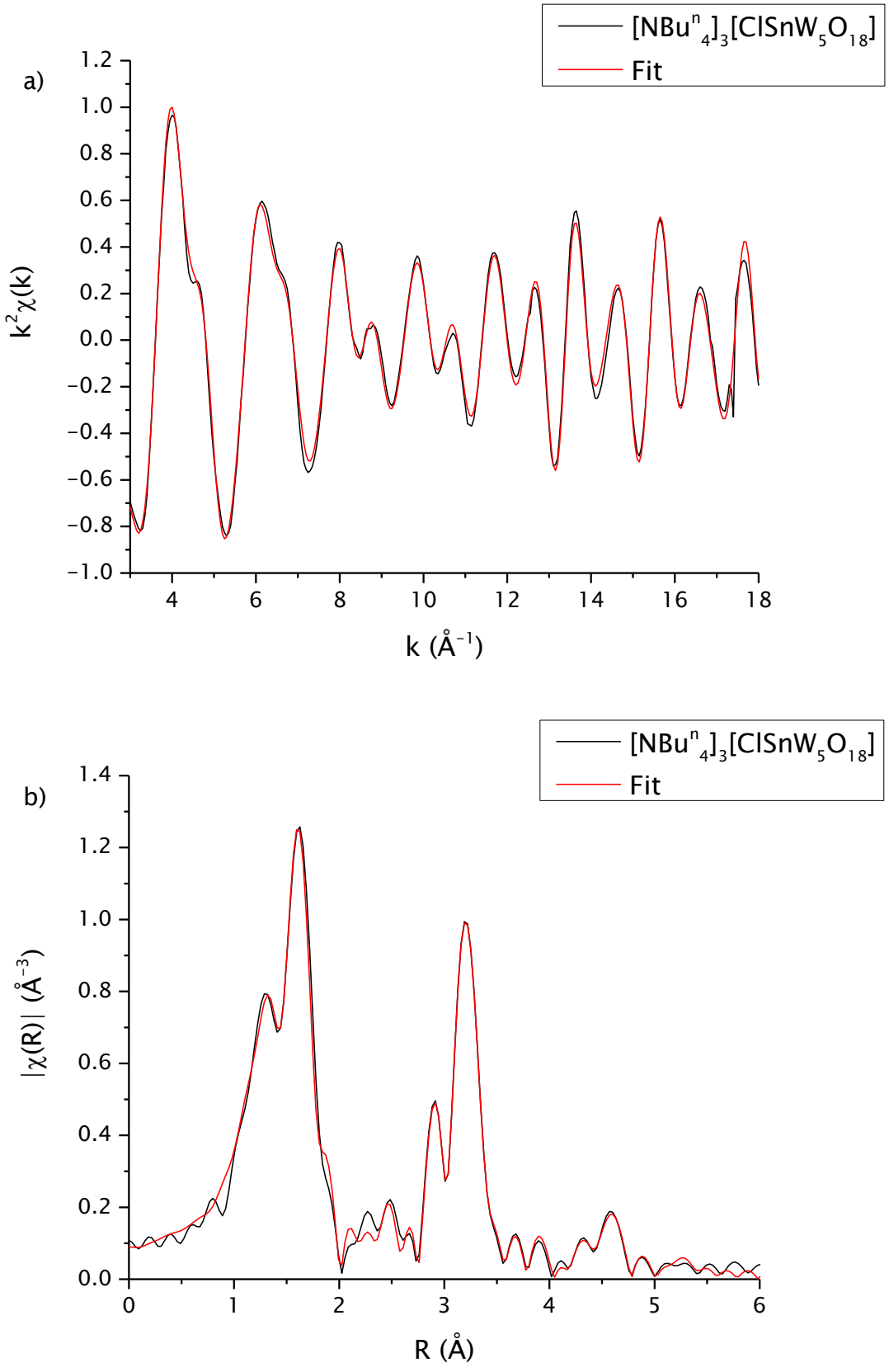

Figure 3.28: W L_{III} edge k^2-weighted a) EXAFS spectrum and b) Fourier transform of [NBu$^n_4$]$_3$[ClSnW$_5$O$_{18}$] in acetonitrile.

Anion	Edge	W site	Path	Degeneracy	σ^2 / Å^2	r / Å	r / Å (XRD)
$[ClSnW_5O_{18}]^{3-}$ Solid	Sn K		Sn↔Cl	1	0.00300 ± 0.00186	2.338 ± 0.017	1.985
			Sn↔O_b	4	0.00413 ± 0.00126	2.041 ± 0.010	2.048
			Sn↔O_i	1	0.00188 ± 0.00443	2.667 ± 0.038	2.271
			Sn↔W	4	0.00382 ± 0.00075	3.271 ± 0.015	3.269
	W L_{III}	Trans to Sn	W↔O_t	1	0.00138 ± 0.00137	1.714 ± 0.017	1.709
			W↔O_bW	4	0.00341 ± 0.00121	1.893 ± 0.011	1.907
			W↔O_i	1	0.00156 ± 0.00244	2.326 ± 0.027	2.361
			W↔W	4	0.00155 ± 0.00102	3.329 ± 0.013	3.312
		Cis to Sn	W↔O_t	1	0.00138 ± 0.00137	1.706 ± 0.017	1.702
			W↔O_bSn	1	0.00341 ± 0.00121	1.855 ± 0.011	1.870
			W↔O_bW	2	0.00341 ± 0.00121	1.906 ± 0.011	1.921
			W↔O_bW	1	0.00341 ± 0.00121	1.934 ± 0.011	1.949
			W↔O_i	1	0.00156 ± 0.00244	2.312 ± 0.027	2.347
			W↔W	3	0.00155 ± 0.00102	3.326 ± 0.013	3.309
			W↔Sn	1	0.00117 ± 0.00301	3.342 ± 0.031	3.271
Solution	Sn K		Sn↔Cl	1	0.00234 ± 0.00091	2.334 ± 0.011	1.985
			Sn↔O_b	4	0.00349 ± 0.00066	2.036 ± 0.006	2.048
			Sn↔O_i	1	0.00564 ± 0.00623	2.626 ± 0.041	2.271
			Sn↔W	4	0.00302 ± 0.00036	3.454 ± 0.006	3.269
	W L_{III}	Trans to Sn	W↔O_t	1	0.00074 ± 0.00057	1.708 ± 0.017	1.708
			W↔O_bW	4	0.00283 ± 0.00057	1.884 ± 0.011	1.902
			W↔O_i	1	0.00176 ± 0.00142	2.287 ± 0.027	2.337
			W↔W	4	0.00205 ± 0.00051	3.307 ± 0.013	3.307
		Cis to Sn	W↔O_t	1	0.00074 ± 0.00057	1.708 ± 0.017	1.708
			W↔O_bSn	1	0.00283 ± 0.00057	1.847 ± 0.011	1.865
			W↔O_bW	3	0.00283 ± 0.00057	1.924 ± 0.011	1.942
			W↔O_i	1	0.00176 ± 0.00142	2.312 ± 0.027	2.361
			W↔W	3	0.00205 ± 0.00051	3.326 ± 0.013	3.322
			W↔Sn	1	0.00200 ± 0.00221	3.288 ± 0.031	3.288

Table 3.11: The EXAFS-derived structural parameters for the Sn K and W L_{III} edges of $[NBu^n_4]_3[ClSnW_5O_{18}]$ in the solid state and in acetonitrile.

Anion	Edge	Parameter	Value
$[ClSnW_5O_{18}]^{3-}$	Sn K	R (%)	2.57
Solid		R, k = 1 (%)	0.64
		R, k = 2 (%)	1.99
		R, k = 3 (%)	5.09
		Chi-square	658
		Reduced chi-square	74
		Amplitude reduction factor	1.03 ± 0.08
		k range ($Å^{-1}$)	3.0 - 14.5
		R range (Å)	1.0 - 5.0
		No. of independent parameters	28
		No. of variables	20
	$W L_{III}$	R (%)	2.08
		R, k = 1 (%)	1.21
		R, k = 2 (%)	1.93
		R, k = 3 (%)	3.18
		Chi-square	5696
		Reduced chi-square	606
		Amplitude reduction factor	0.75 ± 0.10
		k range ($Å^{-1}$)	3.0 - 17.1
		R range (Å)	1.0 - 5.0
		No. of independent parameters	35
		No. of variables	26
Solution	Sn K	R (%)	1.21
		R, k = 1 (%)	0.21
		R, k = 2 (%)	0.88
		R, k = 3 (%)	2.52
		Chi-square	162
		Reduced chi-square	18
		Amplitude reduction factor	0.99 ± 0.05
		k range ($Å^{-1}$)	3.0 - 17.7
		R range (Å)	1.0 - 5.0
		No. of independent parameters	36
		No. of variables	28
	$W L_{III}$	R (%)	0.75
		R, k = 1 (%)	0.38
		R, k = 2 (%)	0.69
		R, k = 3 (%)	1.25
		Chi-square	1677
		Reduced chi-square	148
		Amplitude reduction factor	0.76 ± 0.05
		k range ($Å^{-1}$)	3.0 - 18.0
		R range (Å)	1.0 - 6.0
		No. of independent parameters	47
		No. of variables	36

Table 3.12: Refined parameters for fits to the W L_{III} and Sn K edges of $[NBu^n_4]_3[ClSnW_5O_{18}]$ in the solid state and in acetonitrile.

Another Sn-O_i bond length that commonly occurred in different fits was 2.24 Å. This bond length is in agreement with the crystallographic data so fits were run at the W L_{III} and Sn K edges in acetonitrile and in the solid state in an attempt to refine the structural parameters to agree with the crystallographic data, but with a Sn-O_i bond length of 2.24 Å. EXAFS-derived structural parameters for the W L_{III} and Sn K edges of $[NBu^n_4]_3[ClSnW_5O_{18}]$ in the solid state and in acetonitrile with a Sn-O_i bond length of 2.24 Å are presented in table 3.13 and the data regarding the quality of these fits are presented in table 3.14. Fitting with this bond length caused problems refining either the amplitude reduction factor or the Debye-Waller factor for at least 1 of the single scattering paths for oxygen atoms bonded directly to the absorbing atom. In all the reported fits, the amplitude reduction factor was set to the values given in table 3.13. The EXAFS spectra and Fourier transforms of the Sn K and W L_{III} edges in the solid state and in solution with the Sn-O_i bond set to 2.24 Å are presented in figures 3.29 – 3.32.

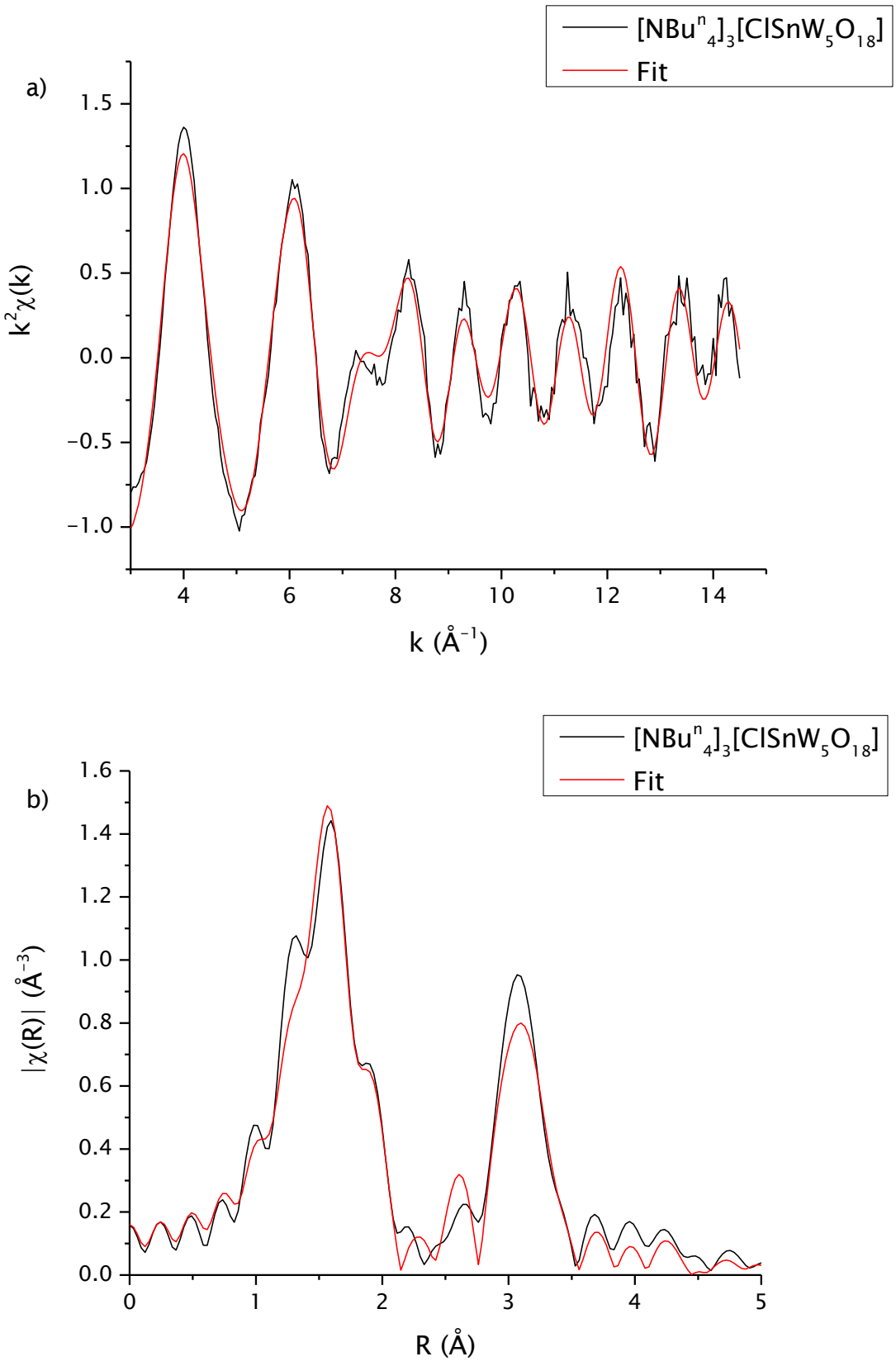

Figure 3.29: Sn K edge k^2-weighted a) EXAFS spectrum and b) Fourier transform of [NBu$^n_4$]$_3$[ClSnW$_5$O$_{18}$] in the solid state with the Sn-O$_i$ distance set to 2.24 Å.

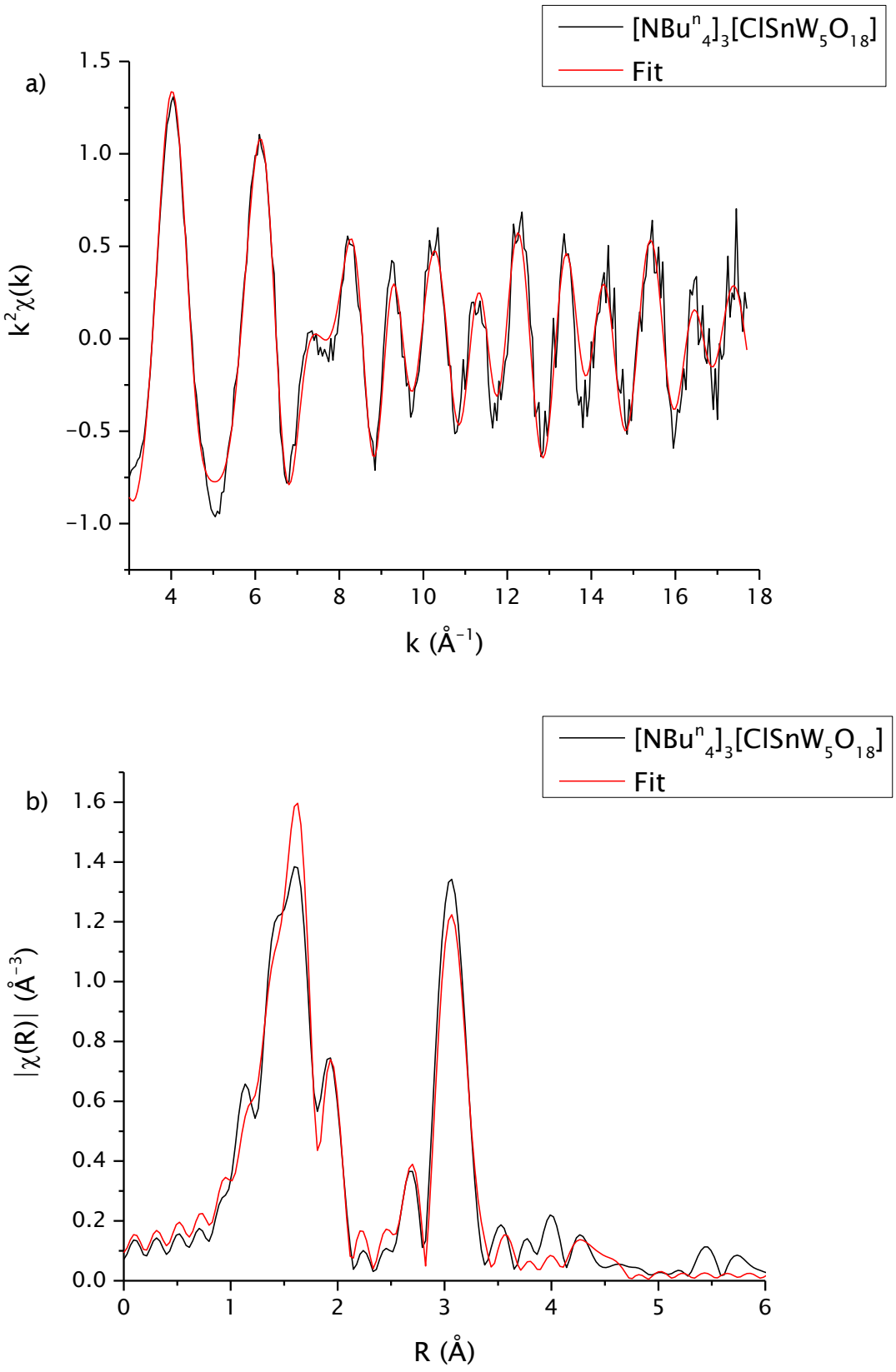

Figure 3.30: Sn K edge k²-weighted a) EXAFS spectrum and b) Fourier transform of [NBu$^n_4$]$_3$[ClSnW$_5$O$_{18}$] in acetonitrilewith the Sn-O$_i$ distance set to 2.24 Å.

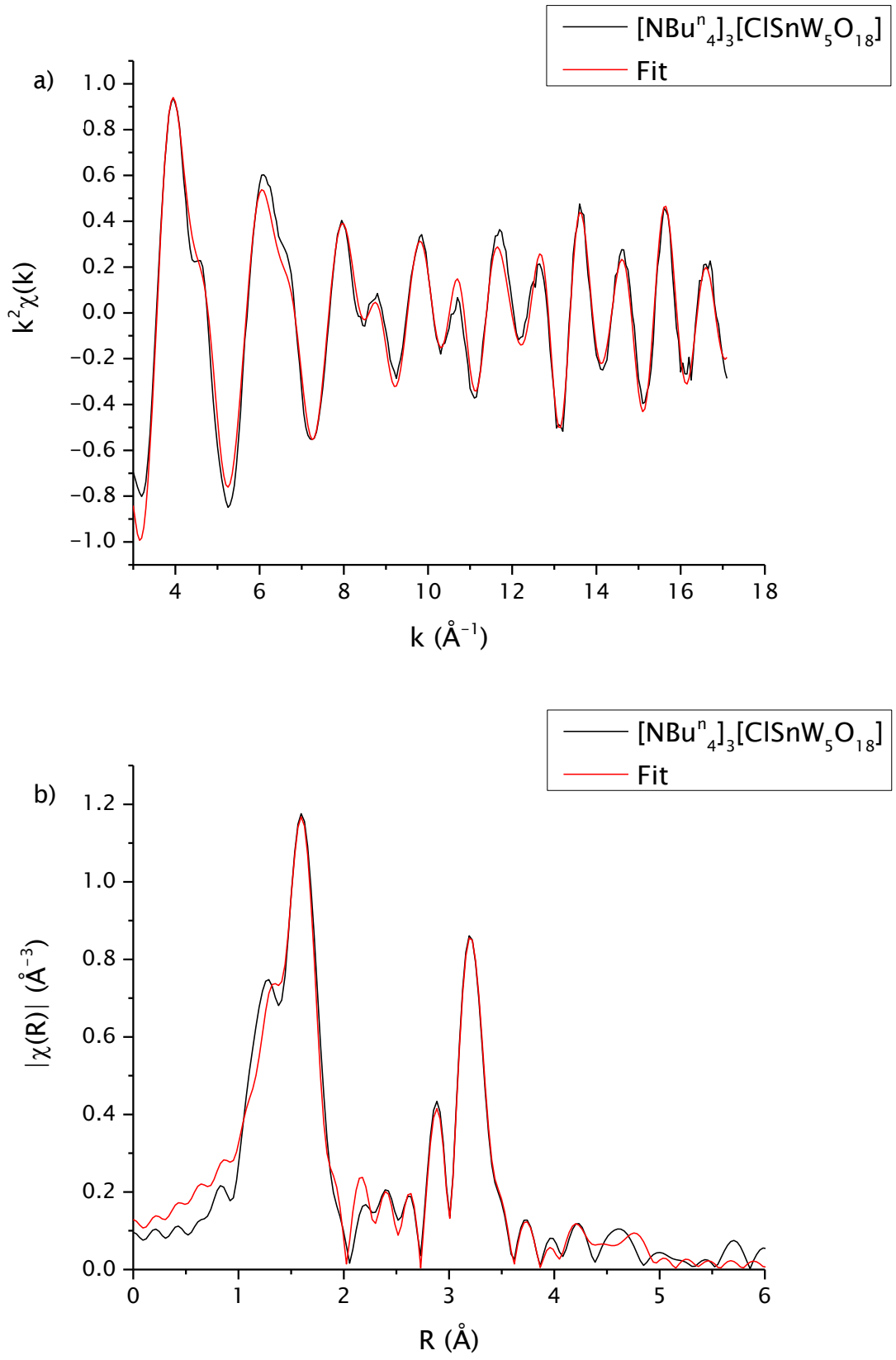

Figure 3.31: W L_{III} edge k^2-weighted a) EXAFS spectrum and b) Fourier transform of [NBu$^n_4$]$_3$[ClSnW$_5$O$_{18}$] in the solid state with the Sn-O_i distance set to 2.24 Å.

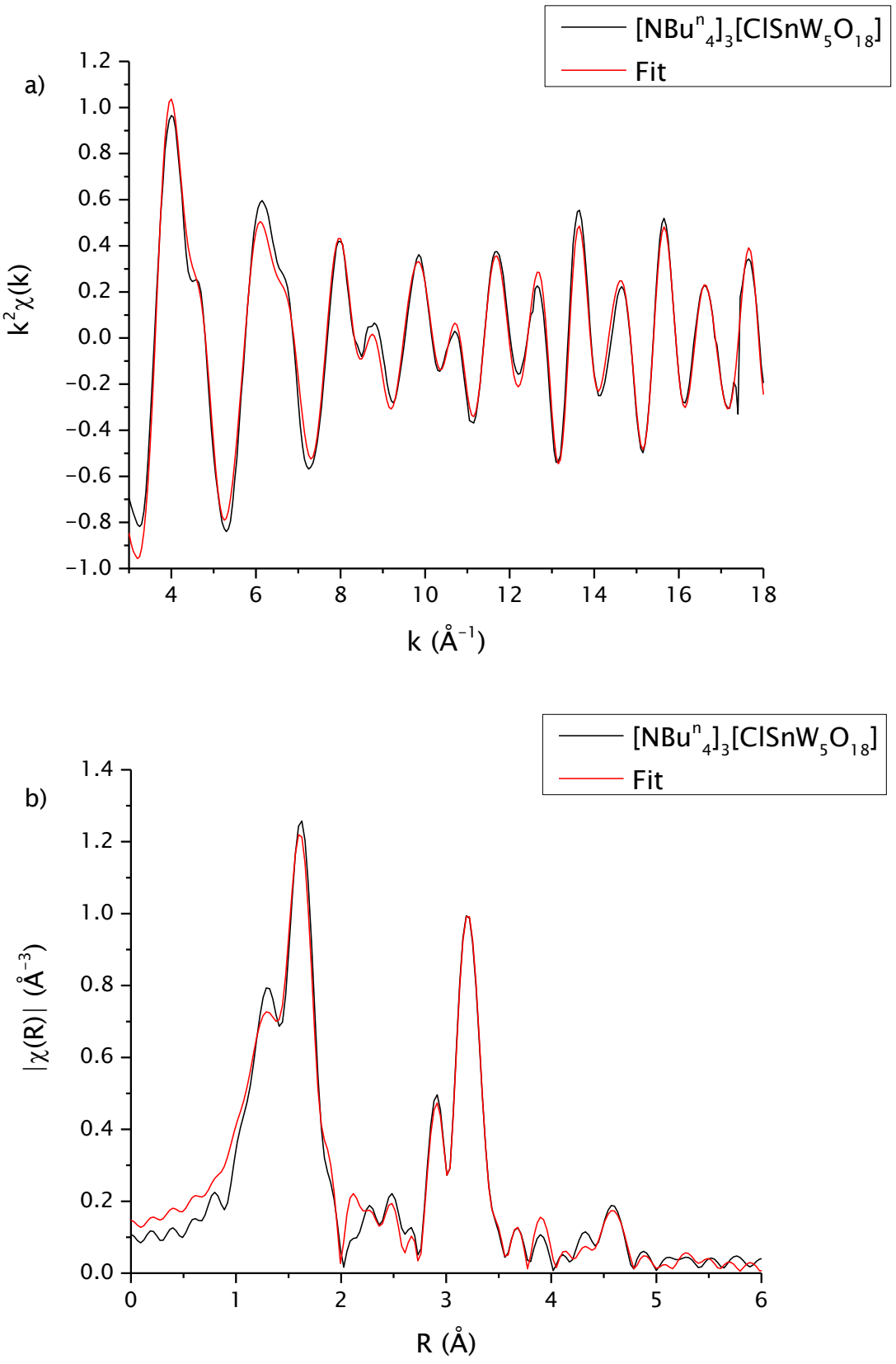

Figure 3.32: W L_{III} edge k^2-weighted a) EXAFS spectrum and b) Fourier transform of [NBu$^n_4$]$_3$[ClSnW$_5$O$_{18}$] in acetonitrile with the Sn-O_i distance set to 2.24 Å.

Anion	Edge	W atom	Path	Degeneracy	σ^2 / Å^2	r / Å	r / Å (XRD)
$[ClSnW_5O_{18}]^{3-}$ Solid	Sn K		Sn↔Cl	1	0.00260 ± 0.00175	2.35 ± 0.019	1.985
			Sn↔O_b	4	0.00307 ± 0.00075	2.05 ± 0.008	2.048
			Sn↔O_i	1	0.00475 ± 0.00778	2.24	2.271
			Sn↔W	4	0.00339 ± 0.00159	3.27 ± 0.015	3.269
	W L_{III}	Trans to Sn	W↔O_t	1	0.00211 ± 0.00128	1.733 ± 0.015	1.709
			W↔O_bW	4	0.00279 ± 0.00051	1.908 ± 0.009	1.907
			W↔O_i	1	0.00143 ± 0.00197	2.347 ± 0.017	2.361
			W↔W	4	0.00118 ± 0.00111	3.347 ± 0.014	3.312
		Cis to Sn	W↔O_t	1	0.00211 ± 0.00128	1.726 ± 0.015	1.702
			W↔O_bSn	1	0.00279 ± 0.00051	1.870 ± 0.009	1.870
			W↔O_bW	2	0.00279 ± 0.00051	1.921 ± 0.009	1.921
			W↔O_bW	1	0.00279 ± 0.00051	1.949 ± 0.009	1.949
			W↔O_i	1	0.00143 ± 0.00197	2.332 ± 0.017	2.347
			W↔W	3	0.00118 ± 0.00111	3.344 ± 0.014	3.309
			W↔Sn	1	-0.00026 ± 0.00206	3.371 ± 0.029	3.271
Solution	Sn K		Sn↔Cl	1	0.00330 ± 0.00201	2.35 ± 0.014	1.985
			Sn↔O_b	4	0.00170 ± 0.00013	2.05 ± 0.002	2.048
			Sn↔O_i	1	0.00136 ± 0.01925	2.23 ± 0.019	2.271
			Sn↔W	4	0.00341 ± 0.00026	3.26 ± 0.004	3.269
	W L_{III}	Trans to Sn	W↔O_t	1	0.00179 ± 0.00113	1.703 ± 0.013	1.708
			W↔O_bW	4	0.00352 ± 0.00060	1.889 ± 0.010	1.902
			W↔O_i	1	0.00128 ± 0.00187	2.294 ± 0.017	2.337
			W↔W	4	0.00246 ± 0.00120	3.321 ± 0.009	3.307
		Cis to Sn	W↔O_t	1	0.00179 ± 0.00113	1.703 ± 0.013	1.708
			W↔O_bSn	1	0.00352 ± 0.00060	1.852 ± 0.010	1.865
			W↔O_bW	3	0.00352 ± 0.00060	1.932 ± 0.010	1.942
			W↔O_i	1	0.00128 ± 0.00187	2.319 ± 0.017	2.361
			W↔W	3	0.00246 ± 0.00120	3.334 ± 0.009	3.322
			W↔Sn	1	0.01040 ± 0.03158	3.364 ± 0.193	3.288

Table 3.13: The EXAFS-derived structural parameters for the Sn K and W L_{III} edges of $[NBu^n_4]_3[ClSnW_5O_{18}]$ in the solid state and in acetonitrile with the Sn-O_i distance set to 2.24 Å.

Anion	Edge	Parameter	Value
$[ClSnW_5O_{18}]^{3-}$	Sn K	R (%)	4.75
Solid		R, k = 1 (%)	1.42
		R, k = 2 (%)	3.03
		R, k = 3 (%)	6.37
		Chi-square	1609
		Reduced chi-square	77
		Amplitude reduction factor	1.00
		k range ($Å^{-1}$)	3.0 - 14.5
		R range (Å)	1.0 - 5.0
		No. of independent parameters	28
		No. of variables	8
	$W L_{III}$	R (%)	2.29
		R, k = 1 (%)	1.67
		R, k = 2 (%)	2.16
		R, k = 3 (%)	3.01
		Chi-square	7183
		Reduced chi-square	369
		Amplitude reduction factor	0.68
		k range ($Å^{-1}$)	3.0 - 17.1
		R range (Å)	1.0 - 6.0
		No. of independent parameters	44
		No. of variables	25
Solution	Sn K	R (%)	5.13
		R, k = 1 (%)	0.21
		R, k = 2 (%)	0.88
		R, k = 3 (%)	2.52
		Chi-square	996
		Reduced chi-square	30
		Amplitude reduction factor	0.96
		k range ($Å^{-1}$)	3.0 - 17.7
		R range (Å)	1.0 - 6.0
		No. of independent parameters	46
		No. of variables	13
	$W L_{III}$	R (%)	1.91
		R, k = 1 (%)	1.76
		R, k = 2 (%)	1.89
		R, k = 3 (%)	2.10
		Chi-square	6271
		Reduced chi-square	410
		Amplitude reduction factor	0.80
		k range ($Å^{-1}$)	3.0 - 18.0
		R range (Å)	1.0 - 6.0
		No. of independent parameters	47
		No. of variables	32

Table 3.14: Refined parameters for fits to the W L_{III} and Sn K edges of $[NBu^n_4]_3[ClSnW_5O_{18}]$ in the solid state and in acetonitrile with the Sn-O_i distance set to 2.24 Å.

3.2.5 QEXAFS Study of $[NBu_4]_6[(Ph_2PO_2)(ZrW_5O_{18})_2]$

The formation of $[Ph_2PO_2(ZrW_5O_{18})_2]^{6-}$ (equation 3.2) has been investigated using EXAFS spectroscopy. As was possible for$[NBu^n_4]_3[ClSnW_5O_{18}]$, it was also possible to look at the EXAFS of $[NBu^n_4]_6[Ph_2PO_2(ZrW_5O_{18})_2]$ from 2 hard edges – the W L_{III} edge and the Zr K edge. The model for the curve fitting analysis of $[NBu^n_4]_6[Ph_2PO_2(ZrW_5O_{18})_2]$ was constructed by editing the crystallographic data for $[NBu^n_4]_6[\{(OCH_3)(ZrW_5O_{18})_2\}]$. The 2 CH_3O groups and one of the POM clusiters were removed from the structure and Ph_2PO_2 was added in the terminal position on the zirconium atom. The second POM cage is too far from the absorbing zirconium atom to be seen in the EXAFS so this was left out of the model giving a $[(Ph_2PO_2)ZrW_5O_{18}]^{3-}$ structure (figure 3.33) to use as a model in the curve fitting analysis.

$$3\ [NBu^n_4]_2[WO_4] + 7\ WO(OCH_3)_4 + 2\ Zr(OR)_4 + H_2O \rightarrow [NBu^n_4]_6[Ph_2PO_2(ZrW_5O_{18})_2]$$

(Equation 3.2)

At the W L_{III} edge the Zr···W5 distance was refined to 4.679 Å in the solid state and 4.694 Å in acetonitrile. In acetonitrile at the Zr K edge the Zr···W5 distance was refined to 4.901 Å. In the crystallographic data the Zr···W5 distance is 4.785. The amplitude of the Zr···W_{cis} (Where W_{cis} is the tungsten that is cis to the Zr) shell is weak and this may be the cause of the difference between refined distances for this shell at the W L_{III} and Zr K edges. The EXAFS-derived structural parameters for the W L_{III} and Zr K edges of $[NBu^n_4]_6[Ph_2PO_2(ZrW_5O_{18})_2]$ in the solid state and in acetonitrile are presented in table 3.15 and the data regarding the quality of these fits are presented in table 3.16. The EXAFS spectra and Fourier transforms of the Zr K and W L_{III} edges of $[NBu^n_4]_6[Ph_2PO_2(ZrW_5O_{18})_2]$ in the solid state and in acetonitrile are presented in figures 3.34 – 3.36. The bond distances reported in the tables agree with the crystallographic data within the error of the EXAFS experiment.

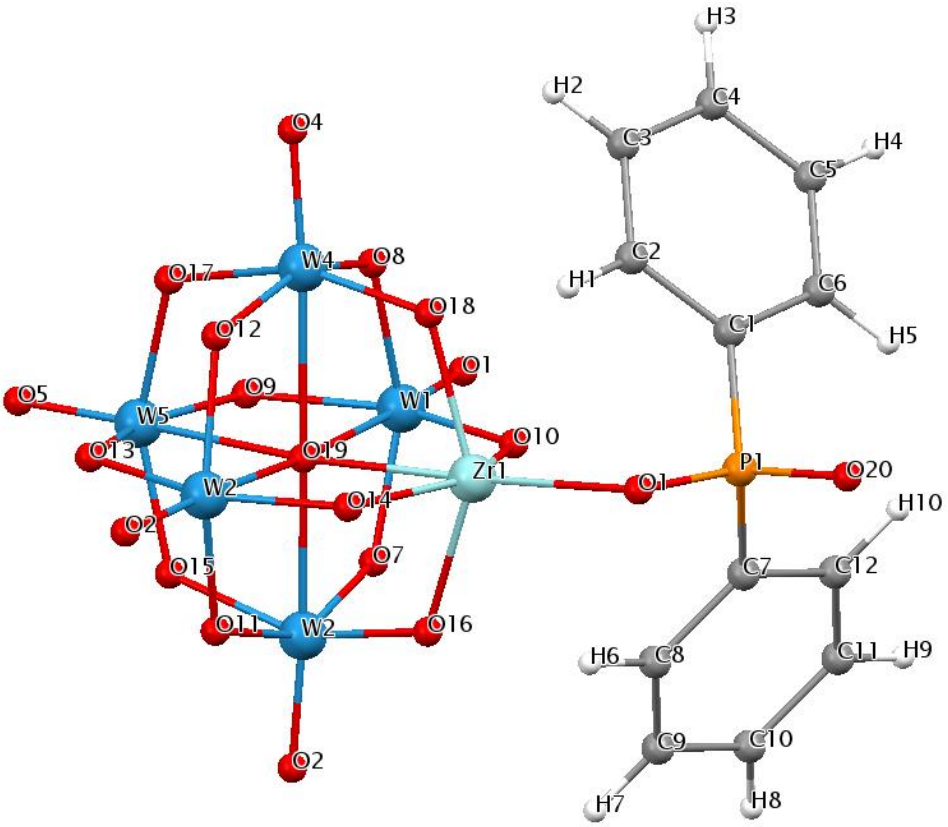

Figure 3.33: Structure of the $(Ph_2PO_2)ZrW_5O_{18}$ fragment of $[(Ph_2PO_2)(ZrW_5O_{18})_2]^{6-}$.

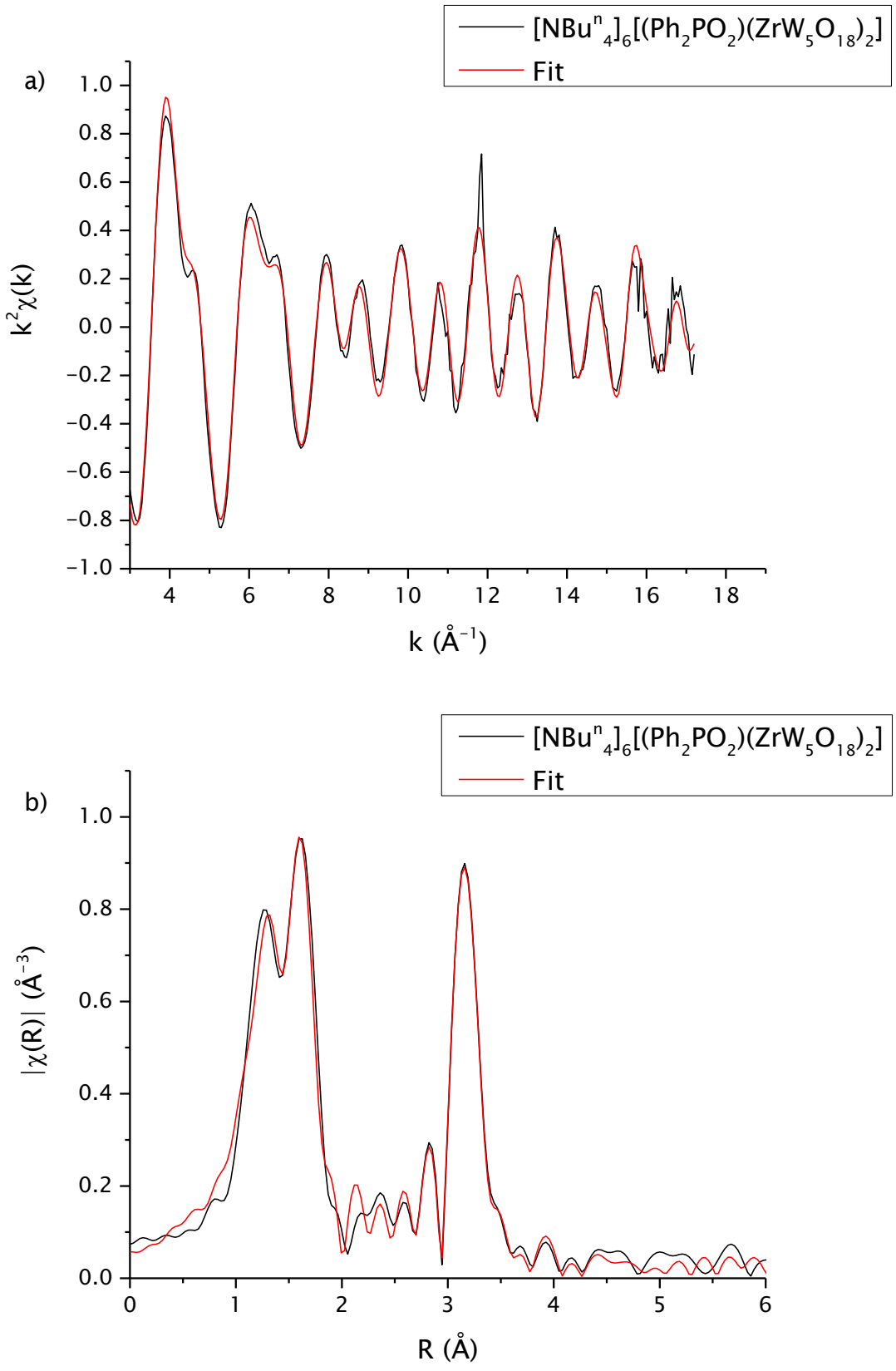

Figure 3.34: W L_{III} edge k^2-weighted a) EXAFS spectrum and b) Fourier transform of [NBu$^n_4$]$_6$[Ph$_2$PO$_2$(ZrW$_5$O$_{18}$)$_2$] in the solid state.

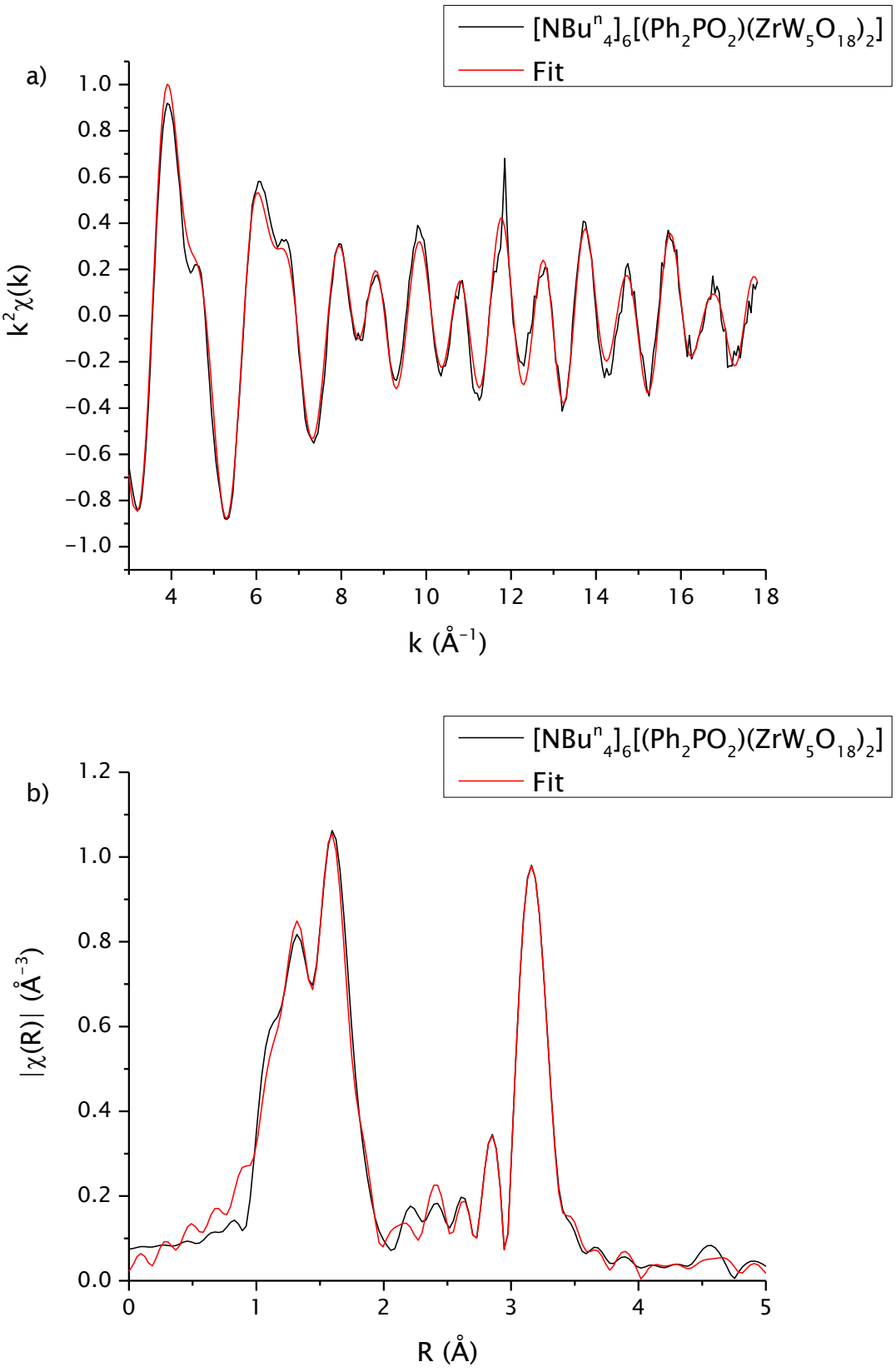

Figure 3.35: W L_{III} edge k^2-weighted a) EXAFS spectrum and b) Fourier transform of [NBu$^n_4$]$_6$[Ph$_2$PO$_2$(ZrW$_5$O$_{18}$)$_2$] in acetonitrile.

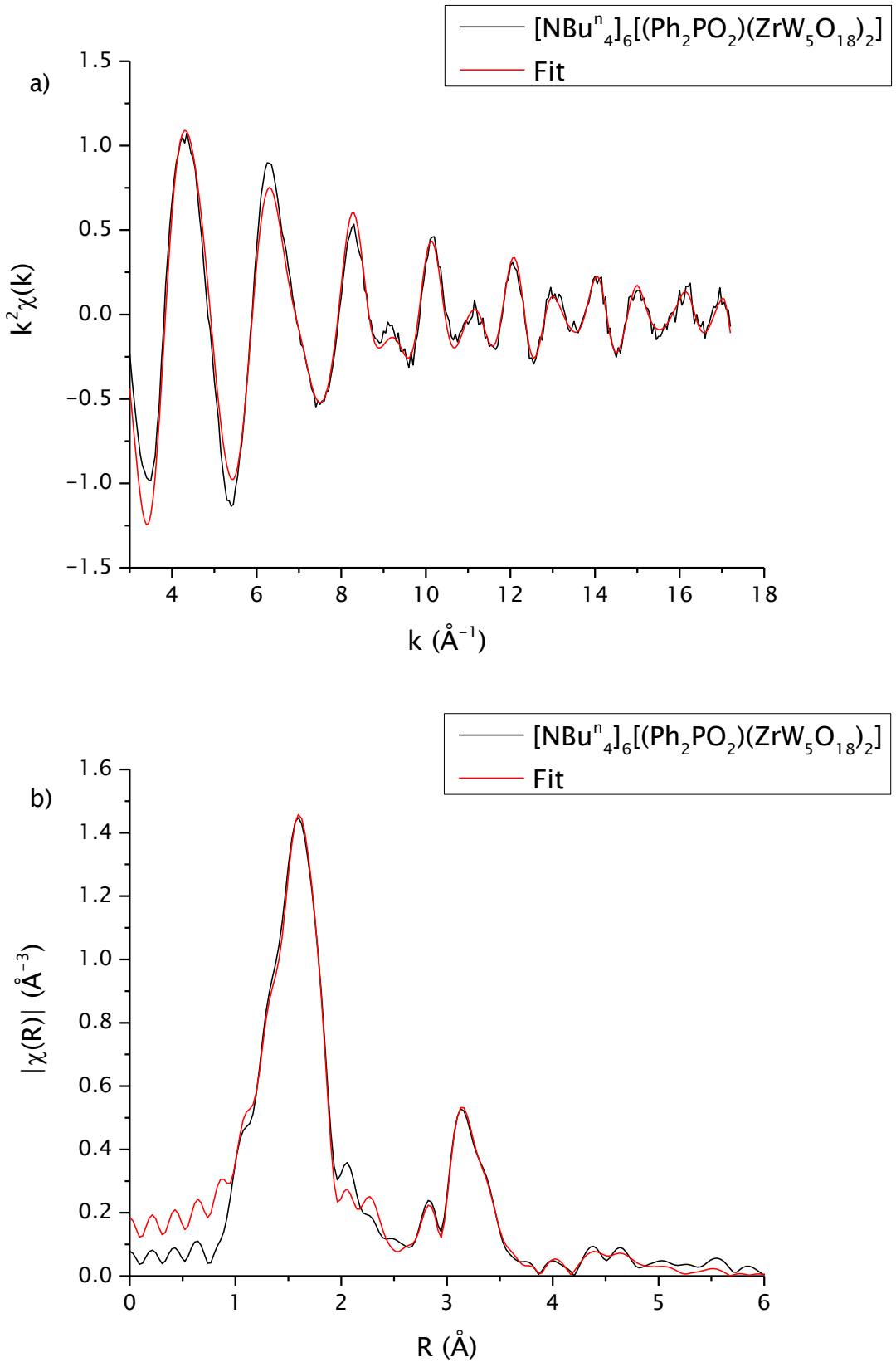

Figure 3.36: Zr K edge k²-weighted a) EXAFS spectrum and b) Fourier transform of [NBu$^n_4$]$_6$[Ph$_2$PO$_2$(ZrW$_5$O$_{18}$)$_2$] in acetonitrile.

Anion	Edge	W site	Path	Degeneracy	σ^2 / Å^2	r / Å	r / Å (XRD)
$[(Ph_2PO_2)(ZrW_5O_{18})_2]^{6-}$	W L_{III}	Trans to Zr	W↔O_t	1	0.00069 ± 0.00073	1.709 ± 0.009	1.725
Solid			W↔O_bW	1	0.00074 ± 0.00059	1.842 ± 0.008	1.903
			W↔O_bW	1	0.00074 ± 0.00059	1.846 ± 0.008	1.907
			W↔O_bW	1	0.00074 ± 0.00059	1.854 ± 0.008	1.915
			W↔O_bW	1	0.00074 ± 0.00059	1.866 ± 0.008	1.928
			W↔O_i	1	0.00229 ± 0.00214	2.307 ± 0.017	2.407
			W↔W	1	0.01172 ± 0.00573	3.115 ± 0.045	3.306
			W↔W	1	0.01172 ± 0.00573	3.129 ± 0.045	3.320
			W↔W	1	0.01172 ± 0.00573	3.144 ± 0.045	3.335
			W↔W	1	0.01172 ± 0.00573	3.147 ± 0.008	3.337
		Cis to Zr	W↔O_t	1	0.00069 ± 0.00073	1.689 ± 0.009	1.704
			W↔O_bZr	1	0.00074 ± 0.00059	1.770 ± 0.008	1.831
			W↔O_bW	1	0.00074 ± 0.00059	1.862 ± 0.008	1.924
			W↔O_bW	1	0.00074 ± 0.00059	1.937 ± 0.008	1.998
			W↔O_bW	1	0.00074 ± 0.00059	1.939 ± 0.008	2.000
			W↔O_i	1	0.00229 ± 0.00214	2.295 ± 0.017	2.394
			W↔W	1	0.01172 ± 0.00573	3.107 ± 0.045	3.298
			W↔W	1	0.01172 ± 0.00573	3.115 ± 0.045	3.306
			W↔W	1	0.01172 ± 0.00573	3.132 ± 0.045	3.323
			W↔Zr	1	-0.00125 ± 0.00061	3.423 ± 0.008	3.360
Solution	W L_{III}	Trans to Zr	W↔O_t	1	0.00104 ± 0.00106	1.718 ± 0.008	1.725
			W↔O_bW	4	0.00418 ± 0.00089	1.883 ± 0.007	1.903
			W↔O_i	1	0.00274 ± 0.00294	2.294 ± 0.016	2.407
			W↔W	4	0.00437 ± 0.00234	3.269 ± 0.013	3.306
		Cis toZr	W↔O_t	1	0.00104 ± 0.00106	1.698 ± 0.014	1.704
			W↔O_bZr	1	0.00418 ± 0.00089	1.812 ± 0.011	1.832
			W↔O_bW	3	0.00418 ± 0.00089	1.904 ± 0.011	1.924
			W↔O_i	1	0.00274 ± 0.00294	2.281 ± 0.026	2.394
			W↔W	3	0.00437 ± 0.00234	3.288 ± 0.040	3.298
			W↔Zr	1	0.00449 ± 0.01696	3.429 ± 0.110	3.360
	Zr K		Zr↔O_t	1	0.00062 ± 0.00245	2.223 ± 0.030	2.430
			Zr↔O_b	4	0.00247 ± 0.00176	2.089 ± 0.019	2.062
			Zr↔O_i	1	0.00062 ± 0.00245	2.176 ± 0.030	2.383
			Zr↔W	4	0.00439 ± 0.02256	3.369 ± 0.144	3.360

Table 3.15: The EXAFS-derived structural parameters for the Zr K and W L_{III} edges of $[NBu^n_4]_3[(py_2PO_2)ZrW_5O_{18}]$ in the solid state and in acetonitrile.

Anion	Edge	Parameter	Value
$[(Ph_2PO_2)(ZrW_5O_{18})_2]^{6-}$	W L_{III}	R (%)	1.96
Solid		R, k = 1 (%)	0.73
		R, k = 2 (%)	1.16
		R, k = 3 (%)	3.60
		Chi-square	1469
		Reduced chi-square	107
		Amplitude reduction factor	0.68
		k range ($Å^{-1}$)	3.0 - 17.2
		R range (Å)	1.0 - 6.0
		No. of independent parameters	44
		No. of variables	31
Solution	W L_{III}	R (%)	0.33
		R, k = 1 (%)	0.53
		R, k = 2 (%)	0.85
		R, k = 3 (%)	1.77
		Chi-square	953
		Reduced chi-square	229
		Amplitude reduction factor	0.80
		k range ($Å^{-1}$)	3.0 - 17.8
		R range (Å)	1.0 - 5.0
		No. of independent parameters	37
		No. of variables	33
	Zr K	R (%)	0.45
		R, k = 1 (%)	1.41
		R, k = 2 (%)	1.24
		R, k = 3 (%)	1.44
		Chi-square	955
		Reduced chi-square	242
		Amplitude reduction factor	0.96 ± 0.14
		k range ($Å^{-1}$)	3.0 - 17.2
		R range (Å)	1.1 - 6.0
		No. of independent parameters	43
		No. of variables	40

Table 3.16: Refined parameters for fits to the W L_{III} and Zr K edges of $[NBu^n_4]_6[Ph_2PO_2(ZrW_5O_{18})_2]^{6-}$ in the solid state and in acetonitrile.

$[(Ph_2PO_2)ZrW_5O_{18}]^{3-}$ does fit the Zr K edge EXAFS spectrum recorded for equation 3.2, but it is not certain that this gives the whole picture. Decreasing the number of tungsten atoms included in the fit to 3, 2, or 1 causes the amplitude to increase to 1.04, 1.06 and 1.10 respectively and the error associated with these figure allows them to drop below 1.00. This could mean that the zirconium is reacting with the tungsten species to form structures containg 2, 3, 4 or 5 metal atoms, similar to the structures discussed for reaction 3.1. At the W L_{III} edge, $[(Ph_2PO_2)ZrW_5O_{18}]^{3-}$ and $[W_6O_{19}]^{2-}$ both fit the spectrum for this reaction and it is possible that that there are clusters being formed by the tungsten species that do not conatin any zirconium. In any case, it is apparent that a reaction is taking place in which POM clusters are being formed. The EXAFS-derived structural parameters for the W L_{III} and Zr K edges of reaction 3.2 are presented in table 3.17 and the data regarding the quality of these fits are presented in table 3.18. The EXAFS spectra and Fourier transforms of the Zr K and W L_{III} edges of $[NBu^n_4]_3[(Ph_2PO_2)ZrW_5O_{18}]$ in the solid state and in acetonitrile are presented in figures 3.37 – 3.39.

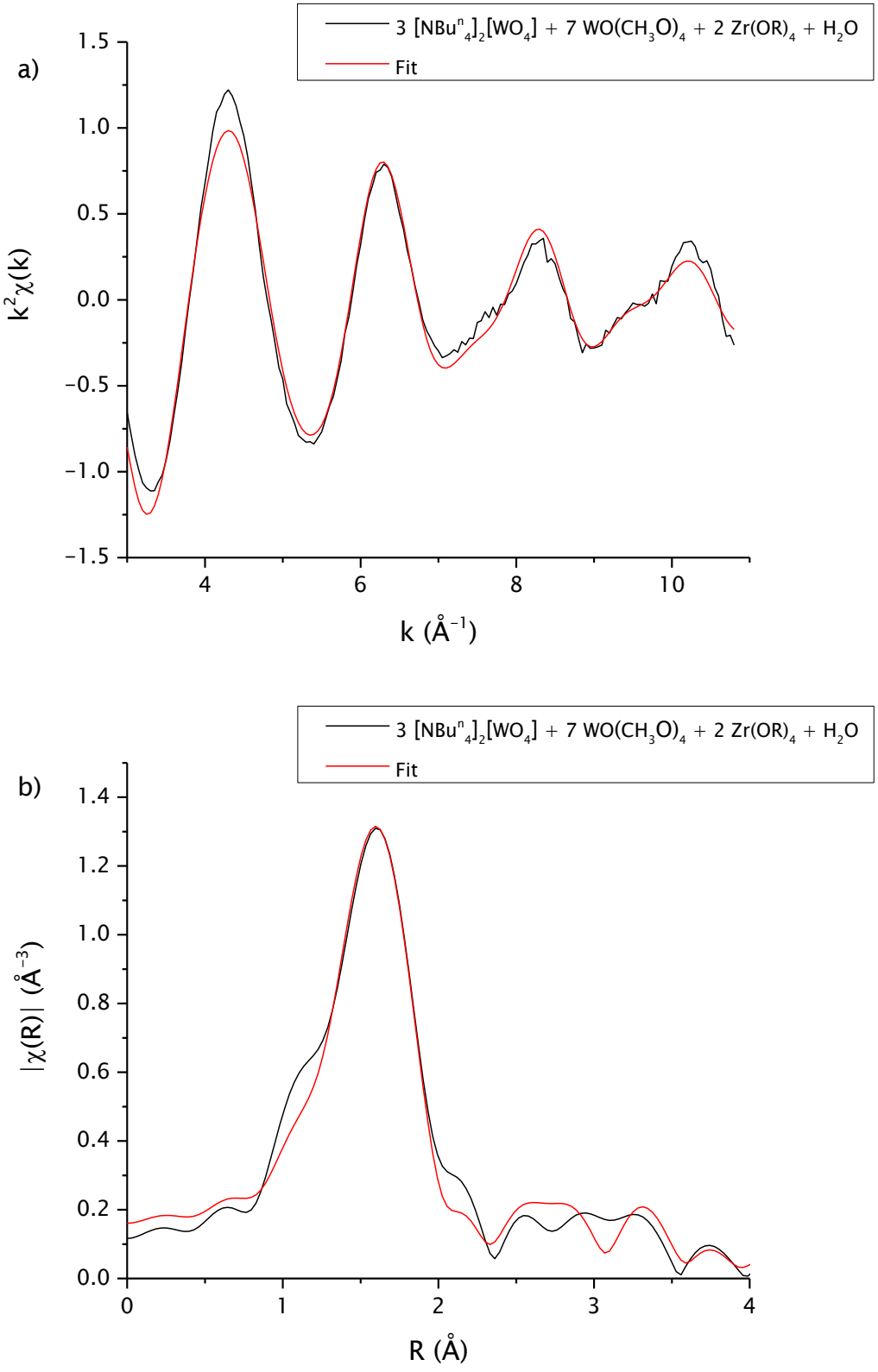

Figure 3.37: $[Ph_2PO_2(ZrW_5O_{18})_2]^{6-}$ fit to Zr K edge k^2-weighted a) EXAFS spectrum and b) Fourier transform of 3 $[NBu^n_4]_2[WO_4]$ + 7 $WO(OCH_3)_4$ + 2 $Zr(OR)_4$ + H_2O in acetonitrile.

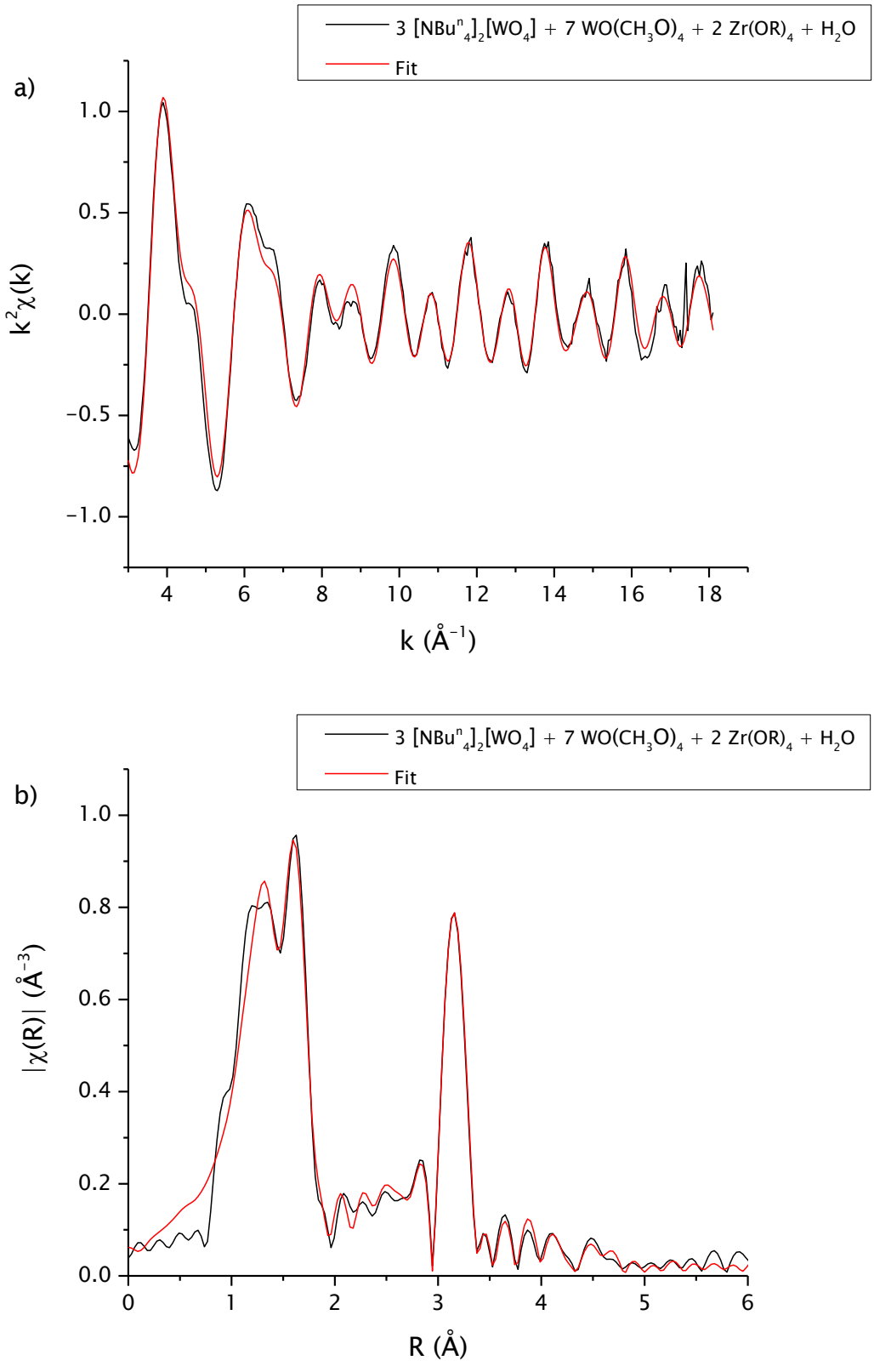

Figure 3.38: $[Ph_2PO_2(ZrW_5O_{18})_2]^{6-}$ fit to W L_{III} edge k^2-weighted a) EXAFS spectrum and b) Fourier transform of 3 $[NBu^n_4]_2[WO_4]$ + 7 $WO(OCH_3)_4$ + 2 $Zr(OR)_4$ + H_2O in acetonitrile.

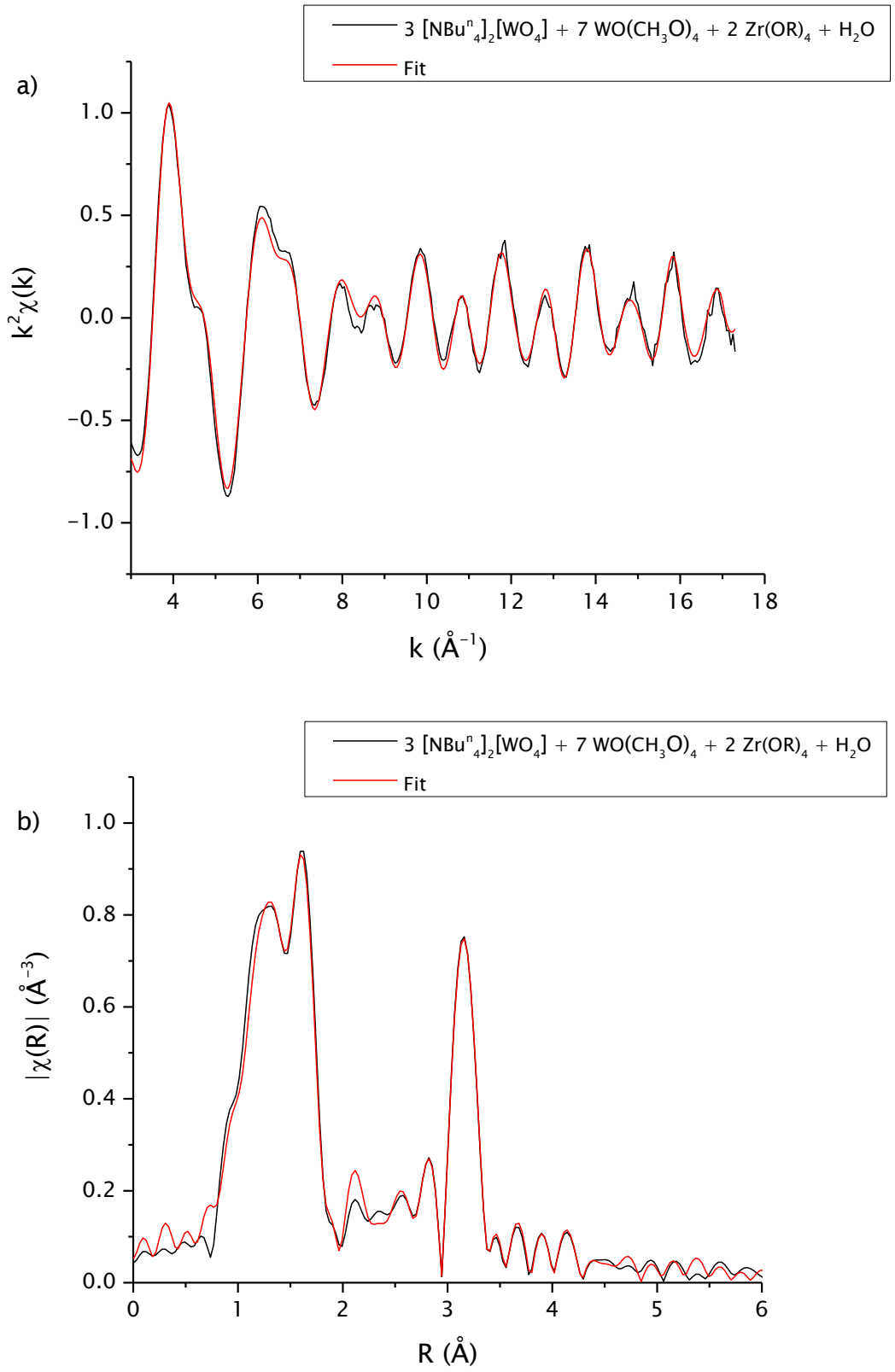

Figure: 3.39: $[W_6O_{19}]^{2-}$ fit to W L_{III} edge k^2-weighted a) EXAFS spectrum and b) Fourier transform of 3 $[NBu^n_4]_2[WO_4]$ + 7 $WO(OCH_3)_4$ + 2 $Zr(OR)_4$ + H_2O in acetonitrile.

Anion	Edge	W atom	Path	Degeneracy	σ^2 / Å^2	r / Å	r / Å (XRD)
$[(Ph_2PO_2)(ZrW_5O_{18})_2]^{6-}$	Zr K		$Zr\leftrightarrow O_t$	1	0.00146 ± 0.00635	2.302 ± 0.029	2.430
			$Zr\leftrightarrow O_b$	4	0.00225 ± 0.00315	2.131 ± 0.017	2.062
			$Zr\leftrightarrow O_i$	1	0.00146 ± 0.00635	2.255 ± 0.029	2.383
			Zr↔W	4	0.01138 ± 0.00330	3.352 ± 0.029	3.360
	W L_{III}	Trans to Zr	$W\leftrightarrow O_t$	1	0.00150 ± 0.00072	1.699 ± 0.008	1.725
			$W\leftrightarrow O_bW$	4	0.00625 ± 0.00097	1.889 ± 0.008	1.903
			$W\leftrightarrow O_i$	1	0.00377 ± 0.00273	2.371 ± 0.028	2.407
			W↔W	4	0.00106 ± 0.01990	3.321 ± 0.020	3.306
		Cis to Zr	$W\leftrightarrow O_t$	1	0.00150 ± 0.00072	1.711 ± 0.008	1.737
			$W\leftrightarrow O_bZr$	1	0.00625 ± 0.00097	1.849 ± 0.008	1.864
			$W\leftrightarrow O_bW$	3	0.00625 ± 0.00097	1.911 ± 0.008	1.925
			$W\leftrightarrow O_i$	1	0.00377 ± 0.00273	2.240 ± 0.028	2.275
			W↔W	3	0.00106 ± 0.01990	3.309 ± 0.020	3.294
			W↔Zr	1	0.01946 ± 0.02812	3.368 ± 0.337	3.366
$[W_6O_{19}]^{2-}$	W L_{III}		$W\leftrightarrow O_t$	1	0.00113 ± 0.00054	1.699 ± 0.006	1.683
			$W\leftrightarrow O_b$	4	0.00666 ± 0.00067	1.883 ± 0.007	1.941
			$W\leftrightarrow O_i$	1	0.00351 ± 0.00135	2.253 ± 0.012	2.325
			W↔W	4	0.00238 ± 0.00055	3.288 ± 0.009	3.288

Table 3.17: The EXAFS-derived structural parameters for the Zr K and W L_{III} edges of 3 $[NBu^n_4]_2[WO_4]$ + 7 $WO(OCH_3)_4$ + 2 $Zr(OR)_4$ + H_2O in acetonitrile.

Anion	Edge	Parameter	Value
$[(Ph_2PO_2)(ZrW_5O_{18})_2]^{6-}$	Zr K	R (%)	0.97
		R, k = 1 (%)	2.53
		R, k = 2 (%)	2.07
		R, k = 3 (%)	2.70
		Chi-square	1222
		Reduced chi-square	183
		Amplitude reduction factor	1.02 ± 0.18
		k range ($Å^{-1}$)	3.0 - 10.8
		R range (Å)	1.0 - 4.0
		No. of independent parameters	14
		No. of variables	8
	$W L_{III}$	R (%)	0.28
		R, k = 1 (%)	0.52
		R, k = 2 (%)	1.01
		R, k = 3 (%)	3.03
		Chi-square	536
		Reduced chi-square	50
		Amplitude reduction factor	0.91 ± 0.10
		k range ($Å^{-1}$)	3.0 - 18.1
		R range (Å)	1.1 - 6.0
		No. of independent parameters	46
		No. of variables	36
$[W_6O_{19}]^{2-}$	$W L_{III}$	R (%)	0.16
		R, k = 1 (%)	0.30
		R, k = 2 (%)	0.51
		R, k = 3 (%)	1.04
		Chi-square	223
		Reduced chi-square	27
		Amplitude reduction factor	0.87 ± 0.05
		k range ($Å^{-1}$)	3.0 - 17.3
		R range (Å)	1.1 - 6.0
		No. of independent parameters	44
		No. of variables	36

Table 3.18: Refined parameters for fits to the W L_{III} and Zr K edges of 3 $[NBu^n_4]_2[WO_4]$ + 7 $WO(OCH_3)_4$ + 2 $Zr(OR)_4$ + H_2O in acetonitrile.

3.3 Experimental

3.3.1 EXAFS Spectroscopy

X-ray absorption spectra were recorded on beamline B18 with a double crystal Si (111) monochromator at Diamond Light Source operating at 3 GeV. Aluminium cells with windows of 3 mm thickness were used to obtain multiple solution spectra. For high temperature experiments (60 °C) cartridge heaters were used to heat the liquid cell. X-ray absorption spectra were recorded in transmission mode at the W L_{III} edge for Lindqvist $[NBu_4]_2[W_6O_{19}]$ hexatungstate and similar heterotungstate species incorporating Co, Fe, Sn, Ti and Zr heteroatoms. Spectra for Zr heterotungstate species were also recorded in transmission mode at the Zr K edge. A 9 element Ge detector was used in fluorescence mode to record soft X-ray K-edge spectra for Ni, Co and Fe heterotungstate species. Scan times were 25 seconds and 20 spectra were recorded for each sample. Sample concentrations were 10 mM in tungsten for measurements at the W L_{III} edge. For measurements at the heterometal K edges, the concentrations of samples were: 30 mM in cobalt and 50 mM in zirconium. Reaction solutions were measured at the Zr K edge using concentrations of 40 mM in zirconium. Solid samples were diluted in boron nitride and held between layers of Kapton tape on aluminium plates. Removal of background and curve-fitting analyses were carried out within IFEFFIT (version 1.2.11). The samples were prepared as previously reported.[11,12,19]

3.4 Conclusions

$[NBu^n_4]_2[W_6O_{19}]^{2-}$ has been characterised in the solid state and in acetonitrile. Possible intermediate species in the formation of $[W_6O_{19}]^{2-}$ have been identified that consist of 3 and 5 tungsten atoms, but the number of oxygen atoms and coordinating solvent molecules present in these structures has not been accurately determined. $[NBu^n_4]_3[(CH_3O)TiW_5O_{18}]$ in the solid state and $[NBu^n_4]_3[ClTiW_5O_{18}]$ in acetonitrile have been characterised at the W L_{III} edge. $[NBu^n_4]_3[(py)CoW_5O_{18}]$ has been characterised in the solid state at the W L_{III} edge and in acetonitrile at the Co K edge. $[NBu^n_4]_3[ClSnW_5O_{18}]$ has been characterised at the W L_{III} edge and the Sn K edge in the solid state and in acetonitrile. The Sn-O_i bond length has not been accurately refined. $[NBu^n_4]_6[Ph_2PO_2(ZrW_5O_{18})_2]^{6-}$ has been characterised in the solid state and in acetonitrile at the W L_{III} edge and the Zr K edge. The formation of this POM in the presence of water has been followed using EXAFS spectroscopy and the EXAFS suggest that tungstate and heteropolyanionic clusters are being formed.

At the W L_{III} edge the bridging oxygen atoms bound to the metal atom trans to the absorbing atom vary from the crystallographic data with a range of 0.10 – 0.56 Å. These atoms make little contribution of the EXAFS. The metal atom trans to the absorbing atom – up to 4.8 Å from the absorbing atom – has been refined to a distance that is within 2 % of the distance defined in the crystallographic data. The equatorial oxygen atoms in the W L_{III} edge refinement for $[ClSnW_5O_{18}]^{3-}$ are different from the crystallographic data by 6 %. In this fit the bridging atoms on the metal atom trans to the absorbing atom are at a distance that is within 1 % of the crystallographic data. At the Sn K edge the equatorial oxygen atoms are refined to a distance that is within 1 % of the crystallographic data, but the bridging atoms on the metal atom trans to the absorbing atom are at a distance that is within 13 % of the crystallographic data. At the Co K edge the equatorial oxygen atoms and the bridging atoms on the metal atom trans to the absorbing atom are at a distance that is within 2 % of the crystallographic data. The fits at the W L_{III} edge of $[LTiW_5O_{18}]^{3-}$ and $[(py)CoW_5O_{18}]^{3-}$ included all 5 of the tungsten sites and the terminal and bridging oxygen atoms that are not bound to the absorbing atom were not included in the fit. The equatorial oxygen atoms were refined at distance that

varied up to 0.40 Å from the crystallographic data. Figure 3.40 shows the fragment of the Lindqvist-type POMs that can be detected by EXAFS spectroscopy. The EXAFS-derived structural parameters, where W5 is the absorbing atom, for atoms coloured yellow vary significantly from crystallographic data. It is possible to distinguish between the POMs investigated in this chapter and this has been demonstrated in figure 3.41 by comparing the EXAFS spectra and Fourier transforms for these clusters in the solid state.

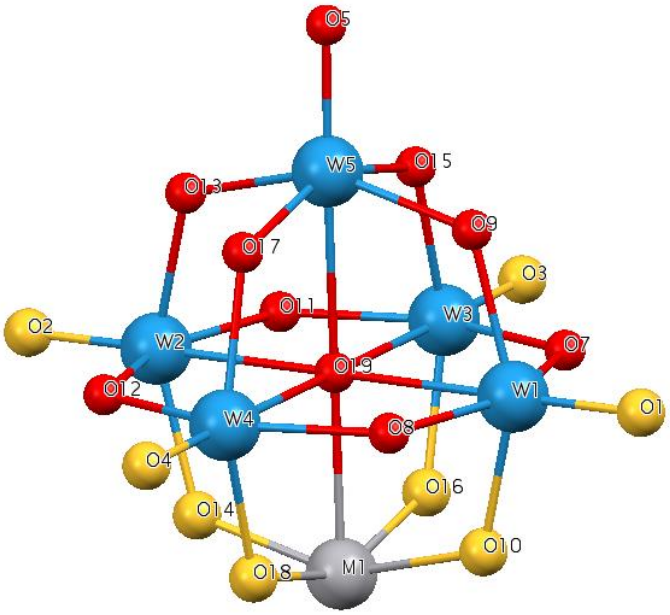

Figure 3.40: Structure of the fragment of the Lindqvist-type POMs that can be detected by EXAFS spectroscopy. Atoms coloured yellow have been refined by EXAFS spectroscopy to distances from the absorbing atom (W5) that vary significantly from crystallographic data.

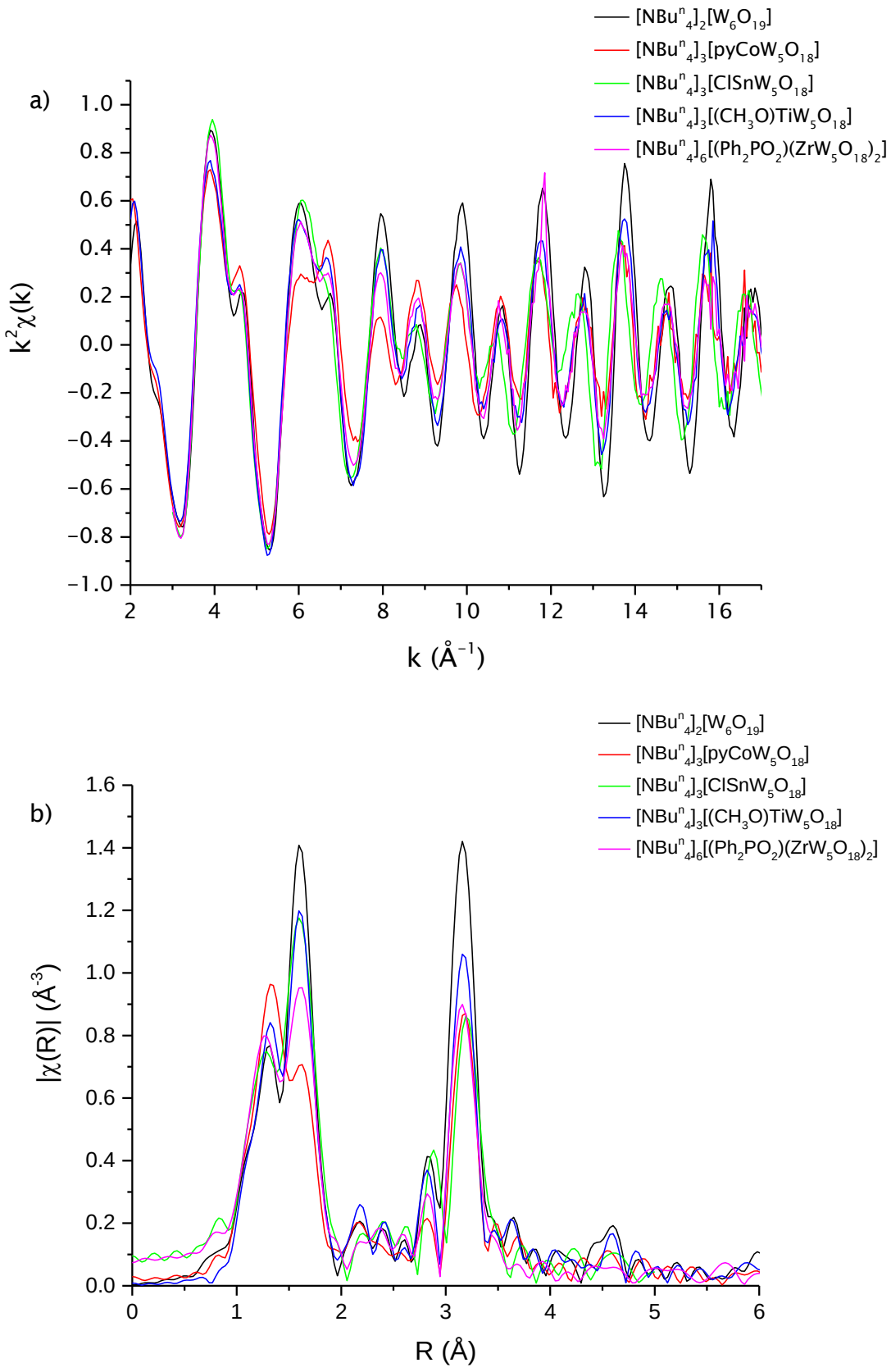

Figure 3.41: W L_{III} edge a) EXAFS spectra and b) Fourier transforms of Lindqvist-type tungstate anions in the solid state.

4. Formation of Electron-Rich Keggin-Type Polyoxometalates by Reductive Aggregation

4.1 Introduction

EXAFS spectroscopy has been used to study the solution behaviour of $[PMo_{12}O_{40}]^{3-}$ (figure 4.1), reduced $[PMo_{12}O_{40}]^{3-}$ and capped Keggin-type anions with a $[PMo_{12}O_{40}]^{3-}$ core structure and monitor the assembly of capped Keggin-type anions by reductive aggregation. EXAFS studies were carried out at the molybdenum K edge and the heterometal K edges (iron, vanadium and yttrium). The secondary metals were present in concentrations of 10 mM and fluorescence detection was required for the softer edges of 3d elements. Reductive aggregation reactions for POMs where the core POM has been capped by iron and yttrium have been followed. Solution phase samples were modelled using crystallographic data instead of writing a FEFF template due to the difficulties involved with producing Cartesian coordinates for a model which has higher symmetry. The same method for adding shells that was used in chapter 3 has been used in this chapter. The most significant peaks in the Fourier transform spectrum for the Mo K edge of $[PMo_{12}O_{40}]^{3-}$ are due to the first shells of oxygen atoms and molybdenum atoms and the different oxygen and molybdenum sites are highlighted in the Fourier transform in figure 4.2. The atom labels used in figure 4.2 match up to the atom labels in figure 4.1. The absorbing atom used in this Fourier transform is Mo1 in figure 4.1.

The samples and reactions studied in this chapter were not heated. Instead of preparing solutions in the solution cell used in chapter 3, a cell was used that can hold a number of samples. This cell is shown in figure 4.3 in a fluorescence experiment set-up. Instead of taking the cell off the beamline each time a new sample needed to be mounted on the stage, the cell could be moved so that the next sample was placed into the path of the beam. This

sped up the experiment as the hutch did not need to be entered to replace the sample.

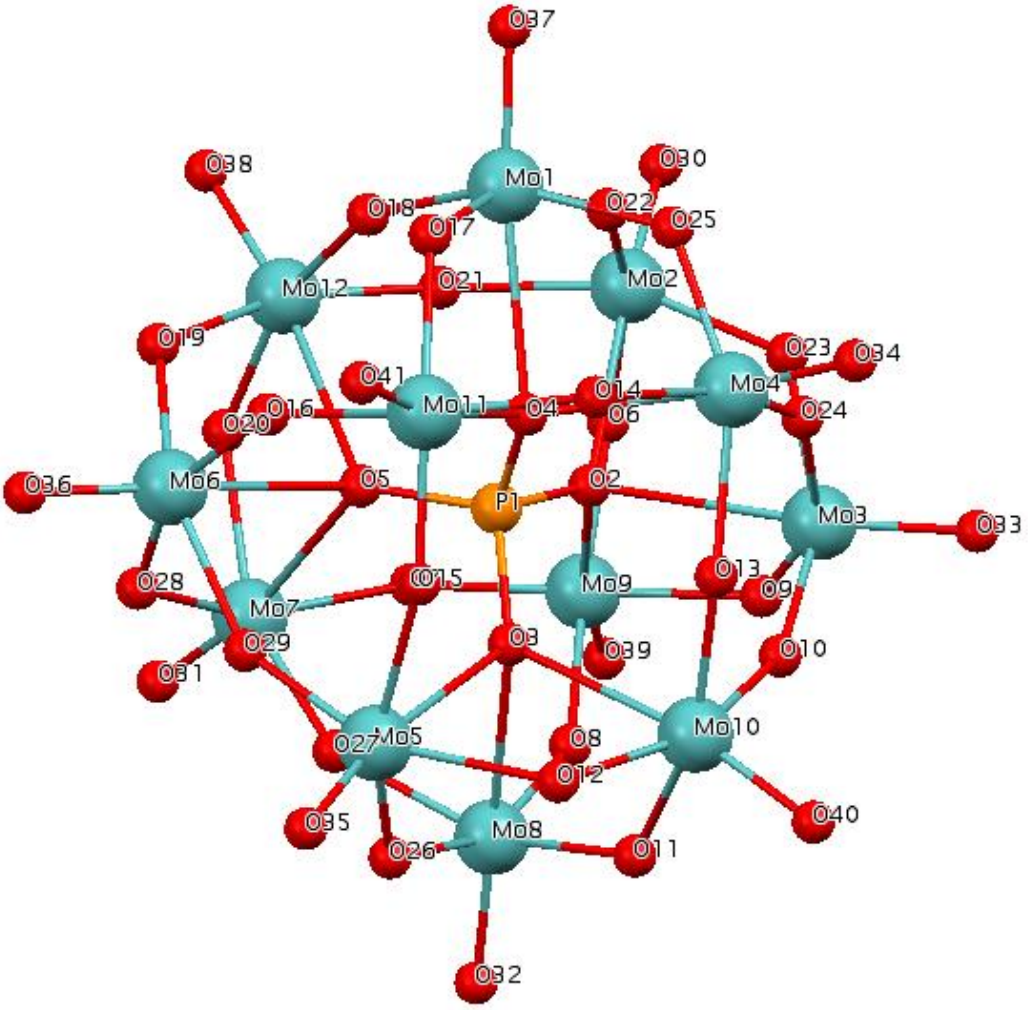

Figure 4.1: Structure of $[PMo_{12}O_{40}]^{3-}$.

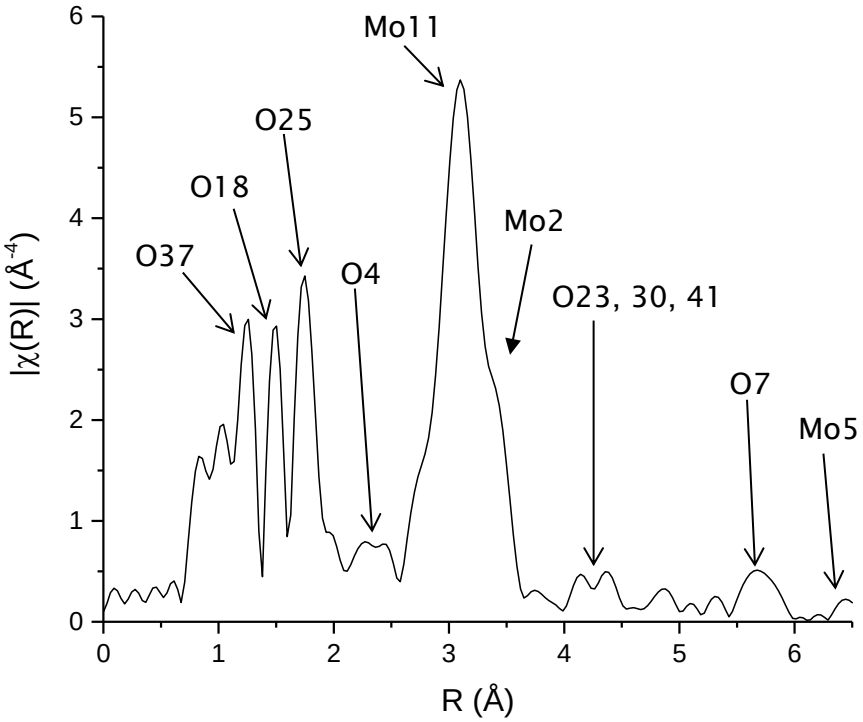

Figure 4.2: k^3-weighted Fourier transform of Mo K edge EXAFS of $[PMo_{12}O_{40}]^{3-}$ where Mo1 is the absorbing atom.

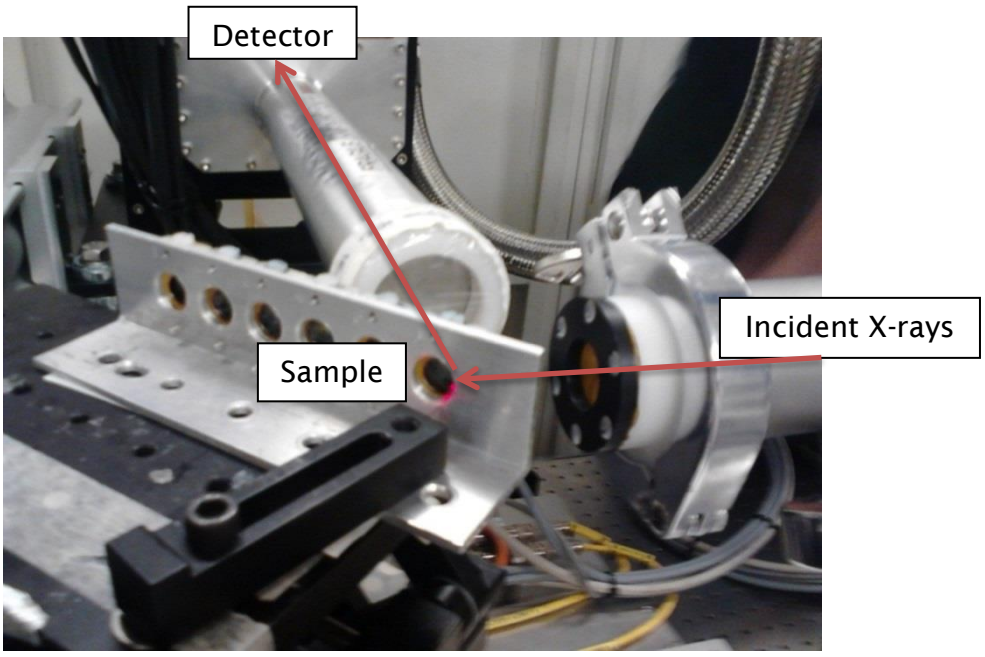

Figure 4.3: XAS solution cell for up to 6 samples.

4.2 Results and Discussion

EXAFS spectroscopy has been used to provide characterisations of $[PMo_{12}O_{40}]^{3-}$ and $[PMo_{12}O_{40}(ML)]^{n-}$ heteropolyanions (where M is a metal and L is a ligand) and the formations of some of these capped Keggin-type POMs have been followed. As the reactions were slow, EXAFS spectra were recorded in situ on the beamline. 5 scans were recorded for each sample at room temperature and the spectra (with the exception of poor spectra) were merged to reduce the noise. An EXAFS spectrum for $[NBu^n_4]_3[PMo_{12}O_{40}]$ in acetonitrile is presented in figure 4.4 to demonstrate the amount and quality of the data that has been collected. Curve-fitting analyses for the uncapped $[PMo_{12}O_{40}]^{3-}$ were performed using a single molybdenum site to represent each molybdenum site in the complex. The capped molybdates were analysed using 2 molybdenum sites: one molybdenum site where an oxygen atom bridges the molybdenum and a heterometal and one molybdenum site where there are only bridging oxygen atoms between 2 molybdenum atoms. R-factors are below 10 % for every k-weighting and the Debye-Waller factors for single scattering paths for the atoms bound to the absorbing atom are low and positive. Negative Debye-Waller factors that are reported can, again, be explained by difficulties in modelling the static and vibrational disorder across pathways involving non-bonded atoms. The EXAFS spectra and the Fourier transforms show that the models have been fitted well to the experimental data and that the peaks in the spectra are real.

Including multiple-scattering paths in the fits helped to refine the EXAFS-derived structural parameters and made it possible to calculate some bond angles for the complexes using the EXAFS-derived structural parameters. Only the single scattering paths have been included in the tables and XRD data have been provided in tables to compare with EXAFS-derived structural parameters. Where no error is given in the tables, this indicates that the parameter was set to the given value. The error reported in the tables shows how the EXAFS-derived structural parameters deviate from XRD data as a percentage of the XRD data. The spectra are not phase corrected. Analyses of all the complexes

in solution were carried out in acetonitrile and solid samples were diluted in boron nitride. All the complexes were prepared by R. J. Errington et. al.[86]

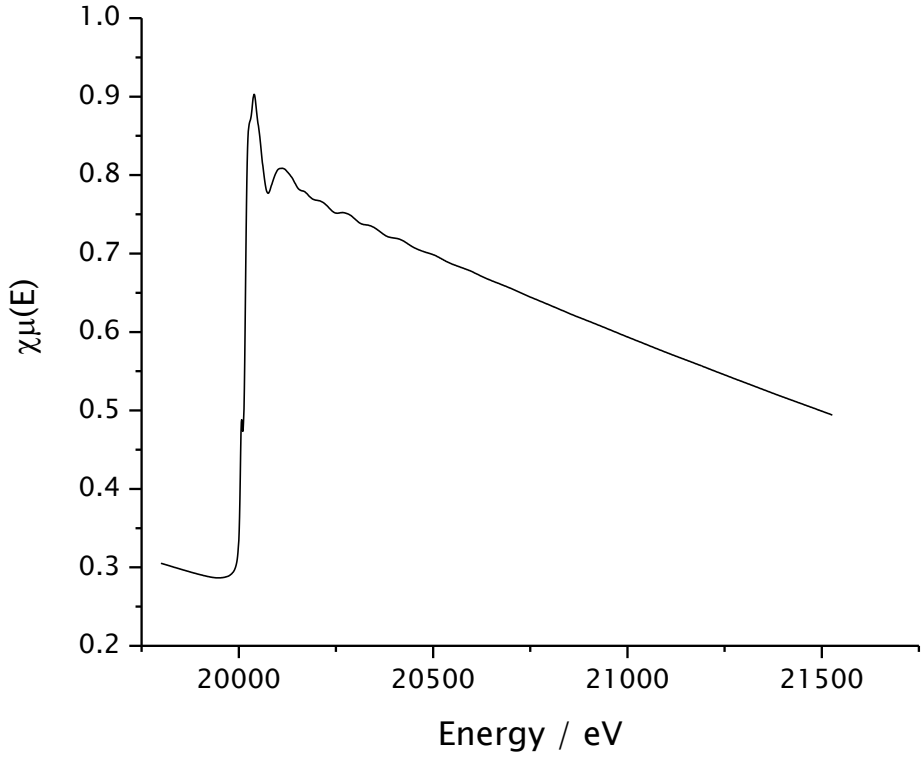

Figure 4.4: EXAFS spectrum for $[NBu^n_4]_3[PMo_{12}O_{40}]$ in acetonitrile.

4.2.1 Effects of Counter Ions on the Structure of $[PMo_{12}O_{40}]^{3-}$

To determine what structural differences to $[PMo_{12}O_{40}]^{3-}$ are caused by the counter ion, EXAFS spectroscopy has been used to characterise $[NBu^n_4]_3[PMo_{12}O_{40}]$ and $[PPN]_3[PMo_{12}O_{40}]$ in acetonitrile. Crystallographic data for $[PPN]_3[PMo_{12}O_{40}]$ (figure 4.1) was fit to the EXAFS spectra for $[NBu^n_4]_3[PMo_{12}O_{40}]$ and $[PPN]_3[PMo_{12}O_{40}]$ in acetonitrile. The Mo K edge EXAFS spectra and Fourier transforms for $[NBu^n_4]_3[PMo_{12}O_{40}]$ and $[PPN]_3[PMo_{12}O_{40}]$ are presented in figures 4.5 and 4.6 respectively. The EXAFS-derived structural parameters for $[PMo_{12}O_{40}]^{3-}$ with the 2 counter ions in acetonitrile are presented in table 4.1. Bond angles have been calculated for the complexes using the EXAFS-derived structural parameters and are presented in table 4.2. Data regarding the quality of both of these fits are presented in table 4.3.

The EXAFS-derived interatomic distances agree with the crystallographic data to within 0.2 Å (including the EXAFS-refined error for r) with the exception of one of the Mo···Mo distances for the complex with each counter ion. The largest differences between the crystallographic data for $[PPN]_3[PMo_{12}O_{40}]$ and the EXAFS-derived structural parameters for $[PPN]_3[PMo_{12}O_{40}]$ and $[NBu^n_4]_3[PMo_{12}O_{40}]$ are 0.082 Å and 0.044 Å respectively. The EXAFS-derived bond angles for the complex with the $[NBu^n_4]^+$ and $[PPN]^+$ counter ions agree with the crystallographic data for $[PPN]_3[PMo_{12}O_{40}]$ to within 10 % of the angle provided by the crystallographic data. The EXAFS-derived structural parameters also provide evidence that the Mo-O-Mo bond angles are smaller when the $[NBu^n_4]^+$ is the counter ion than when $[PPN]^+$ is the counter ion.

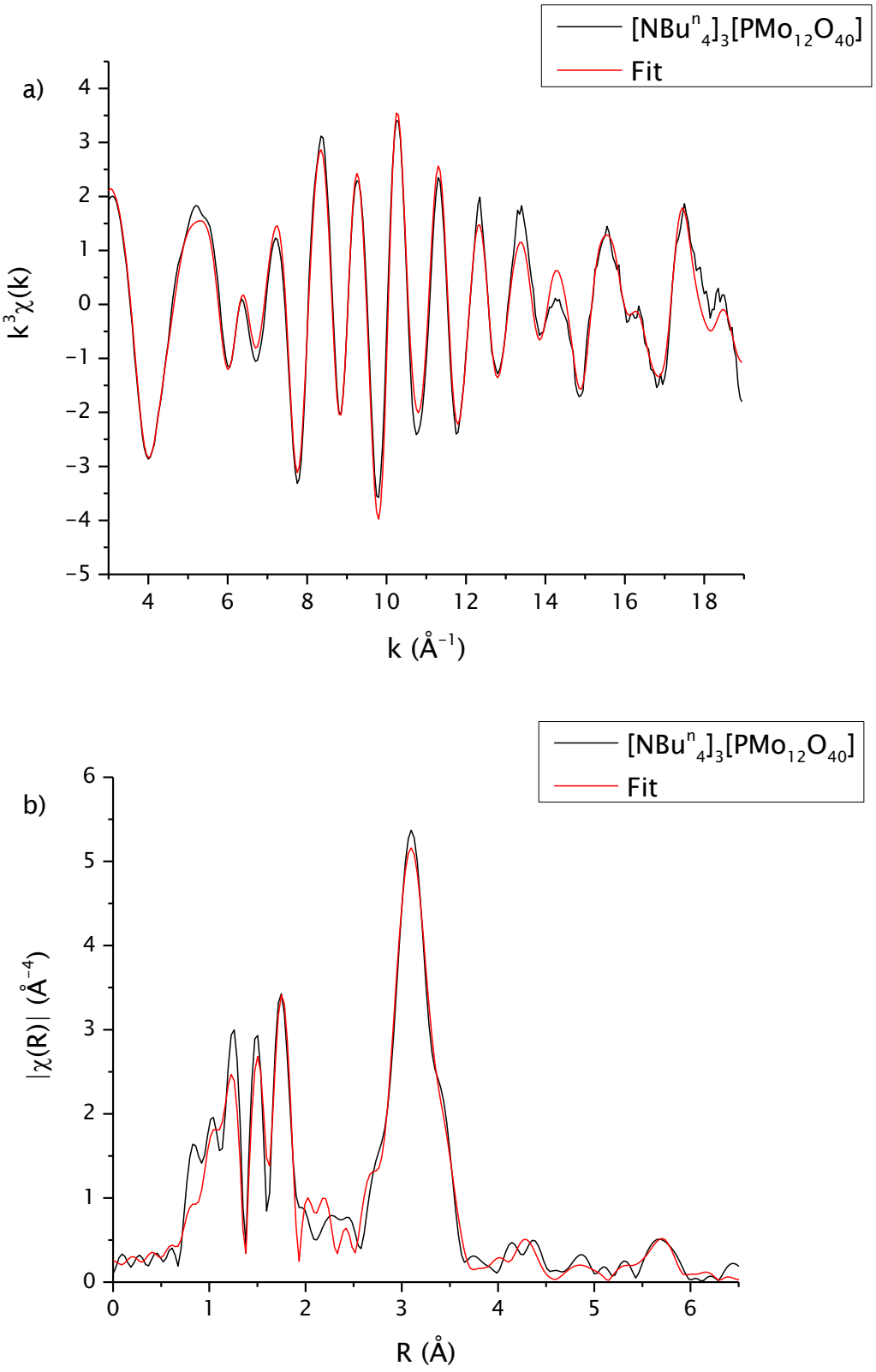

Figure 4.5: Mo K edge k^3-weighted a) EXAFS spectrum and b) Fourier transform of [Bu$^n_4$]$_3$[PMo$_{12}$O$_{40}$] in acetonitrile.

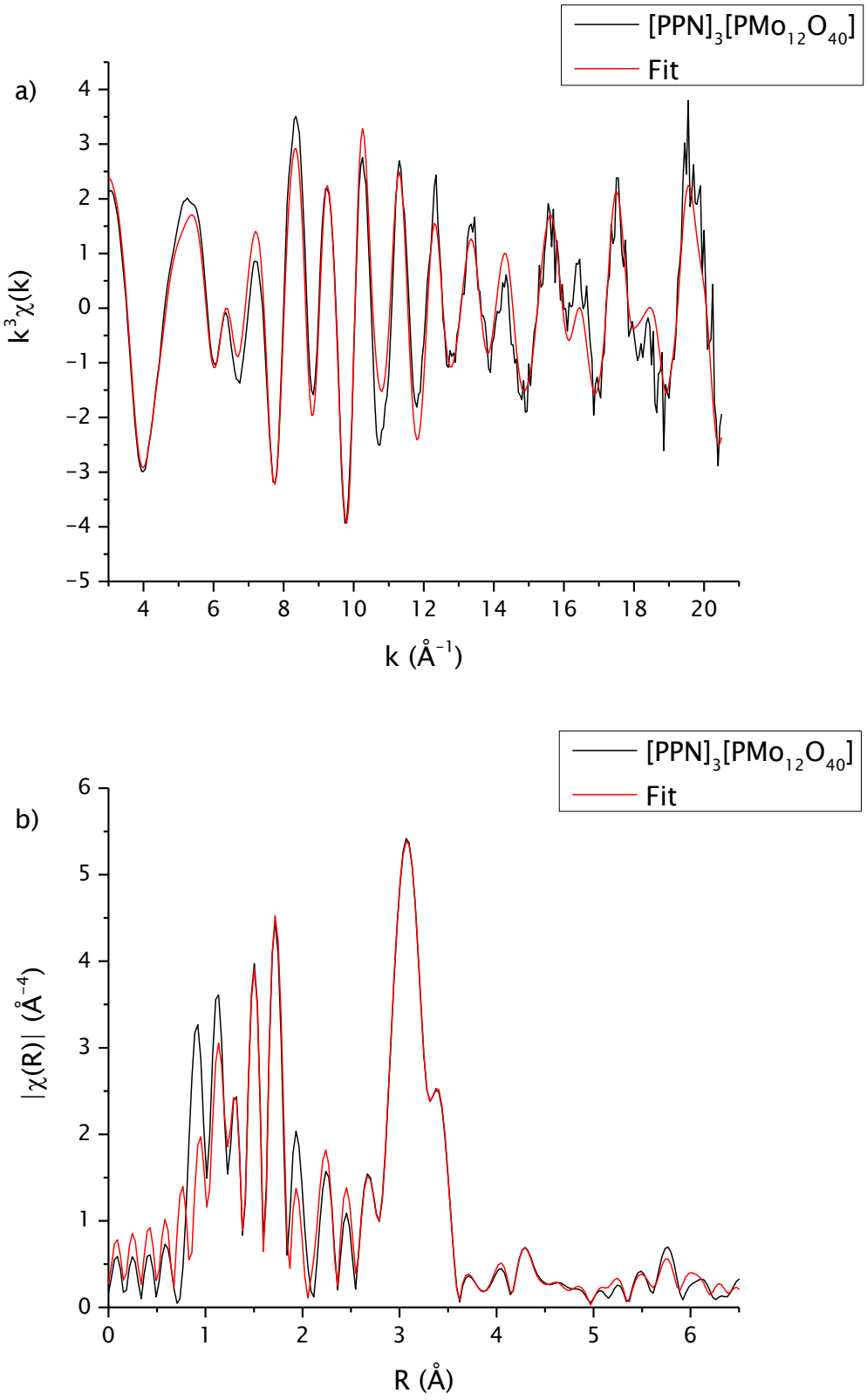

Figure 4.6: Mo K edge k^3-weighted a) EXAFS spectrum and b) Fourier transform of $[PPN]_3[PMo_{12}O_{40}]$ in acetonitrile.

Counter ion	Mo site	Path	Degeneracy	σ^2 / Å^2	r / Å	r / Å (XRD)	Error / %
$[NBu^n_4]^-$	Mo1	Mo↔O37	1	0.0020 ± 0.0004	1.700 ± 0.005	1.678	1.3
		Mo↔O18	2	0.0033 ± 0.0004	1.861 ± 0.006	1.835	1.4
		Mo↔O25	2	0.0033 ± 0.0004	2.028 ± 0.006	2.002	1.3
		Mo↔O4	1	0.0038 ± 0.0013	2.439 ± 0.013	2.423	0.7
		Mo↔Mo11	2	0.0024 ± 0.0012	3.435 ± 0.005	3.419	0.5
		Mo↔Mo2	2	0.0030 ± 0.0071	3.663 ± 0.286	3.707	1.2
		Mo↔P1	1	-0.0016 ± 0.0026	3.533 ± 0.047	3.551	0.5
		Mo↔O14	1	0.0084 ± 0.1405	3.903 ± 1.322	3.556	9.8
		Mo↔O21	2	0.0084 ± 0.1405	3.995 ± 1.322	3.648	9.5
		Mo↔O5	1	0.0015 ± 0.0298	3.951 ± 0.666	3.826	3.3
		Mo↔O2	1	0.0015 ± 0.0298	4.059 ± 0.666	3.933	3.2
		Mo↔O24	1	0.0044 ± 0.0119	3.980 ± 0.118	3.990	0.3
		Mo↔O19	1	0.0044 ± 0.0119	4.195 ± 0.118	4.206	0.2
		Mo↔O23	2	0.0044 ± 0.0119	4.547 ± 0.118	4.558	0.2
		Mo↔O41	1	0.0098 ± 0.0310	4.791 ± 0.297	4.587	4.4
		Mo↔O30	2	0.0098 ± 0.0310	4.864 ± 0.297	4.660	4.4
		Mo↔Mo6	1	0.0099 ± 0.0150	4.791 ± 0.116	4.747	0.9
		Mo↔Mo3	1	0.0099 ± 0.0150	5.324 ± 0.116	5.280	0.8
		Mo↔O15	1	0.0092 ± 0.1445	5.351 ± 0.662	4.810	11.2
		Mo↔O3	2	0.0088 ± 0.0593	5.483 ± 0.424	4.857	12.9
		Mo↔O7	3	0.0017 ± 0.0021	6.021 ± 0.030	6.020	0.0
		Mo↔Mo5	4	0.0122 ± 0.0050	6.250 ± 0.049	6.145	1.7
$[PPN]^-$	Mo1	Mo↔O37	1	0.0015 ± 0.0004	1.694 ± 0.005	1.678	1.0
		Mo↔O18	2	0.0032 ± 0.0005	1.850 ± 0.006	1.835	0.8
		Mo↔O25	2	0.0032 ± 0.0005	2.017 ± 0.006	2.002	0.7
		Mo↔O4	1	0.0031 ± 0.0013	2.442 ± 0.012	2.423	0.8
		Mo↔Mo11	2	0.0074 ± 0.0061	3.501 ± 0.023	3.419	2.4
		Mo↔Mo2	2	0.0005 ± 0.0023	3.749 ± 0.027	3.707	1.1
		Mo↔P1	1	-0.0054 ± 0.0009	3.632 ± 0.019	3.551	2.3
		Mo↔O14	1	-0.0027 ± 0.0009	3.261 ± 0.011	3.556	8.3
		Mo↔O5	1	-0.0071 ± 0.0008	3.935 ± 0.018	3.826	2.8
		Mo↔O2	1	-0.0071 ± 0.0008	4.043 ± 0.018	3.933	2.8
		Mo↔O24	1	-0.0064 ± 0.0009	3.986 ± 0.023	3.990	0.1
		Mo↔O19	1	0.0035 ± 0.0047	4.075 ± 0.059	4.206	3.1
		Mo↔O23	2	0.0035 ± 0.0047	4.427 ± 0.059	4.558	2.9
		Mo↔O41	1	0.0026 ± 0.0048	4.792 ± 0.053	4.587	4.5
		Mo↔O30	2	0.0026 ± 0.0048	4.865 ± 0.053	4.660	4.4
		Mo↔Mo6	1	0.0081 ± 0.0062	4.796 ± 0.060	4.747	1.0
		Mo↔Mo3	1	0.0081 ± 0.0062	5.329 ± 0.060	5.280	0.9
		Mo↔O15	1	-0.0005 ± 0.0028	4.597 ± 0.045	4.810	4.4
		Mo↔O3	2	0.0052 ± 0.0101	5.037 ± 0.083	4.857	3.7
		Mo↔O7	3	0.0042 ± 0.0071	6.022 ± 0.074	6.020	0.0
		Mo↔Mo5	4	0.0098 ± 0.0037	6.245 ± 0.040	6.145	1.6

Table 4.1: The Mo K edge EXAFS-derived structural parameters for $[PMo_{12}O_{40}]^{3-}$ with $[NBu^n_4]^+$ and $[PPN]^+$ as counter ions in acetonitrile compared with XRD data for $[PPN]_3[PMo_{12}O_{40}]$.

	Counter ion		
Bond Angle (°)	$[NBu^n_4]^-$	$[PPN]^-$	$[PPN]_3[PMo_{12}O_{40}]$ (XRD)
Mo1-O18-Mo12	146	160	153
Mo1-O22-Mo2	145	157	150
Mo1-O17-Mo11	130	135	125
O37-Mo1-O25	95	96	99
O37-Mo1-O18	100	99	104
O18-Mo1-O25	-	139	155
O17-Mo1-O22	-	146	156

Table 4.2: The EXAFS-derived bond angles for $[NBu^n_4]_3[PMo_{12}O_{40}]$ and $[PPN]_3[PMo_{12}O_{40}]$ in acetonitrile.

Counter ion	Edge	Parameter	Value
$[Bu^n_4]^-$ Solution	Mo K	R (%)	0.89
		R, k = 1 (%)	0.27
		R, k = 2 (%)	0.63
		R, k = 3 (%)	1.77
		Chi-square	3675
		Reduced chi-square	241
		Amplitude reduction factor	0.79 ± 0.04
		k range ($Å^{-1}$)	3.0 - 18.95
		R range (Å)	1.0 - 6.5
		No. of independent parameters	55
		No. of variables	40
$[PPN]^-$ Solution	Mo K	R (%)	1.33
		R, k = 1 (%)	0.34
		R, k = 2 (%)	1.06
		R, k = 3 (%)	2.59
		Chi-square	993
		Reduced chi-square	60
		Amplitude reduction factor	0.80 ± 0.05
		k range ($Å^{-1}$)	3.0 - 20.5
		R range (Å)	1.0 - 6.5
		No. of independent parameters	60
		No. of variables	44

Table 4.3: Refined parameters for fits to the Mo K edge of $[PMo_{12}O_{40}]^{3-}$ with $[NBu^n_4]^-$ and $[PPN]^-$ as counter ions in acetonitrile.

4.2.2 Effects of Reduction on the Structure of $[NBu^n_4]_3[PMo_{12}O_{40}]$

Electrons can be added to the $[PMo_{12}O_{40}]^{3-}$ core POM structure. To determine what structural differences are caused in the core POM by the addition of electrons, $[PMo_{12}O_{40}]^{3-}$ with different reducing ions, and different amounts of these ions have been studied. EXAFS spectroscopy has been used to characterise $[NBu^n_4]_3[PMo_{12}O_{40}H_2]$, $[NBu^n_4]_3[PMo_{12}O_{40}H_4]$, $[NBu^n_4]_3[PMo_{12}O_{40}Na_2]$ and $[NBu^n_4]_3[PMo_{12}O_{40}Na_4]$ in acetonitrile.

The crystallographic data for $[NBu^n_4]_3[PMo_{12}O_{40}H_2]$ has an asymmetric structure. The hydrogen atoms are not shown in the figure. As the EXAFS spectra were recorded with the sample in acetonitrile, a higher symmetry model was selected for use in the curve-fitting analysis. The FeCl groups were removed from the crystallographic data for $[PMo_{12}O_{40}(FeCl)_2]^{4-}$ and the resulting $[PMo_{12}O_{40}]^{3-}$ with higher symmetry was fit to the spectra for the 4 reduced molybdate species. This $[PMo_{12}O_{40}]$ structure is given in figure 4.7. The hydrogen and sodium atoms would have little impact on the spectra and so have not been included in the curve-fitting analyses. This crystallographic data has been fitted to spectra for $[NBu^n_4]_3[PMo_{12}O_{40}H_2]$, $[NBu^n_4]_3[PMo_{12}O_{40}H_4]$, $[NBu^n_4]_3[PMo_{12}O_{40}Na_2]$ and $[NBu^n_4]_3[PMo_{12}O_{40}Na_4]$ in acetonitrile and the EXAFS spectra and Fourier transforms for these 4 POMs are presented in figures 4.8 – 4.11. The EXAFS-derived structural parameters for these anions in acetonitrile are presented in tables 4.4 – 4.7. Bond angles which have been calculated for the complexes using the EXAFS-derived structural parameters are presented in table 4.8. Data regarding the quality of these fits are presented in table 4.9.

The EXAFS derived Mo-O distances for $[NBu^n_4]_3[PMo_{12}O_{40}H_2]$ are in good agreement with the crystallographic data, but the Mo···Mo distances are 0.07 Å shorter in the EXAFS-derived structural parameters than in the crystallographic data. The Mo-O-Mo bond angles are larger and the O-Mo-O bond angles are smaller in the POMs reduced by Na^+ than the POMs reduced by H^+. In the reduced POMs the average Mo···Mo distances are shorter than in unreduced POMs. Bond angles for the Keggin-type POMs have been derived using the EXAFS data by including multiple scattering paths in the fits. The Mo-O-Mo angles are smaller in the POMs reduced by H^+ than in the unreduced POMs. In

the POMs reduced by Na^+ the Mo-O-Mo angles are larger than in the unreduced POMs. The shorter Mo···Mo distances in the reduced POMs and smaller Mo-O-Mo bond angles in the POMs reduced by H^+ could suggest that Mo-Mo bonds have been formed.

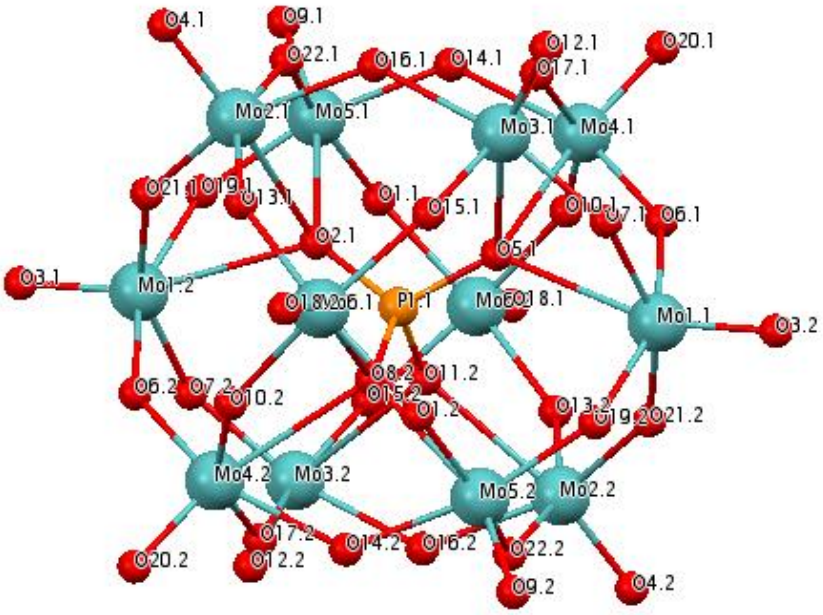

Figure 4.7: Structure of the symmetrical $[PMo_{12}O_{40}]$ anion used to model the anions in curve-fitting analyses.

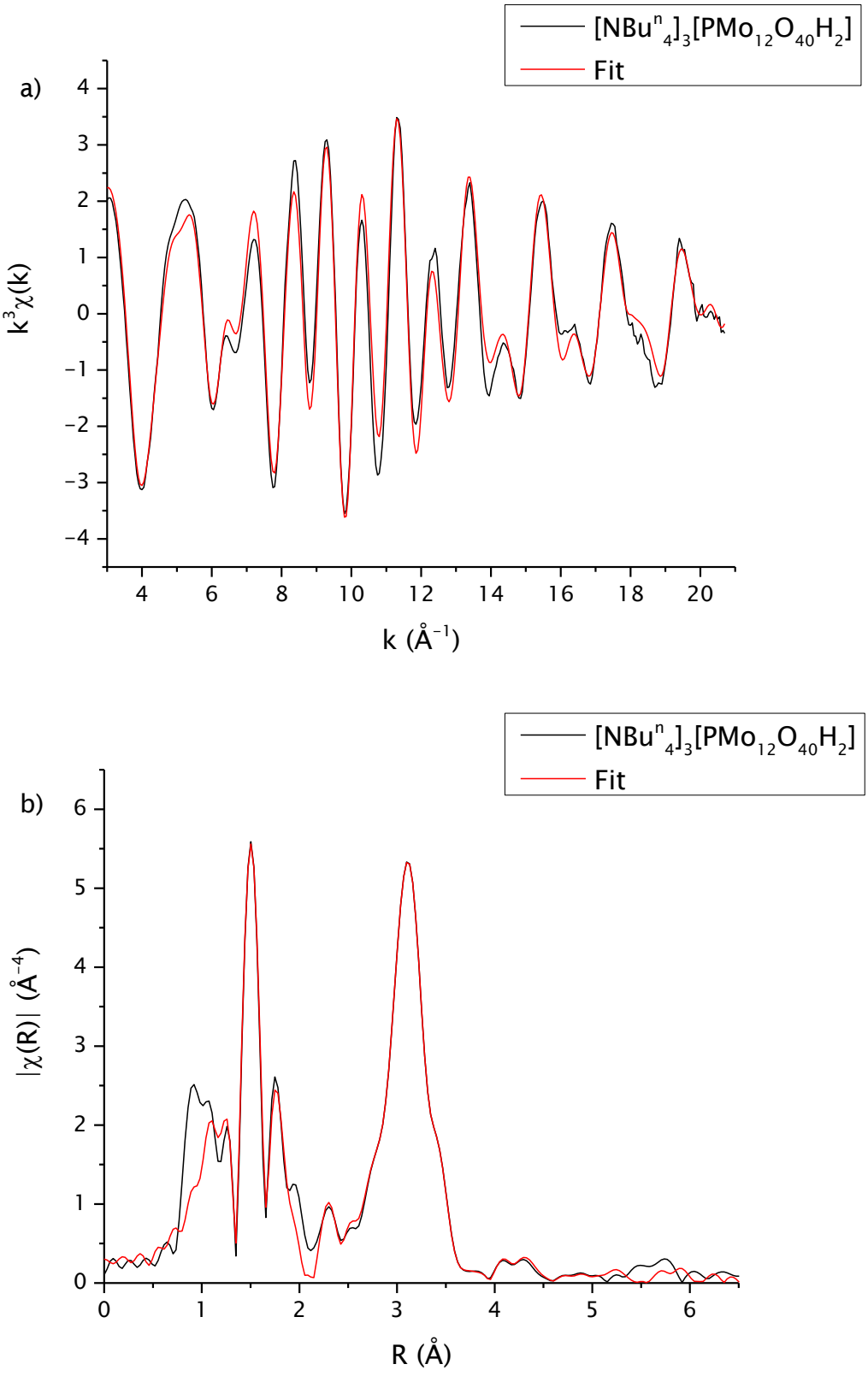

Figure 4.8: Mo K edge k^3-weighted a) EXAFS spectrum and b) Fourier transform of [NBu$^n_4$]$_3$[PMo$_{12}$O$_{40}$H$_2$] in acetonitrile.

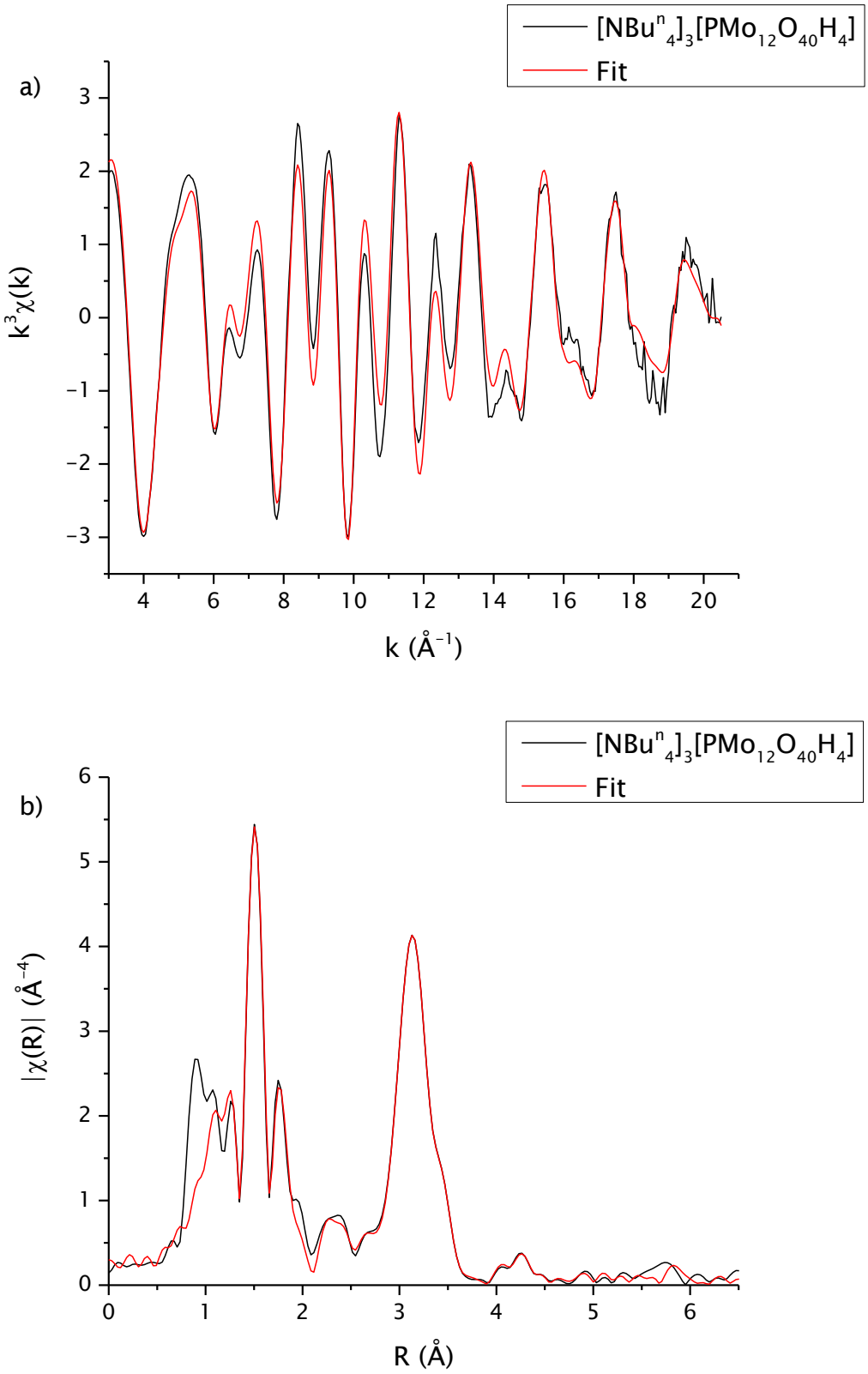

Figure 4.9: Mo K edge k³-weighted a) EXAFS spectrum and b) Fourier transform of [NBu$^n_4$]$_3$[PMo$_{12}$O$_{40}$H$_4$] in acetonitrile.

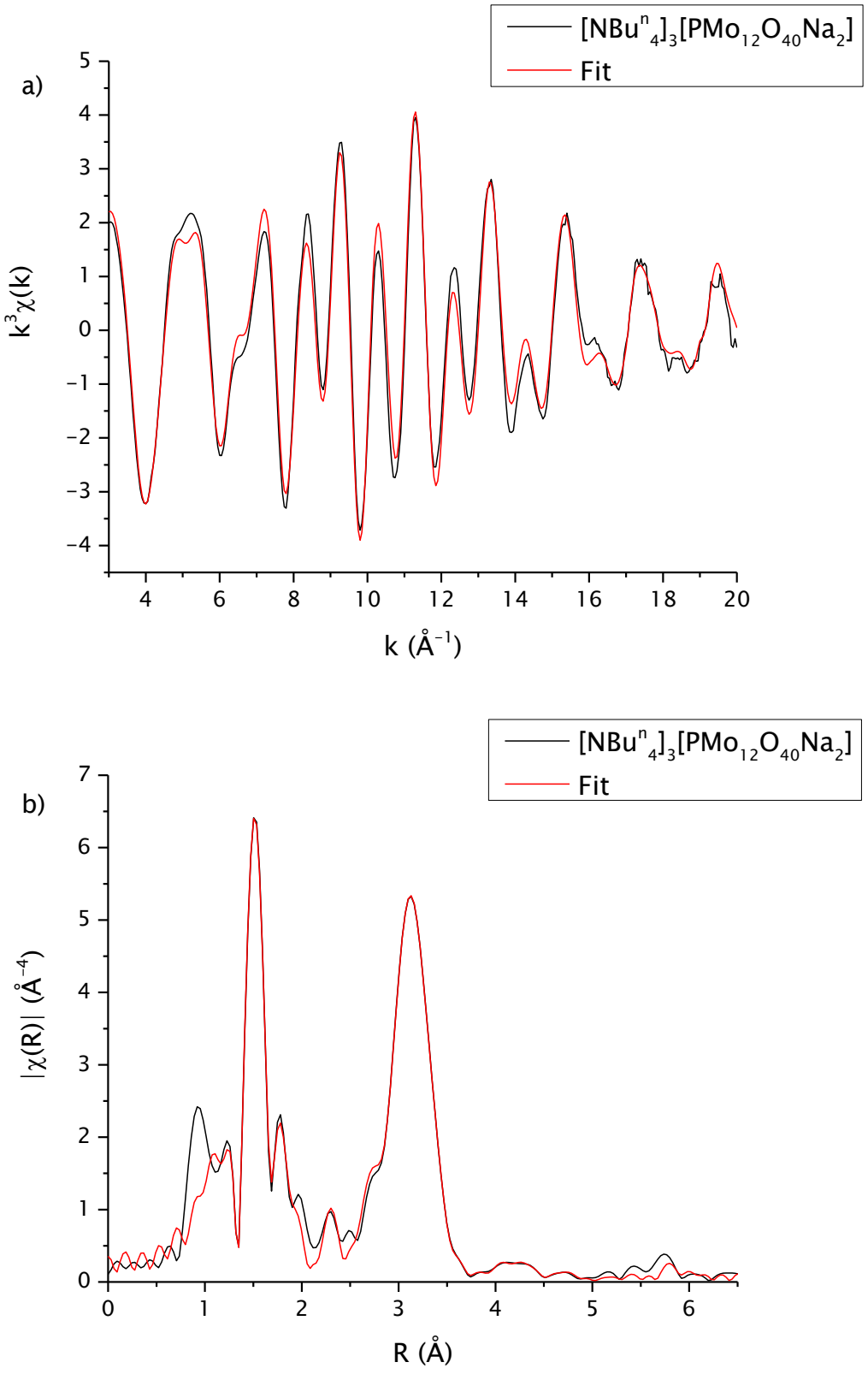

Figure 4.10: Mo K edge k^3-weighted a) EXAFS spectrum and b) Fourier transform of [NBu$^n_4$]$_3$[PMo$_{12}$O$_{40}$Na$_2$] in acetonitrile.

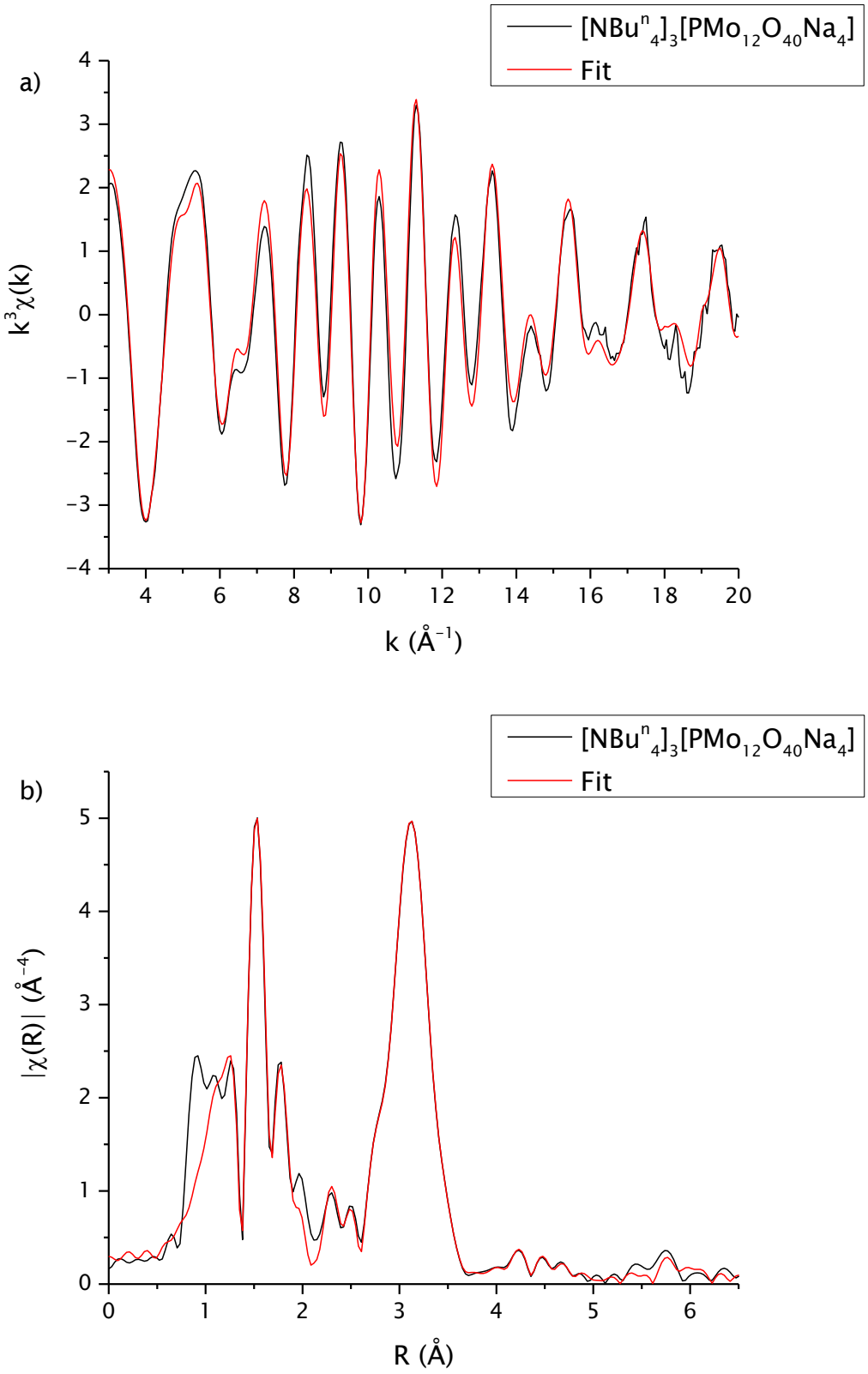

Figure 4.11: Mo K edge k³-weighted a) EXAFS spectrum and b) Fourier transform of [NBu$^n_4$]$_3$[PMo$_{12}$O$_{40}$Na$_4$] in acetonitrile.

Mo site	Path	Degeneracy	σ^2 / Å^2	r / Å	r / Å (XRD)	Error / %
Mo2.1	Mo↔O4.1	1	0.0016 ± 0.0003	1.696 ± 0.004	1.661	2.1
	Mo↔O21.1	2	0.0013 ± 0.0005	1.853 ± 0.006	1.829	1.3
	Mo↔O22.1	2	0.0030 ± 0.0006	2.063 ± 0.008	2.029	1.7
	Mo↔O2.1	1	0.0026 ± 0.0017	2.480 ± 0.016	2.547	2.6
	Mo↔Mo6.1	2	0.0032 ± 0.0022	3.479 ± 0.023	3.547	1.9
	Mo↔Mo3.1	2	0.0032 ± 0.0022	3.658 ± 0.023	3.727	1.9
	Mo↔P1.1	1	-0.0033 ± 0.0029	3.568 ± 0.036	3.578	0.3
	Mo↔O15.1	2	-0.0016 ± 0.0106	3.523 ± 0.084	3.628	2.9
	Mo↔O8.2	1	0.0159 ± 0.1011	4.070 ± 0.412	3.938	3.4
	Mo↔O5.1	3	0.0159 ± 0.1011	4.176 ± 0.412	3.043	37.2
	Mo↔O17.1	2	0.0035 ± 0.0075	4.295 ± 0.094	4.150	3.5
	Mo↔O18.2	2	0.0106 ± 0.0498	4.496 ± 0.294	4.598	2.2
	Mo↔O12.1	2	0.0106 ± 0.0498	4.662 ± 0.294	4.764	2.1
	Mo↔Mo4.2	1	0.0029 ± 0.0018	4.859 ± 0.033	4.860	0.0
	Mo↔Mo4.1	1	0.0029 ± 0.0018	5.269 ± 0.033	5.270	0.0
	Mo↔O1.2	2	-0.0030 ± 0.0020	5.056 ± 0.035	5.132	1.5
	Mo↔O7.1	2	-0.0030 ± 0.0020	5.156 ± 0.035	5.232	1.5
	Mo↔Mo1.1	2	0.0139 ± 0.009	6.273 ± 0.090	6.290	0.3
Mo1.1	Mo↔O3.2	1	0.0016 ± 0.0003	1.691 ± 0.004	1.656	2.1
	Mo↔O6.1	4	0.0013 ± 0.0005	1.951 ± 0.006	1.927	1.2
	Mo↔O5.1	1	0.0026 ± 0.0017	2.353 ± 0.016	2.421	2.8
	Mo↔Mo3.1	4	0.0032 ± 0.0022	3.477 ± 0.023	3.545	1.9
	Mo↔P1.1	1	-0.0033 ± 0.0029	3.626 ± 0.036	3.636	0.3
	Mo↔O22.2	2	-0.0016 ± 0.0106	3.625 ± 0.084	3.730	2.8
	Mo↔O11.2	1	0.0159 ± 0.1011	4.039 ± 0.412	3.907	3.4
	Mo↔O15.1	3	0.0035 ± 0.0075	4.341 ± 0.094	4.196	3.5
	Mo↔O4.2	2	0.0106 ± 0.0498	4.520 ± 0.294	4.621	2.2
	Mo↔Mo6.1	2	0.0029 ± 0.0018	5.152 ± 0.033	5.152	0.0
	Mo↔O16.1	2	-0.0030 ± 0.0020	5.103 ± 0.035	5.179	1.5
	Mo↔Mo2.1	1	0.0139 ± 0.009	6.270 ± 0.090	6.287	0.3

Table 4.4: The EXAFS-derived structural parameters for $[NBu^n_4]_3[PMo_{12}O_{40}H_2]$ in acetonitrile at the Mo K edge. XRD data for $[PMo_{12}O_{40}(FeCl)_2]^{4-}$ is provided for comparison.

Mo site	Path	Degeneracy	σ^2 / Å^2	r / Å	r / Å (XRD)	Error / %
Mo2.1	Mo↔O4.1	1	0.0012 ± 0.0002	1.694 ± 0.003	1.661	2.0
	Mo↔O21.1	2	0.0022 ± 0.0005	1.852 ± 0.005	1.829	1.3
	Mo↔O22.1	2	0.0039 ± 0.0006	2.059 ± 0.008	2.029	1.5
	Mo↔O2.1	1	0.0021 ± 0.0012	2.470 ± 0.012	2.547	3.0
	Mo↔Mo6.1	2	0.0021 ± 0.0007	3.485 ± 0.011	3.547	1.7
	Mo↔Mo3.1	2	0.0021 ± 0.0007	3.665 ± 0.011	3.727	1.7
	Mo↔P1.1	1	-0.0022 ± 0.0023	3.608 ± 0.037	3.578	0.8
	Mo↔O15.1	2	-0.0055 ± 0.0008	3.443 ± 0.013	3.628	5.1
	Mo↔O8.2	1	0.0100 ± 0.0163	3.888 ± 0.070	3.938	1.3
	Mo↔O5.1	3	0.0100 ± 0.0163	3.994 ± 0.070	3.043	31.3
	Mo↔O17.1	2	0.0046 ± 0.0036	4.221 ± 0.048	4.150	1.7
	Mo↔O18.2	2	0.0032 ± 0.0023	4.376 ± 0.041	4.598	4.8
	Mo↔O12.1	2	0.0032 ± 0.0023	4.542 ± 0.041	4.764	4.7
	Mo↔Mo4.2	1	0.0192 ± 0.0213	4.942 ± 0.156	4.860	1.7
	Mo↔Mo4.1	1	0.0192 ± 0.0213	5.352 ± 0.156	5.270	1.6
	Mo↔O1.2	2	0.0235 ± 0.0354	5.366 ± 0.175	5.132	4.6
	Mo↔O7.1	2	0.0235 ± 0.0354	5.466 ± 0.175	5.232	4.5
	Mo↔Mo1.1	2	0.0131 ± 0.0061	6.266 ± 0.058	6.290	0.4
Mo1.1	Mo↔O3.2	1	0.0012 ± 0.0002	1.689 ± 0.003	1.656	2.0
	Mo↔O6.1	4	0.0022 ± 0.0005	1.950 ± 0.005	1.927	1.2
	Mo↔O5.1	1	0.0021 ± 0.0012	2.344 ± 0.012	2.421	3.2
	Mo↔Mo3.1	4	0.0021 ± 0.0007	3.483 ± 0.011	3.545	1.7
	Mo↔P1.1	1	-0.0022 ± 0.0023	3.666 ± 0.037	3.636	0.8
	Mo↔O22.2	2	-0.0055 ± 0.0008	3.545 ± 0.013	3.730	5.0
	Mo↔O11.2	2	0.0100 ± 0.0163	3.857 ± 0.070	3.907	1.3
	Mo↔O15.1	4	0.0046 ± 0.0036	4.268 ± 0.048	4.196	1.7
	Mo↔O4.2	4	0.0032 ± 0.0023	4.400 ± 0.041	4.621	4.8
	Mo↔Mo6.1	2	0.0192 ± 0.0213	5.234 ± 0.156	5.152	1.6
	Mo↔O16.1	3	0.0235 ± 0.0354	5.413 ± 0.175	5.179	4.5
	Mo↔Mo2.1	3	0.0131 ± 0.0061	6.263 ± 0.058	6.287	0.4

Table 4.5: The EXAFS-derived structural parameters for $[NBu^n_4]_3[PMo_{12}O_{40}H_4]$ in acetonitrile at the Mo K edge. XRD data for $[PMo_{12}O_{40}(FeCl)_2]^{4-}$ is provided for comparison.

Mo site	Path	Degeneracy	σ^2 / Å^2	r / Å	r / Å (XRD)	Error / %
Mo2.1	Mo↔O4.1	1	0.0022 ± 0.0003	1.709 ± 0.004	1.661	2.9
	Mo↔O21.1	2	0.0006 ± 0.0004	1.871 ± 0.005	1.829	2.3
	Mo↔O22.1	2	0.0036 ± 0.0006	2.075 ± 0.009	2.029	2.3
	Mo↔O2.1	1	0.0005 ± 0.0009	2.472 ± 0.010	2.547	2.9
	Mo↔Mo6.1	2	0.0063 ± 0.0138	3.446 ± 0.061	3.547	2.8
	Mo↔Mo3.1	2	0.0201 ± 0.0251	3.800 ± 0.264	3.727	2.0
	Mo↔P1.1	1	0.0006 ± 0.0119	3.655 ± 0.101	3.578	2.2
	Mo↔O15.1	2	-0.0069 ± 0.0013	3.462 ± 0.027	3.628	4.6
	Mo↔O8.2	1	0.0156 ± 0.0346	3.745 ± 0.117	3.938	4.9
	Mo↔O5.1	3	0.0156 ± 0.0346	3.851 ± 0.117	3.043	26.6
	Mo↔O17.1	2	0.0104 ± 0.0299	3.912 ± 0.175	4.150	5.7
	Mo↔O18.2	2	0.0012 ± 0.0016	4.496 ± 0.041	4.598	2.2
	Mo↔O12.1	2	0.0012 ± 0.0016	4.662 ± 0.041	4.764	2.1
	Mo↔Mo4.2	1	0.0042 ± 0.0033	4.899 ± 0.051	4.860	0.8
	Mo↔Mo4.1	1	0.0101 ± 0.0087	5.357 ± 0.094	5.270	1.7
	Mo↔O1.2	2	-0.0001 ± 0.0032	5.107 ± 0.049	5.132	0.5
	Mo↔O7.1	2	-0.0001 ± 0.0032	5.207 ± 0.049	5.232	0.5
	Mo↔Mo1.1	2	0.0130 ± 0.0058	6.288 ± 0.056	6.290	0.0
Mo1.1	Mo↔O3.2	1	0.0022 ± 0.0003	1.704 ± 0.004	1.656	2.9
	Mo↔O6.1	4	0.0006 ± 0.0004	1.969 ± 0.005	1.927	2.2
	Mo↔O5.1	1	0.0005 ± 0.0009	2.346 ± 0.011	2.421	3.1
	Mo↔Mo3.1	4	0.0063 ± 0.0138	3.444 ± 0.008	3.545	2.8
	Mo↔P1.1	1	0.0006 ± 0.0119	3.713 ± 0.101	3.636	2.1
	Mo↔O22.2	2	-0.0069 ± 0.0013	3.564 ± 0.027	3.730	4.5
	Mo↔O11.2	2	0.0156 ± 0.0346	3.714 ± 0.117	3.907	4.9
	Mo↔O15.1	4	0.0156 ± 0.0346	4.004 ± 0.117	4.196	4.6
	Mo↔O4.2	4	0.0104 ± 0.0299	4.384 ± 0.175	4.621	5.1
	Mo↔Mo6.1	2	0.0042 ± 0.0033	5.192 ± 0.051	5.152	0.8
	Mo↔O16.1	3	-0.0001 ± 0.0032	5.154 ± 0.049	5.179	0.5
	Mo↔Mo2.1	3	0.0130 ± 0.0058	6.285 ± 0.056	6.287	0.0

Table 4.6: The EXAFS-derived structural parameters for $[NBu^n_4]_3[PMo_{12}O_{40}Na_2]$ in acetonitrile at the Mo K edge. XRD data for $[PMo_{12}O_{40}(FeCl)_2]^{4-}$ is provided for comparison.

Mo site	Path	Degeneracy	σ^2 / Å^2	r / Å	r / Å (XRD)	Error / %
Mo2.1	Mo↔O4.1	1	0.0017 ± 0.0003	1.710 ± 0.006	1.661	3.0
	Mo↔O21.1	2	0.0013 ± 0.0005	1.855 ± 0.007	1.829	1.4
	Mo↔O22.1	2	0.0034 ± 0.0007	2.060 ± 0.010	2.029	1.5
	Mo↔O2.1	1	0.0012 ± 0.0013	2.474 ± 0.016	2.547	2.9
	Mo↔Mo6.1	2	0.0009 ± 0.0045	3.464 ± 0.029	3.547	2.3
	Mo↔Mo3.1	2	0.0063 ± 0.0400	3.558 ± 0.192	3.727	4.5
	Mo↔P1.1	1	-0.0040 ± 0.0024	3.591 ± 0.062	3.578	0.4
	Mo↔O15.1	2	-0.0067 ± 0.0013	3.429 ± 0.015	3.628	5.5
	Mo↔O8.2	1	0.0005 ± 0.0022	3.831 ± 0.052	3.938	2.7
	Mo↔O5.1	3	0.0005 ± 0.0022	3.937 ± 0.052	4.043	2.6
	Mo↔O17.1	2	0.0043 ± 0.0056	4.380 ± 0.098	4.150	5.5
	Mo↔O18.2	2	0.0014 ± 0.0024	4.550 ± 0.056	4.598	1.0
	Mo↔O12.1	2	0.0014 ± 0.0024	4.716 ± 0.056	4.764	1.0
	Mo↔Mo4.2	1	0.0050 ± 0.0045	4.817 ± 0.056	4.860	0.9
	Mo↔Mo4.1	1	0.0124 ± 0.0212	5.150 ± 0.143	5.270	2.3
	Mo↔O1.2	2	0.0034 ± 0.0061	5.011 ± 0.052	5.132	2.4
	Mo↔O7.1	2	0.0034 ± 0.0061	5.111 ± 0.052	5.232	2.3
	Mo↔Mo1.1	2	0.0113 ± 0.0046	6.244 ± 0.047	6.290	0.7
Mo1.1	Mo↔O3.2	1	0.0017 ± 0.0003	1.705 ± 0.006	1.656	3.0
	Mo↔O6.1	4	0.0013 ± 0.0005	1.954 ± 0.007	1.927	1.4
	Mo↔O5.1	1	0.0012 ± 0.0013	2.347 ± 0.016	2.421	3.1
	Mo↔Mo3.1	4	0.0009 ± 0.0045	3.461 ± 0.029	3.545	2.4
	Mo↔P1.1	1	-0.0040 ± 0.0024	3.649 ± 0.062	3.636	0.4
	Mo↔O22.2	2	-0.0067 ± 0.0013	3.531 ± 0.015	3.730	5.3
	Mo↔O11.2	2	0.0005 ± 0.0022	3.800 ± 0.052	3.907	2.7
	Mo↔O15.1	4	0.0043 ± 0.0056	4.427 ± 0.098	4.196	5.5
	Mo↔O4.2	4	0.0014 ± 0.0024	4.574 ± 0.056	4.621	1.0
	Mo↔Mo6.1	2	0.0124 ± 0.0212	5.032 ± 0.143	5.152	2.3
	Mo↔O16.1	3	0.0034 ± 0.0061	5.058 ± 0.052	5.179	2.3
	Mo↔Mo2.1	3	0.0113 ± 0.0046	6.242 ± 0.047	6.287	0.7

Table 4.7: The EXAFS-derived structural parameters for $[NBu^n_4]_3[PMo_{12}O_{40}Na_4]$ in acetonitrile at the Mo K edge. XRD data for $[PMo_{12}O_{40}(FeCl)_2]^{4-}$ is provided for comparison.

	Anion				
Bond Angle (°)	$[PMo_{12}O_{40}H_2]^{3-}$	$[PMo_{12}O_{40}H_4]^{3-}$	$[PMo_{12}O_{40}Na_2]^{3-}$	$[PMo_{12}O_{40}Na_4]^{3-}$	$[PMo_{12}O_{40}(FeCl)_2]^{4-}$ (XRD)
Mo2.1-O13.1-Mo6.1	121	131	160	154	142
Mo2.1-O22.1-Mo5.1	116	125	-	134	134
Mo1.1-O6.1-Mo4.1	-	131	159	152	142
O22.1-Mo2.1-O13.1	163	144	170	140	154
O7.1-Mo1.1-O21.1	168	145	155	140	155
O4.1-Mo2.1-O21.1	98	93	89	88	102
O4.1-Mo2.1-O22.1	96	92	86	87	101
O3.2-Mo1.1-O21.2	98	94	89	88	102
O2.1-Mo2.1-O21.1	63	61	73	60	66
O5.1-Mo1.1-O7.1	62	60	71	60	65
O22.1-Mo2.1-O21.1	93	-	-	-	89
O22.1-Mo2.1-O16.1	79	-	-	83	76
O6.1-Mo1.1-O7.1	91	-	-	95	87

Table 4.8: The EXAFS-derived bond angles for $[NBu^n_4]_3[PMo_{12}O_{40}X_n]$ in acetonitrile. XRD data for $[PMo_{12}O_{40}(FeCl)_2]^{4-}$ is provided for comparison.

Anion	Edge	Parameter	Value
$[PMo_{12}O_{40}H_2]^{3-}$ Solution	Mo K	R (%)	0.72
		R, k = 1 (%)	0.28
		R, k = 2 (%)	0.55
		R, k = 3 (%)	1.33
		Chi-square	5792
		Reduced chi-square	377
		Amplitude reduction factor	0.86 ± 0.06
		k range ($Å^{-1}$)	3.0 - 20.7
		R range (Å)	1.0 - 6.5
		No. of independent parameters	61
		No. of variables	46
$[PMo_{12}O_{40}H_4]^{3-}$ Solution	Mo K	R (%)	0.65
		R, k = 1 (%)	0.18
		R, k = 2 (%)	0.44
		R, k = 3 (%)	1.34
		Chi-square	1930
		Reduced chi-square	103
		Amplitude reduction factor	0.85 ± 0.05
		k range ($Å^{-1}$)	3.0 - 20.5
		R range (Å)	1.0 - 6.5
		No. of independent parameters	60
		No. of variables	42
$[PMo_{12}O_{40}Na_2]^{3-}$ Solution	Mo K	R (%)	0.28
		R, k = 1 (%)	0.19
		R, k = 2 (%)	0.21
		R, k = 3 (%)	0.45
		Chi-square	1273
		Reduced chi-square	117
		Amplitude reduction factor	0.91 ± 0.05
		k range ($Å^{-1}$)	3.0 - 20.0
		R range (Å)	1.0 - 6.5
		No. of independent parameters	58
		No. of variables	48
$[PMo_{12}O_{40}Na_4]^{3-}$ Solution	Mo K	R (%)	0.48
		R, k = 1 (%)	0.28
		R, k = 2 (%)	0.37
		R, k = 3 (%)	0.79
		Chi-square	2636
		Reduced chi-square	204
		Amplitude reduction factor	0.85 ± 0.06
		k range ($Å^{-1}$)	3.0 - 20.0
		R range (Å)	1.0 - 6.5
		No. of independent parameters	58
		No. of variables	46

Table 4.9: Refined parameters for fits to $[NBu^n_4]_3[PMo_{12}O_{40}X_n]^{3-}$ in acetonitrile.

4.2.3 QEXAFS Study of $[NBu_4]_3[PMo_{12}O_{40}(VO)_2]$

EXAFS spectroscopy has been used to characterise $[NBu_4]_3[PMo_{12}O_{40}(VO)_2]$ (figure 4.12) in acetonitrile. The V K edge EXAFS spectrum for this cluster is presented in figure 4.13 to demonstrate the amount and quality of data that has been collected. Data up to 14 $Å^{-1}$ has been used in the curve-fitting analysis. Crystallographic data for $[PMo_{12}O_{40}(FeCl)_2]^{4-}$ with the FeCl groups replaced with VO groups was fitted to the Mo K and V K edge spectra for $[NBu_4]_3[PMo_{12}O_{40}(VO)_2]$ in acetonitrile.

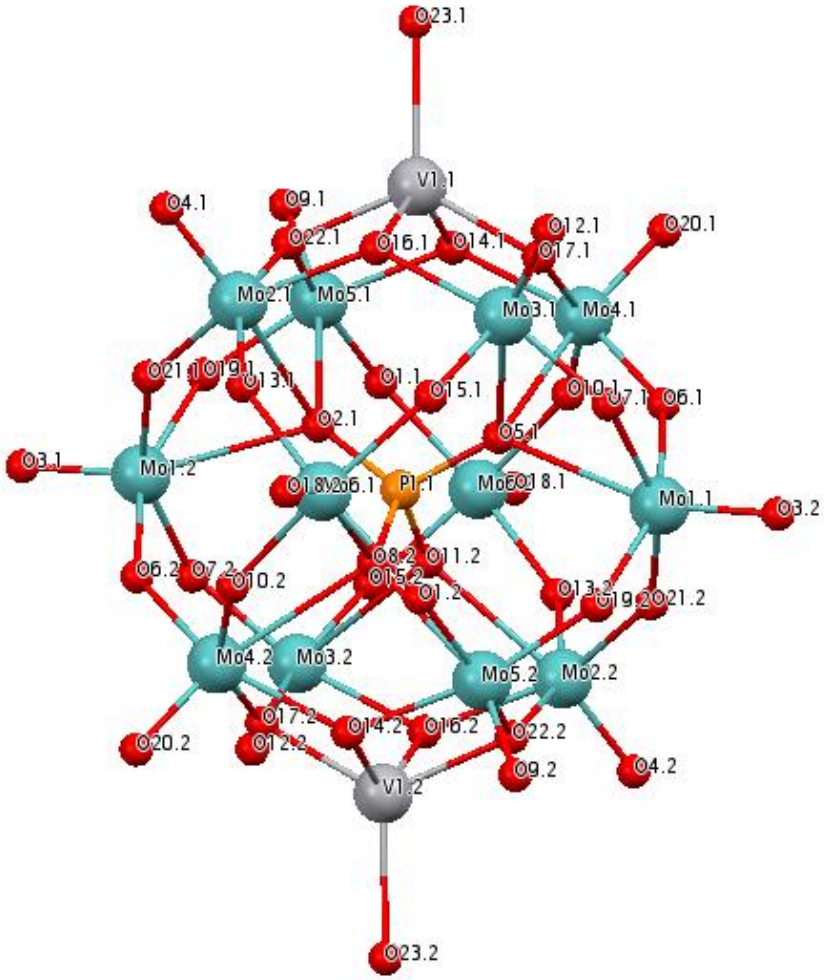

Figure 4.12: Structure of $[PMo_{12}O_{40}(VO)_2]^{3-}$.

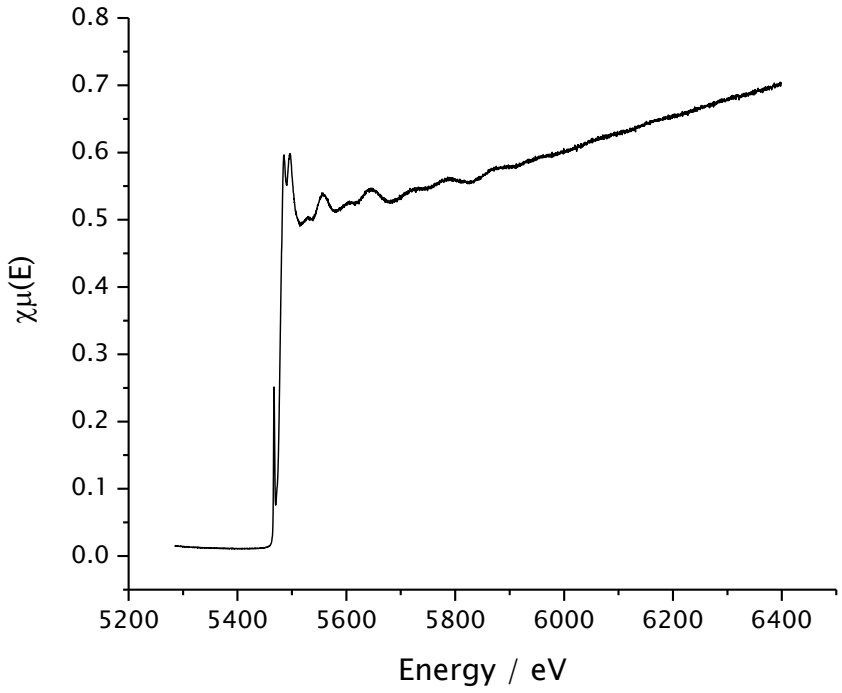

Figure 4.13: V K edge EXAFS spectrum for $[NBu^n_4]_3[PMo_{12}O_{40}(VO)_2]$.

All the EXAFS derived interatomic distances are within 0.2 Å of the analogous distance in the crystallographic data for $[PMo_{12}O_{40}(FeCl)_2]^{4-}$. The bond angles calculated using the EXAFS derived structural parameters vary to significantly from the crystallographic data for $[PMo_{12}O_{40}(FeCl)_2]^{4-}$. The bond angles calculated using the EXAFS derived structural parameters, for the most part, are smaller than the angles in the crystallographic data. The angle with the largest difference is 24 ° smaller in the EXAFS-derived structural parameters than the analogous bond angle in the crystallographic data. The Mo K edge and V K edge EXAFS spectra and Fourier transforms for this model are presented in figures 4.14 and 4.15 respectively. The EXAFS-derived structural parameters for $[NBu_4]_3[PMo_{12}O_{40}(VO)_2]$ in acetonitrile are presented in table 4.10. Bond angles that have been calculated for the complexes using the EXAFS-derived structural parameters are presented in table 4.11. Data regarding the quality of both of these fits are presented in table 4.12.

In the Fourier transform for the V K edge EXAFS of $[NBu_4]_3[PMo_{12}O_{40}(VO)_2]$ there is a peak below 1.0 Å that does not appear to be well refined in the fit. This peak can be removed from the data by increasing the removal of background from 1.0 Å to 1.3 Å. However, a curve-fitting analysis with this background removal causes the terminal oxygen on the vanadium to be refined with a negative Debye-Waller factor. This peak below 1.0 Å in the data is required to give a fit for this complex.

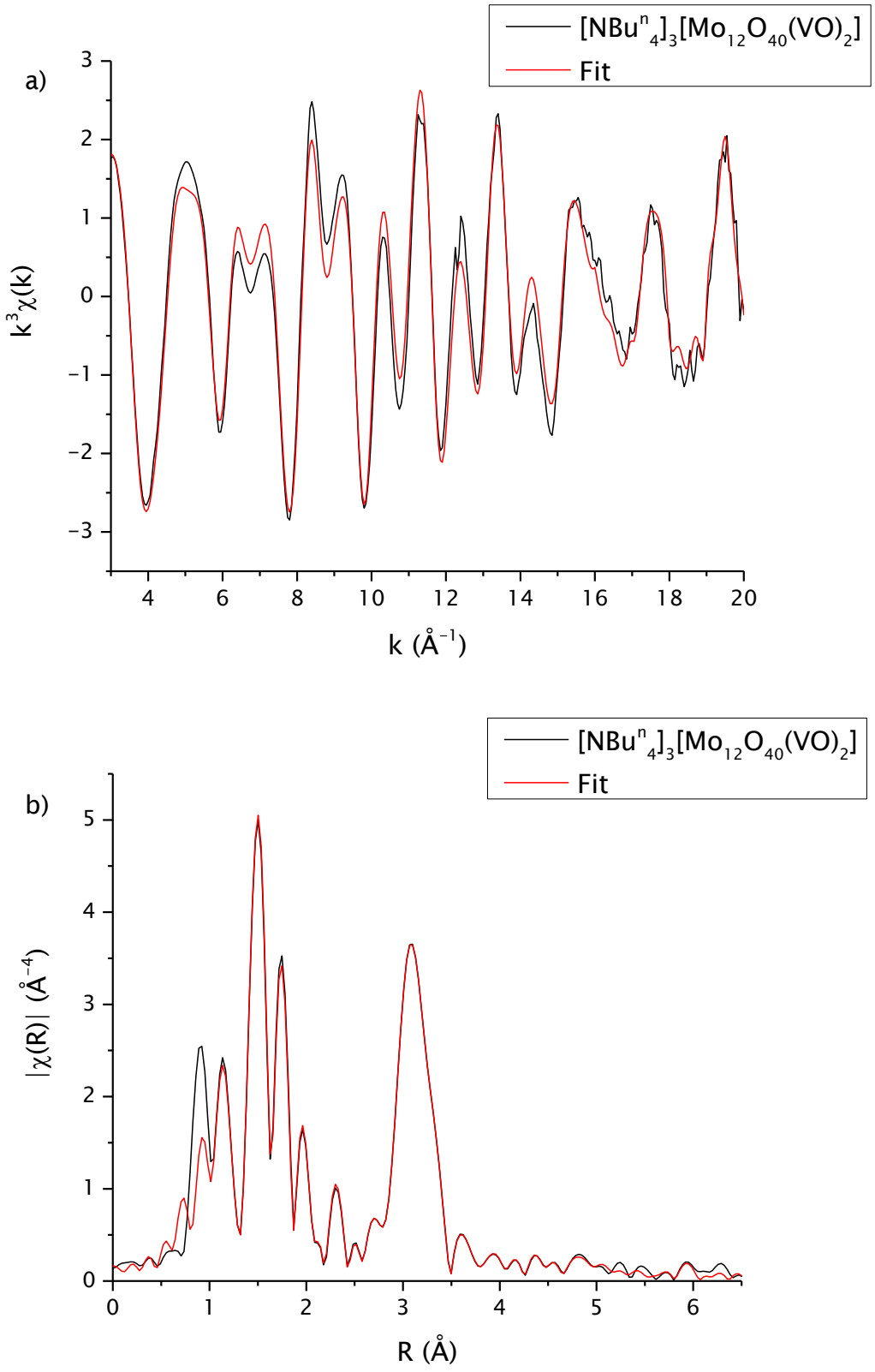

Figure 4.14: Mo K edge k³-weighted a) EXAFS spectrum and b) Fourier transform of [NBu$^n_4$]$_3$[Mo$_{12}$O$_{40}$(VO)$_2$] in acetonitrile.

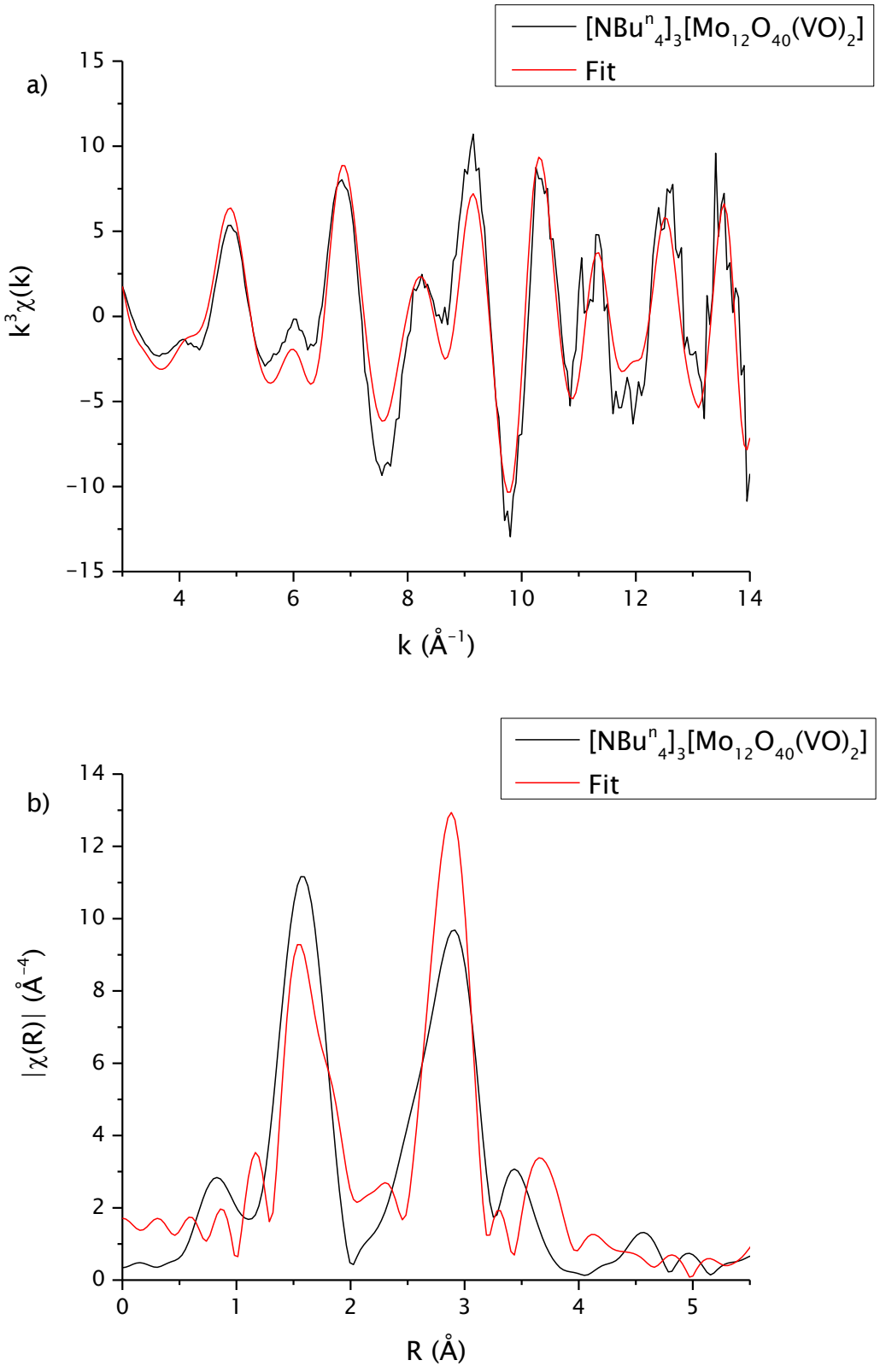

Figure 4.15: V K edge k³-weighted a) EXAFS spectrum and b) Fourier transform of [NBu$^n_4$]$_3$[Mo$_{12}$O$_{40}$(VO)$_2$] in acetonitrile.

Edge	Mo site	Path	Degeneracy	σ^2 / Å^2	r / Å	r / Å (XRD)	Error / %
Mo K	Mo2.1	Mo↔O4.1	1	0.0023 ± 0.0002	1.684 ± 0.003	1.661	1.4
		Mo↔O21.1	2	0.0045 ± 0.0005	1.858 ± 0.004	1.829	1.6
		Mo↔O22.1	2	0.0045 ± 0.0005	2.059 ± 0.004	2.029	1.5
		Mo↔O2.1	1	0.0012 ± 0.0007	2.465 ± 0.007	2.547	3.2
		Mo↔Mo6.1	2	0.0025 ± 0.0021	3.503 ± 0.023	3.547	1.2
		Mo↔Mo3.1	2	0.0025 ± 0.0021	3.682 ± 0.023	3.727	1.2
		Mo↔V1.1	1	0.0046 ± 0.0014	3.090 ± 0.014	3.098	0.3
		Mo↔P1.1	1	-0.0057 ± 0.0017	3.641 ± 0.024	3.578	1.8
		Mo↔O15.1	2	-0.0069 ± 0.0015	3.461 ± 0.025	3.628	4.6
		Mo↔O8.2	1	-0.0075 ± 0.0027	4.022 ± 0.105	3.938	2.1
		Mo↔O5.1	3	-0.0075 ± 0.0027	4.128 ± 0.105	4.043	2.1
		Mo↔O17.1	2	-0.0025 ± 0.0076	4.390 ± 0.144	4.150	5.8
		Mo↔O23.1	3	-0.0035 ± 0.0051	4.240 ± 0.162	4.596	7.7
		Mo↔O12.1	2	-0.0050 ± 0.0020	4.929 ± 0.028	4.764	3.5
		Mo↔Mo4.2	1	0.0128 ± 0.0080	4.944 ± 0.064	4.860	1.7
		Mo↔Mo4.1	1	0.0128 ± 0.0080	5.354 ± 0.064	5.270	1.6
		Mo↔O1.2	2	-0.0020 ± 0.0019	5.061 ± 0.024	5.132	1.4
		Mo↔O7.1	2	-0.0020 ± 0.0019	5.160 ± 0.024	5.232	1.4
		Mo↔Mo1.1	2	0.0160 ± 0.0065	6.319 ± 0.058	6.290	0.5
	Mo1.1	Mo↔O3.2	1	0.0023 ± 0.0002	1.679 ± 0.003	1.656	1.4
		Mo↔O6.1	4	0.0045 ± 0.0005	1.956 ± 0.004	1.927	1.5
		Mo↔O5.1	1	0.0012 ± 0.0007	2.339 ± 0.007	2.421	3.4
		Mo↔Mo3.1	4	0.0025 ± 0.0021	3.501 ± 0.023	3.545	1.2
		Mo↔P1.1	1	-0.0057 ± 0.0017	3.700 ± 0.024	3.636	1.8
		Mo↔O22.2	2	-0.0069 ± 0.0015	3.563 ± 0.025	3.730	4.5
		Mo↔O11.2	2	-0.0075 ± 0.0027	3.907 ± 0.105	3.907	0.0
		Mo↔O15.1	4	-0.0025 ± 0.0076	4.437 ± 0.144	4.196	5.7
		Mo↔O4.2	4	-0.0035 ± 0.0051	4.265 ± 0.162	4.621	7.7
		Mo↔Mo6.1	2	0.0128 ± 0.0080	5.237 ± 0.064	5.152	1.6
		Mo↔O16.1	3	-0.0048 ± 0.0014	5.030 ± 0.023	5.179	2.9
		Mo↔Mo2.1	3	0.0160 ± 0.0065	6.317 ± 0.058	6.287	0.5
V K		V↔O17.1	4	0.0038 ± 0.0025	1.967 ± 0.033	1.951	0.8
		V↔O23.1	1	0.0015 ± 0.0110	2.336 ± 0.084	2.204	6.0
		V↔Mo5.1	4	-0.0036 ± 0.0043	3.109 ± 0.055	3.102	0.2
		V↔O9.1	2	-0.0028 ± 0.0213	3.354 ± 0.1096	3.792	11.6
		V↔O12.1	2	-0.0028 ± 0.0213	3.380 ± 0.1096	3.818	11.5
		V↔O2.1	1	-0.0156 ± 0.0056	3.031 ± 0.058	3.482	13.0
		V↔O5.1	1	-0.0156 ± 0.0056	3.093 ± 0.058	3.544	12.7
		V↔O10.1	8	0.0028 ± 0.0170	4.709 ± 0.146	4.420	6.5
		V↔P1.1	1	-0.0066 ± 0.0066	4.022 ± 0.068	4.069	1.2
		V↔O11.2	2	-0.0046 ± 0.0152	5.717 ± 0.179	5.185	10.3

Table 4.10: The EXAFS-derived structural parameters for $[NBu^n_4]_3[PMo_{12}O_{40}(VO)_2]$ in acetonitrile. XRD data for $[PMo_{12}O_{40}(FeCl)_2]^{4-}$ is provided for comparison.

Bond Angle (°)	Edge		$[PMo_{12}O_{40}(FeCl)_2]^{4-}$ (XRD)
	Mo K	V K	
Mo2.1-O13.1-Mo6.1	119	-	142
Mo2.1-O22.1-Mo5.1	115	-	134
Mo1.1-O6.1-Mo4.1	118	-	142
O4.1-Mo2.1-O21.1	88	-	102
O4.1-Mo2.1-O22.1	88	-	101
O3.2-Mo1.1-O21.2	87	-	102
O2.1-Mo2.1-O21.1	62	-	66
O5.1-Mo1.1-O7.1	61	-	65
V1.1-O22.1-Mo2.1	-	89	103
O17.1-V1.1-O14.1	-	83	79

Table 4.11: The EXAFS-derived bond angles for $[NBu^n_4]_3[PMo_{12}O_{40}(VO)_2]$ in acetonitrile. XRD data for $[PMo_{12}O_{40}(FeCl)_2]^{4-}$ is provided for comparison.

Anion	Edge	Parameter	Value
$[PMo_{12}O_{40}(VO)_2]^{3-}$ Solution	Mo K	R (%)	0.14
		R, k = 1 (%)	0.12
		R, k = 2 (%)	0.12
		R, k = 3 (%)	0.17
		Chi-square	349
		Reduced chi-square	50
		Amplitude reduction factor	0.99 ± 0.04
		k range ($Å^{-1}$)	3.0 - 20.0
		R range (Å)	1.0 - 6.5
		No. of independent parameters	58
		No. of variables	52
	V K	R (%)	9.39
		R, k = 1 (%)	8.53
		R, k = 2 (%)	9.96
		R, k = 3 (%)	9.66
		Chi-square	4595
		Reduced chi-square	1088
		Amplitude reduction factor	0.80
		k range ($Å^{-1}$)	3.0 - 14.0
		R range (Å)	1.0 - 5.5
		No. of independent parameters	31
		No. of variables	27

Table 4.12: Refined parameters for fits to $[NBu^n_4]_3[PMo_{12}O_{40}(VO)_2]$ in acetonitrile.

4.2.4 QEXAFS Study of $[NBu^n_4]_4[PMo_{12}O_{40}(FeCl)_2]$

EXAFS spectroscopy has been used to characterise $[NBu^n_4]_4[PMo_{12}O_{40}(FeCl)_2]$ (figure 4.16) in the solid state and in acetonitrile and also to follow the addition of FeCl groups to $[PMo_{12}O_{40}]^{3-}$ by reductive aggregation to produce $[PMo_{12}O_{40}(FeCl)_2]^{4-}$. Crystallographic data for $[PMo_{12}O_{40}(FeCl)_2]^{4-}$ was fitted to the spectra for $[NBu^n_4]_4[PMo_{12}O_{40}(FeCl)_2]$ in the solid state and in acetonitrile. The Fe K edge EXAFS spectrum for $[NBu^n_4]_4[PMo_{12}O_{40}(FeCl)_2]$ in acetonitrile is presented in figure 4.17 to demonstrate the amount and quality of data that has been collected for this cluster at the Fe K edge. Fe K edge data up to 15 $Å^{-1}$ has been used in the curve-fitting analysis for $[NBu^n_4]_4[PMo_{12}O_{40}(FeCl)_2]$. The Mo K edge and Fe K edge EXAFS spectra and Fourier transforms are presented in figures 4.18 – 4.20. To gain an understanding of the initial state of the reaction solution represented by equation 4.1, the solution behaviour of $FeCl_2$ needed to be understood. Attempts to fit tetrahedral $FeCl_2(CH_3CN)_2$ and cis- and trans-substituted octahedral $FeCl_2(CH_3CN)_4$ to the EXAFS spectrum for $FeCl_2$ in acetonitrile were unsuccessful. In solution, $FeCl_2$ forms 2 ions in a 1:1 mixture: $FeCl_3(CH_3CN)$ and $FeCl(CH_3CN)_3$.[87] Fitting a 1:1 mixture of $FeCl_3(CH_3CN)$ and $FeCl(CH_3CN)_3$ to the EXAFS spectrum for $FeCl_2$ in acetonitrile was successful. The Fe K edge EXAFS spectrum and Fourier transform with this fit are presented in figure 4.21.

$$[PMo_{12}O_{40}]^{3-} + 2\ FeCl_2 + 2\ e^- \rightarrow [PMo_{12}O_{40}(FeCl)_2]^{3-} + 2\ Cl^- \qquad \text{(Equation 4.1)}$$

The reaction solution was analysed at the Mo K edge and the Fe K edge. $[PMo_{12}O_{40}(FeCl)_2]^{4-}$ and a 1:1 mixture of $FeCl_3(CH_3CN)$ and $FeCl(CH_3CN)_3$ were fitted to the spectra. Fe^{II} has undergone ligand substitution to generate Fe^{I} and Fe^{III} ions.[87] Therefore, $FeCl_3(CH_3CN)$ and $FeCl(CH_3CN)_3$ have been treated as the major species in solution. At the Mo K edge there are 3 molybdenum sites: The site adjacent to the iron atom in the capped POM, the equatorial site (Mo1 and Mo6 in figure 4.16) and the site in the uncapped POM. $[PMo_{12}O_{40}]^{3-}$ and $[PMo_{12}O_{40}(FeCl)_2]^{4-}$ were used as standards in a linear combination fit to give the

weighting of each component in the reaction solution. $[PMo_{12}O_{40}]^{3-}$ contributed 84 % of the Mo K edge EXAFS for the reaction solution and $[PMo_{12}O_{40}(FeCl)_2]^{4-}$ contributed 16 % of the Mo K edge EXAFS for the reaction solution, The iron atoms in $[PMo_{12}O_{40}(FeCl)_2]^{4-}$ cannot be detected by the equatorial molybdenum atoms, so these Mo sites and the analogous sites in $[PMo_{12}O_{40}]^{3-}$ can be fitted using one absorbing Mo atom to represent the equatorial atoms in both clusters. This means that contributions from the equatorial Mo site account for $\frac{1}{3}$ of the total Mo K edge EXAFS and this is represented mathematically in equation 4.2 where Mo_{eq} is the equatorial molybdenum. $[PMo_{12}O_{40}(FeCl)_2]^{4-}$ contributes 16 % of the total EXAFS. $\frac{2}{3}$ of the molybdenum sites in $[PMo_{12}O_{40}(FeCl)_2]^{4-}$ are adjacent to the iron atoms (Mo2.1, Mo3.1, Mo4.1, Mo5.1, Mo2.2, Mo 3.2, Mo4.2 and Mo5.2 in figure 4.16). This site can be represented as Mo-OFe and the contribution from this site to the total EXAFS is expressed mathematically in equation 4.3. $[PMo_{12}O_{40}]^{3-}$ contributes 84 % of the total EXAFS. $\frac{2}{3}$ of the contribution from $[PMo_{12}O_{40}]^{3-}$ to the total EXAFS is due to the (Mo-OMo) site (Mo2.1, Mo3.1, Mo4.1, Mo5.1, Mo2.2, Mo 3.2, Mo4.2 and Mo5.2 in figure 4.7). This is expressed mathematically in equation 4.4. The Mo K edge EXAFS and Fourier transform with a fit of $[PMo_{12}O_{40}]^{3-}$ + $FeCl_3(CH_3CN)$ + $FeCl(CH_3CN)_3$ are presented in figure 4.22.

At the iron K edge there are 3 sites in the reaction solution: $FeCl_3(CH_3CN)$, $FeCl(CH_3CN)_3$ and $[PMo_{12}O_{40}(FeCl)_2]^{4-}$. A linear combination fit was run using the spectra for $FeCl_2$ and $[PMo_{12}O_{40}(FeCl)_2]^{4-}$ as standards. The weighting of $FeCl_2$ in the observed EXAFS for the reaction solution was 70 % and the weighting of $[PMo_{12}O_{40}(FeCl)_2]^{4-}$ was 30 %. In the curve-fitting analysis the $FeCl_2$ weighting was divided into 2 due to the 2 ions formed in solution and each ion was included in the fit. The weightings of each ion used in the curve-fitting analysis are expressed mathematically in equations 4.5 – 4.7. The amplitude reduction factor was set to 1.00 and the Fe-Cl bond length was set to 2.364 Å in the reported fit. The Fe K edge EXAFS and Fourier transform with a fit of $FeCl_3(CH_3CN)$, $FeCl(CH_3CN)_3$ and $[PMo_{12}O_{40}(FeCl)_2]^{4-}$ are presented in figure 4.23.

Bond angles which have been calculated for the complexes using the EXAFS-derived structural parameters are presented in table 4.13. The EXAFS-derived structural parameters for $[NBu^n_4]_4[PMo_{12}O_{40}(FeCl)_2]$ in the solid state and in

acetonitrile are presented in tables 4.14 and 4.15 . Data regarding the quality of these fits are presented in table 4.16. The EXAFS-derived structural parameters for the Mo K edge of $[NBu^n_4]_4[PMo_{12}O_{40}(FeCl)_2]$ and $[NBu^n_4]_3[PMo_{12}O_{40}]$ in the reaction solution are presented in table 4.17. The EXAFS-derived structural parameters for the Fe K edge of $[NBu^n_4]_4[PMo_{12}O_{40}(FeCl)_2]$ + $FeCl_3(NCCH_3)$ + $FeCl(NCCH_3)_3$ in the reaction solution are presented in table 4.18. The data regarding the quality of the fits to the EXAFS spectrum for the reaction solution are presented in table 4.19.

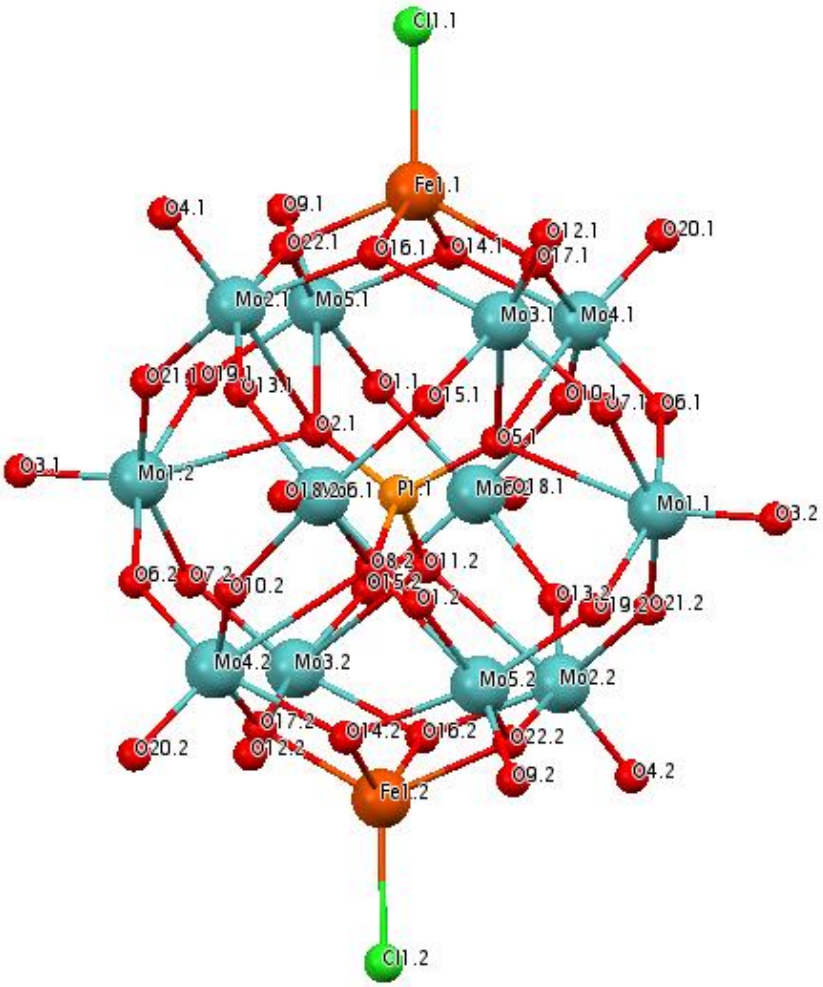

Figure 4.16: Structure of $[PMo_{12}O_{40}(FeCl)_2]^{4-}$.

$$\chi\left(\mathrm{Mo_{eq}}\right) = \frac{1}{3} \times 0.157 + \frac{1}{3} \times 0.84 = \frac{1}{3}$$

(Equation 4.2)

$$\chi\left(\mathrm{Mo-OFe}\right) = \frac{2}{3} \times 0.16$$

(Equation 4.3)

$$\chi\left(\mathrm{Mo-OMo}\right) = \frac{2}{3} \times 0.84$$

(Equation 4.4)

$$\chi\left(\left[\mathrm{FeCl_3(CH_3CN)}\right]\right) = \frac{0.7}{2} = 0.35$$

(Equation 4.5)

$$\chi\left(\left[\mathrm{FeCl(CH_3CN)_3}\right]\right) = \frac{0.7}{2} = 0.35$$

(Equation 4.6)

$$\chi\left(\left[\mathrm{PMo_{12}O_{40}(FeCl)_2}\right]^{4-}\right) = 0.3$$

(Equation 4.7)

It is clear from the Fe K edge EXAFS Fourier transforms in figure 4.24 that a cluster is being formed around the iron (Fourier transforms are not phase corrected). The Fourier transform spectrum for $FeCl_2$ in acetonitrile (black spectrum in figure 4.24) exhibits peaks at 1.90 Å and 2.64 Å due to the Fe-Cl bond and Fe···Fe distances respectively. The Fourier transform spectrum for $[NBu^n_4]_4[PMo_{12}O_{40}(FeCl)_2]$ in acetonitrile (red spectrum in figure 4.24) exhibits peaks at 1.53 Å and 2.82 Å due to the Fe-O bonds and Fe···Mo distances respectively. The peak at 2.82 Å has much higher amplitude, due to the high coordination number for this path as is the case in the spectra for the other Keggin-type molybdates that have been studied. The Fourier transform for the Fe K edge EXAFS of the reaction solution containing $[NBu^n_4]_5[PMo_{12}O_{40}]$ and $FeCl_2$ as starting materials (blue spectrum in figure 4.24) exhibits a peak at 1.63 Å.

This peak is an average of the Fe-Cl peak at 1.90 Å in the $FeCl_2$ spectrum and the Fe-O peak at 1.53 Å in the $[NBu^n_4]_4[PMo_{12}O_{40}(FeCl)_2]$ spectrum. There are two more peaks in the spectrum for the reaction solution at 2.95 Å and 3.65 Å due to the Fe···Mo distance in the POM and Fe···Fe distance in $FeCl_2$ respectively. This provides evidence that a cluster is being formed around the iron atom. These distances are different to the distances reported in the tables because the spectra are not phase corrected. Debye-Waller factors for the multiple scattering paths for the curve-fitting analysis for solution phase $[NBu^n_4]_4[PMo_{12}O_{40}(FeCl)_2]$ were fitted by summing all the Debye-Waller factors for the single scattering paths involved in the multiple scattering paths.

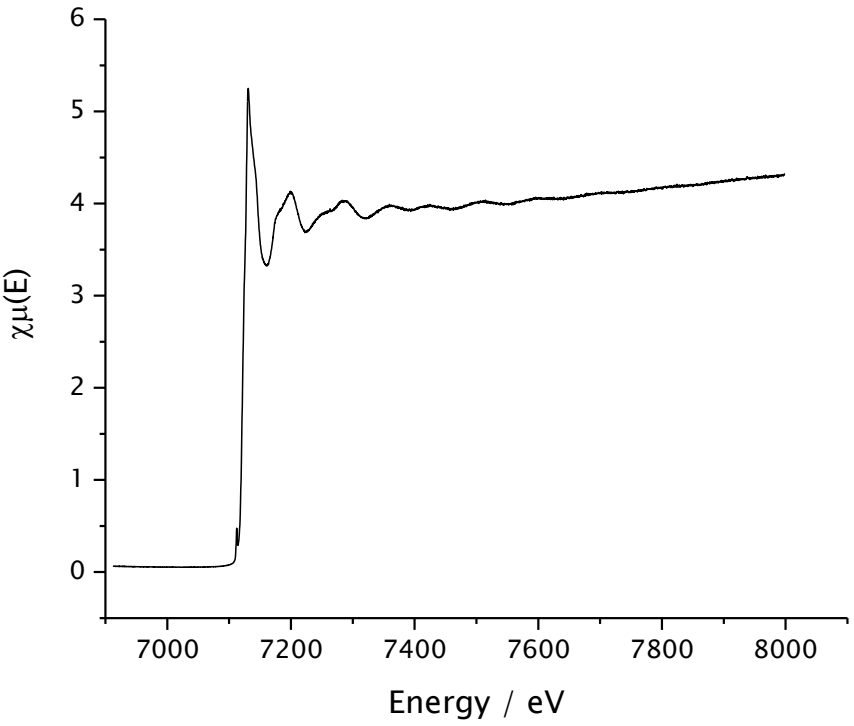

Figure 4.17: Fe K edge EXAFS spectrum for $[NBu^n_4]_4[PMo_{12}O_{40}(FeCl)_2]$ in acetonitrile.

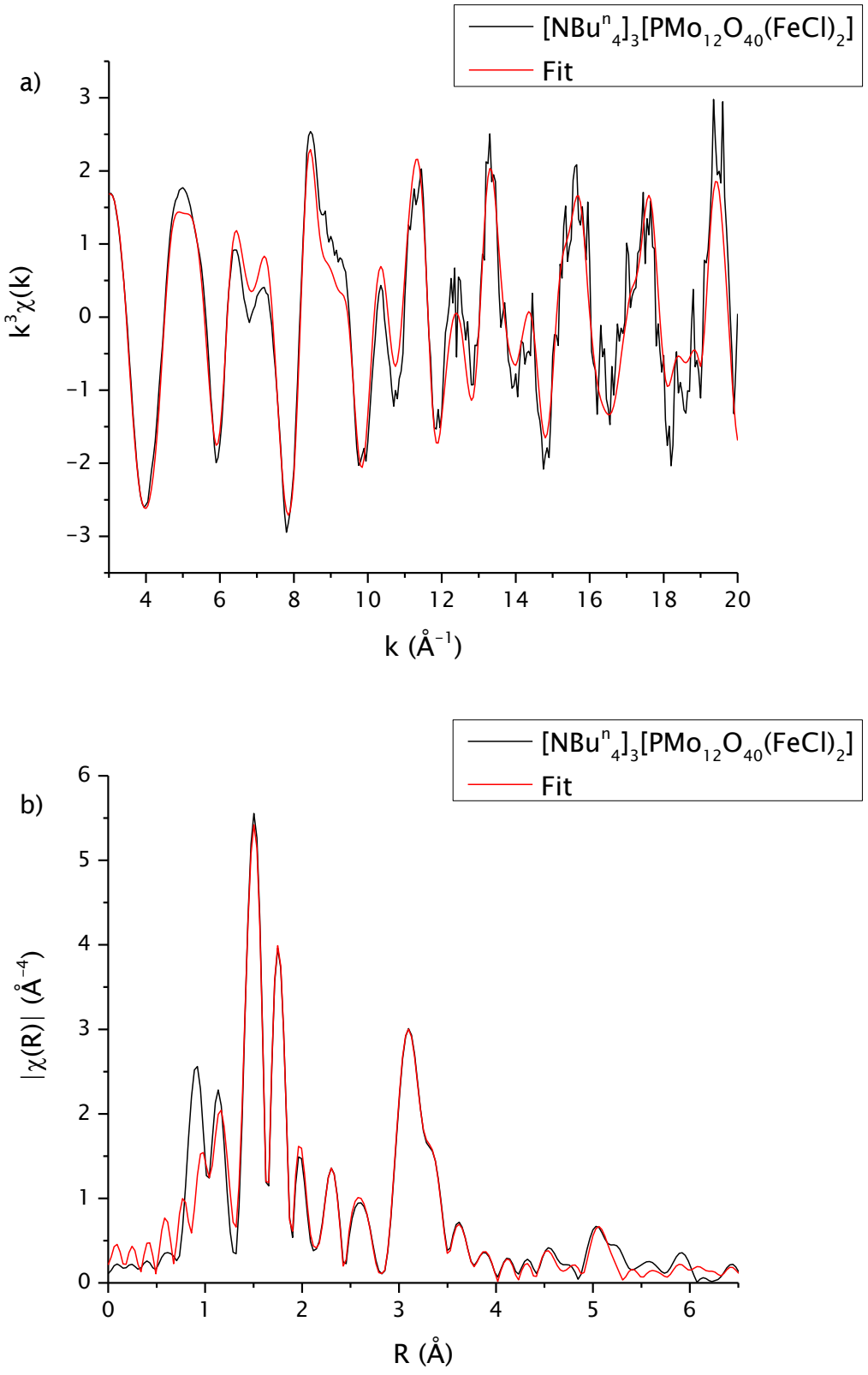

Figure 4.18: Mo K edge k^3-weighted a) EXAFS spectrum and b) Fourier transform of [NBu$^n_4$]$_4$[PMo$_{12}$O$_{40}$(FeCl)$_2$] in the solid state.

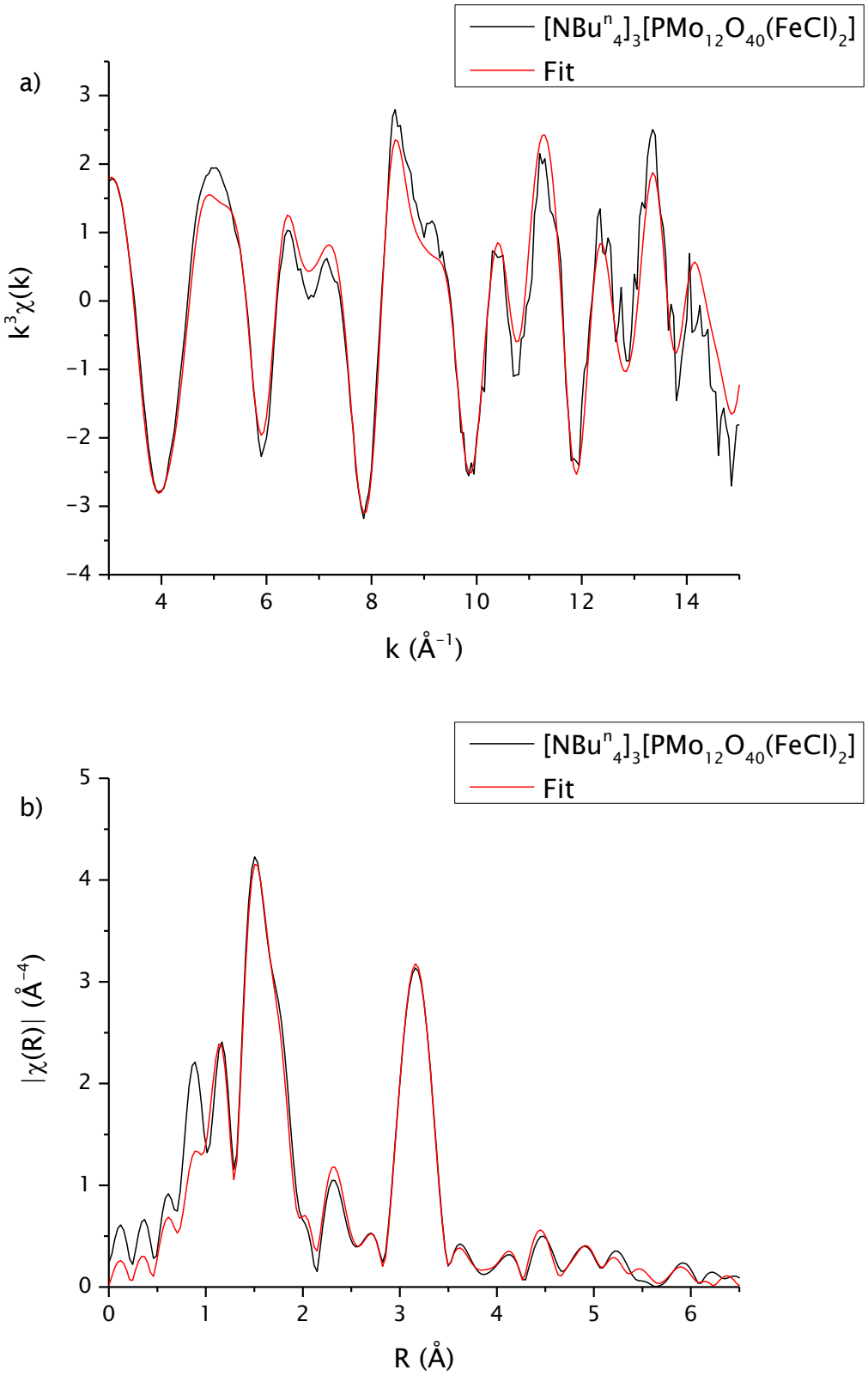

Figure 4.19: Mo K edge k³-weighted a) EXAFS spectrum and b) Fourier transform of [NBu$^n_4$]$_4$[PMo$_{12}$O$_{40}$(FeCl)$_2$] in acetonitrile.

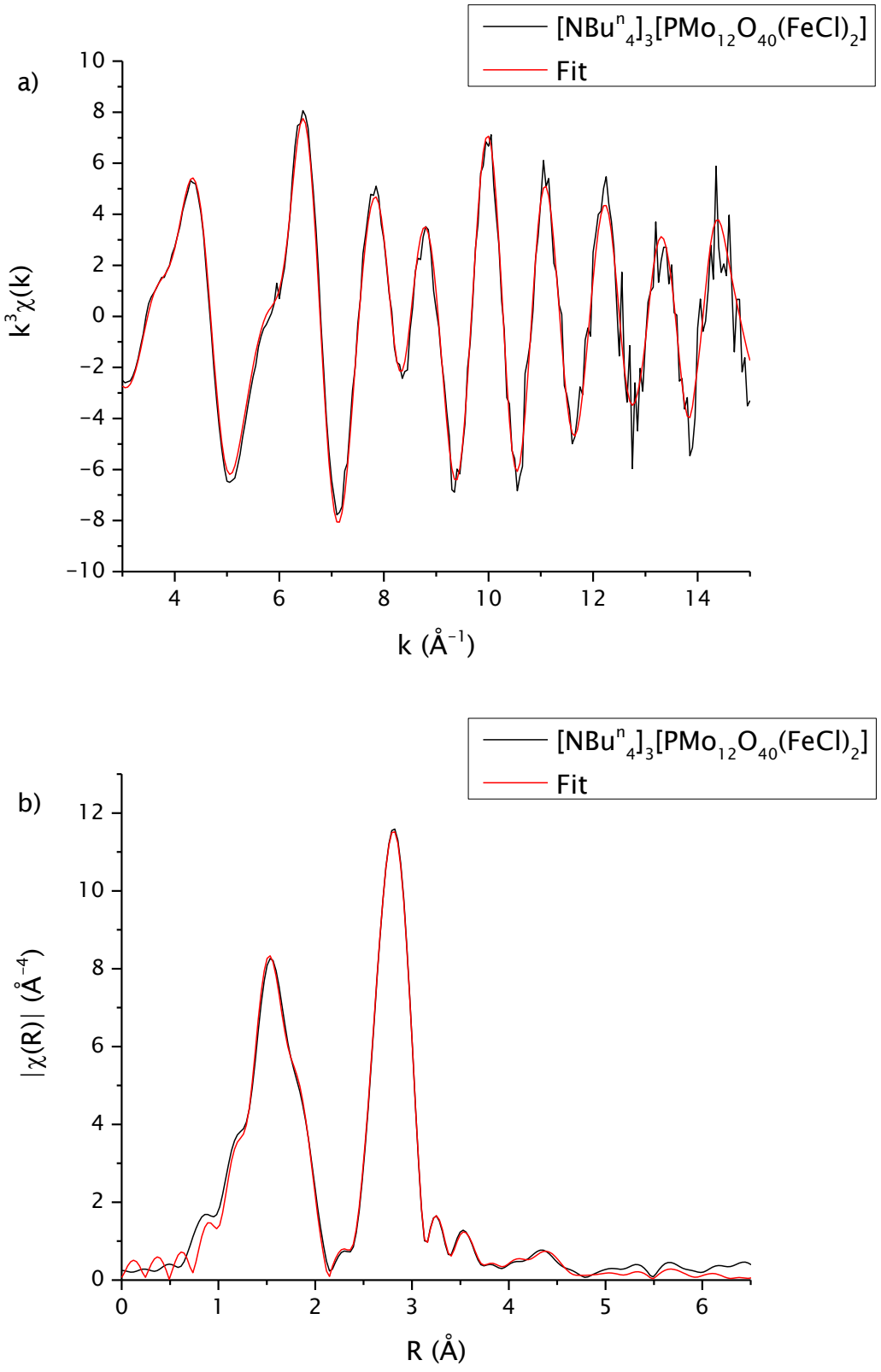

Figure 4.20: Fe K edge k³-weighted a) EXAFS spectrum and b) Fourier transform of [NBu$^n_4$]$_4$[PMo$_{12}$O$_{40}$(FeCl)$_2$] in acetonitrile.

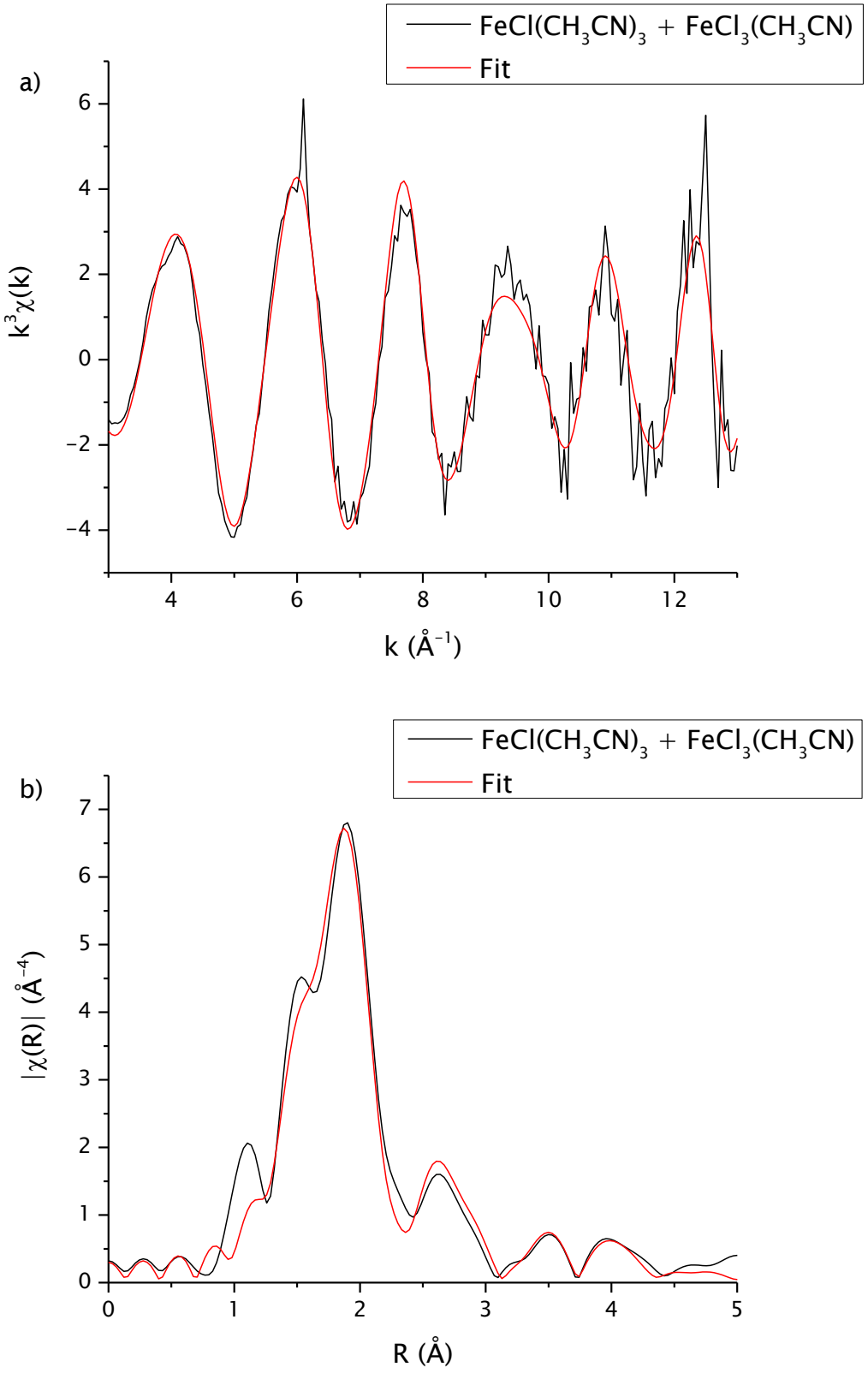

Figure 4.21: Fe K edge k^3-weighted a) EXAFS spectrum and b) Fourier transform of $FeCl_3(NCCH_3)$ + $FeCl(NCCH_3)_3$ in acetonitrile.

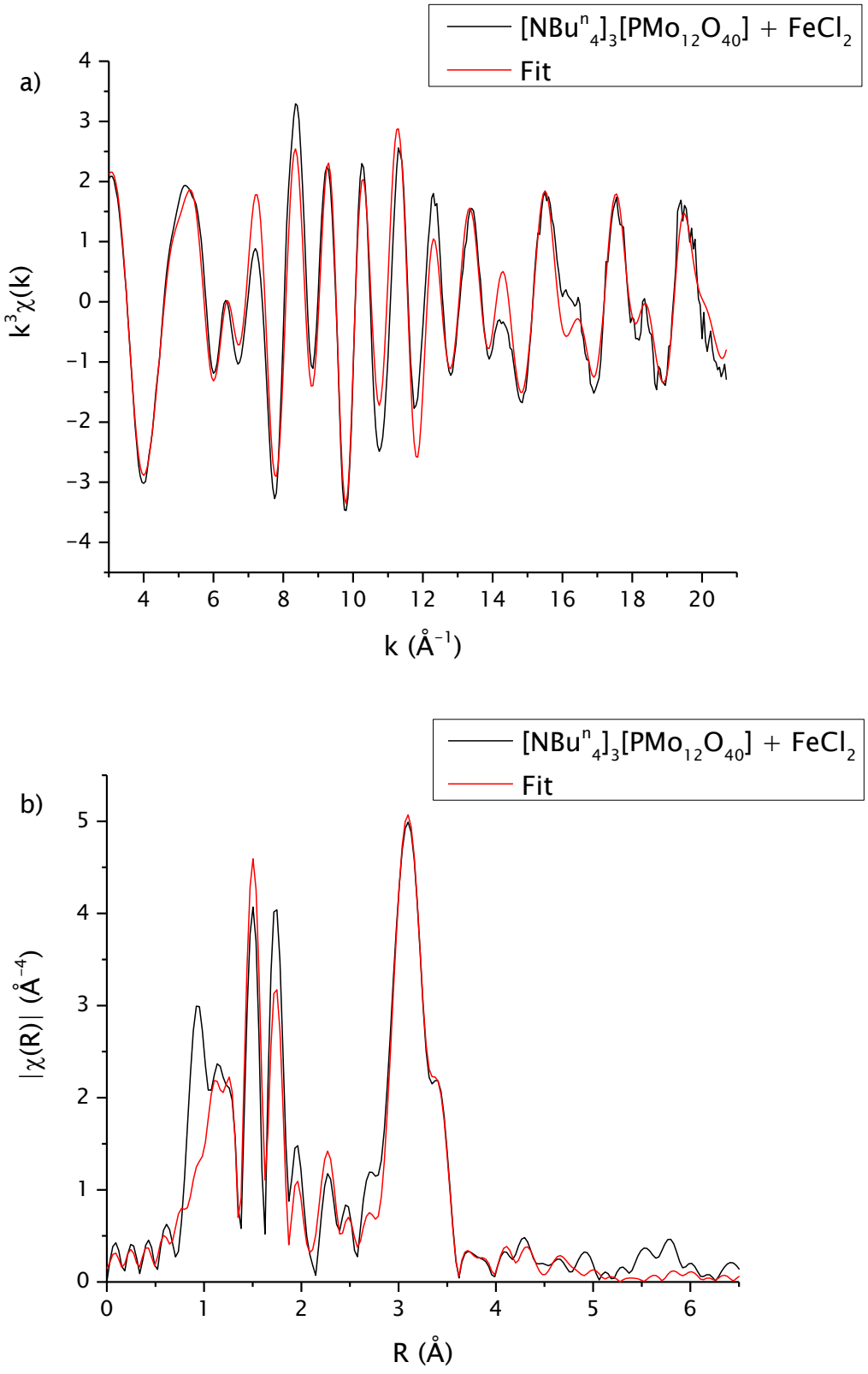

Figure 4.22: Mo K edge k^3-weighted a) EXAFS spectrum and b) Fourier transform of [NBu$^n_4$]$_3$[PMo$_{12}$O$_{40}$] + FeCl$_2$ in acetonitrile.

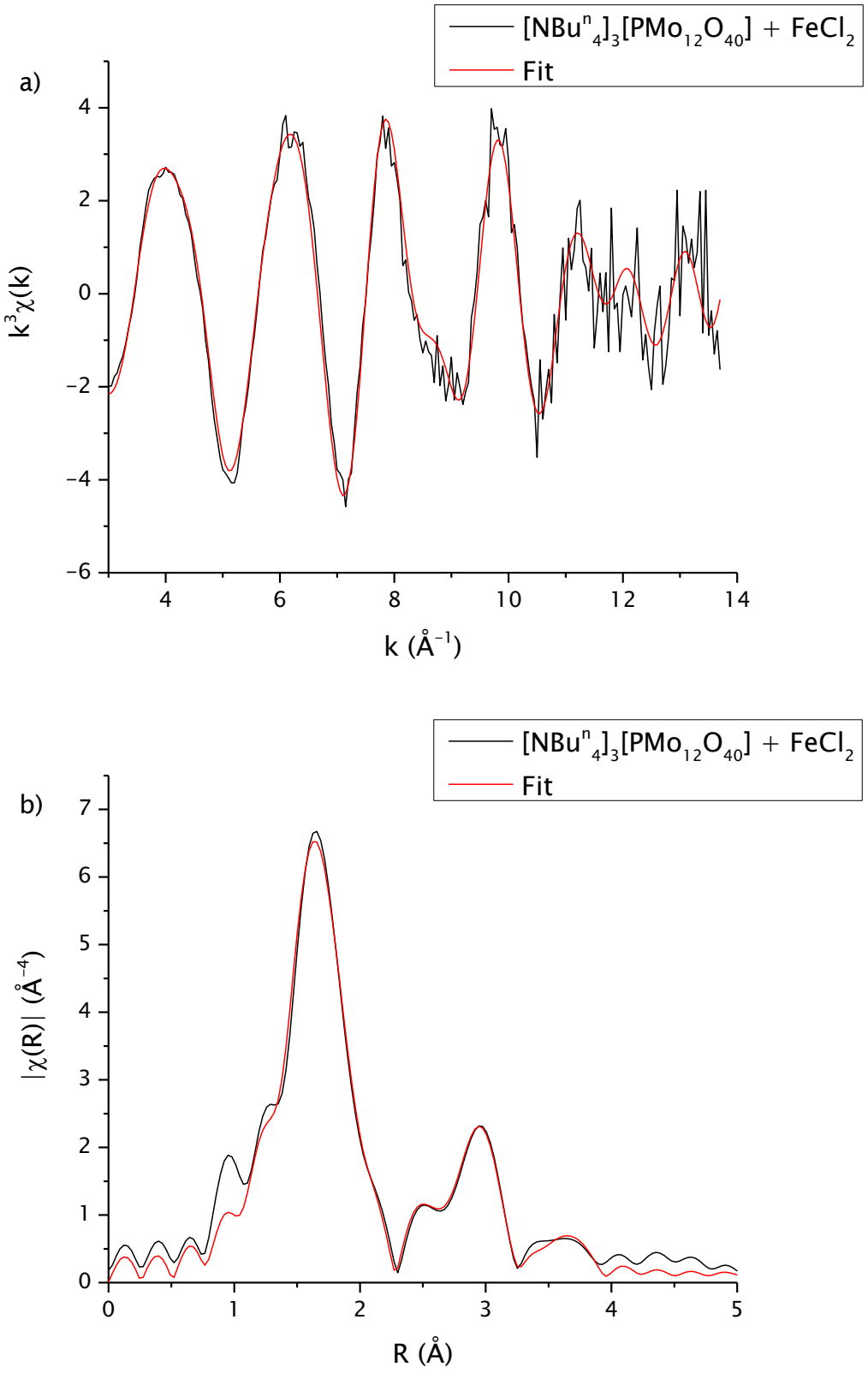

Figure 4.23: Fe K edge k³-weighted a) EXAFS spectrum and b) Fourier transform of [NBu$^n_4$]$_3$[PMo$_{12}$O$_{40}$] + FeCl$_2$ in acetonitrile.

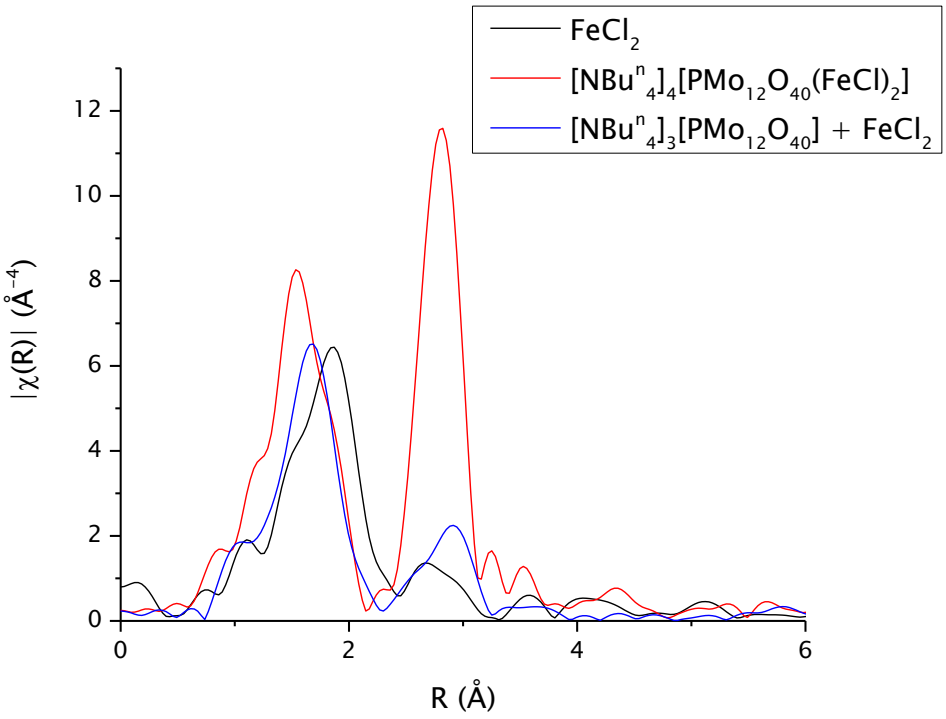

Figure 4.24: k^3-weighted Fourier transforms of the Fe K edge EXAFS of $FeCl_2$ in acetonitrile, $[NBu^n_4]_4[PMo_{12}O_{40}(FeCl)_2]$ in acetonitrile and the reaction between $FeCl_2$ and $[NBu^n_4]_3[PMo_{12}O_{40}]$ in acetonitrile.

Edge	Bond Angle (°)	Solid	Solution	Reaction	$[PMo_{12}O_{40}(FeCl)_2]^{4-}$ (XRD)
Mo K	Mo2.1-O13.1-Mo6.1	136	137	117	142
	Mo2.1-O22.1-Mo5.1	129	133	114	134
	Mo1.1-O6.1-Mo4.1	136	137	117	142
	O22.1-Mo2.1-O13.1	-	155	112	154
	O7.1-Mo1.1-O21.2	-	156	112	155
	O4.1-Mo2.1-O21.1	89	103	-	102
	O4.1-Mo2.1-O22.1	88	101	97	101
	O3.2-Mo1.1-O21.2	89	103	97	102
	O2.1-Mo2.1-O21.1	64	65	-	66
	O5.1-Mo1.1-O7.1	63	64	-	65
	O22.1-Mo2.1-O21.1	66	90	-	89
	O22.1-Mo2.1-O16.1	56	76	-	76
	O6.1-Mo1.1-O7.1	64	87	-	87
Fe K	Fe1.1-O22.1-Mo2.1	-	90	95	103
	O17.1-Fe1.1-O14.1	-	56	43	79
	O17.1-Fe1.1-O22.1	-	117	-	128
	O14.1-Fe1.1-O16.1	-	121	-	130
	O14.1-Fe1.1-Cl1.1	-	97	80	115

Table 4.13: The EXAFS-derived bond angles for $[NBu^n_4]_4[PMo_{12}O_{40}(FeCl)_2]$ in the solid state, in acetonitrile and in the reaction solution (acetonitrile). XRD data for $[PMo_{12}O_{40}(FeCl)_2]^{4-}$ is provided for comparison.

Site	Path	Degeneracy	σ^2 / Å^2	r / Å	r / Å (XRD)	Error / %
Mo2.1	Mo↔O4.1	1	0.0020 ± 0.0003	1.688 ± 0.004	1.661	1.6
	Mo↔O21.1	2	0.0037 ± 0.0005	1.866 ± 0.005	1.829	2.0
	Mo↔O22.1	2	0.0034 ± 0.0006	2.070 ± 0.007	2.029	2.0
	Mo↔O2.1	1	0.0000 ± 0.0008	2.460 ± 0.009	2.547	3.4
	Mo↔Mo6.1	2	0.0031 ± 0.0027	3.595 ± 0.053	3.547	1.4
	Mo↔Mo3.1	2	0.0031 ± 0.0027	3.775 ± 0.053	3.727	1.3
	Mo↔Fe	1	0.0050 ± 0.0010	3.086 ± 0.005	3.098	0.4
	Mo↔P1.1	1	-0.0030 ± 0.0032	3.657 ± 0.044	3.578	2.2
	Mo↔O15.1	2	-0.0068 ± 0.0010	3.501 ± 0.020	3.628	3.5
	Mo↔O8.2	1	-0.0052 ± 0.0011	3.635 ± 0.018	3.938	7.7
	Mo↔O5.1	3	-0.0052 ± 0.0011	3.740 ± 0.018	4.043	7.5
	Mo↔O17.1	2	-0.0003 ± 0.0043	4.030 ± 0.029	4.150	2.9
	Mo↔Cl1.1	1	-0.0001 ± 0.0016	4.778 ± 0.020	4.594	4.0
	Mo↔O18.2	2	0.0178 ± 0.0276	4.307 ± 0.174	4.598	6.3
	Mo↔O12.1	2	0.0178 ± 0.0276	4.473 ± 0.174	4.764	6.1
	Mo↔Mo4.2	1	0.0029 ± 0.0010	4.924 ± 0.015	4.860	1.3
	Mo↔Mo4.1	1	0.0029 ± 0.0010	5.334 ± 0.015	5.270	1.2
	Mo↔O1.2	2	0.0003 ± 0.0015	5.134 ± 0.019	5.132	0.0
	Mo↔O7.1	2	0.0003 ± 0.0015	5.234 ± 0.019	5.232	0.0
	Mo↔Mo1.1	2	0.0123 ± 0.0056	6.356 ± 0.052	6.290	1.0
Mo1.1	Mo↔O3.2	1	0.0020 ± 0.0003	1.683 ± 0.004	1.656	1.6
	Mo↔O6.1	4	0.0037 ± 0.0005	1.964 ± 0.005	1.927	1.9
	Mo↔O5.1	1	0.0000 ± 0.0008	2.333 ± 0.009	2.421	3.6
	Mo↔Mo3.1	4	0.0031 ± 0.0027	3.593 ± 0.053	3.545	1.4
	Mo↔P1.1	1	-0.0030 ± 0.0032	3.715 ± 0.044	3.636	2.2
	Mo↔O22.2	2	-0.0068 ± 0.0010	3.603 ± 0.020	3.730	3.4
	Mo↔O11.2	2	-0.0052 ± 0.0011	3.604 ± 0.018	3.907	7.8
	Mo↔O15.1	4	-0.0003 ± 0.0043	4.077 ± 0.029	4.196	2.8
	Mo↔O4.2	4	0.0178 ± 0.0276	4.331 ± 0.174	4.621	6.3
	Mo↔Mo6.1	2	0.0029 ± 0.0010	5.216 ± 0.015	5.152	1.2
	Mo↔O16.1	3	0.0003 ± 0.0015	5.181 ± 0.019	5.179	0.0
	Mo↔Mo2.1	3	0.0123 ± 0.0056	6.353 ± 0.052	6.287	1.0

Table 4.14: The Mo K edge EXAFS-derived structural parameters for $[NBu^n_4]_4[PMo_{12}O_{40}(FeCl)_2]$ in the solid state. XRD data for $[PMo_{12}O_{40}(FeCl)_2]^{4-}$ is provided for comparison.

Ion	Edge	Site	Path	Degeneracy	σ^2 / Å^2	r / Å	r / Å (XRD)	Error / %
$[PMo_{12}O_{40}(FeCl)_2]^{4-}$ Solution	Mo K	Mo2.1	Mo↔O4.1	1	0.0021 ± 0.0010	1.678 ± 0.008	1.661	1.0
			Mo↔O21.1	2	0.0058 ± 0.0022	1.829 ± 0.014	1.829	0.0
			Mo↔O22.1	2	0.0040 ± 0.0022	2.029 ± 0.016	2.029	0.0
			Mo↔O2.1	1	0.0000 ± 0.0019	2.472 ± 0.017	2.547	2.9
			Mo↔Mo6.1	2	0.0042 ± 0.0025	3.425 ± 0.021	3.547	3.4
			Mo↔Mo3.1	2	-0.0017 ± 0.0031	3.770 ± 0.028	3.727	1.2
			Mo↔Fe1.1	1	0.0034 ± 0.0023	3.112 ± 0.021	3.098	0.5
			Mo↔P1.1	1	-0.0048 ± 0.0042	3.534 ± 0.031	3.578	1.2
			Mo↔O15.1	2	-0.0103 ± 0.0034	3.731 ± 0.028	3.628	2.8
			Mo↔O8.2	1	-0.0095 ± 0.0035	3.902 ± 0.036	3.938	0.9
			Mo↔O5.1	3	-0.0095 ± 0.0035	4.008 ± 0.036	4.043	0.9
			Mo↔O17.1	2	-0.0055 ± 0.0042	4.098 ± 0.043	4.150	1.3
			Mo↔Cl1.1	1	-0.0050 ± 0.0039	4.492 ± 0.044	4.594	2.2
			Mo↔O18.2	2	0.0025 ± 0.0075	4.916 ± 0.043	4.598	6.9
			Mo↔O12.1	2	0.0025 ± 0.0075	5.082 ± 0.043	4.764	6.7
			Mo↔Mo4.2	1	-0.0028 ± 0.0033	4.675 ± 0.037	4.860	3.8
			Mo↔Mo4.1	1	0.0118 ± 0.0230	5.400 ± 0.199	5.270	2.5
			Mo↔O1.2	2	-0.0075 ± 0.0033	4.883 ± 0.038	5.132	4.9
			Mo↔O7.1	2	-0.0075 ± 0.0033	4.983 ± 0.038	5.232	4.8
			Mo↔Mo1.1	2	0.0146 ± 0.0151	6.329 ± 0.133	6.290	0.6
		Mo1.1	Mo↔O3.2	1	0.0021 ± 0.0010	1.656 ± 0.008	1.656	0.0
			Mo↔O6.1	4	0.0058 ± 0.0022	1.950 ± 0.014	1.927	1.2
			Mo↔O5.1	1	0.0000 ± 0.0019	2.346 ± 0.017	2.421	3.1
			Mo↔Mo3.1	4	0.0042 ± 0.0025	3.423 ± 0.021	3.545	3.4
			Mo↔P1.1	1	-0.0048 ± 0.0042	3.592 ± 0.031	3.636	1.2
			Mo↔O22.2	2	-0.0103 ± 0.0034	3.833 ± 0.028	3.730	2.8
			Mo↔O11.2	2	-0.0095 ± 0.0035	3.871 ± 0.036	3.907	0.9
			Mo↔O15.1	4	-0.0055 ± 0.0042	4.144 ± 0.043	4.196	1.2
			Mo↔O4.2	4	0.0025 ± 0.0075	4.940 ± 0.043	4.621	6.9
			Mo↔Mo6.1	2	-0.0028 ± 0.0033	4.967 ± 0.037	5.152	3.6
			Mo↔O16.1	3	-0.0075 ± 0.0033	4.930 ± 0.038	5.179	4.8
			Mo↔Mo2.1	3	0.0146 ± 0.0151	6.326 ± 0.133	6.287	0.6
	Fe K	Fe1.1	Fe↔Cl1.1	1	0.0025 ± 0.0015	2.213 ± 0.015	2.204	0.4
			Fe↔O17.1	4	0.0048 ± 0.0012	1.956 ± 0.013	1.951	0.3
			Fe↔Mo5.1	4	0.0026 ± 0.0037	3.123 ± 0.018	3.102	0.7
			Fe↔O2.1	1	-0.0045 ± 0.0181	3.106 ± 0.096	3.482	10.8
			Fe↔O5.1	1	-0.0045 ± 0.0181	3.168 ± 0.096	3.544	10.6
			Fe↔O9.1	2	-0.0036 ± 0.0321	3.893 ± 0.241	3.792	2.7
			Fe↔O12.1	2	-0.0036 ± 0.0321	3.920 ± 0.241	3.818	2.7
			Fe↔P1.1	1	-0.0072 ± 0.0245	3.912 ± 0.265	4.069	3.9
			Fe↔O10.1	8	-0.0003 ± 0.0088	4.155 ± 0.025	4.420	6.0
			Fe↔O11.2	2	-0.0024 ± 0.0061	5.127 ± 0.042	5.185	1.1
			Fe↔Mo1.1	4	0.0124 ± 0.0212	5.497 ± 0.149	5.462	0.6
			Fe↔O21.2	5	0.0100 ± 0.0119	6.527 ± 0.087	6.429	1.5
			Fe↔O7.2	3	0.0100 ± 0.0119	6.548 ± 0.087	6.450	1.5
$FeCl_2$ Solution	Fe K	Fe^{III}	Fe↔N	1	0.0051 ± 0.0023	2.049 ± 0.029	-	-
			Fe↔Cl	3	0.0038 ± 0.0008	2.293 ± 0.016	-	-
			Fe↔C	1	0.0034 ± 0.0078	3.356 ± 0.054	-	-
			Fe↔C	1	0.0057 ± 0.0258	4.941 ± 0.214	-	-
		Fe^{I}	Fe↔N	3	0.0051 ± 0.0023	2.048 ± 0.029	-	-
			Fe↔Cl	1	0.0038 ± 0.0008	2.293 ± 0.016	-	-
			Fe↔C	3	0.0034 ± 0.0078	3.356 ± 0.054	-	-
			Fe↔C	3	0.0057 ± 0.0258	4.941 ± 0.214	-	-

Table 4.15: The Mo K edge and Fe K edge EXAFS-derived structural parameters for $[NBu^n_4]_4[PMo_{12}O_{40}(FeCl)_2]$ and $FeCl_2$ in acetonitrile. XRD data for $[PMo_{12}O_{40}(FeCl)_2]^{4-}$ is provided for comparison.

Anion	Edge	Parameter	Value
$[PMo_{12}O_{40}(FeCl)_2]^{4-}$ Solid	Mo K	R (%)	0.67
		R, k = 1 (%)	0.23
		R, k = 2 (%)	0.49
		R, k = 3 (%)	1.27
		Chi-square	345
		Reduced chi-square	27
		Amplitude reduction factor	0.97 ± 0.06
		k range ($Å^{-1}$)	3.0 - 20.0
		R range (Å)	1.0 - 6.5
		No. of independent parameters	59
		No. of variables	46
Solution	Mo K	R (%)	0.73
		R, k = 1 (%)	0.72
		R, k = 2 (%)	0.57
		R, k = 3 (%)	0.91
		Chi-square	462
		Reduced chi-square	83
		Amplitude reduction factor	0.99 ± 0.11
		k range ($Å^{-1}$)	3.0 - 15.0
		R range (Å)	1.0 - 6.5
		No. of independent parameters	41
		No. of variables	36
	Fe K	R (%)	0.18
		R, k = 1 (%)	0.11
		R, k = 2 (%)	0.14
		R, k = 3 (%)	0.28
		Chi-square	134
		Reduced chi-square	38
		Amplitude reduction factor	0.82 ± 0.07
		k range ($Å^{-1}$)	3.0 - 15.0
		R range (Å)	1.0 - 6.5
		No. of independent parameters	41
		No. of variables	38
$FeCl_2$ Solution	Fe K	R (%)	0.77
		R, k = 1 (%)	0.45
		R, k = 2 (%)	0.57
		R, k = 3 (%)	1.29
		Chi-square	196
		Reduced chi-square	72
		Amplitude reduction factor	0.81
		k range ($Å^{-1}$)	3.0 - 13.0
		R range (Å)	1.2 - 5.0
		No. of independent parameters	23
		No. of variables	21

Table 4.16: Refined parameters for fits to $[NBu^n_4]_4[PMo_{12}O_{40}(FeCl)_2]$ and $FeCl_2$ in the solid state and in acetonitrile.

Site	Path	Degeneracy	σ^2 / Å^2	r / Å	r / Å (XRD)	Error / %
Mo2.1	Mo↔O4.1	1	0.0011 ± 0.0004	1.694 ± 0.006	1.661	2.0
	Mo↔O21.1	2	0.0019 ± 0.0007	1.833 ± 0.009	1.829	0.2
	Mo↔O22.1	2	0.0019 ± 0.0007	2.034 ± 0.009	2.029	0.2
	Mo↔O2.1	1	0.0000 ± 0.0012	2.508 ± 0.014	2.547	1.5
	Mo↔Mo6.1	2	0.0033 ± 0.0012	3.486 ± 0.011	3.547	1.7
	Mo↔Mo3.1	2	0.0033 ± 0.0012	3.665 ± 0.011	3.727	1.7
	Mo↔Fe	1	0.0041 ± 0.0061	2.793 ± 0.063	3.098	9.8
	Mo↔P1.1	1	-0.0032 ± 0.0012	3.362 ± 0.017	3.578	6.0
	Mo↔O15.1	2	-0.0035 ± 0.0013	3.391 ± 0.020	3.628	6.5
	Mo↔O8.2	1	-0.0017 ± 0.0047	4.056 ± 0.059	3.938	3.0
	Mo↔O5.1	3	-0.0017 ± 0.0047	4.162 ± 0.059	4.043	2.9
	Mo↔O17.1	2	-0.0011 ± 0.0022	3.822 ± 0.024	4.150	7.9
	Mo↔Cl1.1	1	0.0026 ± 0.0414	4.660 ± 0.629	4.594	1.4
	Mo↔O18.2	2	0.0214 ± 0.0633	4.415 ± 0.307	4.598	4.0
	Mo↔O12.1	2	0.0214 ± 0.0633	4.581 ± 0.307	4.764	3.8
	Mo↔Mo4.2	1	0.0112 ± 0.0223	4.962 ± 0.160	4.860	2.1
	Mo↔Mo4.1	1	0.0112 ± 0.0223	5.372 ± 0.160	5.270	1.9
	Mo↔O1.2	2	0.0039 ± 0.0693	4.794 ± 0.515	5.132	6.6
	Mo↔O7.1	2	0.0039 ± 0.0693	4.893 ± 0.515	5.232	6.5
	Mo↔Mo1.1	2	0.0130 ± 0.0270	6.298 ± 0.236	6.290	0.1
Mo1.1	Mo↔O3.2	1	0.0011 ± 0.0004	1.689 ± 0.006	1.656	2.0
	Mo↔O6.1	4	0.0019 ± 0.0007	1.931 ± 0.009	1.927	0.2
	Mo↔O5.1	1	0.0000 ± 0.0012	2.382 ± 0.014	2.421	1.6
	Mo↔Mo3.1	4	0.0033 ± 0.0012	3.483 ± 0.011	3.545	1.7
	Mo↔P1.1	1	-0.0032 ± 0.0012	3.419 ± 0.017	3.636	6.0
	Mo↔O22.2	2	-0.0035 ± 0.0013	3.493 ± 0.020	3.730	6.4
	Mo↔O11.2	2	-0.0017 ± 0.0047	4.025 ± 0.059	3.907	3.0
	Mo↔O15.1	4	-0.0011 ± 0.0022	3.868 ± 0.024	4.196	7.8
	Mo↔O4.2	4	0.0214 ± 0.0633	4.439 ± 0.307	4.621	3.9
	Mo↔Mo6.1	2	0.0112 ± 0.0223	5.254 ± 0.160	5.152	2.0
	Mo↔O16.1	3	0.0039 ± 0.0693	4.841 ± 0.515	5.179	6.5
	Mo↔Mo2.1	3	0.0130 ± 0.0270	6.295 ± 0.236	6.287	0.1
Mo3.2	Mo↔O12.2	1	0.0011 ± 0.0004	1.689 ± 0.006	1.661	1.7
	Mo↔O7.2	2	0.0019 ± 0.0007	1.834 ± 0.009	1.830	0.2
	Mo↔O16,2	2	0.0019 ± 0.0007	2.034 ± 0.009	2.029	0.2
	Mo↔O11.2	1	0.0000 ± 0.0012	2.481 ± 0.014	2.547	2.6
	Mo↔Mo1.2	2	0.0033 ± 0.0012	3.483 ± 0.011	3.545	1.7
	Mo↔Mo2.2	2	0.0033 ± 0.0012	3.671 ± 0.011	3.733	1.7
	Mo↔P1.1	1	-0.0032 ± 0.0012	3.388 ± 0.017	3.604	6.0
	Mo↔O6.2	2	-0.0035 ± 0.0013	3.389 ± 0.020	3.626	6.5
	Mo↔O2.1	1	-0.0017 ± 0.0047	3.936 ± 0.059	3.818	3.1
	Mo↔O8.2	1	-0.0017 ± 0.0047	4.109 ± 0.059	3.991	3.0
	Mo↔O19.1	2	-0.0011 ± 0.0022	3.743 ± 0.024	4.071	8.1
	Mo↔O22.2	2	-0.0011 ± 0.0022	3.828 ± 0.024	4.156	7.9
	Mo↔O18.2	2	0.0214 ± 0.0633	4.423 ± 0.307	4.605	4.0
	Mo↔O4.2	2	0.0214 ± 0.0633	4.592 ± 0.307	4.774	3.8
	Mo↔Mo5.1	1	0.0112 ± 0.0223	4.979 ± 0.160	4.877	2.1
	Mo↔Mo5.2	1	0.0112 ± 0.0223	5.377 ± 0.160	5.275	1.9
	Mo↔O21.1	2	0.0039 ± 0.0693	4.781 ± 0.515	5.120	6.6
	Mo↔O21.2	2	0.0039 ± 0.0693	4.893 ± 0.515	5.231	6.5
	Mo↔Mo2.1	2	0.0130 ± 0.0270	6.151 ± 0.236	6.144	0.1
	Mo↔Mo1.1	2	0.0130 ± 0.0270	6.330 ± 0.236	6.322	0.1

Table 4.17: The EXAFS-derived structural parameters for a $[NBu^n_4]_4[PMo_{12}O_{40}(FeCl)_2]$ + $[NBu^n_4]_3[PMo_{12}O_{40}]$ fit to the Mo K edge EXAFS spectrum for $[NBu^n_4]_3[PMo_{12}O_{40}]$ + $FeCl_2$ in acetonitrile. XRD data for $[PMo_{12}O_{40}(FeCl)_2]^{4-}$ is provided for comparison.

Site	Path	Degeneracy	σ^2 / Å^2	r / Å	r / Å (XRD)	Error / %
Fe^{III}	Fe↔N	1	0.0039 ± 0.0324	2.195 ± 0.104	-	
	Fe↔Cl	3	0.0047 ± 0.0074	2.198 ± 0.107	-	
Fe^{I}	Fe↔N	3	0.0039 ± 0.0324	2.194 ± 0.104	-	
	Fe↔Cl	1	0.0047 ± 0.0074	2.198 ± 0.107	-	
$[PMo_{12}O_{40}(FeCl)_2]^{4-}$	Fe↔Cl	1	0.0108 ± 0.0459	2.364	2.204	7.3
	Fe↔O_b	4	0.0032 ± 0.0020	2.016 ± 0.034	1.951	3.3
	Fe↔Mo	4	0.0093 ± 0.0019	3.143 ± 0.017	3.102	1.3

Table 4.18: The EXAFS-derived structural parameters for a $[NBu^n_4]_4[PMo_{12}O_{40}(FeCl)_2]$ + $FeCl_3(NCCH_3)$ + $FeCl(NCCH_3)_3$ fit to the Fe k edge EXAFS spectrum for $[NBu^n_4]_3[PMo_{12}O_{40}]$ + $FeCl_2$ in acetonitrile. XRD data for $[PMo_{12}O_{40}(FeCl)_2]^{4-}$ is provided for comparison.

Anion	Edge	Parameter	Value
$[Mo_{12}O_{40}]^{4-}$	Mo K	R (%)	2.94
+		R, k = 1 (%)	0.71
$FeCl_2$		R, k = 2 (%)	2.57
+		R, k = 3 (%)	5.56
$[PMo_{12}O_{40}(FeCl)_2]^{4-}$		Chi-square	8592
Solution		Reduced chi-square	368
		Amplitude reduction factor	0.73 ± 0.06
		k range (Å^{-1})	3.0 - 20.7
		R range (Å)	1.0 - 6.5
		No. of independent parameters	61
		No. of variables	38
	Fe K	R (%)	0.43
		R, k = 1 (%)	0.19
		R, k = 2 (%)	0.33
		R, k = 3 (%)	0.78
		Chi-square	145
		Reduced chi-square	21
		Amplitude reduction factor	1.00
		k range (Å^{-1})	3.0 - 13.7
		R range (Å)	1.0 - 5.0
		No. of independent parameters	26
		No. of variables	20

Table 4.19: Refined parameters for fits to $[NBu^n_4]_3[PMo_{12}O_{40}]$ + $FeCl_2$ in acetonitrile.

4.2.5 QEXAFS Study of $[NBu_4]_5[(PMo_{12}O_{40})_2Y]$

Fitting a model to the Y K edge EXAFS of $[NBu_4]_5[(PMo_{12}O_{40})_2Y]$ has not been successful, however, it is clear from the EXAFS Fourier transforms (figure 4.25) that a cluster is being formed around the yttrium (spectra are not phase corrected). The Fourier transform spectrum for YCl_3 in the solid state (black spectrum in figure 4.21) exhibits peaks at 2.24 Å and 3.62 Å due to the Y-Cl bond and Y···Y distance respectively. The Fourier transform spectrum for $[NBu^n_4]_5[(PMo_{12}O_{40})_2Y]$ in acetonitrile (red spectrum in figure 4.21) exhibits peaks at 1.84 Å and 3.07 Å due to the Y-O and Y···Mo distances respectively. The peak at 3.07 Å has much higher amplitude, due to the high coordination number for this path as is the case in the spectra for the other Keggin-type molybdates that have been studied. The Fourier transform for the Y K edge EXAFS of the reaction solution containing $[NBu^n_4]_5[(PMo_{12}O_{40})_2Y]$ and YCl_3 as starting materials exhibits peaks at 2.09 Å. This peak is an average of the Y-Cl peak at 2.24 Å in the YCl_3 spectrum and the Y-O peak at 1.84 Å in the $[NBu^n_4]_5[(PMo_{12}O_{40})_2Y]$ spectrum. There are two more peaks in the spectrum for the reaction solution at 2.91 Å and 3.62 Å due to the Y···Mo distance in the POM and Y···Y distance in YCl_3, respectively. This provides evidence that a cluster is being formed around the yttrium atom.

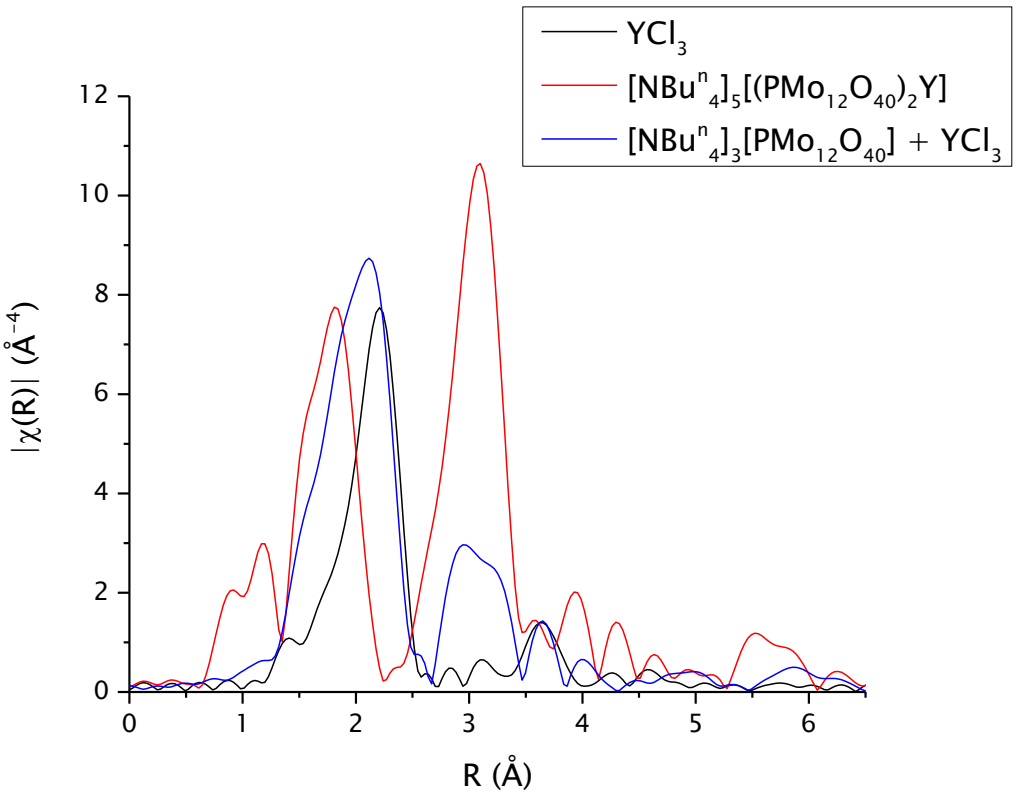

Figure 4.25: k^3-weighted Fourier transforms of Y K edge EXAFS of YCl_3 in the solid state, $[NBu^n_4]_5[(PMo_{12}O_{40})_2Y]$ in acetonitrile and the reaction between YCl_3 and $[NBu^n_4]_3[PMo_{12}O_{40}]$ in acetonitrile.

4.3 Experimental

4.3.1 XAFS Spectroscopy

X-ray absorption spectra were recorded on beamline B18 with a Si (111) double crystal monochromator at Diamond Light Source operating with an electron energy of 3 GeV and a current kept near 300 mA by top up mode. An Ortec Ge SSD 9 element detector was used in fluorescence mode to record soft X-ray K-edge spectra. Scan times were 0.3 sec / point, 1 eV / point and 2200 points per spectrum. X-ray absorption spectra were recorded in fluorescence mode at the metal K edges. Solid samples were diluted in boron nitride and held in a pellet mount. Aluminium cells with windows of 3mm thickness were used to obtain multiple solution spectra. Sample concentrations were 120 mM in molybdenum for Mo K edge measurements and 20 mM in the heterometal for heterometal K edge measurements. Removal of background and curve-fitting analyses were carried out with Demeter (version 5.12.3.0).

4.4 Conclusions

XAFS spectroscopy has proved a powerful method for studying Keggin-type POMs. $[PMo_{12}O_{40}]^{3-}$ has been characterised in acetonitrile with $[Bu^n_4]^-$ and $[PPN]^-$ as the counter ion. EXAFS spectroscopy has been used to characterise and compare a number of capped Keggin-type POMs at the Mo K edge: $[NBu^n_4]_3[PMo_{12}O_{40}H_2]$, $[NBu^n_4]_3[PMo_{12}O_{40}H_4]$, $[NBu^n_4]_3[PMo_{12}O_{40}Na_2]$, $[NBu^n_4]_3[PMo_{12}O_{40}Na_4]$, $[NBu_4]_3[PMo_{12}O_{40}(VO)_2]$ and $[NBu^n_4]_4[PMo_{12}O_{40}(FeCl)_2]$. $[NBu_4]_3[PMo_{12}O_{40}(VO)_2]$ and $[NBu^n_4]_4[PMo_{12}O_{40}(FeCl)_2]$ have also been characterised at the V K adge and Fe K edge respectively. $[NBu^n_4]_4[PMo_{12}O_{40}(FeCl)_2]$ has been characterised in the solid state and in acetonitrile at the Mo K edge and in acetonitrile at the Fe K edge. The reductive aggregation reaction adding $FeCl_2$ to $[PMo_{12}O_{40}]^{3-}$ to produce $[PMo_{12}O_{40}(FeCl)_2]^{4-}$ has been followed at the Mo K edge and Fe K edge. The reductive aggregation reaction adding yttrium to $[PMo_{12}O_{40}]^{3-}$ has been followed. The EXAFS suggest that a heteropolyanionic cluster is being formed. It is possible to distinguish between the POMs investigated in this chapter. This has been demonstrated in figure 4.26.

Figure 4.27 shows the fragment of the Keggin-type molybdate that is detectable from the absorbing atom (Mo2.1 in figure 4.27) using EXAFS spectroscopy. The oxygen atoms that are highlighted in yellow in the figure vary to a large degree from the XRD crystallographic data that was used to model the POMs in the curve-fitting analysis. The distance of these oxygen atoms from the absorbing atom vary by a range of 0.10 Å – 0.32 Å from the crystallographic data. The ligand (L1.1) on the heterometal (M1.1) in the figure may also vary from the crystallographic data by ca. 0.2 Å. It is possible that some of these discrepancies are due to the use of crystallographic data for solid $[NBu^n_4]_4[PMo_{12}O_{40}(FeCl)_2]$ to model structures with different capping groups and reduced $[PMo_{12}O_{40}]$ structures in solution, however the curve-fitting analysis for $[NBu^n_4]_4[PMo_{12}O_{40}(FeCl)_2]$ in the solid state also gives the same discrepancies. The contribution to the EXAFS by these atoms are weak and it is possible that EXAFS spectroscopy is not currently a powerful enough technique to give well refined distances for these weakly contributing scattering atoms.

In previous EXAFS studies of nickel complexes and POMs (including $[PMo_{12}O_{40}]^{3-}$ structures), the error between the EXAFS-derived structural parameters and XRD data was 1 – 1.5 %.[5,6,88] Absolute error reported in this chapter for Mo K edge EXAFS are as high as 37 %. For these shells (1 shell in each of the fits for the reduced POMs), the contribution to the EXAFS is weak and the error margins for all other shells are below 15 %. For the first shells of oxygen atoms and molybdenum atoms, error margins are less than 5 %. Many more shells are included in the fits reported in this chapter than are included in the previously reported experiments. All the shells of atoms up to 6.3 Å from the absorbing atoms are included in these fits. The use of extra variable parameters in the fits to include all these extra shells with weak contributions to the EXAFS makes the model much more complicated and this may contribute to the larger error margins. $[NBu^n_4]_4[PMo_{12}O_{40}(FeCl)_2]$ XRD data was used to compare with the EXAFS-derived structural parameters, so the error may be larger as the POM is reduced or the capping group is different to the XRD data. Multiple scattering paths have also been included which has made it possible to determine some bond angles. This has required more variable parameters to be used in the fits, further complicating the model. With the use of so many parameters in the fit, it may be expected that the absolute error may be higher.

The data range that can now be collected by XAFS spectroscopy for these POMs has been shown to be larger now in comparison to previous experiments. In 1996, saturated solutions were used to collect data for $[PMo_{12}O_{40}]^{3-}$ structures up to ca. 18 $Å^{-1}$,[5] but in this chapter 120 mM solutions have been used to collect data up to ca. 20 $Å^{-1}$.

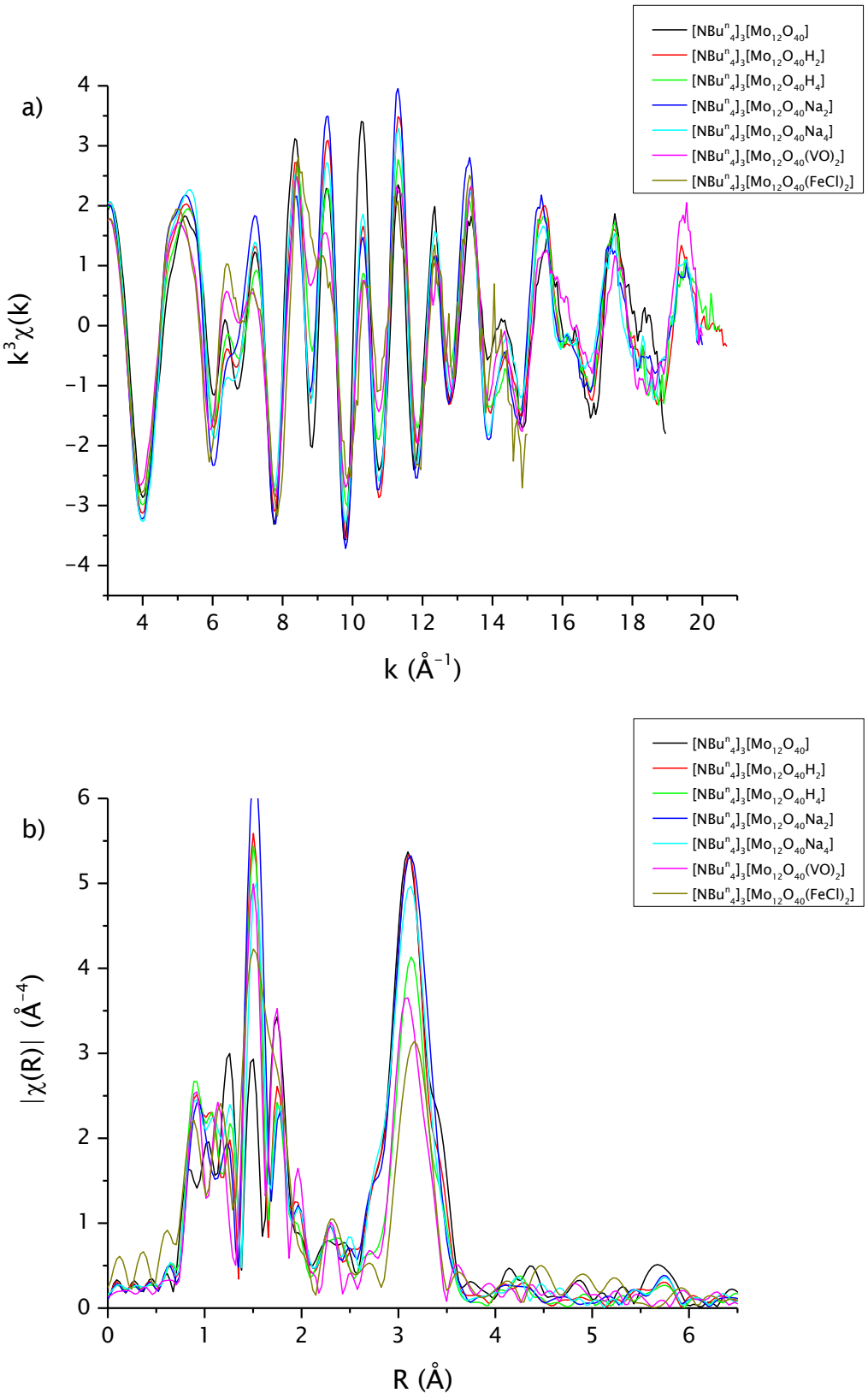

Figure 4.26: k^3-weithed Mo K edge a) EXAFS spectra and b) Fourier transforms of Keggin-type molybdate anions in the acetonitrile.

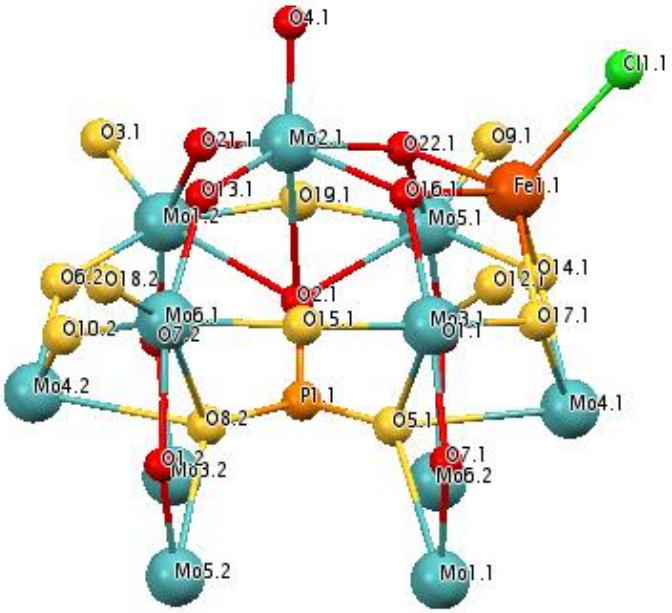

Figure 4.27: Fragment of the Keggin-type molybdate that can be detected by EXAFS spectroscopy. Atoms coloured yellow have been refined by EXAFS spectroscopy to distances from the absorbing atom (Mo2.1) that vary significantly from crystallographic data.

5. Differentiation of Ground and Excited States of Copper Complexes by X-Ray Emission Spectroscopy

5.1 Introduction

XAFS has been used to study the steps in photochemical reactions[89] and the photo-excitation reactions of Cu^{I} bisphenanthroline complexes (figure 5.1) are understood in more detail since they have been analysed on the nanosecond timescale using XAFS spectroscopy.[42] XAFS measurements have demonstrated that the copper site in the ^{3}MLCT excited state of these Cu^{I} complexes resembles a Cu^{II} site.[42] This excited complex acquires a flattened pseudo-tetrahedral geometry and in cases where the substituents ortho to the nitrogen atoms are small, for example hydrogen atoms or methyl groups, an exciplex forms in which a solvent molecule binds to the complex. Large substituents ortho to the nitrogen atoms, for example tertiary butyl groups, block the access of the solvent molecule to the complex.[90] The flattening of the complex is reduced by the presence of bulky substituents.[91] Distinguishing between the ground and excited states is difficult due to the low proportions of the transient species (less than 10 % of the components in the solution) and the overlap of their spectra.

The positions of the K_{β} emission for some 3d transition metals (for example, iron and manganese) have a linear dependence on the oxidation state of the metal, whereas the position of the K_{α} emission depends on peak width.[92] The K_{β} emission is more sensitive to the oxidation state than the K_{α} emission due to the larger interaction of the 3p3d multiplet than the 2p3d. Multiplets are not present in Cu^{I} and Cu^{II} species. The excited state has a $1s^{1}3d^{10}$ electron arrangement, with emission to form $1s^{2}2p^{5}3d^{10}$ (K_{α}) or $1s^{2}3p^{5}3d^{10}$ (K_{β}). It is reasonable to expect the K_{α} to be more sensitive than the K_{β} in copper systems

because there are no multiplet effects and the 2p orbital is closer to the nucleus and less shielded from the nuclear charge than the 3p orbital.

RIXS spectroscopy has been used previously to study CuO.[93-95] Preliminary 1s2p (K_α) and 1s3p (K_β) RIXS calculations have been performed for Cu_2O and CuO (model Cu^{I} and Cu^{II} structures) using FEFF9.[96] The 1s2p RIXS plots (energy transfer vs incident energy) are shown in figure 5.2. These RIXS calculations are not optimised for any parameters. The difference between the K_α RIXS emission energy in these plot is ~4 eV and only ~1 eV for the K_β. For this reason the K_α emission was investigated in this experiment.

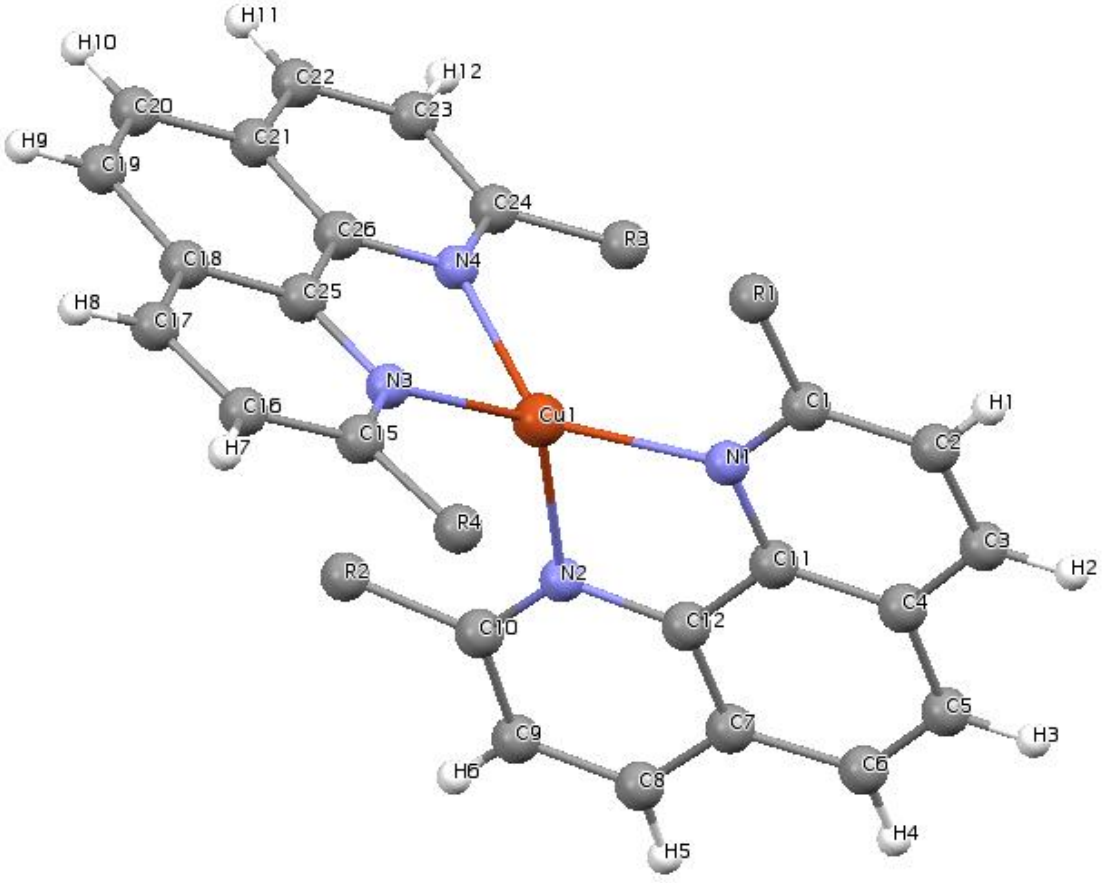

Figure 5.1: Structure of $[Cu(diimine)_2]^+$.

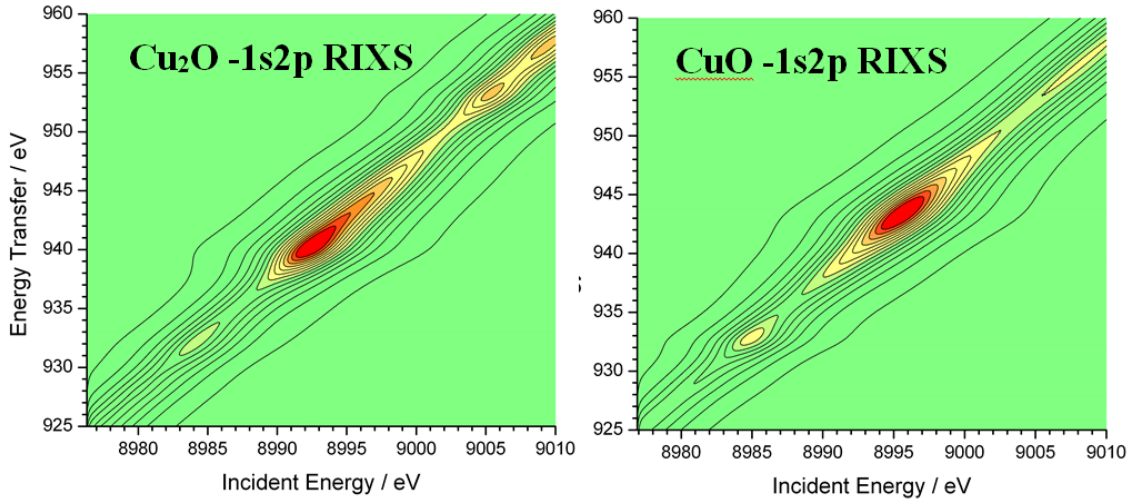

Figure 5.2: FEFF9 1s2p (K_α) RIXS calculations for Cu_2O and CuO.[96]

5.2 Results and Discussion

X-ray emission spectroscopy (XES) and resonant inelastic X-ray scattering (RIXS) can provide a means of increased chemical speciation by selecting specific excitation and emission energies and provides a means of better probing the excited states of the copper diimine complexes. This has been tested using the Cu K_α XES (1s-2p transitions) and RIXS. Transient absorption (TA) measurements for $[Cu^{I}(dmp)_2][PF_6]$, $[Cu^{I}(dpp)_2][PF_6]$, $[Cu^{I}(dbp)_2][PF_6]$ (dbp = 2,9-di-n-butyl-1,10-phenanthroline) and $[Cu^{I}(bcp)_2][PF_6]$ (bcp = 2,9-dimethyl-4,7-diphenyl-1,10-phenanthroline) have been carried out on ULTRA (LSF at RCaH), using a circulating flow cell system under anaerobic conditions. The structures of the ligands in these copper complexes are presented in figure 5.3.

CuO and Cu_2O were used to establish the K_α emission spectrum, for a Cu^{I} and a Cu^{II} species. The K_α emission is more intense than the K_β emission and measuring the K_α emission will allow quicker experiment times. In order to measure copper species which are as close as possible to the photochemistry system of interest (geometry and hybridisation may affect the position of the XAS / XES lines, in addition to the oxidation state), the ground state $[Cu^{I}(dmp)_2]^+$ was measured. Spectra for the Cu^{I} ground state were recorded in the solid state and the sample mount for the pellets used in these experiments is shown in figure 5.4. The full 1s2p K_α RIXS plane was measured to identify all the different XANES / XES features at high resolution. Once the RIXS and XES measurements had been collected for $[Cu^{I}(dmp)_2][PF_6]$, the same XES measurements for an electrochemically oxidised sample of the complex in CH_3CN was recorded to create the ^{3}MLCT-exciplex state.[42] The anaerobic circulating flow system was connected to an electrochemical cell (figure 5.5) to allow X-ray fluorescence XAS measurements. A platinum mesh was attached to the electrode in the cell to allow uniform oxidation of the copper complex throughout the cell. The mesh was placed behind the Kapton window and the X-ray beam was aligned so that it passed through one of the holes in the mesh. The setup of the electrochemical cell with the UV / Vis spectrometer on the beamline is displayed in figure 5.6. Between scans the cell was moved relative

to the laser / X-ray irradiation region to prevent sample decay from either the X-Ray beam or the UV / Vis laser.

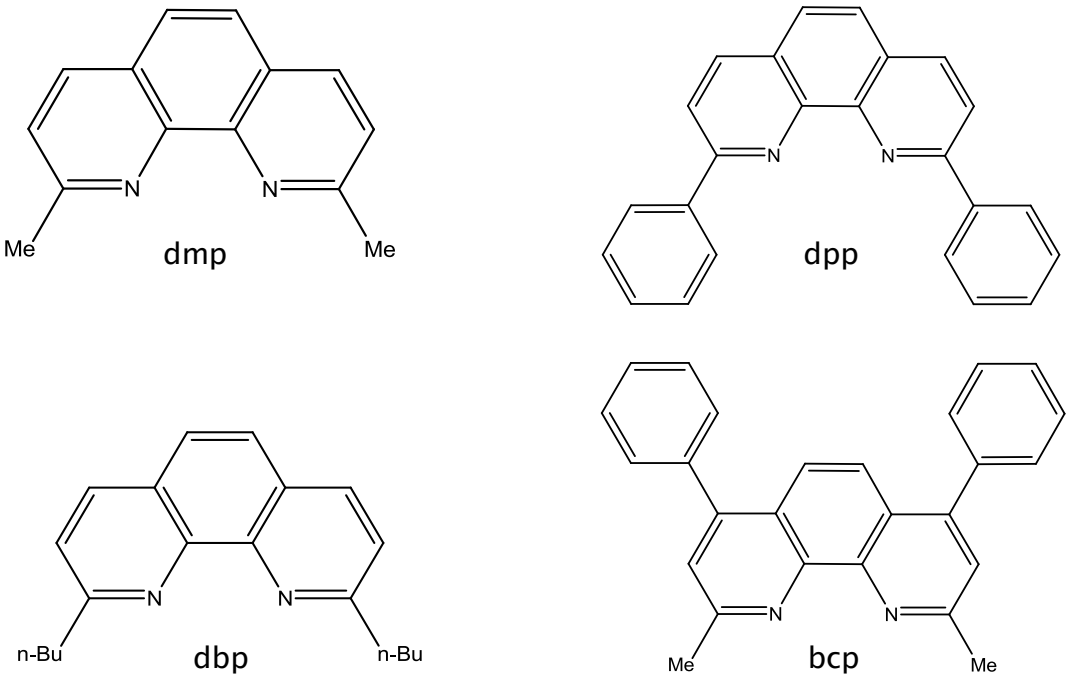

Figure 5.3: Phenanthroline derivatives used as ligands in copper complexes.

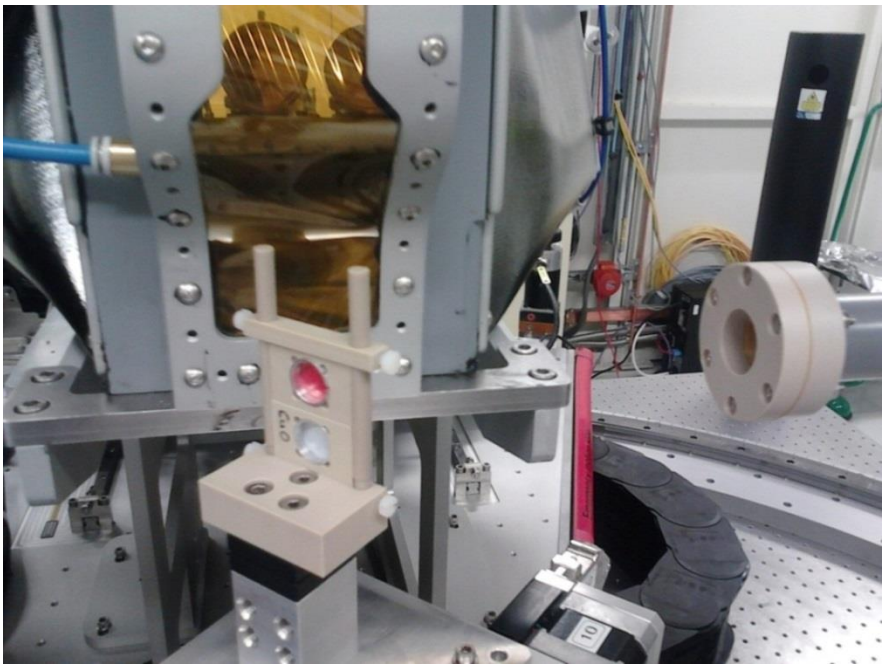

Figure 5.4: XAS pellet mount in the X-ray beam.

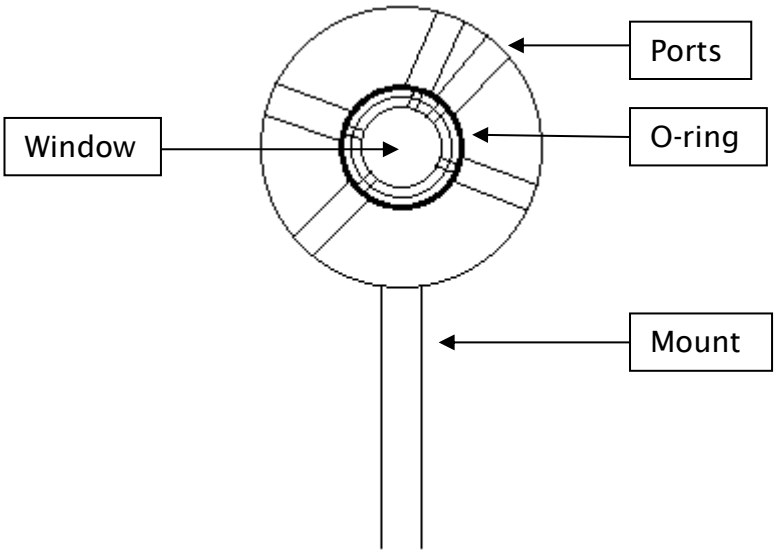

Figure 5.5: Diagram of the electrochemical cell used in the XAS experiments.

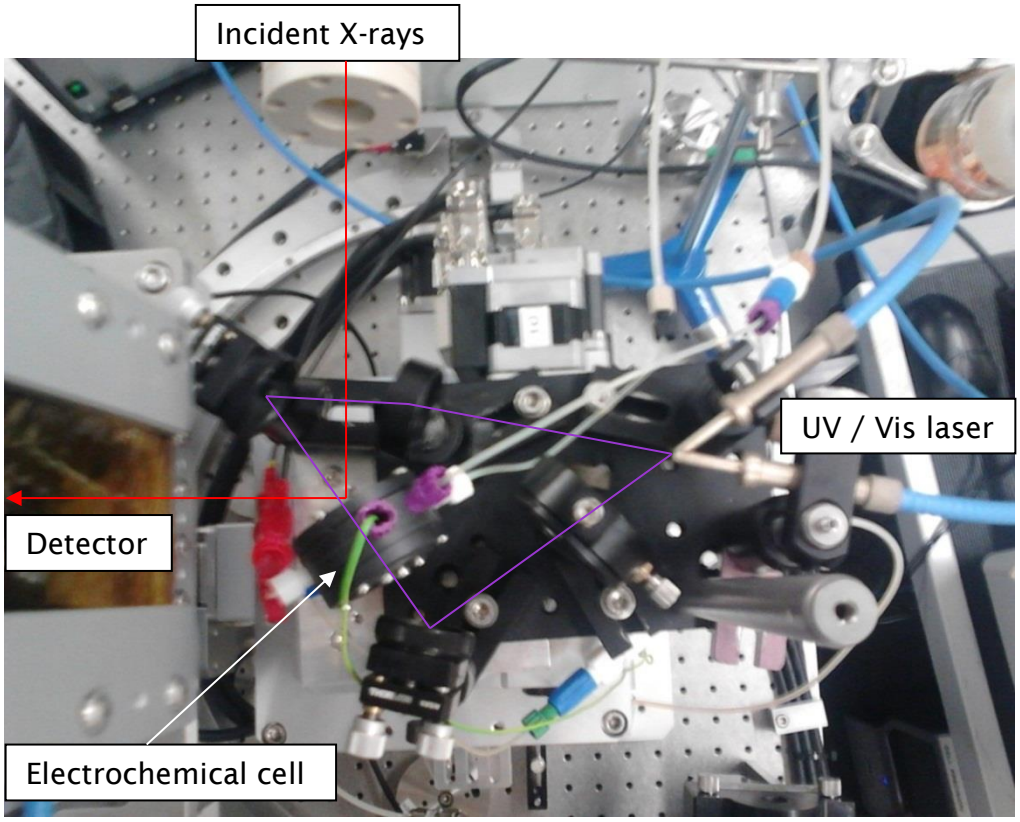

Figure 5.6: Electrochemical XAS cell with UV / Vis spectrometer on the beamline. Red line = X-Ray beam, purple line = UV / Vis beam.

5.2.1 Stability of Copper Diimine Complexes

UV / Vis spectra have been measured for the ground states of $[Cu^{I}(dmp)_2][PF_6]$ $[Cu^{I}(dpp)_2][PF_6]$, $[Cu^{I}(dbp)_2][PF_6]$ and $[Cu^{I}(bcp)_2][PF_6]$ and the spectra are in agreement with previously reported spectra.[91,97-101] The peaks between 400 and 500 nm correspond to MLCT transitions. The UV / Vis spectra and Beer-Lambert plots are presented in 5.7 – 5.10. There is no positive or negative deviation from the Beer-Lambert law for any of the complexes, indicating that they do not associate or dissociate. UV / Vis spectra were measured in acetonitrile in quartz cuvettes with a path length of 1 cm.

The UV / Vis spectrum for $[Cu^{I}(dpp)_2][PF_6]$ has a shoulder feature from 500 – 650 nm. It has been reported,[102] based on previous studies of Cu^{I} diimine complexes with substituents in the 2 and 9 positions of the diimine ligand,[91,101] that the shoulder feature corresponds to MLCT transitions from the flattened pseudotetrahedral geometry. The weaker shoulder features in the UV / Vis spectra for the other 3 copper diimine complexes indicate that they have a tetrahedral geometry.[97-99]

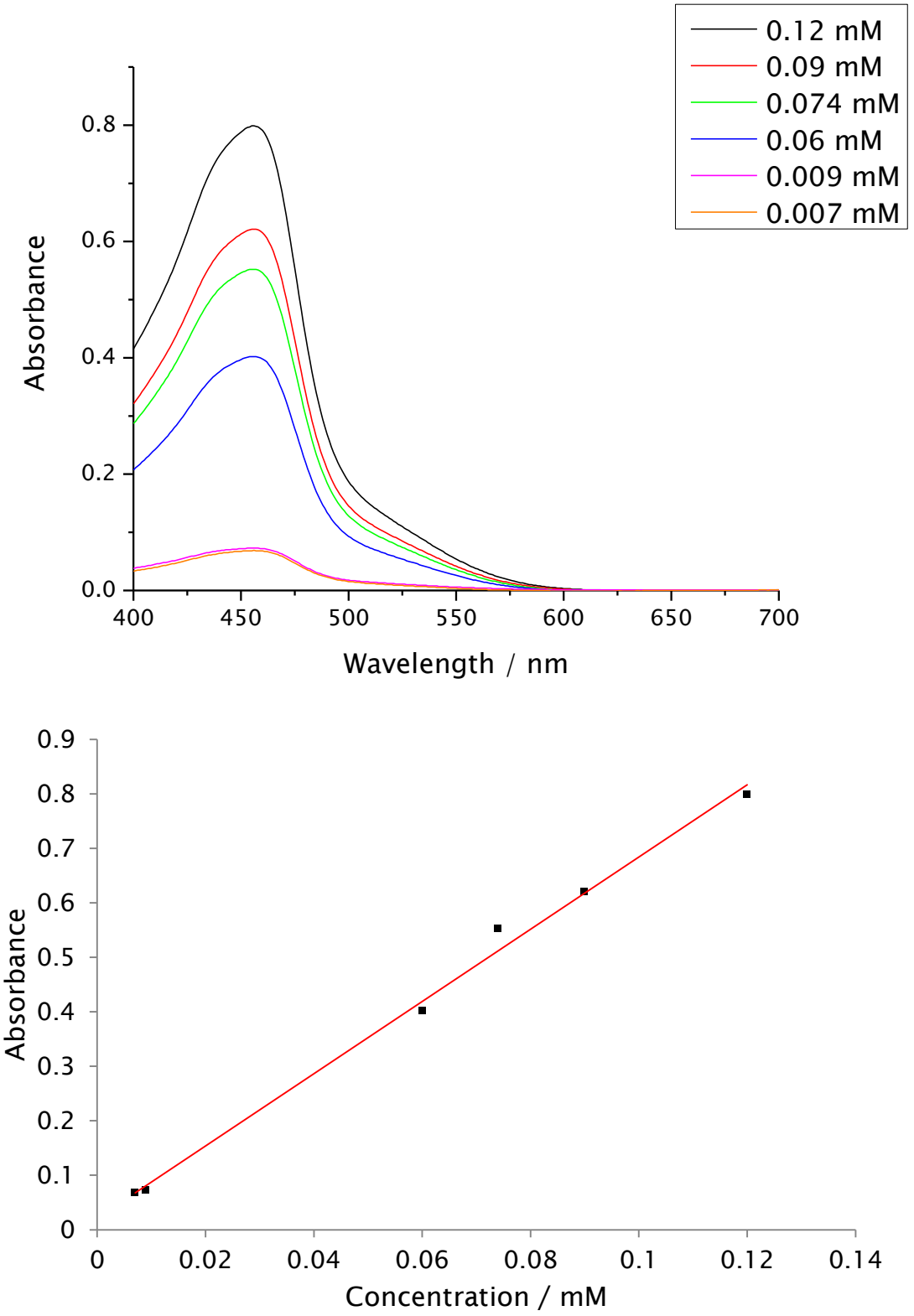

Figure 5.7: a) UV / Vis spectra at various concentrations and b) Beer-Lambert plot for $[Cu(dmp)_2][PF_6]$ in acetonitrile.

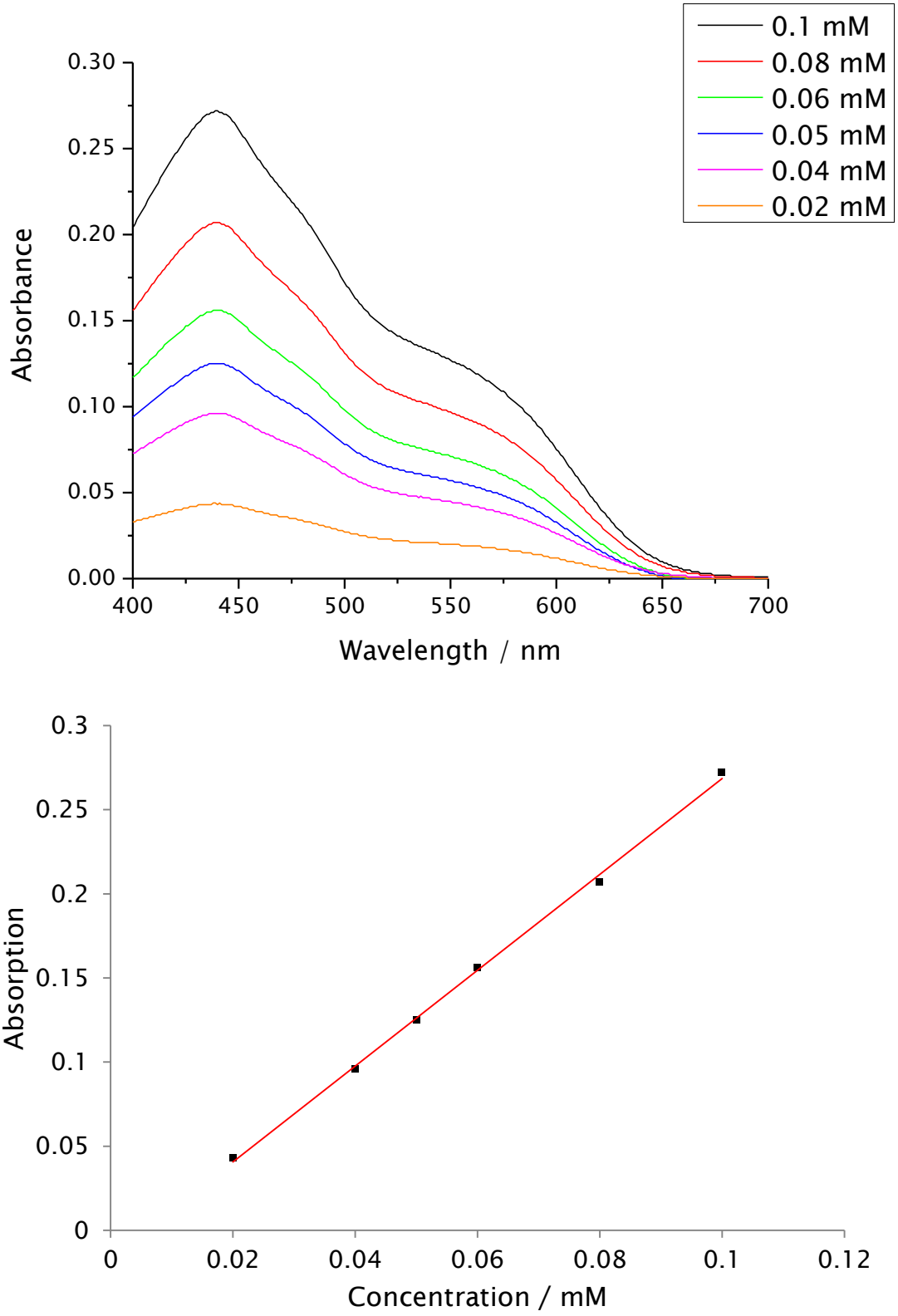

Figure 5.8: a) UV / Vis spectra at various concentrations and b) Beer-Lambert plot for $[Cu(dpp)_2][PF_6]$ in acetonitrile.

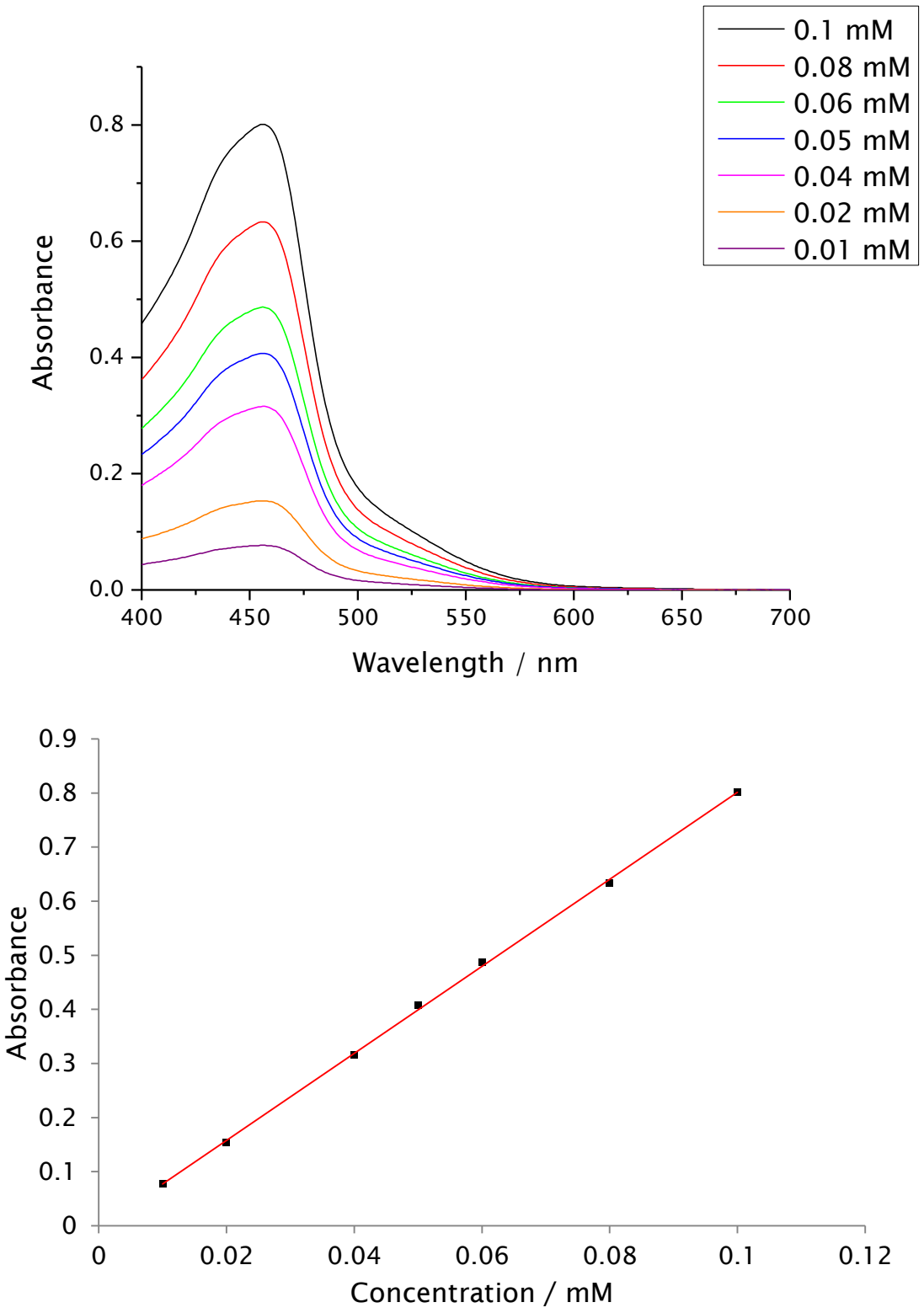

Figure 5.9: a) UV / Vis spectra at various concentrations and b) Beer-Lambert plot for [Cu^{I}(dbp][PF_6] in acetonitrile.

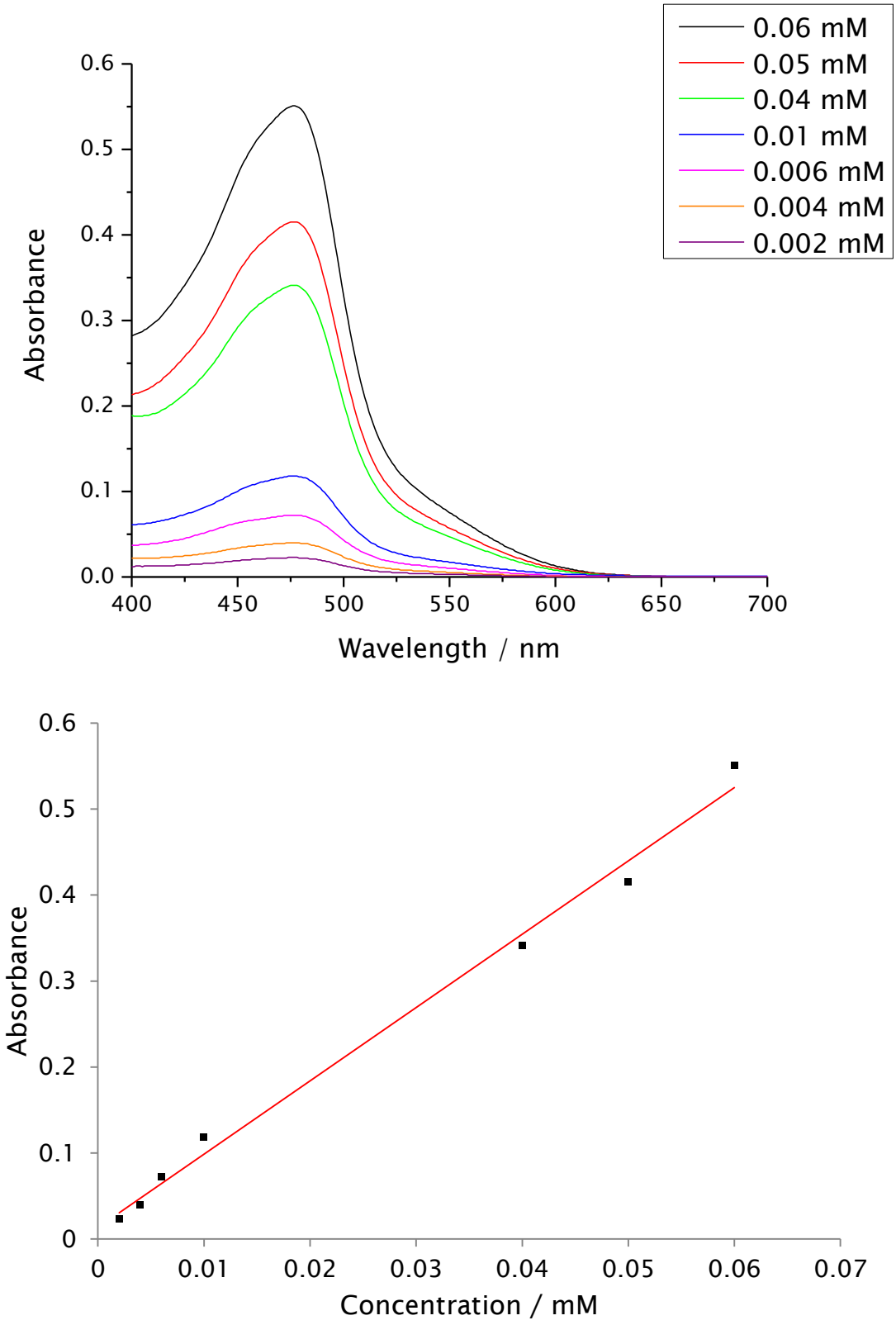

Figure 5.10: a) UV / Vis spectra at various concentrations and b) Beer-Lambert plot for $[Cu^{I}(bcp)][PF_6]$ in acetonitrile.

5.2.2 Excited State Lifetimes of Copper Diimine Complexes

$[Cu^{I}(dmp)_2]$, $[Cu^{I}(dpp)_2]$, $[Cu^{I}(dbp)_2]$ and $[Cu^{I}(bcp)_2]$ have been studied by TA spectroscopy. These TA spectra, with the excited state lifetime decays for these complexes are presented in figures 5.11 – 5.14 respectively. The TA spectra for $[Cu^{I}(dmp)_2]$ (2 mM in CH_2Cl_2) and $[Cu^{I}(dpp)_2]$ (2 mM in CH_3CN) were measured using a 200 nJ, 355 nm laser to excite the complex. The TA spectra for $[Cu^{I}(dbp)_2]$ (2 mM in CH_3CN) and $[Cu^{I}(bcp)_2]$ (4 mM in CH_3CN) were measured using a 100 nJ, 200 nm laser. Decay constants for the transient peaks have been calculated by fitting a first order decay to the graphs. The decay of the bleach peaks have also been calculated to check that the decay of transient and bleach peaks are consistent with each other. The decay of the transient peak and bleach peaks are the same within the standard error. The lifetimes of the excited states of $[Cu^{I}(dbp)_2]$ and $[Cu^{I}(bcp)_2]$ are shorter than expected – 29 ns and 3 ns respectively. The measured air pressure in the flow system was higher for $[Cu^{I}(dbp)_2]$ and $[Cu^{I}(bcp)_2]$ than for $[Cu^{I}(dmp)_2]$ and $[Cu^{I}(dpp)_2]$ so the short lifetimes of the former two were possibly due to the presence of oxygen in the solution.

The average lifetimes of the excited state of $[Cu^{I}(dmp)_2]$ have been calculated using 5 laser powers: 0.2 μJ, 0.3 μJ, 0.5 μJ, 0.6 μJ and 1.2 μJ. Plots for the excited state lifetime decays for the latter 4 laser powers are presented in figure 5.15. As the power of the laser is increased, the absorbance is increased to the same degree (figure 5.16). The gradient of the curves are 1.1 ± 0.5. The absorptions after 2 ns have been used in these plots. The wavelengths of the absorption maximums and average lifetimes of the excited states of $[Cu(dmp)_2][PF_6]$ and $[Cu(dpp)_2][PF_6]$ are consistent with previously reported excited state lifetimes. [1,102] The decay constants that have been derived from this study are presented in table 5.1.

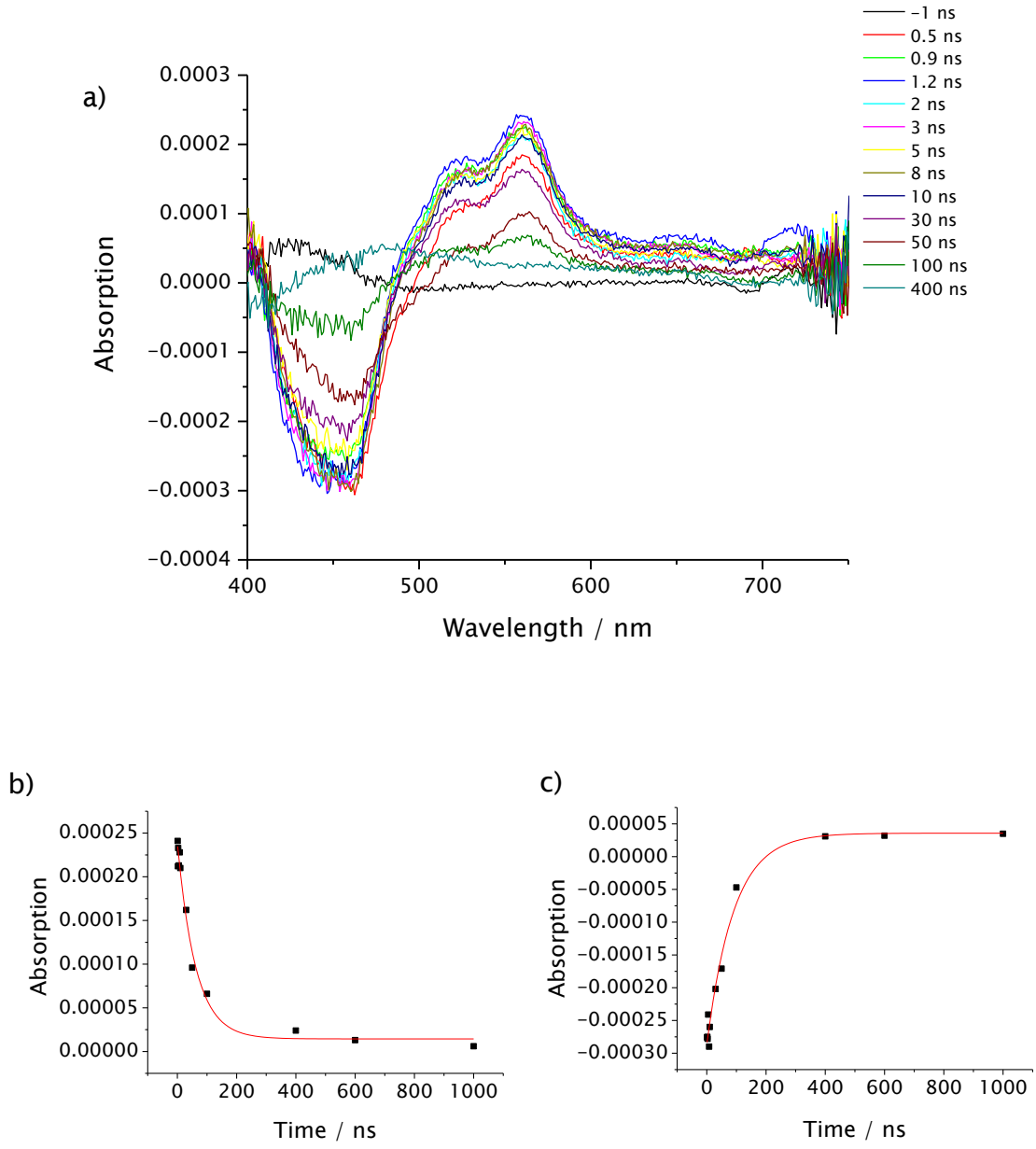

Figure 5.11: a) Transient absorption spectra for $[Cu(dmp)_2][PF_6]$ in CH_2Cl_2 at various time delays after photo-excitation and kinetics for decay of b) transient and (c) bleach of peaks using a 0.2 μJ laser at 355 nm.

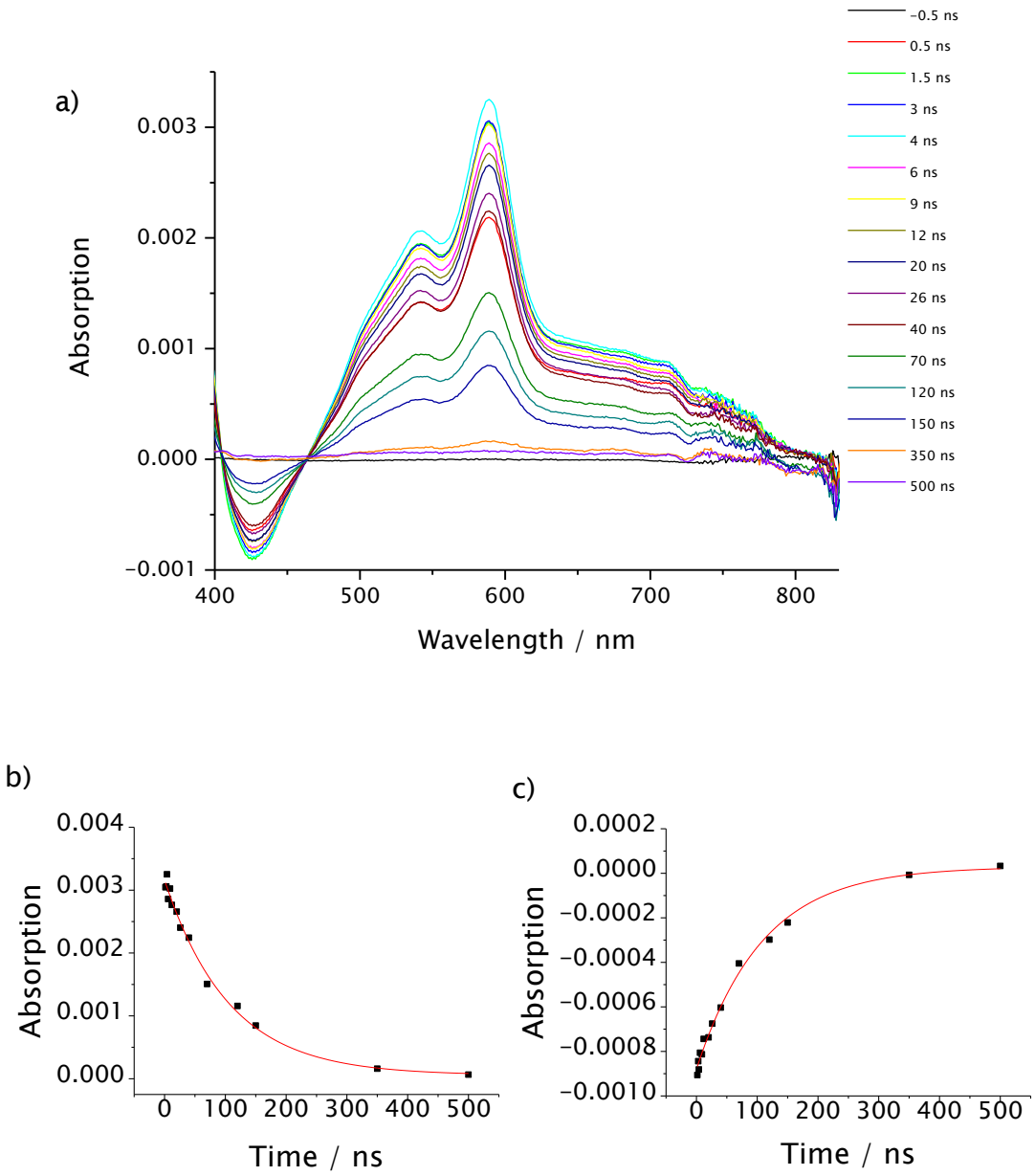

Figure 5.12: a) Transient absorption spectra of $[Cu^{I}(dpp)_2][PF_6]$ in acetonitrile at various time delays after photo-excitation and kinetics for decay of b) transient and c) bleach peaks using a 0.2 μJ laser at 355 nm.

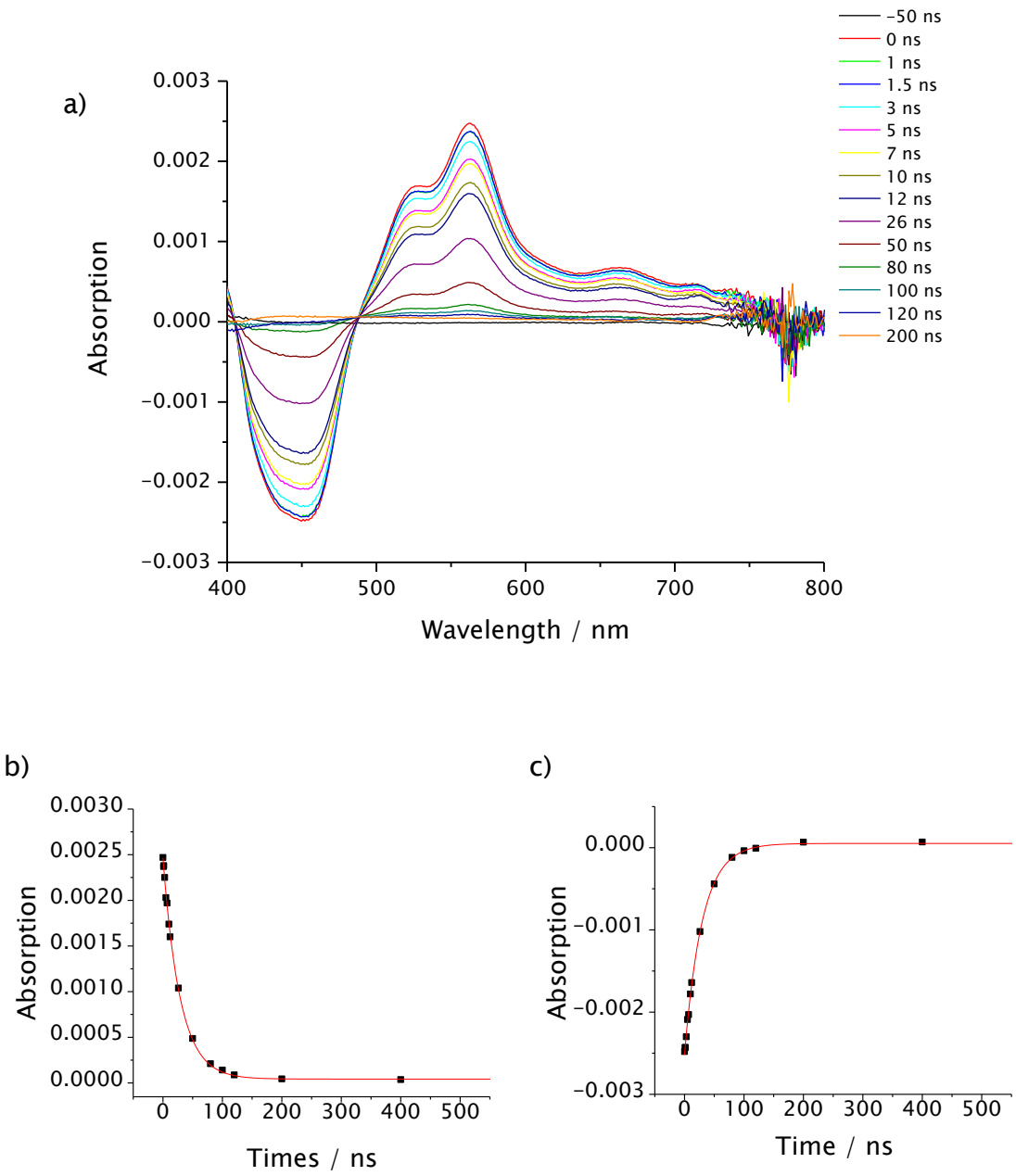

Figure 5.13: a) Transient absorption spectra of $[Cu^{I}(dbp)_2][PF_6]$ in acetonitrile at various time delays after photo-excitation and kinetics for decay of b) transient and c) bleach peaks using a 0.1 μJ laser at 200 nm.

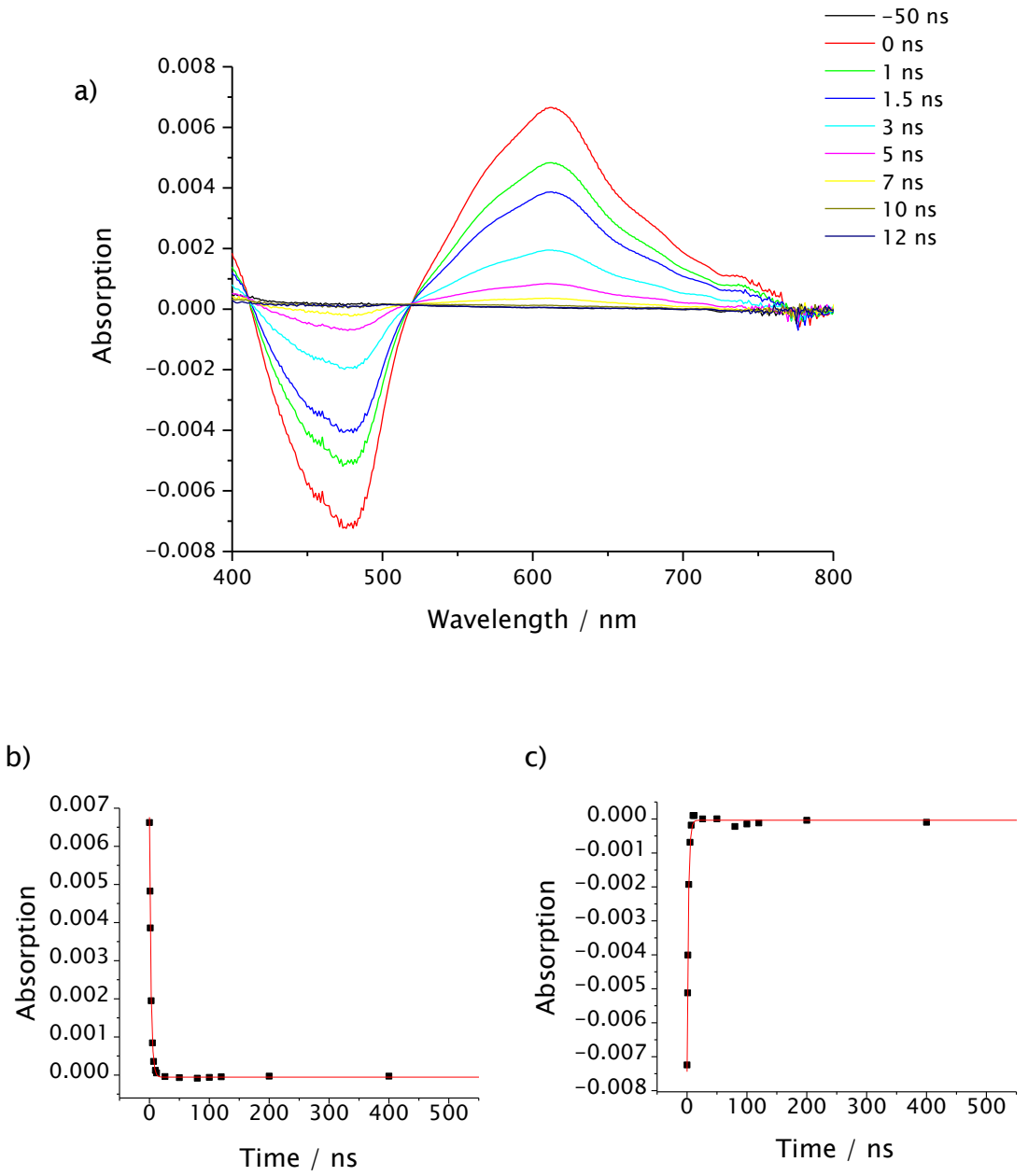

Figure 5.14: a) Transient absorption spectra of $[Cu^{I}(bcp)_2][PF_6]$ in acetonitrile at various time delays after photo-excitation and kinetics for decay of b) transient and c) bleach peaks using a 0.1 μJ laser at 200 nm.

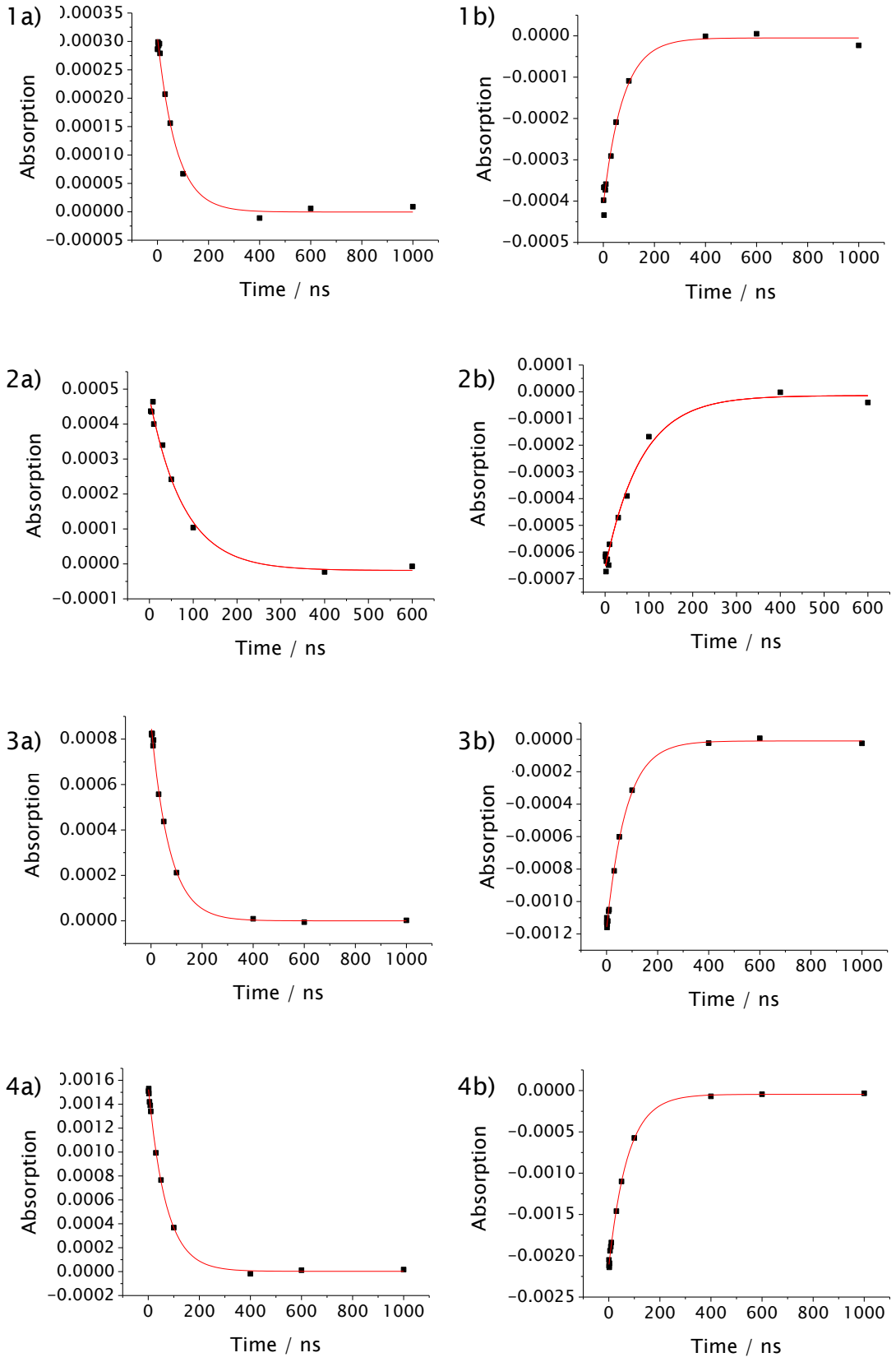

Figure 5.15: Kinetics for decay of a) transient peak and b) bleach peak of $[Cu(dmp)_2]^+$ using a (1) 0.3 μJ, (2) 0.5 μJ, (3) 0.6 μJ and (4) 1.2 μJ, 355 nm laser.

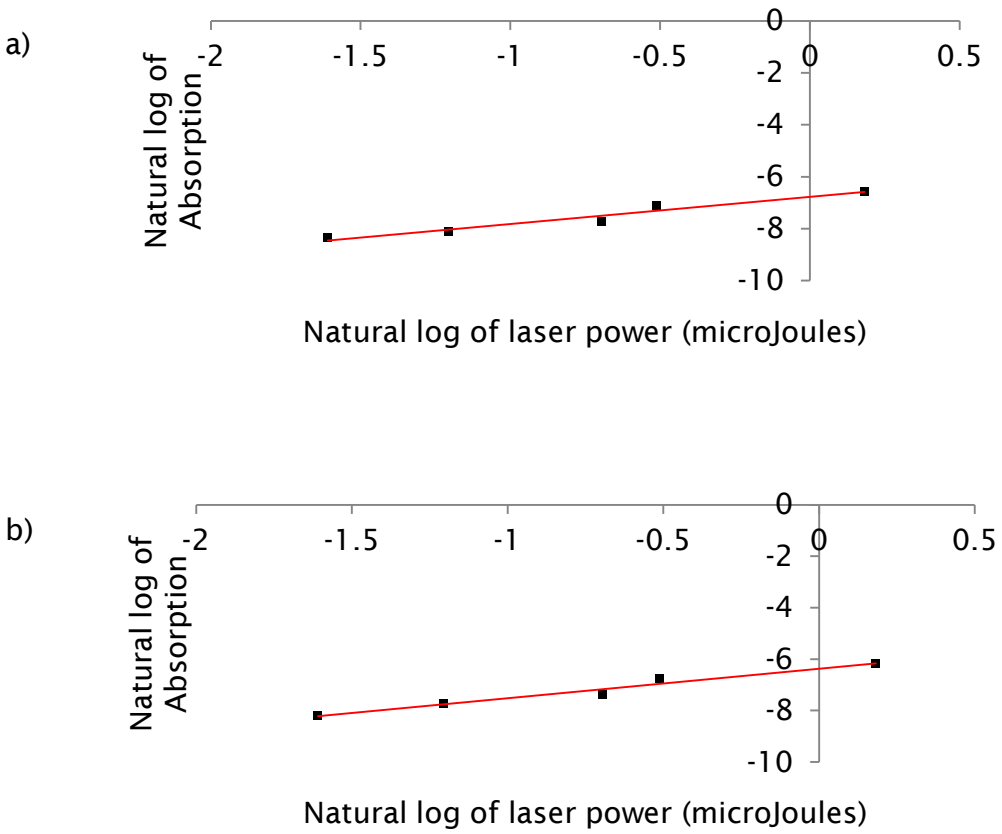

Figure 5.16: Kinetics of the a) transient and b) bleach during the photo-excitation of [Cu(I)(dmp)$_2$] in CH_2Cl_2 2 ns after excitation.

Complex	Laser Power (μJ)	Wavelength (nm)	Decay Constant (ns)	Reduced Chi-Square	Adj. R-Square
$[Cu(dmp)_2]^+$	0.2	561	62 ± 8	0.0000000002	0.98
		455	91 ± 12	0.0000000003	0.98
	0.3	561	73 ± 7	0.0000000002	0.99
		455	76 ± 9	0.0000000004	0.99
	0.5	561	78 ± 9	0.0000000005	0.99
		455	82 ± 10	0.0000000011	0.98
	0.6	561	72 ± 4	0.0000000004	1.00
		455	77 ± 4	0.0000000006	1.00
	1.2	561	69 ± 2	0.0000000003	1.00
		455	73 ± 3	0.0000000015	1.00
$[Cu(dpp)_2]^+$	0.2	589	107 ± 7	0.0000000100	0.99
		426	108 ± 8	0.0000000008	0.99
$[Cu(dbp)_2]^+$	0.2	563	29 ± 1	0.0000000006	1.00
		454	30 ± 1	0.0000000006	1.00
$[Cu(bcp)_2]^+$	0.2	610	3 ± 0	0.0000000076	1.00
		476	2 ± 0	0.0000000252	0.99

Table 5.1: Kinetic studies of the TA spectra for copper diimine complexes.

5.2.3 XAS / XES Study of $[Cu(dmp)_2][PF_6]$

The Cu K edge XAFS for solid ground state $[Cu(dmp)_2][PF_6]$ has been analysed. Two fits are reported. The first fit includes the shells containing the nitrogen atoms and 8 carbon atoms – model 1 (figure 5.17). The second fit includes the shells containing the nitrogen atoms and 12 carbon atoms – model 2 (figure 5.18). The XAFS-derived structural parameters refined in these fits are presented in table 5.2. Bond angles have been calculated from multiple scattering paths included in the fits and these are presented in table 5.3. Atom labels in the tables refer to the atom labels in the models. Data regarding the quality of the fits are presented in table 5.4. Refinement of the fit for model 1 gave Cu-N distances that agree with the crystallographic data used to model the $[Cu(dmp)_2][PF_6]$ complex. Inclusion of C4, C7, C18 and C21 in model 2 resulted in a refinement with shorter Cu-N bonds than are refined in the fit of model 1, but within the error margins of the fit, both fits agree strongly with the crystallographic data. The carbon atoms fit the peaks above 2.5 Å in the Fourier transform spectra. The Debye-Waller factors that are negative for the single scattering paths in the fit for model 1 are positive when model 2 is fitted to the XAFS spectrum. There is also better peak splitting in the XAFS for the fit of model 2 than in the fit of model 1.

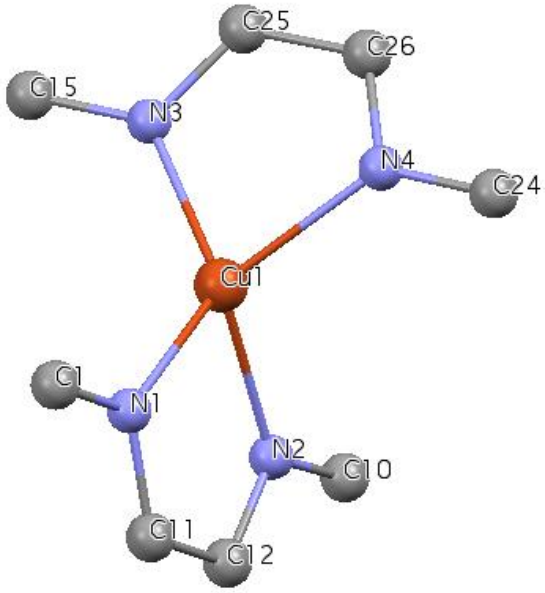

Figure 5.17: Structure of model 1 used in XAFS fitting.

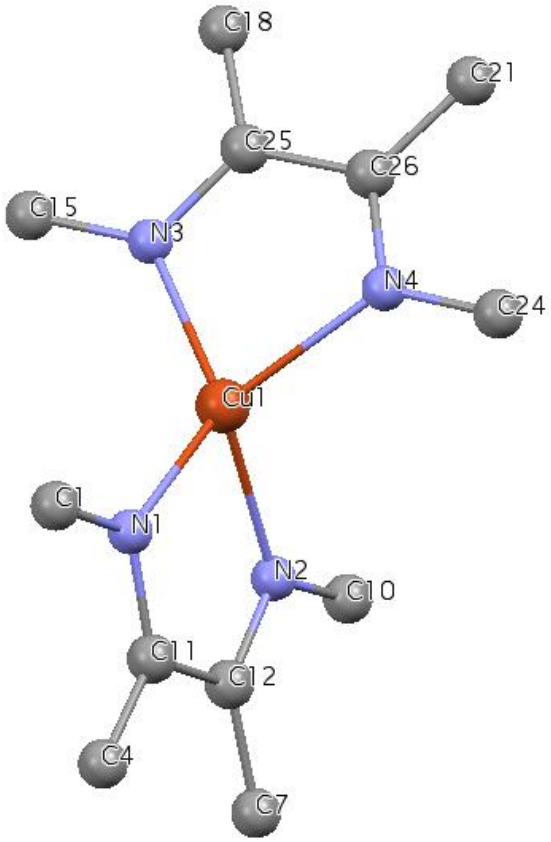

Figure 5.18: Structure of model 2 used in XAFS fitting.

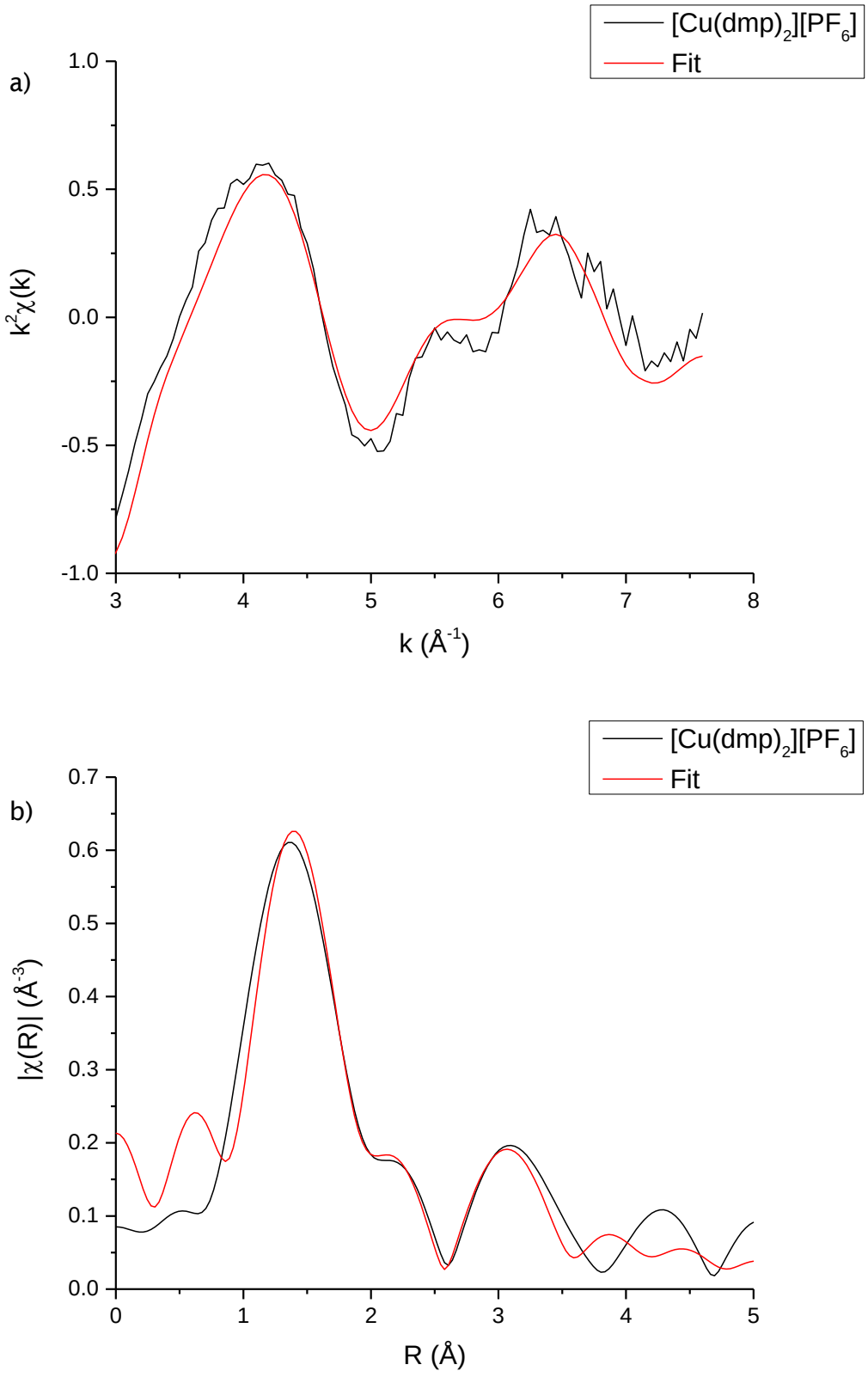

Figure 5.19: Model 1 fit to Cu K edge k^2-weighted a) XAFS spectrum and b) Fourier transform of $[Cu(dmp)_2]^+$ in acetonitrile.

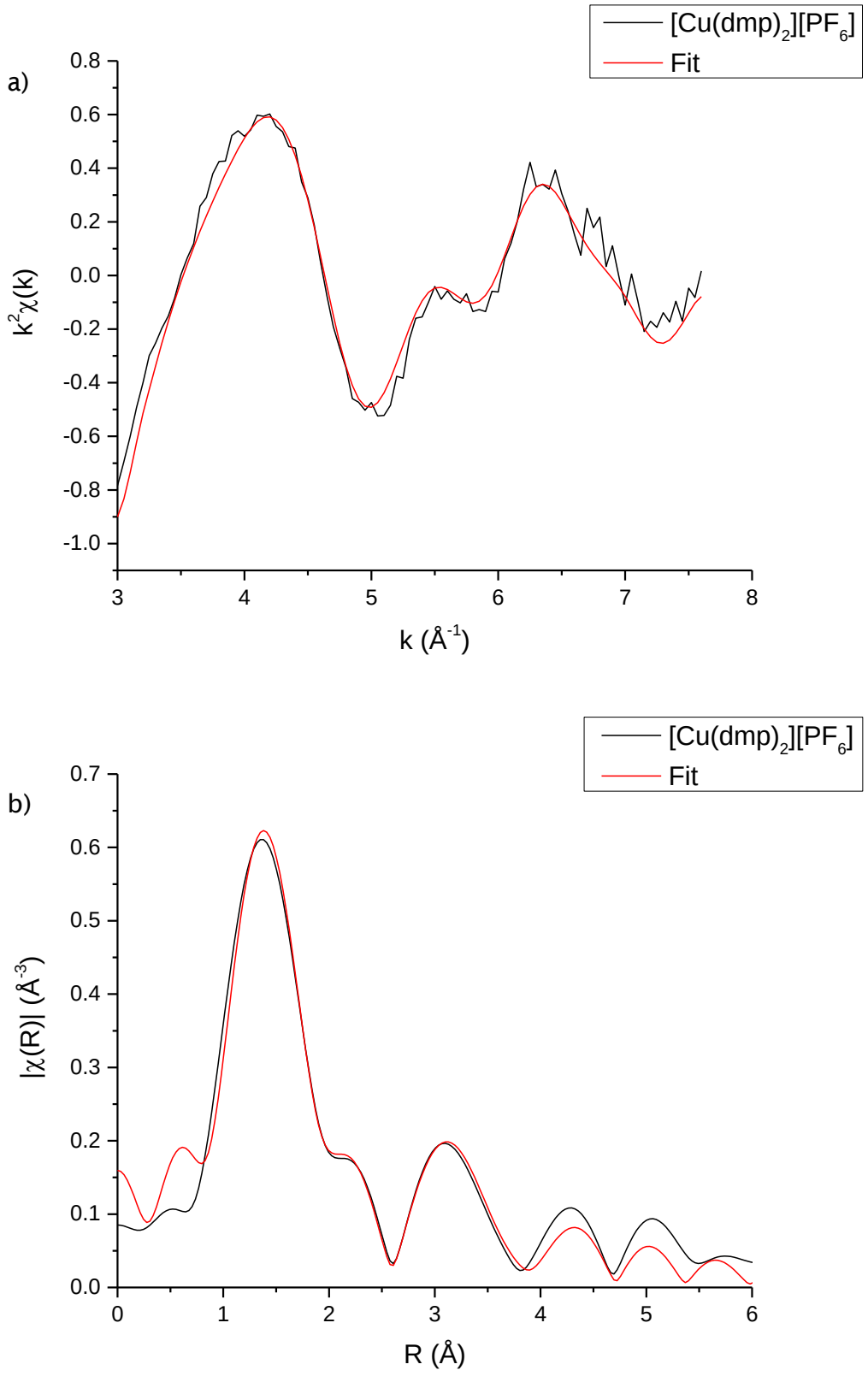

Figure 5.20: Model 2 fit to Cu K edge k^2-weighted a) XAFS spectrum and b) Fourier transform of $[Cu(dmp)_2]^+$ in acetonitrile.

Model	Shell	Degeneracy	σ^2 / Å^2	r / Å	r / Å (XRD)
1	N1	3	0.009 ± 0.007	2.04 ± 0.03	2.04
	N2	1	0.009 ± 0.007	2.07 ± 0.03	2.07
	C25	4	-0.013 ± 0.009	2.90 ± 0.06	2.85
	C1	2	-0.017 ± 0.008	3.16 ± 0.07	3.06
	C15	2	-0.017 ± 0.008	3.18 ± 0.07	3.09
2	N1	3	0.008 ± 0.016	1.98 ± 0.09	2.04
	N2	1	0.008 ± 0.016	2.01 ± 0.09	2.07
	C25	4	0.008 ± 0.032	2.78 ± 0.37	2.85
	C1	2	0.008 ± 0.032	2.99 ± 0.37	3.06
	C15	2	0.008 ± 0.032	3.02 ± 0.37	3.09
	C4	4	-0.017 ± 0.025	4.44 ± 0.22	4.22

Table 5.2: The EXAFS-derived structural parameters for $[Cu(dmp)_2][PF_6]$ in acetonitrile compared with XRD data for $[Cu(dmp)_2][PF_6]$.

Bond Angle (°)	Model 1	Model 2	XRD
Cu-N1-C11	112	114	112
Cu-N2-C12	110	111	111
Cu-N1-C1	-	132	129
Cu-N2-C10	-	132	130

Table 5.3: EXAFS-derived bond angles for $[Cu(dmp)_2][PF_6]$ in acetonitrile compared with XRD data for $[Cu(dmp)_2][PF_6]$.

Model	Parameter	Value
1	R (%)	2.20%
	R, k = 1 (%)	1.26%
	R, k = 2 (%)	1.96%
	R, k = 3 (%)	3.84%
	Chi-square	294.82
	Reduced chi-square	201.4
	Amplitude reduction factor	0.87 ± 0.32
	k range ($Å^{-1}$)	3.0 – 7.6
	R range (Å)	1.0 – 5.0
	No. of independent parameters	11
	No. of variables	10
2	R (%)	1.00%
	R, k = 1 (%)	1.04%
	R, k = 2 (%)	0.89%
	R, k = 3 (%)	1.08%
	Chi-square	161.89
	Reduced chi-square	408.31
	Amplitude reduction factor	0.78 ± 0.81
	k range ($Å^{-1}$)	3.0 – 7.6
	R range (Å)	1.0 – 6.0
	No. of independent parameters	14
	No. of variables	14

Table 5.4: Refined parameters for fits to the Cu K edge of $[Cu(dmp)_2][PF_6]$ in acetonitrile.

RIXS spectra and energy transfer contour plots for Cu_2O, CuO and $[Cu^{I}(dmp)_2][PF_6]$ are presented in figures 5.21 – 5.23 respectively. The theoretical energy transfer plots for Cu_2O and CuO appear very similar, with the absorption edge for CuO being 3 eV higher in incident energy and energy transfer for CuO than for Cu_2O. There are significant differences between the experimental Cu_2O energy transfer plot and the theoretical calculation. The absorption edge is 7 eV lower in transfer energy and 10 eV lower in incident energy in the experimental spectrum. It is also broader in incident energy in the experimental spectrum. The contours are narrower and straighter at lower fluorescence in the experimental spectrum. The pre-edge peak at the incident energy of 8984 eV in the theoretical spectrum is not present in the experimental spectrum. The experimental and theoretical energy transfer spectra for CuO are very similar. The contours are a similar shape in the experimental and theoretical spectra, but broader in the theoretical spectrum, and the absorption edge in the experimental energy transfer spectrum is 4 eV higher in energy transfer. The experimental energy transfer spectrum for the 4-coordinate $[Cu^{I}(dmp)_2][PF_6]$ complex exhibits some similarities to the theoretical energy transfer spectrum for the 2-coordinate Cu_2O. The absorption edge is higher in incident energy and energy transfer, closer to the absorption edge in the theoretical spectrum, and the pre-edge feature is present in the experimental spectrum.

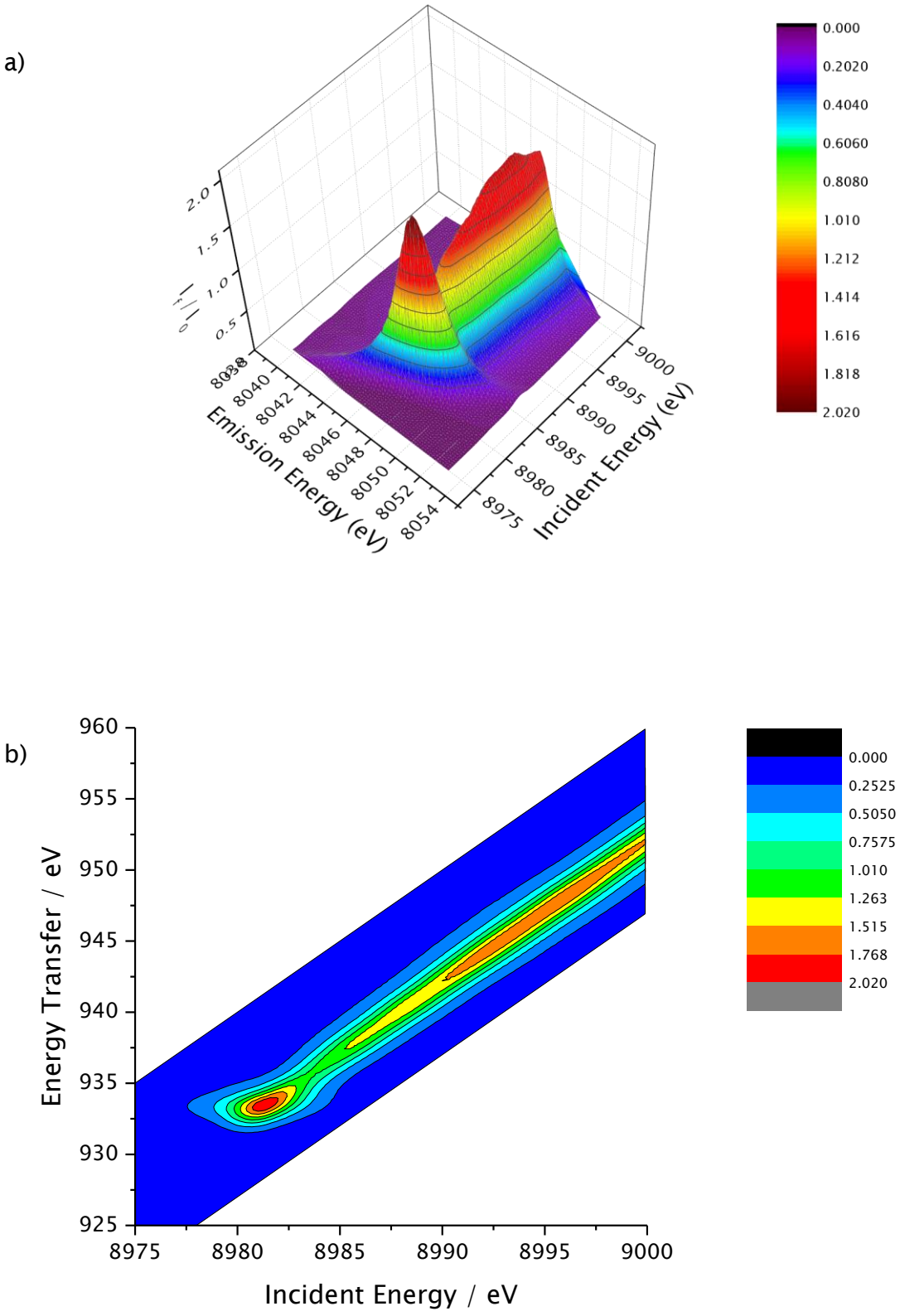

Figure 5.21: a) RIXS and b) energy transfer contour plot for Cu_2O.

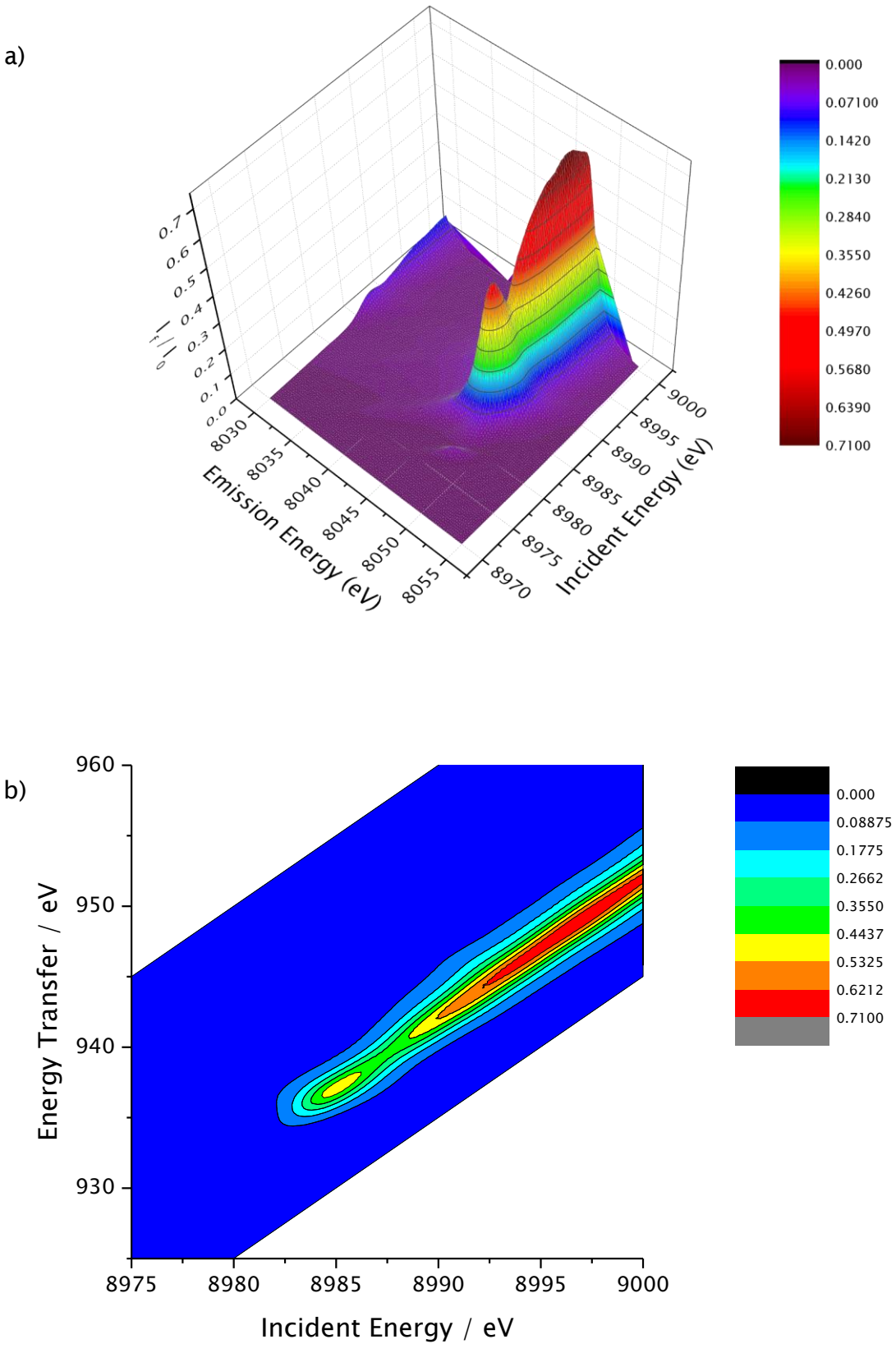

Figure 5.22: a) RIXS and b) energy transfer plot for CuO.

a)

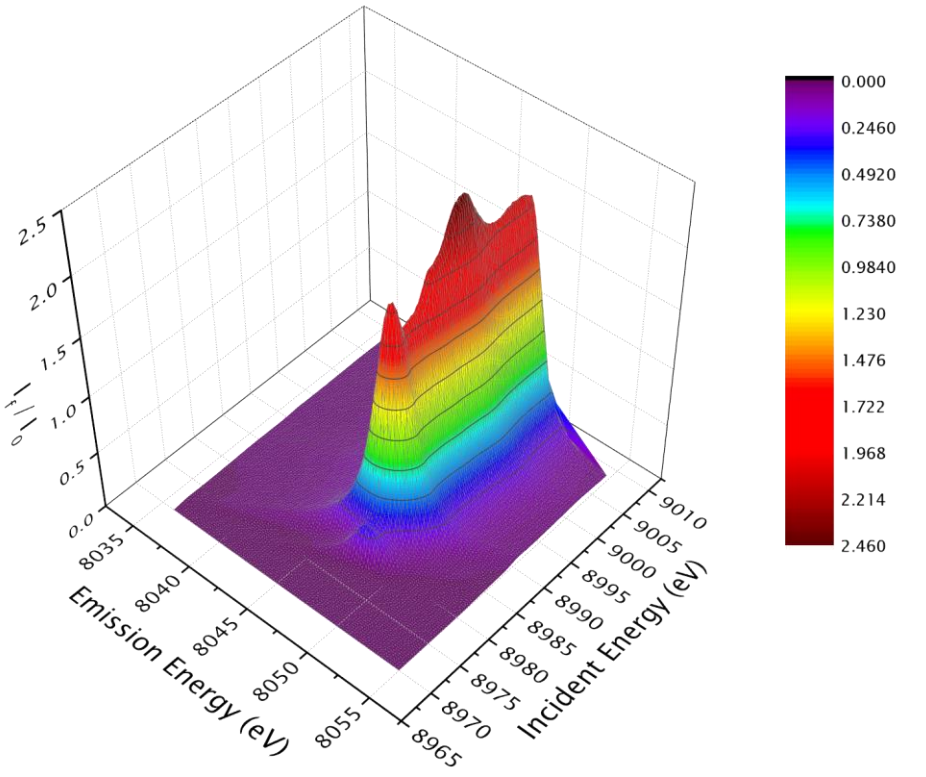

b)

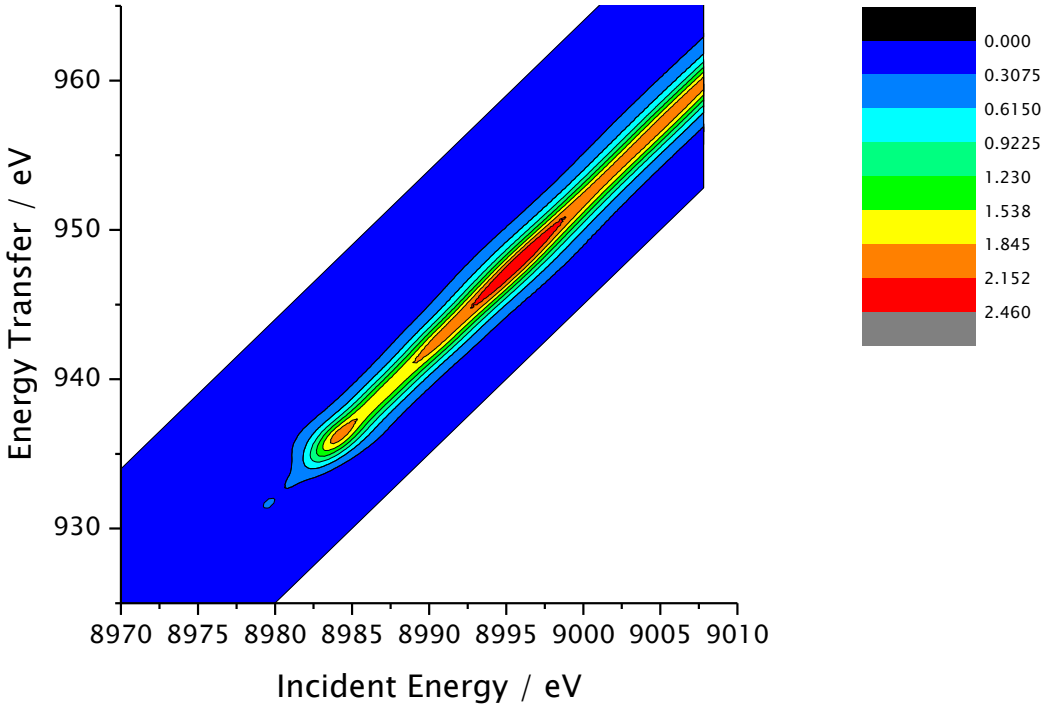

Figure 5.23: a) RIXS and b) energy transfer plot for $[Cu^{I}(dmp)_2][PF_6]$.

A high energy resolution fluorescence detection (HERFD) XANES spectrum has been measured for $[Cu^{I}(dmp)_2][PF_6]$ (figure 5.24). The marked peaks have been used in XES studies of the $[Cu^{I}(dmp)_2]^{+}$ ground state and $[Cu^{II}(dmp)_2]^{2+}$ excited state. The XANES for the Cu^{I} and Cu^{II} sites are compared in figure 5.25 and there are some significant differences. In the $[Cu^{II}(dmp)_2]^{2+}$ XANES, the shoulder at 8984.1 eV is much less pronounced and the absorption edge has lower intensity in comparison with the $[Cu^{I}(dmp)_2]^{+}$ XANES.

The XES spectra for $[Cu^{I}(dmp)_2]^{+}$ and $[Cu^{II}(dmp)_2]^{2+}$ at the marked emission energies in the HERFD spectrum are presented in figure 5.26. The intensity of the peaks are lower for the excited state than the ground state as would be expected from the intensity of the peaks in the XANES spectra for the 2 states. The XES spectrum exhibits significant differences at an emission energy of 8981 eV. In the spectrum for the Cu^{I} ground state, there are 2 peaks in the spectrum, at 8048 eV and 8045 eV. The lower energy peak shifts to 8043 eV at an emission energy of 8979.4 eV. In the XES spectra for Cu^{II} at the same energies, the peaks are much less intense and the second peak at lower energy is not as distinguishable. The XES spectra for the Cu^{II} excited state at emission energies of 8981.1 eV and 8979.5 eV have been expanded in figure 5.27. There are no distinguishable peaks in the 8979.5 eV XES spectrum, but in the 8981.1 eV XES spectrum, the peak at 8045 eV can be distinguished from the peak at 8048 eV. This is possibly due to a trace amount of the Cu^{I} site being present in the oxidised sample. The peak would therefore change intensity as the ratio of Cu^{I} and Cu^{II} in the sample changes and could be used as an indicator of the amount of each copper site present in the sample.

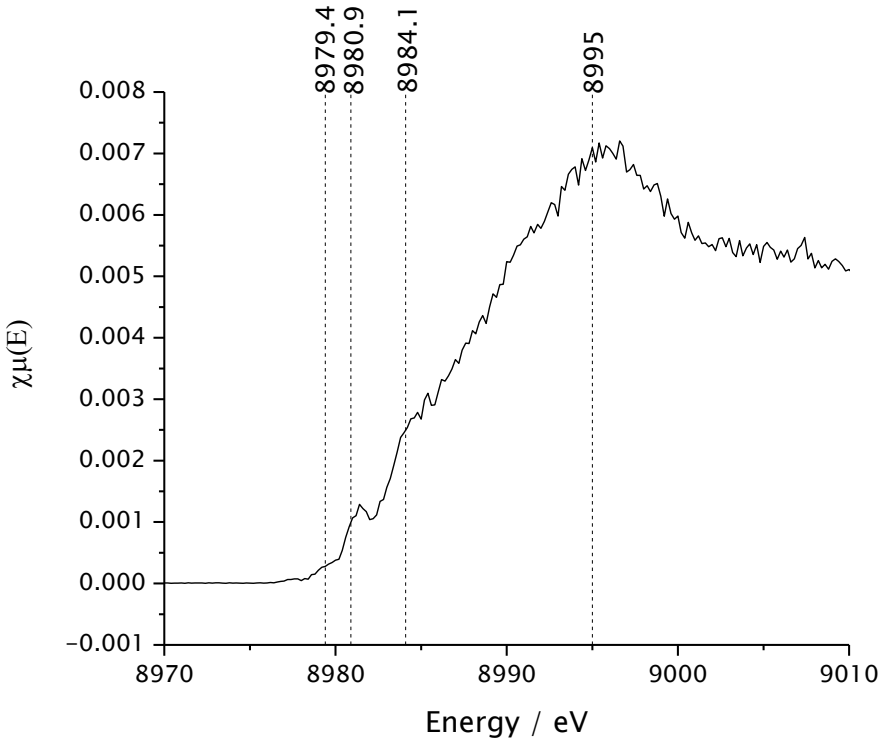

Figure 5.24: HERFD XANES spectrum for $[Cu^{I}(dmp)_2][PF_6]$ in acetonitorle with marked peaks.

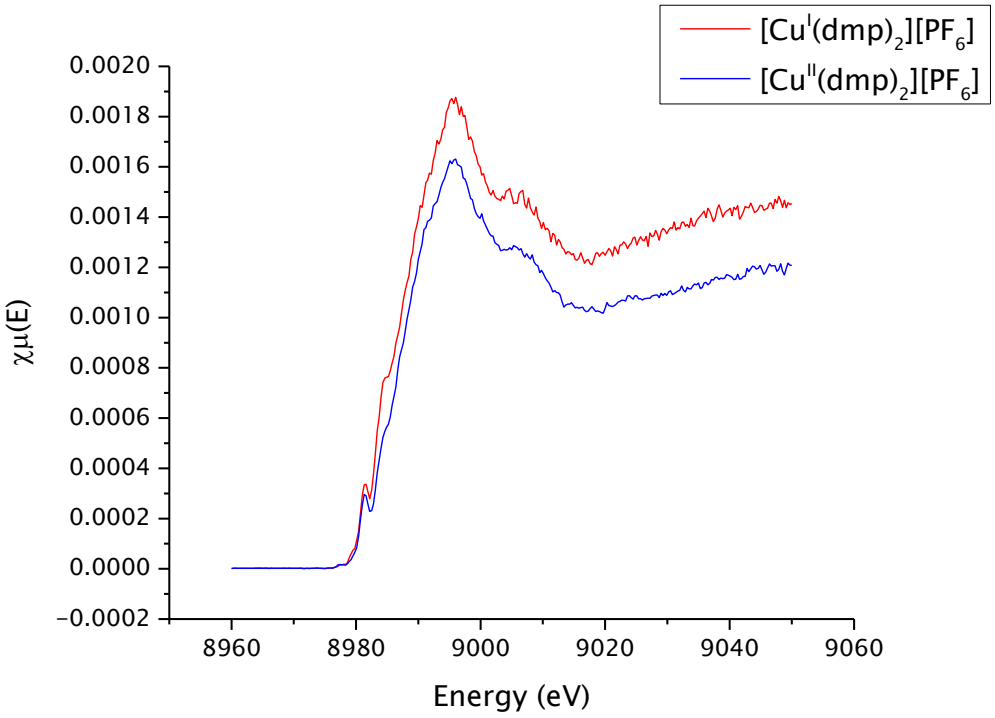

Figure 5.25: XANES for $[Cu^{I}(dmp)_2][PF_6]$ and $[Cu^{II}(dmp)_2][PF_6]$ in acetonitrile.

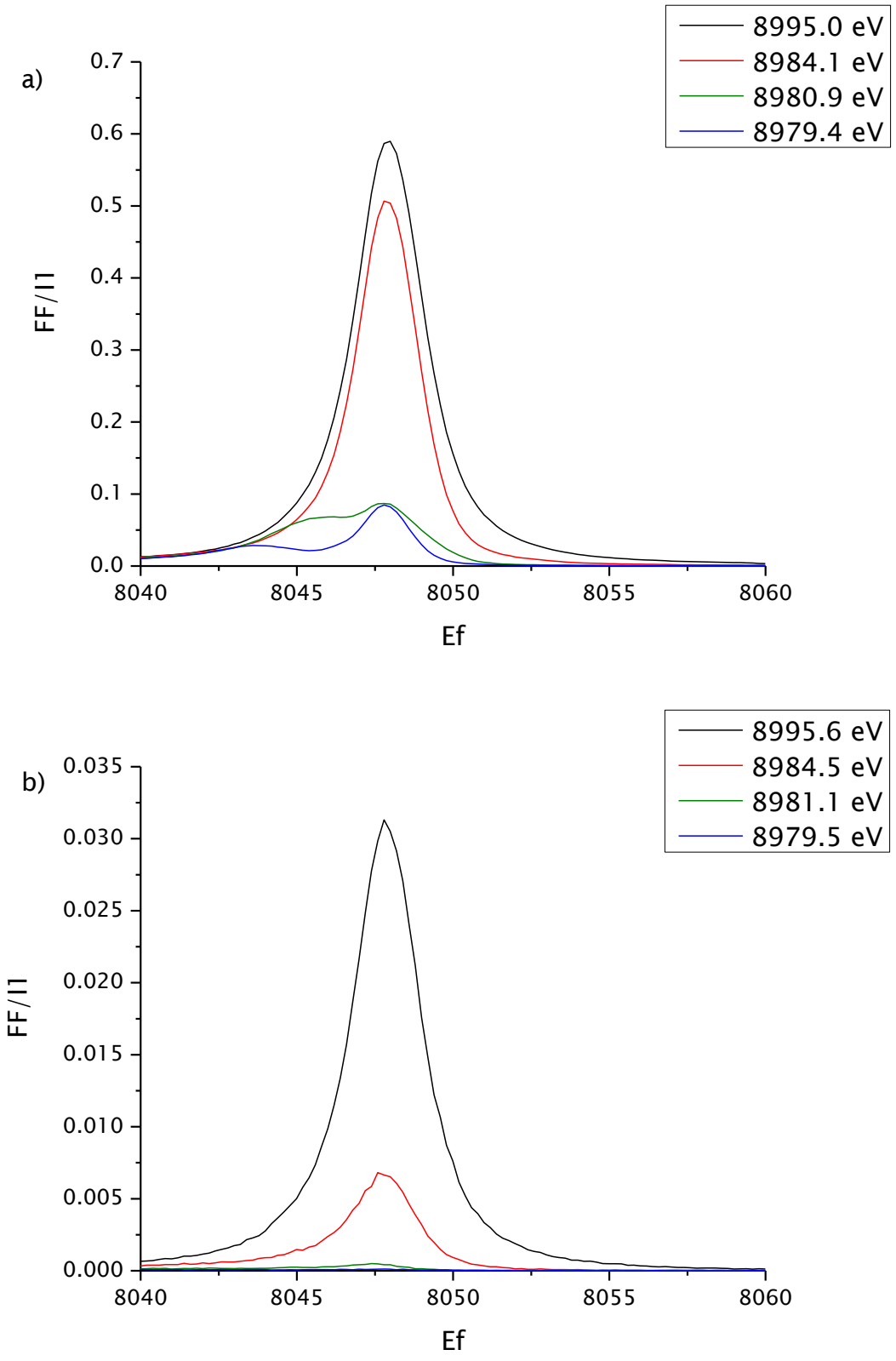

Figure 5.26: XES spectra at incident energies for peaks in the XANES spectrum for a) $[Cu^{I}(dmp)_2]^{+}$ and b) $[Cu^{II}(dmp)_2]^{2+}$ in acetonitrile.

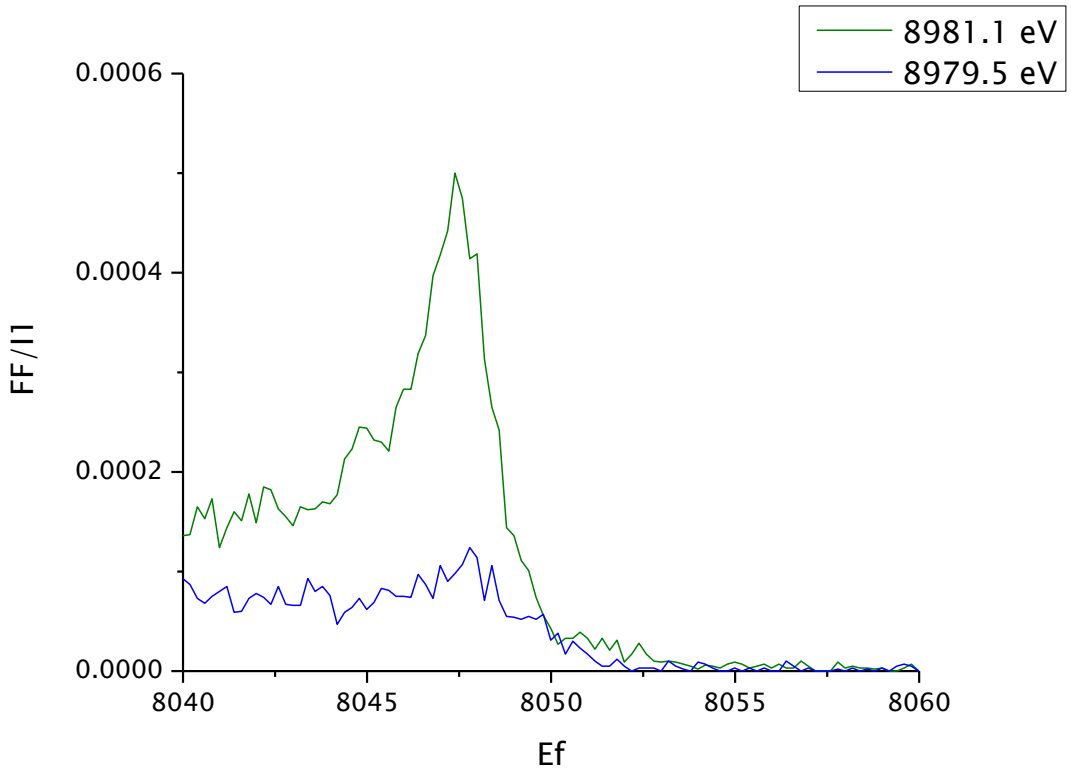

Figure 5.27: Expanded XES spectra at incident energies for peaks in the XANES spectrum for $[Cu^{II}(dmp)_2]^{2+}$ in acetonitrile.

5.3 Experimental

5.3.1 X-Ray Absorption Spectroscopy

X-ray absorption spectra were recorded on beamline I20 with a Si (111) double crystal monochromator at Diamond Light Source operating with an electron energy of 3 GeV and a current range of 300 mA. XAS and UV / Vis measurements were recorded in situ at beamline I20 at Diamond Light Source using a Si(111) 4 bounce monochromator, 3 Si(444) XES analysers, a He/Ar 20 % abs ion chamber and a silicon drift diode detector. X-ray absorption spectra were recorded in fluorescence mode at the copper K edge. The Cu^{II} complex was generated by electrochemical excitation using a tetrabutylammonium hexafluorophosphate / silver nitrate electrolyte.[54] Solid samples were diluted in boron nitride. Removal of background and curve-fitting analyses were carried out with Demeter (version 5.12.3.0).

5.3.2 Preparation of $[Cu(CH_3CN)_4][PF_6]$

HPF_6 (60 %) (56 mmol) (5 ml) was added to a suspension of copper(I) oxide (14 mmol) (2.0 g) in acetonitrile (40 ml) in 0.5 ml portions with stirring under nitrogen. The solution was stirred for 3 min and filtered hot through a medium-porosity frit. Any crystallised white $[Cu(CH_3CN)_4][PF_6]$ was washed through the frit with a minimum of acetonitrile. The pale-blue solution was cooled to -20 °C for several hours. The blue-tinged white microcrystalline precipitate was collected by filtration, washed with diethyl ether and immediately dissolved in acetonitrile (50 ml) and filtered. Diethyl ether (50 ml) was added to the filtrate and was allowed to stand for several hours at -20 °C. A second recrystallization was carried out with a mixture of acetonitrile (40 ml) and diethyl ether (40 ml) to purify the product if a bluish cast was retained after the first recrystallization. The product was washed with diethyl ether and

dried in *vacuo.* for 30 min to give white crystals of $[Cu(CH_3CN)_4][PF_6]$[53] (5.578 g) (10.77 mmol) (53%), IR (nujol) ν_{max} (cm^{-1}) 2312, 2273, 1458, 1376, 1038, 835, 722, 559; λ_{max} (nm) (CH_2Cl_2) 260 (literature); ^1H NMR (300 MHz, $CDCl_3$) δ 2.15; ^{13}C NMR (75 MHz, $CDCl_3$) δ 2.3.[12]

5.3.3 Preparation of 2,9-dialkyl-1,10-phenanthroline

An alkylllithium (8 mmol) in di-n-butyl ether was added dropwise under nitrogen to a suspension of 1,10-phenanthroline (2 mmol) in anhydrous toluene (7 ml) with stirring. The reaction temperature was maintained at 30 ˚C. The dark red mixture was stirred at room temperature overnight. H_2O (10 ml) was slowly added at 0 ˚C under nitrogen. The organic phase was separated, the aqueous phase was extracted 3 times with CH_2Cl_2 (40 ml) and the organic fractions were collected. Activated MnO_2 (20 g) was added to the intense yellow solution and the mixture was stirred at room temperature for 30 min after which time partial decolouration occurred. Magnesium sulphate (20 g) was added and stirred for 30 min. The mixture was filtered and the filtrate was evaporated to give 2,9-dialkyl-1,10-phenanthroline (0.42 mmol) (21%).[55]

2,9-diphenyl-1,10-phenanthroline: ^1H NMR (300 MHz, $CDCl_3$) δ 8.37 (2H, d), 8.22 (2H, d), 8.05 (2H, d), 7.70 (2H, s), 7.49 (2H, t), 7.38 (2H, t); ^{13}C NMR (75 MHz, $CDCl_3$) δ 155.8, 144.9, 138.3, 136.0, 128.5, 127.8, 126.9, 126.7, 125.0, 119.1.[103]

2,9-dibutyl-1,10-phenanthroline: ^1H NMR (300 MHz, $CDCl_3$) δ 8.05 (2H, d), 7.61 (2H, s), 7.42 (2H. d), 3.12 (4H, t), 1.82 (4H, quin), 1.54 (4H, sex), 0.90 (6H, t); ^{13}C NMR (75 MHz, $CDCl_3$) δ 163.3, 145.4, 136.2, 127.1, 125.4, 122.4, 39.2, 31.9, 22.9, 14.1.[103]

5.3.4 Preparation of Copper Bis-phenanthroline Derivatives

A phenanthroline derivative (2 mmol) was dissolved in degassed acetonitrile (10 ml). $[Cu(CH_3CN)_4][PF_6]$ (1 mmol) (280 mg) was added under nitrogen. The red solution was stirred for 10 min. The product was precipitated by adding degassed diethyl ether (50 ml). The mixture was filtered and the solid was dissolved in a minimum of CH_2Cl_2. Diethyl ether was added slowly to the solution and the solid was filtered to give air-stable, red-brown crystals of the copper phenanthroline derivative (87 %).[54,98,104-106]

$[Cu(dmp)_2][PF_6]$: IR (nujol) ν_{max} (cm^{-1}) 1589, 1508, 1458, 1377, 1310, 1149, 842, 729, 557; λ_{max} (nm) (CH_3CN) 456; ^1H NMR (300 MHz, $CDCl_3$) δ 8.54 (2H, d), 8.08 (2H, s), 7.81 (2H, d), 2.48 (6H, s); ^{13}C NMR (75 MHz, $CDCl_3$) δ 158.3, 143.6, 137.5, 128.1, 126.3, 125.9, 26.0.

$[Cu(dpp)_2][PF_6]$: IR (nujol) ν_{max} (cm^{-1}) 1795, 1444, 1261, 1096, 1022, 876, 803, 713, 557; λ_{max} (nm) (CH_3CN) 439; ^1H NMR (300 MHz, $CDCl_3$) δ 8.40 (2H, d), 7.93 (2H, s), 7.79 (2H, d), 7.31 (2H, d), 6.72 (2H, t), 6.44 (2H, t); ^{13}C NMR (75 MHz, $CDCl_3$) δ 157.1, 143.9, 137.7, 135.2, 129.2, 128.1, 127.5, 126.8, 125.1, 119.2.

$[Cu(dbp)_2][PF_6]$: IR (nujol) ν_{max} (cm^{-1}) 1587, 1508, 1498, 1463, 1377, 1155, 869, 843, 773, 558; λ_{max} (nm) (CH_3CN) 456; ^1H NMR (300 MHz, $CDCl_3$) δ 8.58 (2H, d), 8.09 (2H, s), 7.82 (2H, d), 2.77 (4H, t), 1.38 (4H, quin), 0.72 (4H, sex), 0.28 (6H, t); ^{13}C NMR (75 MHz, $CDCl_3$) δ 162.3, 143.7, 137.8, 128.3, 126.5, 125.3, 40.5, 32.1, 22.7, 13.2.

$[Cu(bcp)_2][PF_6]$: IR (nujol) ν_{max} (cm^{-1}) 557, 702, 733, 769, 839, 1377, 1459, 1569, 1621; λ_{max} (nm) (CH_3CN) 477; ^1H NMR (300 MHz, $CDCl_3$) δ 8.11 (2H, s), 7.82 (2H, s), 7.68 (10H, m), 2.64 (6H, s) ^{13}C NMR (75 MHz, $CDCl_3$) δ 157.6, 150.1, 144.4, 137.3, 130.0, 129.6, 129.4, 126.2, 126.1, 124.2, 26.3.

5.3.5 Spectroscopic Methods

5.3.5.1 NMR Spectroscopy

1H NMR and 13 C NMR measurements were performed in acetonitrile using a Bruker AV300 NMR spectrometer.

5.3.5.2 Infrared Spectroscopy

Infrared nujol mull measurements were performed using a Nicolet is10 FT-IR with KBr discs in the range 400 – 4000 cm-1.

5.3.5.3 UV / Vis Spectroscopy

Absorption measurements were performed using a Shimadzu UV-1800 UV / Vis spectrometer. Spectra were collected in the range 200 – 800 nm in acetonitrile using a quartz cuvette with a 1 cm path length.

5.4 Conclusions

The Beer-Lambert plots show that the copper diimine complexes investigated in this chapter do not associate or dissociate in solution. The lifetimes of $[Cu(dmp)_2][PF_6]$ and $[Cu(dpp)_2][PF_6]$ have been calculated to be 71 ns and 108 ns, respectively. These excited state lifetimes agree with literature. The calculated lifetimes of $[Cu(bcp)_2][PF_6]$ and $[Cu(dbp)_2][PF_6]$ have been calculated to be 3 ns and 29 ns respectively, but they are likely to have been exposed to oxygen in the flow cell system, causing the lifetime of the excited states to be significantly decreased.

2 models have been fit the Cu K edge XAFS spectrum for the ground state of $[Cu(dmp)_2][PF_6]$. The fits for model 1 and model 2 have been refined up to distances of 3.2 Å and 4.5 Å respectively. The Cu-N bond distances refined in the fit for model 1 agree with the crystallographic data and previously reported data. Adding the extra shell of carbon atoms in model 2 causes the Cu-N bond distances to deviate more from the crystallographic data, but the error margins allow for stronger agreement with literature. The Debye-Waller factors for the shells of carbon atoms are negative in the fit for model 1, but are positive for model 2 with the extra shell of carbon atoms.

RIXS spectra have been recorded for Cu_2O, CuO and $[Cu(dmp)_2][PF_6]$. The experimental RIXS spectrum for CuO exhibits similar features to the calculated theoretical RIXS spectrum for CuO. The experimental RIXS spectrum for Cu_2O is quite different to the theoretical spectrum calculated for Cu_2O. The experimental RIXS spectrum for the ground state of $[Cu(dmp)_2][PF_6]$ exhibits more similarities to the theoretical spectrum calculated for Cu_2O than the experimental spectrum for Cu_2O. It has not been possible to measure a RIXS spectrum of electrochemically oxidised $[Cu(dmp)_2][PF_6]$ due to gas being evolved in the solution cell within the time it takes to record the spectrum. It has been proved that it is possible to distinguish between Cu^{I} and Cu^{II} using XES spectroscopy. The XES spectra Cu^{I} ground state and Cu^{II} excited state of $[Cu(dmp)_2][PF_6]$ exhibit different features at incident energies of 8979.5 eV and

8981 eV which could be used to determine the ratio of the ground and excited states in the solution during excitation.

6. Conclusions and Further Research

POM clusters have been characterised using QEXAFS. EXAFS spectra have been recorded up to 20.7 $Å^{-1}$ and distances of 6.2 Å have been resolved. Differentiation between different capped $[PMo_{12}O_{40}(MX)_2]^{n-}$ species, where the capping species is bound to the core POM by 4 bridging oxygen atoms, and reduced $[PMo_{12}O_{40}]^{n-}$ species has been demonstrated. In the curve-fitting analyses for the Lindqvist-type POMs the refined distances of the multiple scattering paths are not consistent with refined lengths of the single scattering paths and in these cases it has not been possible to calculate the bond angles. Despite this, when weakly contributing single scattering paths are included in the fit, including the multiple scattering paths in the fits helps to refine the lengths of the single scattering paths associated with the multiple scattering paths. The distances of longer, weakly contributing single scattering paths deviate from crystallographic data by 0.3 – 0.6 Å, but the EXAFS fitting does provide confirmation that the atoms are present in the samples. Where forward scattering multiple scattering paths are involved, the distances of the weakly contributing atoms from the absorbing atom can be more accurately refined.

In a previous study of $K_7[HNb_6O_{19}] \cdot nH_2O$, high thermal and static disorder has been observed in the bond between the interstitial oxygen atoms and the Nb atoms.[5] In a study of $[Mo_6O_{19}][NBu_4]_2$, R-factors of 29.4 % and 26 % were obtained for solid and solution spectra respectively.[5] High Debye-Waller factors were observed for the shells incorporating Mo-O_b bonds (where O_b is the bridging oxygen in the Mo-O-Mo unit) and this has been attributed to high vibrational disorder in the bond.[107,108] R-factors of 30.5 % and 32.6 % were obtained in curve-fitting analyses for $[Nb_2W_4O_{19}]^{4-}$ and $[Nb_4W_2O_{19}]^{6-}$ respectively. In the studies of POM species reported here, R factors are below 10 %, often below 1 % of the Keggin-type POMs with a $[PMo_{12}O_{40}]^{3-}$ core structure. The Debye-Waller factors for Mo-O_b bonds have been refined to 0.0005 – 0.005.

Reactions on the minute time scale have been studied by EXAFS spectroscopy. Two techniques have been employed for studying reactions on this timescale. For the first method, 20 spectra were recorded over 10 minutes and the spectra were merged. Linear combination fitting was used to remove

contributions from starting materials and side products from the observed EXAFS spectrum, leaving contributions from intermediate species which have been fitted to the remaining EXAFS spectrum. Using this method of studying reactions, possible intermediate species in the formation of Lindqvist-type POMs have been identified; clusters consisting of 3 and 5 metal atoms. In this investigation a 1:5 ratio of $[WO_4]^{2-}$:$WO(OR)_4$ was studied. A reaction has been reported in which a cluster consisting of 5 tungsten atoms is produced.[11] This reaction uses a $[WO_4]^{2-}$:$WO(OR)_4$ ratio of 3:2. After this reaction is complete the heterometal ion is added to the reaction solution to produce the Lindqvist-type POM consisting of 6 metal atoms. Measuring the EXAFS for this reaction solution may provide a spectrum more suited to resolving the structure of the cluster consisting of 5 tungsten atoms. For the second method, 5 – 10 spectra for reaction solutions were recorded over 1 – 2 hours. All the species present in the reaction solution were fitted to the observed EXAFS spectrum of the reaction solution for the formation reactions of capped Keggin-type POMs by reductive aggregation. The EXAFS spectra show that clusters are being formed around the metal ions in the reaction solution. By recording in situ EXAFS spectra for the POMs reaction over a period of several hours, kinetic information and rate constants can be derived by measuring the intensity of the EXAFS features as in previous experiments in suitably slow reactions.[56,109]

The photo-excitation reaction of copper diimine complexes, causing the Cu^{I} site to be oxidised, producing a Cu^{II} site occurs on a nanosecond timescale. It has been possible to differentiate between $[Cu^{I}(dmp)_2]^{+}$ and $[Cu^{II}(dmp)_2]^{2+}$ using K_α XES. There is a peak in the XES spectrum for $[Cu^{I}(dmp)_2]^{+}$ that is significantly smaller in the XES spectrum for electrochemically generated $[Cu^{II}(dmp)_2]^{2+}$. This peak could be present in the XES spectrum for electrochemically generated $[Cu^{II}(dmp)_2]^{2+}$ due to the presence of trace amounts of Cu^{I} remaining in the solution. In XES photo-excitation experiments for copper complexes, it may be possible to determine the ratio of Cu^{I} and Cu^{II} in the solution using this peak. The absorption edge and pre-edge features in the XAFS spectra for $[Cu^{I}(dmp)_2]^{+}$ and $[Cu^{II}(dmp)_2]^{2+}$ occur at the same incident energies so the contribution from both copper sites are combined in the same peak. In a previous XANES analysis of the photo-excitation of $[Cu^{I}(dmp)_2]^{+}$, it has been possible to separate the contributions of Cu^{I} and Cu^{II} and to determine the ratio of Cu^{I} and Cu^{II} sites.[42] RIXS measurements have been recorded for $[Cu^{I}(dmp)_2]^{+}$, but it has not been

possible to measure a RIXS spectrum for $[Cu^{II}(dmp)_2]^{2+}$ due to gas being evolved in the electrochemical solution cell during the RIXS measurement. XAFS experiments have been reported in which reaction intermediates have been investigated by freezing reaction solutions using liquid nitrogen.[110] A cryostream could be used to freeze a sample of electrochemically generated $[Cu^{II}(diimine)_2]$ in acetonitrile. This could solve the problem of gas being evolved in the RIXS experiments for the electrochemically excited state of the complex in solution.

Glossary

Bcp: 2,9-dimethyl-4,7-diphenyl-1,10-phenanthroline (Bathocuproine).

Dbp: 2,9-di-n-butyl-1,10-phenanthroline.

Dmp: 2,9-dimethyl-1,10-phenanthroline (Neocuproine)

Dpp: 2,9-diphenyl-1,10-phenanthroline.

Brilliance: Degree to which photon beam generated by a small small source with small divergence is collimated.

Flux: Total number of photons per second in a beam.

Polyoxometalate: Polyatomic ion consisting of 3 or more metal ions with bridging and terminal oxygen atoms.

Bibliography

1. G. Bunker, *Introduction to XAFS*, Cambridge University Press, 2010

2. M. Newville, *Fundamentals of XAFS*, Consortium of Advanced Radiation Sources, University of Chicago, Chicago, IL, 2008.

3. N. N. Greenwood and A. Earnshaw, *Chemistry of the Elements*, Butterworth-Heinemann, Second Edi., 1997.

References

1. T. Onfroy, G. Clet, and M. Houalla, *J. Phys. Chem. B*, 2005, **109**, 3345–3354.

2. M. Filowitz, R. K. C. Ho, W. G. Klemperer, and W. Shum, *Inorg. Chem.*, 1979, **18**, 93–103.

3. L. Pettersson, I. Andersson, and L.-O. Ohman, *Inorg. Chem.*, 1986, **25**, 4726–4733.

4. C. Rocchiccioli-Deltcheff, R. Thouvenot, and M. Dabbabi, *Spectrochim. Acta, Part A*, 1977, **33**, 143–153.

5. J. Evans, M. Pillinger, and J. M. Rummey, *J. Chem. Soc., Dalton Trans.*, 1996, 2951–2961.

6. J. Evans, M. Pillinger, and J. J. Zhang, *J. Chem. soc., Dalton Trans.*, 1996, 2963–2974.

7. M. S. S. Balula, I. Santos, J. A. F. Gamelas, A. M. V Cavaleiro, N. Binsted, and W. Schlindwein, *Eur. J. Inorg. Chem.*, 2007, 1027–1038.

8. L. C. W. Baker and J. S. Figgis, *J. Am. Chem. Soc.*, 1970, **92**, 3794–3797.

9. I. Lindqvist, *Ark. Kemi*, 1953, **5**, 247–250.

10. W. Clegg, R. J. Errington, P. Kraxner, and C. Redshaw, *J. Chem. Soc., Dalton Trans.*, 1992, 1431–1438.

11. R. J. Errington, G. Harle, W. Clegg, and R. W. Harrington, *Eur. J. Inorg. Chem.*, 2009, 5240–5246.

12. R. J. Errington, S. S. Petkar, P. S. Middleton, W. McFarlane, W. Clegg, R. A. Coxall, and R. W. Harrington, *J. Am. Chem. Soc.*, 2007, **129**, 12181–12196.

13. N. Belai, M. Sadakane, and M. T. Pope, *J. Am. Chem. Soc.*, 2001, **123**, 2087–2088.

14. A. Harriman, K. J. Elliott, M. A. H. Alamiry, L. Le Pleux, M. Severac, Y. Pellegrin, E. Blart, C. Fosse, C. Cannizzo, C. R. Mayer, and F. Odobel, *J. Phys. Chem. C*, 2009, **113**, 5834–5842.

15. C. Schaffer, A. Merca, H. Bogge, A. M. Todea, M. L. Kistler, T. Liu, R. Thouvenot, P. Gouzerh, and A. Muller, *Angew. Chem. Int. Ed.*, 2009, **48**, 149–153.

16. A. M. Todea, A. Merca, H. Bogge, T. Glaser, L. Engelhardt, R. Prozorov, M. Lubanc, and A. Muller, *Chem. Comm.*, 2009, 3351–3353.

References

17. K. F. Jahr and J. Fuchs, *Chem. Ber.*, 1963, **96**, 2457–2459.

18. W. Clegg, M. R. J. Elsegood, R. J. Errington, and J. Havelock, *J. Chem. Soc., Dalton Trans.*, 1996, 681–690.

19. R. J. Errington, S. S. Petkar, P. S. Middleton, W. McFarlane, W. Clegg, R. A. Coxall, and R. W. Harrington, *Dalton Trans.*, 2007, 5211–5222.

20. R. J. Errington, S. S. Petkar, B. R. Horrocks, A. Houlton, L. H. Lie, and S. N. Patole, *Angew. Chem. Int. Ed.*, 2005, **44**, 1254–1257.

21. J. A. Fernandez, X. Lopez, and J. M. Poblet, *J. Mol. Catal. A Chem*, 2007, **262**, 236–242.

22. X. Lopez, C. Bo, and J. M. Poblet, *J. Am. Chem. Soc.*, 2002, **124**, 12574–12582.

23. R. Vilanneau, A. Proust, F. Robert, and P. Gouzerh, *Chem. Comm.*, 1998, 1491–1492.

24. R. D. Peacock and T. J. R. Weakley, *J. Chem. Soc. A*, 1971, 1836–1839.

25. J. Iball, J. N. Low, and T. J. R. Weakley, *J. Chem. Soc., Dalton Trans.*, 1974, 2021–2024.

26. S. J. Angus-Dunne, R. C. Burns, D. C. Craig, and G. A. Lawrance, *J. Chem. Soc., Chem. Comm.*, 1994, 523–524.

27. K. A. Campbell, M. J. Janik, R. J. Davis, and M. Neurock, *Langmuir*, 2005, **21**, 4738–4745.

28. J. M. Mayer, *Polyhedron*, 1995, **14**, 3273–3292.

29. M. Nandi, D. Rhubright, and A. Sen, *Inorg. Chem.*, 1990, **29**, 3065–3066.

30. W. Cho, H. S. Jang, K. S. An, Y. K. Lee, T. M. Chung, C. G. Kim, Y. Kim, B. S. So, J. H. Hwang, and D. Jung, *J. Vac. Sci. Technol. A*, 2006, **24**, 1208–1212.

31. T. S. Yang, K. S. An, E. J. Lee, W. Cho, H. S. Jang, S. K. Park, Y. K. Lee, T. M. Chung, C. G. Kim, S. Kim, J. H. Hwang, C. Lee, N. S. Lee, and Y. Kim, *Chem. Mater.*, 2005, **17**, 6713–6718.

32. T. M. Che, V. W. Day, L. C. Francesconi, W. G. Klemperer, D. J. Main, A. Yagasaki, and O. M. Yaghi, *Inorg. Chem.*, 1992, **31**, 2920–2928.

33. M. Aberg and J. Glaser, *Inorg. Chim. Acta*, 1993, **206**, 53–61.

34. A. Dolbecq, C. Mellot-Draznieks, P. Mialane, J. Marrot, G. Ferey, and F. Secheresse, *Eur. J. Inorg. Chem.*, 2005, 3009–3018.

35. B. Nohra, H. El Moll, L. M. R. Albelo, P. Mialane, J. Marrot, C. Mellot-Draznieks, M. O'Keeffe, R. N. Biboum, J. Lemaire, B. Keita, L. Nadjo, and A. Dolbecq, *J. Am. Chem. Soc.*, 2011, **133**, 13363–13374.

36. J. Lehmann, A. Gaita-Arino, E. Coronado, and D. Loss, *Nat. Nano.*, 2007, **2**, 312–317.

37. J. Lehmann, A. Gaita-Arino, E. Coronado, and D. Loss, *J. Mater. Chem.*, 2009, **19**, 1672–1677.

38. R. J. Errington, in *Comprehensive Coordination Chemistry*, Elsevier, New York, 2003, vol. 2, pp. 759–773.

39. R. J. Errington, J. J. Borras-Almenar, E. Coronado, A. Muller, and M. T. Pope, in *Polyoxometalate Molecular Science*, Kluwer, Dordrecht, 2003, pp. 55–77.

40. R. J. Errington, M. T. Pope, and A. Muller, in *Polyoxometalate Chemistry: From Topology via Self-Assembly to Applications*, Kluwer, Dordrecht, 2001, pp. 1–22.

41. R. Bakri, A. Booth, G. Harle, P. S. Middleton, C. Wills, W. Clegg, R. W. Harrington, and R. J. Errington, *Chem. Comm.*, 2012, **48**, 2779–2781.

42. L. X. Chen, G. B. Shaw, I. Novozhilova, T. Liu, G. Jennings, K. Attenkofer, G. J. Meyer, and P. Coppens, *J. Am. Chem. Soc.*, 2003, **125**, 7022–7034.

43. G. B. Shaw, C. D. Grant, H. Shirota, E. W. Castner Jr., G. Meyer J., and L. X. Chen, *J. Am. Chem. Soc.*, 2007, **129**, 2147–2160.

44. F. S. Stephens and P. A. Tucker, *J. Chem. Soc., Dalton Trans.*, 1973, 2293–2297.

45. J. Kaiser, G. Brauer, F. A. Schroder, I. F. Taylor, and Rasmusse.Se, *J. Chem. Soc., Dalton Trans.*, 1974, 1490–1493.

46. O. P. Anderson, *Inorg. Chem.*, 1975, **14**, 730–734.

47. W. D. Harrison, B. J. Hathaway, and D. Kennedy, *Acta Crystal. Sect. B*, 1979, **35**, 2301–2306.

48. K. Shinozaki and Y. Kaizu, *Bull. Chem. Soc. Jpn.*, 1994, **67**, 2435–2439.

49. D. Tran, B. W. Skelton, A. H. White, L. E. Laverman, and P. C. Ford, *Inorg. Chem.*, 1998, **37**, 2505–2511.

50. K. L. Cunningham, C. R. Hecker, and D. R. McMillin, *Inorg. Chim. Acta*, 1996, **242**, 143–147.

51. Z. A. Siddique, Y. Yamamoto, T. Ohno, and K. Nozaki, *Inorg. Chem.*, 2003, **42**, 6366–6378.

52. C. E. A. Palmer, D. R. McMillin, C. Kirmaier, and D. Holten, *Inorg. Chem.*, 1987, **26**, 3167–3170.

53. G. J. Kubas, *Inorg. Synth.*, 1979, **19**, 90–91.

54. M. Ruthkosky, F. N. Castellano, and G. J. Meyer, *Inorg. Chem.*, 1996, **35**, 6406–6412.

55. C. O. Dietrick-Buchecker, P. A. Marnot, and J. P. Sauvage, *Tet. Lett.*, 1982, **23**, 5291–5294.

56. A. J. Dent, L. J. Farrugia, A. G. Orpen, and S. E. Stratford, *J. Chem. Soc., Chem. Comm.*, 1992, 1456–1457.

57. G. Guay, G. Tourillon, E. Dartyge, A. Fontaine, J. McBreen, K. I. Pandya, and W. E. O'Grady, *J. Electroanal. chem.*, 1991, **305**, 83–95.

58. D. Hecht, R. Frahm, and H.-H. Strehblow, *J. Phys. Chem.*, 1996, **100**, 10831–10833.

59. R. J. Mathew and A. E. Russell, *Top. Catal.*, 2000, **10**, 231–239.

60. P. G. Allen, S. D. Conradson, M. S. Wilson, S. Gottesfeld, I. D. Raistrick, J. Valerio, and M. Lovato, *Electrochim. Acta*, 1994, **39**, 2415–2418.

61. P. G. Allen, S. D. Conradson, M. S. Wilson, S. Gottesfeld, I. D. Raistrick, J. Valerio, and M. Lovato, *J. Electroanal. Chem.*, 1995, **384**, 99–103.

62. M. A. Newton, D. G. Burnaby, A. J. Dent, S. Diaz-Moreno, J. Evans, S. G. Fiddy, T. Neisius, S. Pascarelli, and S. Turin, *J. Phys. Chem. A*, 2001, **105**, 5965–5970.

63. I. J. Shannon, G. Sankar, T. Maschmeyeer, J. M. Thomas, R. D. Oldroyd, M. Sheehy, D. Madill, A. Waller, and R. P. Townsend, *Catal. Lett.*, 1997, **44**, 23–27.

64. T. Ressler, O. Timpe, T. Neisius, J. Find, G. Mestl, M. Dieterle, and R. Schlogl, *J. Catal.*, 2000, **191**, 75–85.

65. T. Ressler, M. Hagelstein, U. Hatje, and W. Metz, *J. Phys. Chem. B*, 1997, **101**, 6680–6687.

66. A. Yamaguchi, T. Shido, Y. Inada, T. Kogure, K. Asakura, M. Nomura, and Y. Iwasawa, *Catal. Lett.*, 2000, **68**, 139–145.

67. J. W. Couves, J. M. Thomas, D. Waller, R. H. Jones, A. J. Dent, G. E. Derbyshire, and G. N. Greaves, *Nature*, 1991, **354**, 465–468.

68. A. J. Dent, M. P. Wells, R. C. Farrow, C. A. Ramsdale, G. E. Derbyshire, G. N. Greaves, J. W. Couves, and J. M. Thomas, *Rev. sci. Instrum.*, 1992, **63**, 903–906.

69. B. S. Clausen, H. Topsoe, and R. Frahm, *Adv. Catal.*, 1998, **42**, 315–344.

70. G. Sankar and J. M. Thomas, *Top. Catal.*, 1999, **8**, 1–21.

71. M. Newville, *Fundamentals of XAFS*, Consortium of Advanced Radiation Sources, University of Chicago, Chicago, IL, 2008.

72. M. A. Newton, A. J. Dent, and J. Evans, *Chem. Soc. Rev.*, 2002, **31**, 83–95.

73. J. D. Grunwaldt, D. Lutzenkirchen-Hecht, M. Richwin, S. Grundmann, B. S. Clausen, and R. Frahm, *J. Phys. Chem. B*, 2001, **105**, 5161–5168.

74. D. Lutzenkirchen-Hecht, S. Grundmann, and R. Frahm, *J. Synch. Radiat.*, 2001, **8**, 6–9.

75. R. Frahm, *Nucl. Instrum. Meth. Phys. Res., Sect. A*, 1988, **270**, 578–581.

76. T. Matsushita and R. P. Phizackerley, *Jpn. J. Appl. Phys.*, 1981, **20**, 2223–2228.

77. U. Bergmann and P. Glatzel, *Photosynth. Res.*, 2009, **102**, 255–66.

78. L. J. P. Ament, M. van Veenendaal, T. P. Devereaux, J. P. Hill, and J. van den Brink, *Rev. Mod. Phys.*, 2011, **83**, 705–767.

79. *www.diamond.ac.uk*.

80. M. Newville, *J. Synchrotron Rad.*, 2001, **8**, 96–100.

81. M. Newville, *J. Synchrotron Rad.*, 2001, **8**, 322–324.

82. J. Fuchs, W. Freiwald, and H. Hartl, *Acta Crystallogr., Sect. B*, 1978, **34**, 1764–1770.

83. W. H. Bi, D. F. Sun, R. Cao, J. T. Chen, and M. C. Hong, *Acta Crystal. Sec. E*, 2002, **58**, 611–612.

84. N. N. Greenwood and A. Earnshaw, *Chemistry of the Elements*, Butterworth-Heinemann, Second Edi., 1997.

85. D. T. Richens, A. G. Sykes, and Z. Dori, *Inorg. Synth.*, 1985, **23**, 130–140.

86. R. Bakri, A. Booth, G. Harle, P. S. Middleton, C. Wills, W. Clegg, R. W. Harrington, and R. J. Errington, *Chem. Comm.*, 2012, **48**, 2779–2781.

87. K. I. Pokhodnya, M. Bonner, A. G. DiPasquale, A. L. Rheingold, J.-H. Her, P. W. Stephens, J.-W. Park, B. S. Kennon, A. M. Arif, and J. S. Miller, *Inorg. Chem.*, 2007, **46**, 2471–2477.

88. J. M. Corker, J. Evans, H. Leach, and W. Levason, *J. Chem. Soc., Chem. Comm.*, 1989, 181–183.

References

89. C. Bressler and M. Chergui, *Ann. Rev. Phys. Chem.*, 2010, **61**, 263–282.

90. M. Tromp, A. J. Dent, J. Headspith, T. Easun, X.-Z. Sun, M. W. George, O. Mathon, G. Smolentsev, M. L. Hamilton, and J. Evans, *J. Phys. Chem. B*, 2013, **117**, 7381–7387.

91. N. A. Gothard, M. W. Mara, J. Huang, J. M. Szarko, B. Rolczynski, J. V Lockard, and L. X. Chen, *J. Phys. Chem. A*, 2012, **116**, 1984–1992.

92. P. Glatzel and U. Bergmann, *Coord. Chem. Rev.*, 2005, **249**, 65–95.

93. H. Hayashi, Y. Udagawa, W. Caliebe, and C.-C. Kao, *Phys. Rev. B*, 2002, **66**, 033105–1 – 033105–4.

94. H. Hayashi, R. Takeda, Y. Udagawa, T. Nakamura, H. Miyagawa, H. Shoji, S. Nanao, and N. Kawamura, *Phys. Rev. B*, 2003, **68**, 045122–1 – 045122–9.

95. H. Hayashi, Y. Udagawa, and C.-C. Kao, *J. Elect. Spect. Rel. Phen.*, 2004, **137-140**, 277–280.

96. J. J. Kas, J. J. Rehr, J. A. Soininen, and P. Glatzel, *Phys. Rev. B*, 2011, **83**, 235114–1 – 235114–10.

97. R. Hamalainen, M. Ahlgren, U. Turpeinen, and T. Raikas, *Cryst. Struct. Comm.*, 1979, **8**, 75–80.

98. M. T. Miller, P. K. Gantzel, and T. B. Karpishin, *Inorg. Chem.*, 1998, **37**, 2285–2290.

99. M. Z. J. Zgierski, *J. Chem. Phys.*, 2003, **118**, 4045–4051.

100. N. Armaroli, *Chem. Soc. Rev.*, 2001, **30**, 113–124.

101. J. V Lockard, S. Kabehie, J. I. Zink, G. Smolentsev, A. Soldatov, and L. X. Chen, *J. Phys. Chem. B*, 2010, **114**, 14521–14527.

102. M. W. Mara, N. E. Jackson, J. Huang, A. B. Stickrath, X. Zhang, N. A. Gothard, M. A. Ratner, and L. X. Chen, *J. Phys. Chem. B*, 2013, **117**, 1921–1931.

103. G. J. ten Brink, I. Arends, M. Hoogenraad, G. Verspui, and R. A. Sheldon, *Adv. Synth. Catal.*, 2003, **345**, 1341–1352.

104. J. R. Kirchhoff, R. E. Gamache, M. W. Blaskie, A. A. Delpaggio, R. K. Lengel, and D. R. McMillin, *Inorg. Chem.*, 1983, **22**, 2380–2384.

105. A. K. Ichinaga, J. R. Kirchhoff, D. R. McMillin, C. O. Dietrichbuchecker, P. A. Marnot, and J. P. Sauvage, *Inorg. Chem.*, 1987, **26**, 4290–4292.

106. D. R. McMillin, M. T. Buckner, and B. T. Ahn, *Inorg. Chem.*, 1977, **16**, 943–945.

107. N. Miyanaga, T. Matsubayashi, T. Fukumoto, K. Yokoi, I. Watanabe, K. Murata, and S. Ikeda, *Chem. Lett.*, 1988, 487–490.

108. T. Miyanaga, T. Fujikawa, N. Matsubayashi, T. Fukumoto, K. Yokoi, I. Watanabe, and S. Ikeda, *Bull. Chem. Soc. Jpn*, 1989, **62**, 1791–1796.

109. M. Epple, L. Troger, and N. Hilbrandt, *J. Chem. Soc., Faraday Trans.*, 1997, **93**, 3035–3037.

110. S. A. Bartlett, P. P. Wells, M. Nachtegaal, A. J. Dent, G. Cibin, G. Reid, J. Evans, and M. Tromp, *J. Catal.*, 2011, **284**, 247–258.